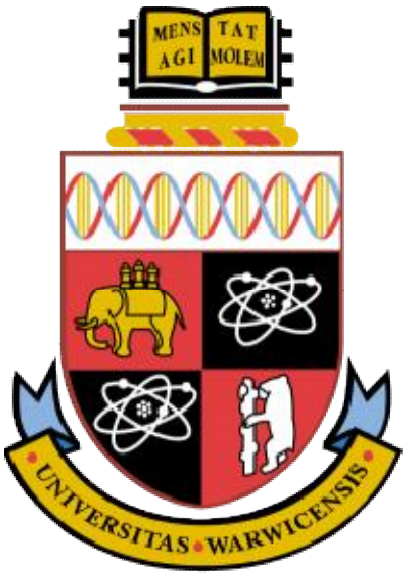

Radiative Heat Transfer for Modelling Fire and Fire Suppression

by

Ivan Sikic

Thesis

Submitted to the University of Warwick

for the degree of

Doctor of Philosophy

School of Engineering

March 2018

Table of contents

List of Figures

List of Tables

Acknowledgements

I would like to thank Prof. Jennifer Wen and Dr. Siaka Dembele (Kingston University London) for all their guidance and support throughout this project. Special thanks go to my sponsors FM Global and all at the Fire Research team for their technical advice and training (Drs. Yi Wang, Ankur Gupta, Prateep Chaterjee, Karl Meredith, Ning Ren, Dong Zeng, Marcos Chaos, Luwi Oluwayemisi, Sergey Dorofeev, and anyone I forgot). Thanks to our friendly Warwick Fire (and Kingston) PhD students and postdoctorates, particularly Drs. Kazui Fukumoto, Zaki Saldi, Madhav Rao for introducing me to the art of OpenFOAM programming. Last but not least, thanks to my parents for the support through thick and thin.

Declarations

This thesis is submitted to the University of Warwick in support of my application for the degree of Doctor of Philosophy. It has been composed by myself and has not been submitted in any previous application for any degree. The work presented (including data generated and data analysis) was carried out by the author except in the cases outlined below:

- Benchmark data and/or test cases provided by the literature, which are indicated by a reference number in tables, figures or body of text.

Abstract

Non-grey radiation modelling of non-scattering gas-phase combustion products is considered within the frame of FireFOAM, the turbulent flame solver part of the open source CFD platform OpenFOAM®. FireFOAM's built-in finite volume-based radiation solver (FVM) was modified to account for banded solutions of the radiative transfer equation (RTE). The author implemented six gas radiation property models: two grey and three non-grey variants the weighted-sum-of-grey-gases (WSGG) and a 'box' model based on the exponential wide band model (EWB), specially optimised for fire scenarios. The models were first tested and validated in a series of canonical pure-radiation scenarios, then used for runtime radiation calculations in large eddy simulations (LES) of methanol and heptane pool fires based on the experiments of Klassen and Gore (1992) and Weckman and Strong (1996), where the effects of turbulence-radiation interaction (TRI) were discussed. Finally, the author coupled the box model with a Mie theory-based radiation model accounting for the scattering and absorbing/emitting properties of lagrangian objects such as water droplets, ultimately to be used in future, full-physics fire suppression CFD simulations. The thesis highlights the fact that the differences in accuracy between the grey and non-grey approaches are less striking in the canonical pure-radiation scenarios than in the fire simulations. However, the non-grey WSGG approach offers much potential for fires where the mean beam length cannot be trivially estimated. Older and more CPU-efficient WSGG correlations performed just as well as newer ones in this particular open boundary fire context. The optimised box model offered CPU performance that is comparable to WSGG, and coupled with the Mie model, it showed promising results in a two-non-grey-phase radiation context. Overall, this work has been largely useful for the community of FireFOAM scientists and engineers (who now have access to these new gas radiation models via the Github repository), but also it has contributed to a better assessment of such well-known radiation models in fire scenarios that are more practical for CFD engineers seeking all-in-one solutions, than the decoupled approach usually favoured in radiation works.

Nomenclature

Acronyms

CFD	computational fluid dynamics
CK	correlated k
DOM	discrete ordinates method
DTM	discrete transfer method
EDC	eddy dissipation concept
EWB	exponential wide band
FDS	Fire Dynamics Simulator
FVM	finite volume method
HRR	heat release rate
LES	large eddy simulation
MBL	mean beam length
MC	Monte-Carlo
NIST	National Institute of Standards and Technology
RANS	Reynolds-averaged Navier-Stokes
RE	ray effects
RTE	radiative transfer equation
RTM	ray tracing method
SLW	spectral line weighted sum of grey gases
SNB	statistical narrow band
SPH	smoke point height
WSGG	weighted sum of grey gases

Latin symbols

a	WSGG weighting coefficient
A	absorptance (cm^{-1}) or area (m^2)
b	EWB pressure parameter

c_0	speed of light in vacuum ($3x10^8$ m/s)
Cp	specific heat capacity
d	diameter of droplet (m)
D	diameter of pool fire (m)
E	energy (J)
F	fractional blackbody energy function
fv	soot or water droplet volume fraction
G	total incident radiation (W/m²)
h	Planck constant ($6.626x10^{-34}$ J.s)
h_s	specific enthalpy (J/kg)
h_c	enthalpy of combustion
H	height (m)
I	total radiative intensity (W/m²)
k	WSGG pressure-absorption coefficient ($m^{-1}.atm^{-1}$)
k_B	Boltzmann constant ($1.38x10^{-23}$J/K)
m	complex index of refraction of particulate phase
n	complex index of refraction of gas or EWB pressure parameter
p	total pressure (Pa or atm)
Pr	Prandtl number
q'''	conductive heat source term (W/m^3)
q_r''	radiative heat flux (W/m^2)
Q	heat release rate (W) or (absorption, scattering, extinction) efficiency
R	radius (m)
s	spatial position (m) or unit vector
S	mean beam length (m) or unit area (dS, m²)
T	temperature (K)
u	velocity (m/s)

V volume (m^3)

x spatial position (m)

X mass path length (g/m^2) or mole fraction

X_r total radiant power fraction

Y mass fraction

Greek symbols

α thermal diffusivity (m^2/s) or absorptivity or EWB integrated band intensity ($cm^{-1}/(g/m^2)$)

β EWB band overlap parameter

κ absorption coefficient (linear: m^{-1}, mass abs. coeff.: $1/(g/m^2)$)

ε emissivity

τ transmissivity or EWB optical thickness at band head

θ polar angle (sr)

φ azimuthal angle (sr) or unit radiative flux ($d^5\varphi$, W/m^2)

ρ density (kg/m^3or g/m^3)

λ wavelength (μm)

η wavenumber (cm^{-1})

$\Delta\eta_e$ box model equivalent band width (cm^{-1})

v kinematic viscosity (m^2/s) or frequency (Hz) or EWB energy level

σ scattering coefficient (m^{-1})

σ_{SB} Stefan-Boltzmann constant ($5.67x10^{-8}$ $W/m^2/K^4$)

ω gas specie/soot formation term or EWB bandwidth parameter (cm^{-1})

Φ radiative scattering phase function

Θ radiative scattering angle (sr)

Ω solid angle (sr)

Subscripts

0 reference (e.g. for temperature)

λ	electromagnetic spectrum(wavelength-dependent)
η	electromagnetic spectrum (wavenumber-dependent)
b	blackbody/Planck law
g	gas
w	water vapour or wall
c	carbon dioxide
i	angular direction or spatial position
j	grey gas or band or spatial position
L	lower (band limit)
r	radiation
s	soot
t	turbulence
U	upper (band limit)

Chapter 1 - Introduction

1.1. Radiative properties of non-grey gases in fires

Thermal radiation in combustion systems with high temperatures is an important mode of energy transport that needs to be considered for both fundamental understanding and implementation in practical combustion systems. In the context of fire applications, thermal radiation plays a crucial role in the coupling of combustion, heat transfer, and fluid dynamics in fires and fire suppression. Radiation can significantly affect the flame temperature, which ultimately affects the yield of combustion products, and hence the concentrations of gaseous species and particulates that influence emission, absorption and scattering of radiation [1-2]. Pool fires, a main focus in this work, are characterised by buoyant diffusion flames developing over a horizontal fuel surface (Fig. 1-1). They are the most basic type of fires and relevant in many domestic or industrial scenarios [3-4]. At the pool surface, the fuel (liquid or gaseous) receives heat from the flame above, influencing the burning rate. A fraction of the heat feedback originates from thermal radiation, which generally increases with both fire size and flame luminosity [5]. Even in pool fires as small as 30cm in diameter, with non-luminous flames (e.g. methanol), radiative feedback represents a large fraction of the energy received by the pool surface [6]. Accurate representation of radiative heat transfer mechanisms in pool fires is therefore essential for realistic fire simulations, but the radiative properties of gaseous combustion products represent a serious challenge in computational fluid dynamics modelling (CFD).

Thermal radiation consists of electromagnetic waves with a spectral range covering the ultraviolet (UV), visible and infrared, between 0.1 and 100 microns in wavelengths, or 100 to 100,000 cm^{-1} in wavenumbers. In a typical fire environment, the participating medium consists of combustion gases (H_2O, CO_2, CO) and soot particles. When thermal radiation interacts with such a participating gaseous medium, the energy spectrum consists of discrete and irregularly-spaced lines which correspond to the absorption or emission of energy within the participating medium. Gas molecules gain or lose energy through absorption or emission of photons, which travel through vacuum at various wavelengths, so that the variation of energy is $\Delta E = h\nu$. Molecules have various degrees of freedom depending on their geometry, hence energy transfer by radiation may arise from molecular vibration, rotation, or combined rotation and vibration [7]. At macroscopic scale, the energy loss from an incident ray propagating in the medium is quantified by an absorption coefficient, which varies strongly with wavelength as per the number of absorption lines and the strength of each of them. This characteristic, called non-greyness, is extremely strong in combustion gases like carbon dioxide or water vapour, which have nearly a million absorption lines in the thermal radiation range (Fig. 1-2) [8]. This means that in order to obtain the radiative source term of the energy equation, the radiative transfer equation (RTE) should be solved as many times as there are lines, and that is only for one position and one direction of energy propagation. The prohibitive cost of this line-by-line approach (LBL) strictly confines it to generation of benchmark data, making band and global models more desirable for practical applications.

Fig. 1-1: Large scale hydrocarbon pool fire (internet at large)

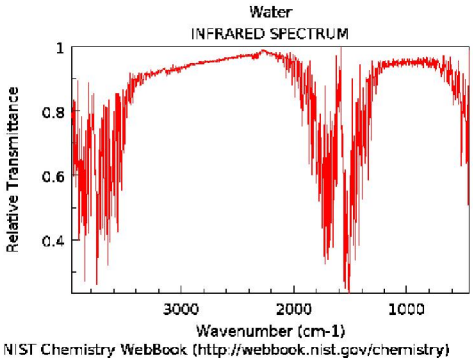

Fig. 1-2: Small portion of the absorption-emission spectrum of water vapour (NIST)

At first approximation, band models were developed to deal with portions of the spectrum at once rather than individual lines. The accuracy depends much on the spectral resolution, hence for this family of models one may distinguish the narrow band (higher resolution, Fig. 1-3) and wide band (lower resolution, Fig. 1-4) approaches, which both simplify the spectral dependency in a considerable way. Still, they mostly remain too involved for CFD applications, at least if the goal is to perform coupled calculations of the radiation and reactive flow fields. For decoupled calculations, narrow band approaches such as the statistical narrow band (SNB) and the narrow band correlated-k (NBCK) methods provide a good compromise between accuracy and computational time in fire conditions [9]. Wide band models like the exponential wide band (EWB) are more practical and can retain some spectral information, but in their spectral form they remain too expensive for many CFD applications, and may not directly yield absorption coefficients [10] (the RTE can be formulated in terms of transmissivity rather than absorption coefficients, but many CFD solvers use the latter formulation).

Besides band models, global models deal with the entire spectrum at once, with more or less sophistication. The more accurate global models are the full-spectrum CK (FSCK) [11], which is based on a re-arrangement of wavenumbers, or the spectral line weighted-sum-of-grey-gases (SLW, a refinement from the WSGG discussed hereafter) [12]. Both have

experienced major developments in recent years; however they are still not suitable for coupled simulations in large scale CFD applications due to relatively high computational costs (although progress has been recently reported in [13]). These methods contrast with the very crude grey approximations (single constant absorption coefficient for the whole spectrum), which are fastest but generally lead to poor predictions in combustion applications [14]. Alternatively to just one grey gas, several grey gases can be combined to reconstruct the total (spectral-integrated) properties of a real gas. Such is the approach of the weighted-sum-of-grey-gases (WSGG) [15], which curve-fits the total emissivity (spectral-integrated) of a real gas with polynomials. The polynomial coefficients are the radiative properties of a few fictitious grey gases, determined for certain conditions of temperature and concentrations. The total emissivity is determined beforehand, from a band model or measurements or both combined, hence the WSGG involves no actual spectral data. This flexible, fast, and easy to implement method is popular in CFD codes, but its accuracy is debated in the radiation literature (see next chapter). Also, due to its lack of spectral information the WSGG cannot be coupled with another non-grey phase (e.g. water droplets).

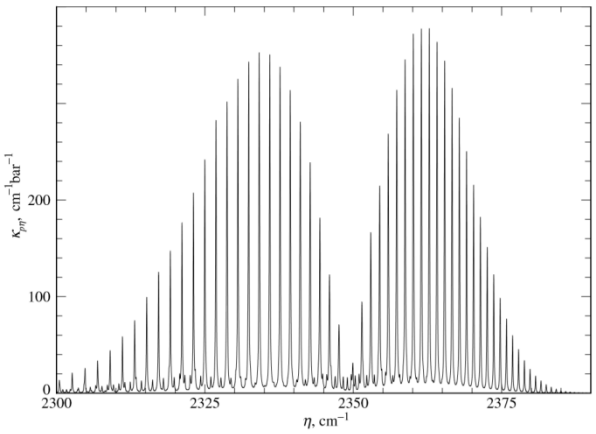

Fig. 1-3: Narrow band modelling of the 4.3µm rotation-vibrational region of CO_2 (reproduced from [7])

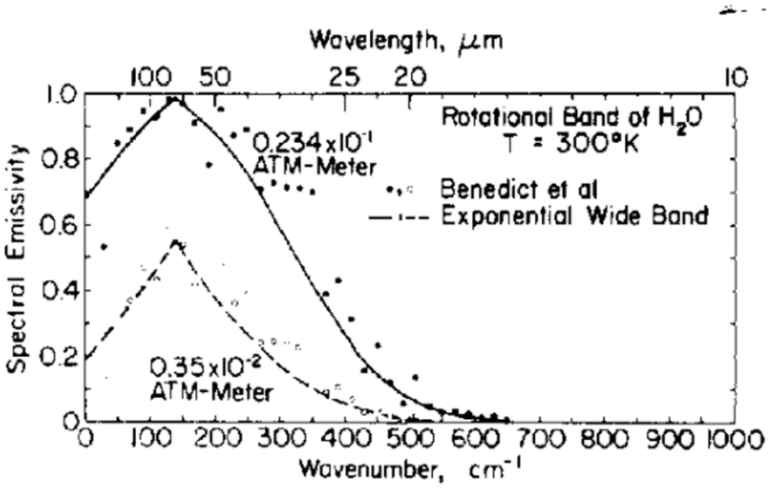

Fig. 1-4: Wide band modelling of the 71µm (140cm^{-1}) rotational region of H_2O (reproduced from [16])

1.2. Radiative properties of particulates in fires or fire suppression

Besides the gas phase, the presence of particulate media like soot (present in most fires and responsible for flame luminosity) or the liquid water droplets from a quenching system such as sprinklers or water sprays can radically alter the radiative properties of fires. Particulate media introduce radiative scattering [7], a group of three non-grey phenomena which describe the possible interactions between a particle and an incident ray: diffraction (ray deviated without contact), reflection (ray deviation after contact) and refraction (like reflection, with partial absorption). Depending on the new direction of the scattered ray, scattering can contribute positively or negatively to radiative intensity. The Mie theory describes the ensemble of these behaviours in a general way, by calculating the amplitudes of the electric and magnetic fields that constitute electromagnetic radiation. This model is thus very rigorous, but also very complex. Mie theory is advantageously replaced with simpler methods in some cases.

The soot particles usually produced by hydrocarbon fires are small enough to fall under the Rayleigh limit which treats the particulate phase as continuous. In this case the radiative properties of soot particles are described by their volume fraction [17]. As a further simplification, unlike in molecular gases the soot absorption spectrum is continuous (no transparent windows), and it is possible under certain conditions to use a Planck (grey) approximation with good accuracy [18,19]. The Rayleigh approach is however not valid for larger, coal-like soot particles for which Mie theory must be considered. Liquid droplets such as found in water sprays also require Mie modelling. The radiative properties of droplets change importantly with particle size; even if a monodisperse distribution is initially injected into the fire, droplets characteristics will change as a result of heat transfer. Moreover, heated-up droplets eventually evaporate, thus completely changing the gas mixture and its absorptive properties, and then it all changes again as temperature decreases. This problem has not yet been investigated in CFD.

1.3. Motivation, aims & objectives and contribution of the thesis

The main goal of the current thesis is to develop a simulation tool based on models capable of handling multiphase (gas, soot, liquid droplets), non-grey radiation that remains computationally efficient to be coupled with CFD calculations of the reactive flow field as well as a water spray in fire suppression. The software environment is the open-source fire modelling project FireFOAM, created in 2008 by FM Global, who supported this work technically and financially. Based on the C++ toolbox OpenFOAM [20], FireFOAM performs large eddy simulations (LES) of turbulent diffusion flames using different submodels for turbulence, combustion, sooting, pyrolysis, etc. At the time this PhD started in 2014, the radiation modelling capability was limited to grey gas models and a "constant scatter" model. Two scenarios were identified, for which the radiation package would have to be improved: fire simulations with soot and fire suppression simulations with water droplets (and possibly soot). For fire simulations without water droplets suppression, a grey soot radiation model is easy to couple with a non-grey gas model, as the soot absorption coefficient is simply added in each gas band. A non-grey global gas radiation model like the WSGG could potentially

provide a good accuracy/computing times compromise. In the fire suppression scenario, the absorption coefficients of the liquid and gaseous phases are both non-grey. Hence to be added in the RTE, both phases must use the same spectral intervals. Since the WSGG gas model does not retain the physical information on the actual absorption bands of the gas, a wide band based box model is adopted in the current thesis to handle fire suppression scenarios involving gases and water droplets. The exponential wide band (EWB) model uses a small number of bands in each gas species (CO_2, H_2O, etc.). In each band an averaged absorptance is calculated, from which one can extract an absorption coefficient averaged over an equivalent bandwidth. This method, called the box model, or stepwise-grey wide band model [21], offers significant computational gain from the spectral formulation of the EWB, since for each band the absorption coefficient has a single average value instead of being a continuous function of wavenumber, which is analogous to a grey gas in WSGG. However unlike the WSGG, a box model relies on the assumption of an isothermal and homogeneous medium, hence to fit the inhomogeneous conditions of fires it must be scaled with a Curtis-Godson type method. Also, a box model may work with different band limits than the Mie theory model for water droplets.

The WSGG and EWB-box models were pioneered decades ago and have been improved over time. There are many WSGG correlations in the literature, obtained from older and newer spectral databases, developed for specific applications. However their accuracy in the particular context of pool fire CFD have been seldom assessed - at least some of the newest models have not been, to the best of this author's knowledge. Moreover, the works that did perform such studies have undertaken decoupled radiation/fluid flow approaches, whereas this work is aiming for an assessment in fully coupled simulations. For the box model, there are equally as few works available in the pool fire context, and on the topic of fire suppression, it is almost certain that the coupling of a box model with a Mie theory has not been attempted before. Hence the current work will make an important contribution not only to the growing community of FireFOAM users, but to the fire community in general.

In the thesis, five WSGG models (three banded, and two grey) and three box models (two with variable band limits, and one with fixed bands) have been implemented and investigated by this author in FireFOAM version 2.2.x for fire applications. The Mie theory model was implemented by FM Global at the same time and tested for liquid-only radiation scenarios. Eventually, in the last phases of this project the fixed bands box model was coupled with the Mie model in the developing version FireFOAM-dev available on the Github platform (https://github.com/firefoam-dev).

1.4. Layout of the thesis

The thesis will be structured as follows. Chapter 2 will be a summarised overview of the literature on the WSGG, the EWB/box model, experimental and CFD works with radiation in pool fires, and the common techniques for numerical solutions of the RTE. Chapter 3 will describe the mathematical modelling techniques. Chapter 4 will contain the results and discussion of the implemented WSGG and box models, organised in two sections: WSGG models in static media (4-1) and box models in static media (4-2). Section 4-1 will start with

an assessment of FireFOAM's RTE solver in purely grey and transparent media to gauge the accuracy independently of any absorption-emission model, and then the accuracy assessment of the five WSGG implementations will be carried out through an exhaustive range of 1D, 2D and 3D scenarios involving only radiative heat transfer. Section 4-2 will investigate the three box models with the same test cases as 4-1, including a detailed study of the influence of path length in box model calculations. Chapter 5 will feature the WSGG and box models in simulations of sooty and non-sooty pool fires of different sizes. Mesh grid sensitivity will be discussed, the gas radiation models will be compared, and guidelines will be issued on CPU efficiency and the appropriate choice of gas radiation model. Chapter 6 will present the box-Mie models coupling in two-phase (gas-droplet) static media, with preliminary results for a set of 1D liquid-only scenarios, and then for a 3D enclosure with a gas phase mixed with a liquid phase. Finally, conclusions and perspectives for future work will be discussed in Chapter 7.

Chapter 2 - Literature review

This chapter presents an overview of the literature available on the solution methods of the radiative transfer equation (RTE), the weighted-sum-of-grey-gases (WSGG), the exponential wide band (EWB) and box models, and radiation modelling in pool fires.

2.1. Overview of solution methods for the radiative transfer equation (RTE)

The RTE is a first-order difference equation with an integral term. If radiative heat transfer is considered instantaneous (an electromagnetic wave propagates at the speed of light), the transient term may be neglected and the general form of the RTE may be written as:

$$n^2(\boldsymbol{s},\boldsymbol{x})\frac{d}{dx}\left(\frac{I_\lambda}{n^2}\right)(\boldsymbol{s},\boldsymbol{x}) = -(\sigma_\lambda+\kappa_\lambda)I_\lambda(\boldsymbol{s},\boldsymbol{x}) + \kappa_\lambda n^2(\boldsymbol{s},\boldsymbol{x})I^0_{b,\lambda}(T) + \frac{\sigma_\lambda}{4\pi}\int_0^{4\pi}\Phi_\lambda(\boldsymbol{s}',\boldsymbol{s})\,I_\lambda(\boldsymbol{s},\boldsymbol{x})d\Omega' \quad (2.1)$$

This equation has three dependencies of space and one of solid angle. The wavelength subscript denotes Eq. (2.1) may be solved for a single wavelength, or band, or the entire spectrum, depending on the spectral modelling strategy. An RTE solver thus generally discretises the spatial and/or angular domains, leaving the spectral properties to a sub-model. For heat transfer engineers, the interest is usually less in spectral information than in total properties such as the radiative heat flux or its divergence. To obtain these, it is not always mandatory to use an actual RTE solver. For example, a constant radiative fraction may be inputted by the user to yield the radiative source term trivially [22]; or an optically thin approximation (OTA) may directly yield the source term, assuming that the gas medium has a weak propensity to self-absorption, which means most of the radiative energy escapes to the surroundings [23]. In the opposite case, at the optically thick limit where self-absorption is strong, the P1 model assumes diffusive radiation where spherical harmonics replace the directional dependence of the RTE. Although the RTE is transformed into a second order difference equation this method saves significant computational time [24]. These fast methods contrast with the massive computational demands of the Monte-Carlo (MC) or ray tracing (RTM) methods based on statistical tracking of photons, which are thus more recommended for decoupled RTE calculations.

For CFD users, a more viable compromise comes with solid angle-based methods such as the discrete ordinates method (DOM) or the finite volume method (FVM) (both mathematically summarised in [25]). The DOM allows radiation energy to travel along discrete directions and is preferably used with a quadrature set. The FVM, on the other hand, integrates the radiative intensity over a solid angle, where the choice of subdivisions in each direction is arbitrary. Although relatively cheap in computational costs and relatively straightforward to use, both the FVM and DOM suffer a similar drawback known as ray effects (RE). Radiative intensity is a scalar field continuous in space, hence the discretisation of the angular space affects the solution accuracy in an analogous way a coarse mesh grid would for the Navier-Stokes equations. The problem is complicated by the interaction between the spatial mesh grid and the angular grid. If the domain's computational cells are large enough, solid angles may numerically "smeared" over the cells faces, reducing RE. This

phenomenon, also called false scattering, is thus responsible for the increase of RE when working with grid refinements (commonplace in CFD). Hence angular and spatial grid size should be increased simultaneously, which can lead to a much increased computational effort. The work to eliminate RE from CFD simulations with the DOM or FVM is ongoing and some methods have been proposed in [26-28], where alternative angular discretisation schemes are proposed to avoid direct grid increases. RE elimination is a separate area of work to gas radiation modelling, but throughout this thesis RE will be briefly mentioned when needed as they can greatly affect the quality of prediction of the radiative heat flux. FVM theory will be summarised in the Mathematical Modelling chapter as well.

2.2. The weighted-sum-of-grey-gases (WSGG) model

Hottel and Sarofim developed the WSGG method [15] to reproduce their own measurements of total emissivities and absorptivities with polynomial curve fits. The method evolved both with band models and spectroscopic techniques, as both could be combined to overcome each other's shortcomings. In the early 1980s Smith et al. released their well-known WSGG correlations obtained from the EWB model [29]. For a long time the WSGG was used like a grey model, since it is easy to obtain a grey equivalent absorption coefficient from Beer's law, if a mean beam length can be determined. Later on, in the early 1990s Modest [30] showed that the WSGG could be used to solve the RTE for each grey gas individually, giving way to the non-grey WSGG implementation. This method increases the computational time from the grey version but it has the advantage of avoiding mean beam length approximations. Soufiani and Djavdan [31] used the non-grey formulation, generated WSGG correlations from an accurate statistical narrow band model (SNB) and compared both in a furnace-like scenario. In the last few years, some WSGG correlations based on up-to-date spectral data and narrow band modelling have been developed for oxy-fuel combustion, as in Cassol et al. and Johansson et al. [32,33]. These two newer models have been very recently tested in oxy-fuel conditions by Kez et al. [55], where large differences were noticed, while the older correlations from Smith et al. [29] were deemed unreliable even for qualitative analysis. The Cassol and Johansson WSGG models have however not yet been assessed for fire applications, which is a knowledge gap this work will attempt to address.

On the topic of reliability, Smith et al. [29] studied the WSGG's sensitivity on the number of grey gases employed, finding that there was no significant improvement past three grey gases. Their updated coefficients offered better performance than older models, but lose some accuracy at lower temperatures and/or small pressure-path lengths. It is usually agreed [34-36] that the non-grey WSGG significantly improves the accuracy over grey models, even in the presence of soot and/or inhomogeneous media, while remaining computationally attractive. However Soufiani and Djavdan [31] noted poor WSGG performance in strongly non-isothermal media bounded by grey walls, as well as a tendency to underpredict the cold absorbing gas/hot emitting wall scenario (which does not happen in fires). Still in inhomogeneous media, the WSGG performance is also significantly inferior to more advanced gas radiation models [34, 35]. It could be argued, on the one hand, that [34,35] i) were not carried out using typical CFD solution methods and the radiation models may have behaved differently if coupled with a dynamic flow field, ii) the gas concentrations employed

in [34] are not necessarily representative of fire conditions, and iii) newer WSGG correlations than those employed in [35] may have given different results. On the other hand, it is true that a WSGG cannot ever be expected to be as accurate as an SNB model, but it could be used with confidence if its errors in typical fire scenarios were quantified, as proposed in [37]. Hence the idea for this work of implementing the older Smith et al. model, and the newer WSGGs by Cassol et al. [32] and Johansson et al. [33] for a comparative study in fire conditions with a CFD finite volume radiation solver. These models will be described in more detail in the next chapter.

2.3. Exponential wide band (EWB) and box models

The EWB model was developed in the 1960s by Edwards [38]. By 1970, it had been extended for non-isothermal or inhomogeneous media, notably by Chan and Tien [39] or Cess and Wang [40], and in 1975 Felske and Tien proposed a method to remedy the band overlap problem [41]. The treatment of the pure rotational band of water vapour was refined by Modak in 1978 [42]. While spectral databases were not as developed as they are nowadays, the EWB model was deemed accurate enough to generate WSGG coefficients (e.g. Smith et al. [29]), and there are examples of that exercise even recently, e.g. in [43]. The box model, first proposed by Penner [44], is a stepwise-grey (spectrally coarser) version of the EWB. Unlike what Soufiani of Djavdan [31] observed with the WSGG (previous section), Modest and Sikka noticed that the box model performs better for a colder gas absorbing radiation emitted by hot walls, than the other way around [45]. Elsewhere, Nilsson and Sundén noticed an important sensitivity of EWB parameters to path length in [46]. This later issue will be investigated exhaustively in this work. On computational efficiency, several studies aimed at speeding up the EWB as CFD applications started in the 1990s, notably Lallemant and Weber [47] who greatly simplified some of the more tedious aspects of the original EWB formulation. Multidimensional applications of the EWB/box model also appeared around that time, e.g. in [45] where the P1 model was used with the banded EWB formulation (stepwise-grey absorption coefficient, as opposed to the smooth absorption coefficient of the spectral EWB). By the mid-1990s, there are examples of coupled radiation and convective heat transfer calculations, but without combustion, using spectral or box model versions of the EWB with a P1 approximation, see for instance the works of Seo et al. [48], Nilsson and Sundén [49] or Kaminsky et al. [50]. Seo et al. notably used a Curtis-Godson scaling technique to account for inhomogeneous gas radiation but reported accuracy issues for strong temperature and concentration gradients. In a related study, an early example of EWB (and narrow band) calculations in fires was from Komornicki and Tomeczek [51] who constructed a synthetic 750kW natural gas flame from experimental measurements, hence performing decoupled calculations in the inhomogeneous gas and (non-scattering) soot mixture. Such works however predate the era of modern CFD software with finite volume methods.

2.4. WSGG and EWB/box models in CFD codes and fire simulations

Compared with radiation-only scenarios, modelling radiation in pool fires is more complex due to possible ray effects, turbulence-radiation interaction, or presence of cold soot for which grey approximations are invalid. Few studies assessed WSGG or EWB models in

CFD fire simulations where the radiation and flow fields are coupled. In 2004 Snegirev [52] compared grey and banded WSGG implementations in 30cm propane pool fires, coupling a Monte-Carlo (MC) RTE solver with a RANS approach and including a simplified turbulence-radiation interaction (TRI) correction. Overall the banded WSGG tended to reduce the over-prediction of radiant fluxes, consistently with the pure-radiation works from [34-36]. In 2005, Dembele et al. [37] tested a banded formulation of an older WSGG model by Truelove within the frame of RANS CFD. While neglecting the turbulence-radiation interaction (TRI) they achieved good overall agreement between the predicted temperatures using the WSGG and the benchmark SNB data. Some CFD studies have employed and investigated other gas radiation models (e.g. SNB, NBCK, FSCK) by either coupling or decoupling the radiation and flow fields in jet flames [53]. Few recent works have investigated the effects of various gas models in oxy-fuel combustion [54-55]. On the EWB, an early CFD study (1998) is due to Cumber et al. [56] who performed a fully coupled RANS CFD jet flame simulation with both a spectral and a banded implementation of the EWB model. Among their conclusions, they i) underlined the superior accuracy of the spectral EWB over the banded implementation in the highly inhomogeneous, non-isothermal flame, and ii) remarked that radiation predictions were reasonably but not overly impacted by the errors on temperature and specie fractions resulting from the combustion model. Nilsson and Sunden [49] did a CFD simulation of bio-fuel combustion using the EWB and P1, solving the momentum equation but not the specie fractions [49], concluding that radiation in that case was more driven by the soot volume fraction. Nilsson et al. followed that in 2003 by showing how to optimise the EWB formulation for faster CFD calculations [46], resulting in two box models which turned out to be at least ten times faster than the regular EWB formulation, but become very sensitive to mean beam length approximations. Cumber and Fairweather [57] again tested a spectral EWB implementation in CFD studies of flames with a discrete transfer method (DTM), remarking that the radiation and combustion fields had different cell size requirements, which may cause problems [57]. Hostikka et al. [58] performed wide band modelling of various methanol and methane flames with Fire Dynamics Simulator (FDS, a LES CFD code with a FVM radiation solver), with Planck-averaging of the absorption coefficient in each band. Their predicted radiative fluxes were at times significantly larger than their experimental measurements, and they attributed the error to temperature overprediction from the combustion model while stressing the necessity to separate the error sources. More recently, coupled CFD simulations of 30cm methanol, heptane and toluene fires with FireFOAM were published by Chen et al. [23,59] and Chaterjee et al. [18], which relied on grey gas and/or grey soot modelling. The total radiative fractions approached the experimental values of [4] but the radiative fluxes to the flame surroundings were not reported.

In light of Hostikka et al.'s remarks above, errors can come from the combustion model (temperature and gaseous mass fractions), the soot model (soot volume fraction), the grid sensitivity of these models, etc. Some researchers remove or separate the error sources with a two or three-step strategy, by e.g. performing fire experiments, then reproducing the temperature and specie fields with a simulation, then calculating radiation with different models. For example, Wakatsuki et al. [5] calculated an axial radiative intensity for an idealised 30cm methanol flame from experimental and FDS simulation data to investigate fuel

vapour radiation near the pool surface. Recently Consalvi and Liu [6] compared approximate gas radiation models for idealised methane fires with FDS, several variants of the CK method and a stepwise-grey wide band model (similar to [58]) which performed poorly in the fuel rich core. Another decoupled method consists of reconstructing the temperature, gas species and soot fields from scaling techniques, such as McCaffrey's correlations [60], thus creating a synthetic pool fire. Krishnamoorthy [61] recently used that method combined with the experimental data of [4] to construct synthetic 30cm heptane and toluene fires. A comparison was made for grey and non-grey implementations of the EWB, (Smith et al.'s [29]) WSGG, SLW and RADCAL coupled with a DOM solver. The results show that the solution method (grey or non-grey) has more influence on the radiant flux and source term than the model itself. The same 30cm toluene fire was further investigated by Consalvi et al. [19] who used an accurate SNBCK model with the FVM. They studied the separate influences of TRI/no TRI and banded/grey soot treatments with normal and lighter (more heptane-like) soot loadings. The neglecting of TRI resulted in an important decrease of the radiative heat flux and source term, whereas the error induced by the grey soot modelling was visible but not as important (the grey soot model was acceptable for the lighter soot loading). Consalvi et al.'s radiant flux at the pool surface held comparison with the experimental values of [4], however Krishnamoorthy's fluxes are largely underpredicted [61], despite also using a TRI correction. On the issue of TRI, Coelho issued exhaustive reviews in [62,63] and recommended the use of different types of correlations depending on the optical thickness. Among the works listed here, however, TRI corrections were often neglected (mentions of implemented TRI in [18,19,52,53,61] but not in [5,6,37,56,58,59]).

With the relative rarity of WSGG or EWB box model usage in pool fires, it is worth mentioning some recent CFD works in oxy-fuel combustion, such as Marzouk and Huckaby [64] who implemented an EWB/box model in ANSYS Fluent 13 and carried out radiation calculations for gas mixtures at typically high CO_2 and H_2O gas mole fractions with grey walls. The many band overlaps induced by the high mole fractions of each specie resulted in box model spectra of 20+ bands (CO_2 and H_2O have only 6 and 5 bands in the EWB). They however include detailed data of their box model absorption spectra calculations which may come useful to verify our own box model implementations. EWB and box models for oxy-fuel and furnace combustion are also studied within the last decade by Stefanidis et al. [65] (coupled convective and radiative heat transfer, but non-reactive flow).

2.5. Fire suppression by water sprays

This part of the current work is still at a preliminary stage and does not constitute the bulk of the study, hence this paragraph will provide only a brief overview of water spray modelling in scenarios relevant to this work. These scenarios can be classified under two categories, direct fire suppression and radiation shielding (between an emitting source and a target). As far as the radiative aspects are concerned there is more literature available with the latter case. The water curtain lends itself well to one-dimensional modelling, with the flame zone replaced by a blackbody-like boundary emitting the heat. Such 1D water curtains were tested with a two-flux scattering approximation coupled with the Mie theory by e.g. Dembele et al.

[66] or Buchlin [67]. More recently Dembele and Wen pointed out the possible inadequacy of blackbody assumption for optically thin flames with low soot production, stressing that their narrow band modelling of the real gas spectrum decreased the overprediction induced in some cases by the blackbody method [68]. Wide band modelling of two-phase radiation with the EWB and Mie theory has been performed by e.g. Yanga et al. [69] for a CO_2-H_2O-spray mixture, albeit in a non-CFD environment (finite-differences) and with 47 bands which remains arguably too much for CFD. Hostikka and McGrattan [70] performed a related study, implementing EWB wide band modelling in CFD software (FDS) with a finite volume radiation solver for a soot-liquid-gas mixture. Although they used a much smaller number of bands than Yanga et al. (six bands), with coupled tracking of droplets the simulation remained very computational-intensive. As a matter of fact, for a long time CFD codes appear to have largely relied on grey approximations for water mist radiation, just like with combustion gases [71]. At this time of writing this does not appear to have changed much, indeed some of the most recent works on water mist fire suppression with CFD codes like FireFOAM or FDS still use grey radiation [72], or non-grey absorption coefficients calculated externally [73]. In recent years the more sophisticated modelling appears to remain confined to costly, thus non-CFD, decoupled calculations such as [74-75] which use Monte-Carlo modelling. In this work, the FVM approach to radiation solving will also apply to the particulate phase radiation, where for each solid angle a corrective term (the asymmetry factor) is used as an approximation of the actual ray redirection from scattering. The motivation behind such an approach is that using the complex Mie phase function to account for droplets scattering is too time consuming and tedious. A realistic and time efficient approach is to employ a calculated asymmetry factor and then use its value in an approximated phase function such as Henyey-Greenstein.

Chapter 3 - Mathematical modelling

3.1. Governing equations

The Navier-Stokes equations are briefly outlined here, in their averaged form suitable for the large eddy simulation (LES) approach. The over-bars and tildes stand for spatial filtering and Favre averaging respectively.

Mass:

$$\frac{\partial \bar{\rho}}{\partial t} + \frac{\partial \bar{\rho}\widetilde{u_j}}{\partial x_j} = 0 \tag{3.1}$$

Momentum:

$$\frac{\partial \bar{\rho}\widetilde{u_i}}{\partial t} + \frac{\partial \bar{\rho}\widetilde{u_i}\widetilde{u_j}}{\partial x_j} = \frac{\partial \bar{p}}{\partial x_i} + \frac{\partial}{\partial x_j}\left\{\bar{\rho}(\nu + \nu_t)\left(\frac{\partial \widetilde{u_i}}{\partial x_j} + \frac{\partial \widetilde{u_j}}{\partial x_i} - \frac{2}{3}\frac{\partial \widetilde{u_k}}{\partial x_k}\delta_{ij}\right)\right\} + \bar{\rho}g_i \tag{3.2}$$

$$(i,j,k = 1,2,3)\ ,\ \delta_{ij} = \begin{cases} 1 & i = j \\ 0 & i \neq j \end{cases}$$

Gas species:

$$\frac{\partial \bar{\rho}\widetilde{Y_m}}{\partial t} + \frac{\partial \bar{\rho}\widetilde{u_j}\widetilde{Y_m}}{\partial x_j} = \frac{\partial}{\partial x_j}\left\{\bar{\rho}\left(D + \frac{\nu_t}{Sc_t}\right)\frac{\partial \widetilde{Y_m}}{\partial x_j}\right\} + \bar{\omega}_{m,g} + \bar{\omega}_{m,sf} + \bar{\omega}_{m,so} \tag{3.3}$$

$$(m = fuel, O_2, CO_2, H_2O)$$

Soot:

$$\frac{\partial \bar{\rho}\widetilde{Y_s}}{\partial t} + \frac{\partial \bar{\rho}\widetilde{u_j}\widetilde{Y_s}}{\partial x_j} = \frac{\partial}{\partial x_j}\left\{\bar{\rho}\left(D + \frac{\nu_t}{Sc_t}\right)\frac{\partial \widetilde{Y_s}}{\partial x_j}\right\} + \bar{\omega}_{s,f} + \bar{\omega}_{s,o} \tag{3.4}$$

Sensible enthalpy - Energy:

$$\frac{\partial \bar{\rho}\widetilde{h_s}}{\partial t} + \frac{\partial \bar{\rho}\widetilde{u_j}\widetilde{h_s}}{\partial x_j} = \frac{D\bar{p}}{Dt} + \frac{\partial}{\partial x_j}\left\{\bar{\rho}\left\{\alpha + \frac{\nu_t}{Pr_t}\right\}\frac{\partial \widetilde{h_s}}{\partial x_j}\right\} + \dot{q}''' - \nabla.\dot{q}''_r \tag{3.5}$$

$$\tilde{h}_s = \int_{T_0}^{\tilde{T}} \sum_m Cp_m(\tau)\tilde{Y}_m d\tau \tag{3.6}$$

$$\frac{Dp}{Dt} = \frac{\partial p}{\partial t} + u.\nabla p \tag{3.7}$$

$$\dot{q}''' = \omega_{fu,g}\Delta h_c - \omega_{s,o}\Delta h_{c,s} \tag{3.8}$$

Where $-\nabla.q''_r$ is the divergence of the radiative flux, or radiative source term, or radiative power dissipated per unit volume. This last term is responsible for the coupling of radiation energy expressing the conservation of total energy. At a spatial location $\boldsymbol{x}$ and time t the radiative source term is expressed as:

$$P_r(\boldsymbol{x}, t) = -\nabla.\dot{q}''_r = \int_0^\infty d\lambda \int_0^{4\pi} \nabla.I_\lambda(\boldsymbol{x}, \boldsymbol{s}) d\Omega \tag{3.9}$$

Where $\boldsymbol{s}$ is the direction vector of the unit solid angle $d\Omega$ through which the monochromatic radiative intensity I_λ propagates. I_λ is the solution of the radiative transfer equation [76].

3.2. The general radiative transfer equation

3.2.1. Blackbody intensity

A blackbody is an idealised object that perfectly absorbs and re-emits radiation at any wavelength. Thus continuous, the spectrum follows Planck's distribution. The monochromatic intensity of a blackbody at equilibrium temperature T is given by the law of Planck [76]:

$$I_{b,\lambda}(\boldsymbol{x},\boldsymbol{s},T) = \frac{2hc^2(\boldsymbol{x},\boldsymbol{s})}{\lambda^5}\left(\mathrm{e}^{\frac{\mathrm{hc}(\boldsymbol{x},\boldsymbol{s})}{\lambda \mathrm{k_B T}}} - 1\right)^{-1} = n^2(\boldsymbol{x},\boldsymbol{s}) I^0_{b,\lambda}(T) \tag{3.10}$$

Where $I^0_{b,\lambda}(T)$ is the isotropic blackbody intensity in vacuum (superscript *0*). The velocity of electromagnetic wave propagation in the medium, c, depends on the real part of the medium's complex index of refraction, i.e. $n(\boldsymbol{x},\boldsymbol{s}) = c_0/c(\boldsymbol{x},\boldsymbol{s})$ is the isotropic blackbody intensity in vacuum.

3.2.2. Radiative heat flux

The elementary flux of the elementary ray propagating at position $\boldsymbol{x}$, inside $d\Omega$ and normally to the elementary surface dS (Fig. 3-1) may be defined as [76]:

$$d^5\varphi_\lambda = I_\lambda dS d\Omega d\lambda \tag{3.11}$$

Where I_λ is the intensity at position $\boldsymbol{x}$ and may or may not be at radiative equilibrium. The variation of $d^5\varphi_\lambda$, for a small displacement $\boldsymbol{dx}$ along the path length, is:

$$d^6\varphi_\lambda = d^5\varphi_\lambda(\boldsymbol{x}+\boldsymbol{dx}) - d^5\varphi_\lambda(\boldsymbol{x}) \tag{3.12}$$

Clausius' relation of conservation yields:

$$n^2(\boldsymbol{x}+\boldsymbol{dx}) dS(\boldsymbol{x}+\boldsymbol{dx}) d\Omega(\boldsymbol{x}+\boldsymbol{dx}) = n^2 dS(\boldsymbol{x}) d\Omega(\boldsymbol{x}) \tag{3.13}$$

The flux of Eq. 3.11 can be redefined as:

$$d^5\varphi_\lambda(\boldsymbol{x}) = \frac{I_\lambda}{n^2}(\boldsymbol{x}) n^2(\boldsymbol{x}) dS(\boldsymbol{x}) d\Omega(\boldsymbol{x}) d\lambda \tag{3.14}$$

Hence:

$$d^5\varphi_\lambda(\boldsymbol{x}) = \frac{I_\lambda}{n^2}(\boldsymbol{x}) n^2(\boldsymbol{x}+\boldsymbol{dx}) dS(\boldsymbol{x}+\boldsymbol{dx}) d\Omega(\boldsymbol{x}+\boldsymbol{dx}) d\lambda \tag{3.15}$$

Writing Eq. 3.14 for **x** + **dx** and subtracting Eq. 3.15, the variation of the flux is:

$$d^6\varphi_\lambda = \frac{d}{dx}\left(\frac{I_\lambda}{n^2}\right) n^2(x) d\Omega(x) dV d\lambda \tag{3.16}$$

Where $dV = dSdx$, and the thermal radiative capacity was considered negligible compared with the thermal material capacity, which underlies the instantaneity of the propagation of radiation compared with the other heat transfer modes.

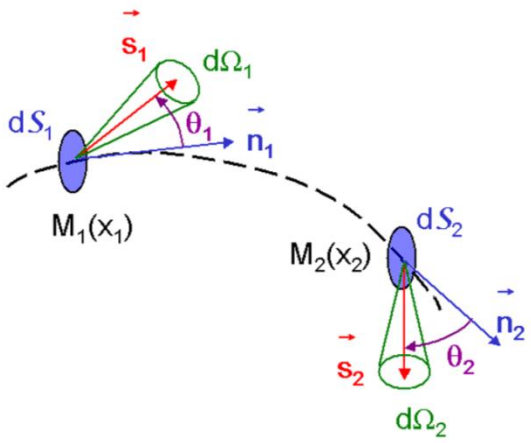

Fig. 3-1: Optical path between two arbitrary points in an arbitrary medium (reproduced from [76])

3.2.3. Absorption and spontaneous emission

The flux absorbed by the volume dV between two positions must be proportional to that volume, the solid angle, the spectral interval and the incident intensity:

$$d^6\varphi_\lambda^a = \kappa_\lambda I_\lambda d\Omega dV d\lambda \tag{3.17}$$

Where κ_λ is the monochromatic absorption coefficient (m^{-1}). The medium is also characterised by its monochromatic emission coefficient $\xi_\lambda(\boldsymbol{x})$, defined as:

$$d^6\varphi_\lambda^e = \xi_\lambda d\Omega dV d\lambda \tag{3.18}$$

At thermal equilibrium, the intensity in all directions and at any position is $n^2(\boldsymbol{x},\boldsymbol{s})I_{b,\lambda}^0(T)$ as defined earlier by the law of Planck. If the equilibrium is stable or near stable, the emitted flux is equal to the absorbed flux, hence the monochromatic emission coefficient $\xi_\lambda(\boldsymbol{x})$ can be expressed from Eq. 3.17 and 3.18 as:

$$\xi_\lambda = \kappa_\lambda n^2(\boldsymbol{x},\boldsymbol{s})I_{b,\lambda}^0(T) \tag{3.19}$$

Which yields the flux emitted by the medium inside the volume dV and solid angle $d\Omega$:

$$d^6\varphi_\lambda^e = \kappa_\lambda n^2(\boldsymbol{x},\boldsymbol{s})I_{b,\lambda}^0(T)d\Omega dV d\lambda \tag{3.20}$$

3.2.4. Scattering

Scattering can contribute positively and negatively to the flux $d^5\varphi_\lambda$ (see Eq. 3.11) i.e. a ray initially in the direction of $\boldsymbol{s}$ can be deviated away (hence contributing to its extinction between $\boldsymbol{x}$ and $\boldsymbol{x}+\boldsymbol{dx}$), or a ray initially directed elsewhere than $\boldsymbol{s}$ can be deviated within the

solid angle $d\Omega$ (Fig. 3-2). The first case, subscripted *d*-, is analogous to absorption, hence it can be characterised by a monochromatic scattering coefficient σ_λ (also in m^{-1}) defined by:

$$d^6\varphi_\lambda^{d-} = \sigma_\lambda I_\lambda d\Omega dV d\lambda \tag{3.21}$$

In the second case, let $\boldsymbol{s}'$ be the initial direction of the ray reaching position $\boldsymbol{x}$ and $\boldsymbol{s}$ the new direction of the ray exiting at $\boldsymbol{x}+\boldsymbol{dx}$. The ray scattered in a random direction is $\sigma_\lambda I_\lambda d\Omega' dV d\lambda$. The probability P for the incident flux to scatter within $d\Omega$ must depend on a phase function $\Phi_\lambda(s', s)$ veryfying:

$$P = \frac{d\Omega}{4\pi}\Phi_\lambda(\boldsymbol{s}', \boldsymbol{s}) \tag{3.22}$$

The flux $d^6\varphi_\lambda^{d+}$coming from all directions and scattered constructively by the volume dV inside the solid angle $d\Omega$, is defined by:

$$d^6\varphi_\lambda^{d+} = \frac{\sigma_\lambda}{4\pi} dV d\Omega d\lambda \int_0^{4\pi} \Phi_\lambda(\boldsymbol{s}', \boldsymbol{s}) I_\lambda(\boldsymbol{s}') d\Omega' \tag{3.23}$$

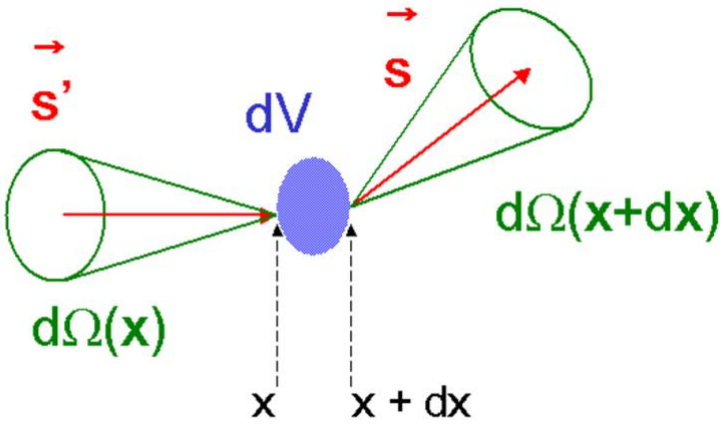

Fig. 3-2: Radiative scattering from unit volume *dV* (reproduced from [76])

3.2.5. Energy conservation

Finally, the radiative transfer equation (RTE) is constructed from the terms defined above. If the flux variation though dV (Eq. 3.16) is the sum of the absorbed flux (Eq. 3.17), the emitted flux (Eq. 3.20) and the two flux contributions due to scattering (Eq. 3.21 and 3.23), then the RTE takes the form:

$$n^2(\boldsymbol{s}, \boldsymbol{x}) \frac{d}{dx}\left(\frac{I_\lambda}{n^2}\right)(\boldsymbol{s}, \boldsymbol{x}) =$$
$$-(\sigma_\lambda + \kappa_\lambda) I_\lambda(\boldsymbol{s}, \boldsymbol{x}) + \kappa_\lambda n^2(\boldsymbol{s}, \boldsymbol{x}) I^0_{b,\lambda}(T) + \frac{\sigma_\lambda}{4\pi}\int_0^{4\pi} \Phi_\lambda(\boldsymbol{s}', \boldsymbol{s})\, I_\lambda(\boldsymbol{s}, \boldsymbol{x}) d\Omega' \tag{3.24}$$

3.3. Non-scattering media

For molecular gases such as combustion products, the refraction index can be set to unity, the exact value in vacuum, hence $I^0_{b,\lambda} = I_{b,\lambda}$. Scattering is also negligible, which cancels out

the integro-differential term from Eq. 3.24, and the scattering coefficient which, with the absorption coefficient, contributes to extinction. The RTE reduces to an ordinary difference equation with constant term (i.e. blackbody radiation is only a function of temperature, which is always known locally in the simulation):

$$\boldsymbol{s}.\nabla I_\lambda(\boldsymbol{s},\boldsymbol{x}) = \kappa_\lambda(I_{b,\lambda}(T) - I_\lambda(\boldsymbol{s},\boldsymbol{x})) \tag{3.25}$$

Where κ_λ is the linear monochromatic absorption coefficient (m^{-1}). The radiative source term defined in Eq. 3.9 may now be rewritten as:

$$-\nabla.\dot{q}''_r = \int_0^\infty \kappa_\lambda \left(4\pi I_{b,\lambda} - \int_0^{4\pi} I_\lambda d\Omega\right) d\lambda \tag{3.26}$$

The total radiant power dissipated through a volume by a source can be obtained by a volume integration of the source term, but also by a surface integration of the flux at radiative equilibrium ($q''_{net} = q''_{incident} - q''_{background}$) since the flux must verify the divergence theorem.

3.4. Solutions of the non-scattering RTE

The non-scattering spectral RTE (Eq. 3.25) is solved along a line of sight, or optical path. At a distance L from the origin, if the medium between 0 and L is isothermal and homogeneous, then an analytical solution is given:

$$I_\lambda(L) = I_\lambda(0)e^{-\kappa_\lambda L} + I_{b,\lambda}(1 - e^{-\kappa_\lambda L}) \tag{3.27}$$

Where the non-dimensional product $\kappa_\lambda L$ is the optical thickness of the medium at wavelength λ. An absorption line with $\kappa_\lambda L >> 1$ is opaque, respectively transparent if $\kappa_\lambda L << 1$. The quantity $e^{-\kappa_\lambda L}$ is the spectral transmissivity, or Beer's law, expressing the decrease of radiative energy as it traverses the absorbing medium. In the general case of an inhomogeneous or non-isothermal medium Beer's law generalises to:

$$\tau_\lambda = e^{-\int_0^L \kappa_\lambda(l)dl} \tag{3.28}$$

In Eq. 3.28 the integration of the optical depth between the origin and the optical path is only possible along a line of sight. CFD solvers which deal with multidimensional problems must adopt an approximation called the uncorrelated method. Rewriting the exact (correlated) solution of Eq. 3.27 in terms of transmissivity, for a path discretised in i elements between 0 and n, yields [33]:

$$I_{\lambda,n} = I_{\lambda,0}\tau_{\lambda,0\to n} + \sum_{i=0}^{n-1} I_{b,\lambda,i+1/2}\left(\tau_{\lambda,i+1\to n} - \tau_{\lambda,i\to n}\right) \tag{3.29}$$

The uncorrelated solution retains history only from the previous neighbouring cell:

$$I_{\lambda,n} = I_{\lambda,n-1}\tau_{\lambda,n} + I_{b,\lambda,n-1/2}\left(1 - \tau_{\lambda,n}\right) \tag{3.30}$$

In Eq. 3.30 the length of the cell replaces the actual path length. Assuming temperature, mole fractions, etc. are uniform in each cell, this allows local computations of the absorption

coefficient, but a grid dependency may be introduced in inhomogeneous media. For gas radiation models where a path length is required to calculate the absorption coefficient, the mean beam length (MBL) is a common approximation.

3.5. Mean beam lengths

First developed by Hottel [7], the idea is that from the perspective of an elementary black surface, there is no difference whether incident radiation is coming from all directions within a hemisphere or a distant emitting object, hence a certain hemisphere radius R can be defined such as R is equal to a mean beam length S (Fig. 3-3). MBL are usually not trivial to calculate directly and are distinguished between geometrical MBL and spectral-averaged MBL. Geometrical MBL are calculated at the optically thin limit, where energy escapes easily from the medium to its (black) surroundings. The geometric MBL is defined by $S_0 = 4V/A$, where V and A are the volume and area of the radiating medium. Spectral-averaged MBL, on the other hand, rely on Hottel's observation that the spectral radiative flux is not very sensitive to the spectral fluctuations of S, hence the MBL can be made independent from the spectral absorption coefficient with reasonable accuracy [7]. Further empirical observations have confirmed that the ratio between the spectral-averaged and geometric MBL is close to 0.9, hence the spectral-averaged MBL may be written as:

$$S \approx 0.9S_0 = 3.6V/A \tag{3.31}$$

In [7] Modest gives a table of MBL for various geometries. The MBL is easy to calculate for e.g. participating media entirely filling an enclosure of simple geometry, or a 1D slab of thickness L (in which case $S = 1.8L$). It is less easy in the case of a pool fire (the methods from this author and others' works will be discussed in the dedicated chapter), and it gets further more difficult for freely spreading fires whose shapes are irregular and change with time. Even with just pure radiation inside 2D or 3D box scenarios, the MBL method may introduce errors (see next chapter).

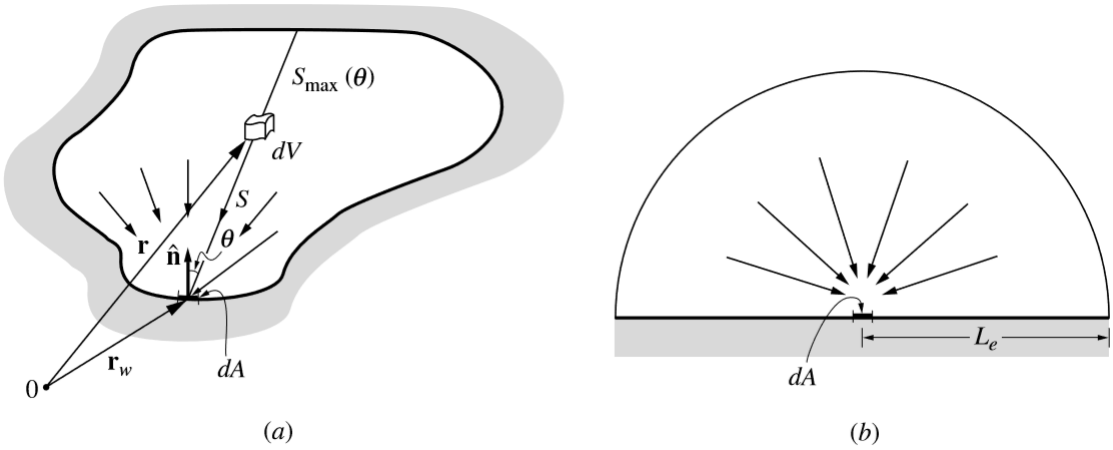

Fig. 3-3: Isothermal gas volume radiating to surface element for (a) an arbitrary gas volume, and (b) for an equivalent hemisphere radiating to the centre of its base where L_e = mean beam length (reproduced from [7])

3.6. Angular and Spatial discretisation of the non-scattering RTE

The finite volume (FVM) method is the mathematical tool of choice for solving most equations in OpenFOAM, hence in FireFOAM, such as the Navier-Stokes equations (Eq. 3.1-3.8 above). The P1 and optically thin approximation methods are available in FireFOAM, giving direct access to the radiative source term without actual solution of the non-scattering RTE (Eq. 3.25) but these ready solutions only work for the optically thin and optically thick limits, whereas the FVM is for any thickness. Called "fvDOM" in the code, the method integrates Eq. 3.25 over the computational cell volume V_{ijk} and solid angle Ω^l, respectively expressed in Cartesian and spherical coordinates. For the latter, the polar angle θ is between the z axis and the xy plane, and the azimuthal angle φ is between the x and y axes. Subdivisions in each angular direction determines Ω^l, portion of the total solid angle equal to 4π. Eq. 3.25 thus becomes:

$$\int_0^{\Omega^l}\int_0^{V_{ijk}} \boldsymbol{s}.\nabla I_\lambda(\boldsymbol{s},\boldsymbol{x})dVd\Omega = \int_0^{\Omega^l}\int_0^{V_{ijk}} \kappa_\lambda(\boldsymbol{x})(I_{b,\lambda}(\boldsymbol{x}) - I_\lambda(\boldsymbol{s},\boldsymbol{x}))\,dVd\Omega \tag{3.32}$$

The divergence theorem can be used to replace the volume integration on the left side with a surface integration on all 6 faces. Assuming the intensity is equal on each face, the integral can be replaced with a summation. Also, if the intensity is constant inside V_{ijk} and on the solid angle Ω^l, then:

$$\sum_{m=1}^{6} A_m I_{\lambda,m}^l \int_0^{\Omega^l}(\boldsymbol{s}.\boldsymbol{n}_m)d\Omega = \kappa_{\lambda,ijk}\left[I_{b,\lambda,ijk} - I_{\lambda,ijk}^l\right]V_{ijk}\delta\Omega^l \tag{3.33}$$

Where $I_{\lambda,ijk}^l$ is the monochromatic intensity in the direction l, $I_{\lambda,m}^l$the intensity on the face m, $\delta\Omega^l$ the solid angle corresponding to direction l, $A_m$the area of the face m, $\boldsymbol{n}_m$ the unit vector normal to face m. $I_{\lambda,m}^l$is calculated with a Gauss linear upwind, second order scheme. To provide closure, the following boundary condition is used, where walls are assumed to be diffusive but can be nonblack (i.e. partially reflective):

$$I_{\lambda,w}^l = \varepsilon_{\lambda,w}I_{\lambda,b,w} + \frac{1-\varepsilon_{\lambda,w}}{\pi}\sum_{D_w^{l'}<0} I_{\lambda,w}^{l'}\left|D_w^{l'}\right| \tag{3.34}$$

Where

$$D_w^{l'} = \int_0^{\delta\Omega^l}(\boldsymbol{s}.\boldsymbol{n}_w)d\Omega \tag{3.35}$$

The first term on the right hand side of Eq. 3.34 is the intensity emitted by the wall, where $\varepsilon_{\lambda,w}$ is the monochromatic wall emissivity, i.e. the ratio of the energy emitted by the surface over the energy emitted by a blackbody at the same temperature, both integrated over all directions of space. The wall emissivity is sometimes called emittance to avoid confusion with the gas emissivity, defined in the next section. If the wall is black ($\varepsilon_{\lambda,w} = 1$), the reflective term (second-right) cancels out. n_w is the unit vector normal to the wall. The constraint $D_w^{l'} < 0$ means that only the directions incident to the wall are considered in the reflective term.

3.7. Weighted-sum-of-grey-gases (general formulation)

The WSGG is a relatively simple but powerful way of modelling the total radiative properties of a gas. From the spectral transmissivity (Eq. 3.28), the spectral emissivity ε_λ and spectral absorptivity α_λ are defined as:

$$\alpha_\lambda(0 \to L) = \varepsilon_\lambda(0 \to L) = 1 - \tau_\lambda = 1 - e^{-\int_0^L \kappa_\lambda(l)dl} \tag{3.36}$$

The total emissivity and total absorptivity are obtained by spectral integration, but then they are no longer rigorously equal since they have different temperature dependencies. Total emissivity thus depends only local gas temperature:

$$\varepsilon(T_g, L) = \frac{1}{I_b(T_g)} \int_0^\infty \left(1 - e^{-\int_0^L \kappa_\lambda(T_g(l))dl}\right) I_{b,\lambda}(T_g) d\lambda \tag{3.37}$$

Whereas the total absorptivity:

$$\alpha(T, T_g, X) = \frac{1}{I_b(T)} \int_0^\infty \left(1 - e^{-\int_0^L \kappa_\lambda(T_g(l))dl}\right) I_{b,\lambda}(T) d\lambda \tag{3.38}$$

Where T can be either the gas temperature T_g or the wall temperature T_w [7]. Hence, the total absorptivity depends on the spectral structure of the incident radiation intensity and cannot be tabulated in a general way (to quote Soufiani and Djavdan in [31]). In a pool fire, the more likely radiation scenario is that the medium is a net emitter to colder boundaries. The emissivity-formulated WSGG is thus more likely to work better for fires; also, WSGG models like those of Cassol et al. [32] and Johansson et al. [33] are only formulated in that manner. The total emissivity is then approximated by a weighted sum of grey gases:

$$\varepsilon(T, S) = 1 - e^{-\kappa S} \approx \sum_{j=0}^{J} a_j(T)\left(1 - e^{-k_j p_a S}\right) \tag{3.39}$$

Where κ is the spectral-independent effective absorption coefficient of the gas in m^{-1}, not to be mistaken with k_j, the pressure-absorption coefficient of the j^{th} grey gas in $(atm.m)^{-1}$ or $(bar.m)^{-1}$. T is the gas temperature, p_a is the partial pressure (atm or bar) of the participating species (CO_2, H_2O or both), expressed with the mole fraction i.e. $p_a = X_a p_T$. The temperature-dependent weights a_j are dimensionless and can be described as fractional blackbody energies in the spectral intervals where the j^{th} grey gas exists. The k_j and a_j are tabulated from emissivity coefficients for an emissivity-formulated WSGG (respectively absorptivity coefficients). Generally $J = 3$ or 4, inclusive of one clear gas that accounts for all the windows in the spectrum, hence why the addition starts from zero in Eq. 3.39. Each grey gas represents a different optical thickness (e.g. one thin, one intermediate and one thick if $J = 3$) [29]. WSGG parameters are usually specified for certain ratios of H_2O and CO_2 mole fractions, noted p_w/p_c, that are common in combustion applications. Lastly, S is a mean beam length. Note that in Eq. 3.39 there are no integrals in the total and grey gas transmissivities; this involves an homogeneous and isothermal assumption.

3.7.1. Grey WSGG formulation

Once the approximate total emissivity is calculated, Eq. 3.39 easily yields the grey absorption coefficient:

$$\kappa(T,S) = -\frac{ln(1-\varepsilon(T,S))}{S} \tag{3.40}$$

Eq. 3.25 thus becomes:

$$\boldsymbol{s}.\nabla I(\boldsymbol{x},\boldsymbol{s}) = \kappa(\boldsymbol{x})[I_{\mathrm{b}}(T(\boldsymbol{x})) - I(\boldsymbol{x},\boldsymbol{s})] \tag{3.41}$$

Which may be solved for each solid angle. The term $I_b = \sigma_{SB}T^4/\pi$ is the total blackbody energy. The finite volume solution of Eq. 3.41 yields the total directional intensity (W/m²/sr), which is integrated over the solid angle to yield the total incident radiation G (W/m²):

$$G(\boldsymbol{x}) = \int_0^{4\pi} I(\boldsymbol{x},\boldsymbol{s})d\Omega \tag{3.42}$$

From which the total radiative source term is obtained (where the absorption coefficient and blackbody intensity may vary locally if the gas is inhomogeneous and/or non-isothermal):

$$\nabla.\dot{q}''_r(\boldsymbol{x}) = \kappa(\boldsymbol{x})[4\pi I_b(\boldsymbol{x}) - G(\boldsymbol{x})] \tag{3.43}$$

The total radiative flux incident to a boundary with normal unit vector $\boldsymbol{n_w}$ is:

$$\dot{q}''_{r,in}(\boldsymbol{x}) = \int_{\boldsymbol{s}.\boldsymbol{n_w}<0} I(\boldsymbol{x},\boldsymbol{s})|\boldsymbol{s}.\boldsymbol{n_w}|d\Omega \tag{3.44}$$

3.7.2. Banded or non-grey WSGG formulation

While computationally attractive, the "grey" WSGG method is not necessarily the most accurate, due to the averaging over the mean beam length of Eq. 3.40 and the non-rigorous validity of the Beer law for total emissivity. Also, as said before the mean beam length can be difficult to evaluate for some fires. As an alternative to that, Modest [30] proposed a non-grey (banded) formulation of the WSGG method , showing that the k_j and a_j could be used directly in gas-by-gas solutions the RTE (thus solved J times in each direction). The total intensity, solution of the total non-scattering RTE may be expressed as a function of total emissivity:

$$I(s) = I_{b,w}[1 - \varepsilon(T_w, 0 \to s)] - \int_0^s \frac{\partial \varepsilon}{\partial s'}[T(s'), s \to s']I_b(s')ds' \tag{3.45}$$

Substituting Eq. 3.39 into 3.45 leads to:

$$I(s) = \sum_{j=0}^{J} \varepsilon_j e^{-k_j p_a s} I_{b,w} + \int_0^s \sum_{j=0}^{J} a_j k_j p_a e^{-k_j p_a (s-s')} I_b(s')ds' = \sum_{j=0}^{J}\{[a_j I_b]e^{-k_j p_a s} + \int_0^s [a_j I_b]e^{-k_j p_a (s-s')} k_j p_a ds'\} \tag{3.46}$$

By identification, the total intensity is thus simply the summation on all grey gas intensities:

$$I(s) = \sum_{j=0}^{J} I_j(s) \tag{3.47}$$

Which finally verifies the RTE for an individual grey gas:

$$\boldsymbol{s}.\nabla I_j = \kappa_j p_a \left[a_j(T) I_{\mathrm{b}}(T) - I_j\right] \tag{3.48}$$

With the following boundary condition for a diffusive black wall:

$$I_{j,w} = a_j(T_w) I_b(T_w) \tag{3.49}$$

Note that Eq. 3.49 is simply the black (non-reflective) version of Eq. 3.34. The mean beam length approximation is now altogether bypassed. To calculate the incident radiation G and incident flux $q''_{r,in}$, Eq. 3.47 is simply injected in Eq. 3.42 and 3.44. However the source term (Eq. 3.43) now takes this form:

$$\nabla.\dot{q}''_r(\boldsymbol{x}) = \sum_{j=0}^{J} \kappa_j(\boldsymbol{x}) p_a(\boldsymbol{x}) \left[4\pi a_j(\boldsymbol{x}) I_b(\boldsymbol{x}) - \sum_i \omega_i(\boldsymbol{x}) I_{i,j}(\boldsymbol{x}, \boldsymbol{s})\right] \tag{3.50}$$

Where ω_i is the i^{th} solid angle. The original FireFOAM code for the finite volume solver (fvDOM) was modified accordingly to accommodate for banded RTE solutions involving the WSGG weighting coefficient. This was done by adding the temperature-dependent weighting factor in the expression of blackbody intensity in the Radiative Intensity Ray and fvDOM classes. The expression of the source term or radiant flux divergence was also modified in fvDOM so that the incident radiation is directly factored by the band or grey gas absorption coefficient, upon each iteration of the band loop. The incident radiation itself is now calculated and stored for each band, and likewise for the boundary fluxes (incident, emitted, net) in the fvDOMclass and the Wide Band Diffusive Radiation (boundary condition). The total fluxes are reconstructed during post-processing by simply adding the contributions from each band. These modifications work with a banded WSGG or any other band model (where the WSGG weighting factor may be replaced by the physical Planck function).

3.8. The three sets of WSGG correlations implemented in FireFOAM

Smith et al. [29] generated their WSGG correlations in the early 1980s from the exponential wide band model (EWB) as formulated by Edwards [38], with update from Modak for the pure rotational band of H_2O [16], as at the time there was a lack of available data for ranges of temperatures and pressure-path lengths other than featured in the original emissivity charts by Hottel and Sarofim [15]. Recently Cassol et al. [32] and Johansson et al. [33] have presented new sets of WSGG coefficients generated from a combination of the statistical narrow band model and recent spectroscopic databases, respectively the up-to-date HITEMP2010 for [32] and HITRAN92 for [33].

Smith et al.'s WSGG parameters for emissivity are listed as follows in Table 3-1, for small amounts of CO_2, small and large amounts of H_2O and two H_2O-CO_2 mixtures. They are valid for temperatures between 600 and 2400K, and pressure-path lengths between 10^{-3} and 10 atm.m. The pressure absorption coefficients k_j are in $(atm.m)^{-1}$ and the emissivity factors $b_{i,j}$ are in powers of temperature.

Table 3-1: Emissivity correlations for Smith et al.'s WSGG model [29]

	j	k_j	$b_{j,1}.10^1$	$b_{j,2}.10^4$	$b_{j,3}.10^7$	$b_{j,4}.10^{11}$
CO_2 (p_c->0)	1	0.3966	0.4334	2.62	-1.56	2.565
	2	15.64	-0.4814	2.822	-1.794	3.274
	3	394.3	0.5492	0.1087	-0.35	0.9123
H_2O (p_w->0)	1	0.4098	5.977	-5.119	3.042	-5.564
	2	6.325	0.5677	3.333	-1.967	2.718
	3	120.5	1.8	-2.334	1.008	-1.454
H_2O (p_w=1atm)	1	0.4496	6.324	-8.358	6.135	-13.03
	2	7.113	-0.2016	7.145	-5.212	9.868
	3	119.7	3.5	-5.04	2.425	-3.888
P_W/P_C = 1	1	0.4304	5.15	-2.303	0.9779	-1.494
	2	7.055	0.7749	3.399	-2.297	3.77
	3	178.1	1.907	-1.824	0.5608	-0.5122
P_W/P_C = 2	1	0.4201	6.508	-5.551	3.029	-5.353
	2	6.516	-0.2504	6.112	-3.882	6.528
	3	131.9	2.718	-3.118	1.221	-1.612

The non-dimensional temperature dependent weight for a grey gas is given by:

$$a_j(T) = \sum_{i=1}^{4} b_{j,i} T^{i-1} \tag{3.51}$$

The fourth "band" is a clear gas meant to account for all the windows in the real gas' spectrum, hence k_4 is always zero and a_4 must verify:

$$a_4 = 1 - \sum_{j=1}^{3} a_j \tag{3.52}$$

Cassol et al. [32] retain the traditional WSGG formulation of Smith et al., hence their model is mathematically analogous, except that there is a fourth grey gas (hence five with the clear gas) and the temperature polynomial for weights is of order five. Coefficients are given in Table 3-2. They are valid for temperatures between 600 and 2500K, and pressure-path lengths between 10^{-3} and 10 atm.m.

Table 3-2: Emissivity correlations for Cassol et al.'s WSGG model [32]

	J	k_j	$b_{j,1}.10^0$	$b_{j,2}.10^5$	$b_{j,3}.10^8$	$b_{j,4}.10^{11}$	$b_{j,5}.10^{15}$
CO_2	1	0.138	0.0999	64.41	-86.94	41.27	-67.74
	2	1.895	0.00942	10.36	-2.277	-2.134	6.497
	3	13.301	0.14511	-30.73	37.65	-18.41	30.16
	4	340.811	-0.02915	25.23	-26.1	9.965	-13.26
H_2O	1	0.171	0.06617	55.48	-48.41	22.27	-40.17
	2	1.551	0.11045	0.576	24	-17.01	30.96
	3	5.562	-0.04915	70.63	-70.12	26.07	-34.94
	4	49.159	0.23675	-18.91	-0.907	4.082	-8.778
$P_W/P_C = 2$	1	0.192	0.05617	78.44	-85.63	42.46	-74.4
	2	1.719	0.1426	17.95	-1.077	-6.971	17.74
	3	11.37	0.1362	25.74	-37.11	15.7	-22.67
	4	111.016	0.1222	-2.327	-7.492	4.275	-6.608

The weighting coefficient of grey gas j is given by:

$$a_j(T) = \sum_{i=1}^{5} b_{j,i} T^{i-1} \tag{3.53}$$

For the clear gas, $k_5 \equiv 0$ and

$$a_5 = 1 - \sum_{j=1}^{4} a_j \tag{3.54}$$

The WSGG model by Johansson et al. [33] is slightly more complex, as the absorption coefficient is not constant but linearly dependent on the mole fraction ratio of water and carbon dioxide (or partial pressures), and two polynomials determine the weighting coefficients. The parameters are given by Table 3-3. Since the absorption coefficients account for variations of the mole fraction ratio, these coefficients can apply for any mixture between p_w/p_c = 0.125 and p_w/p_c = 2, but the model is not suitable for gas media containing either specie alone. Correlations are valid for temperatures between 500 and 2500K, and pressure-path lengths between 10^{-2} and 60 bar.m.

Table 3-3: Emissivity correlations for Johansson et al.'s WSGG model [33]

j	$K1_j$	$K2_j$	$C1_{j,1}$	$C1_{j,2}$	$C1_{j,3}$	$C2_{j,1}$	$C2_{j,2}$	$C2_{j,3}$	$C3_{j,1}$	$C3_{j,2}$	$C3_{j,3}$
1	0.055	0.012	0.358	0.0731	-0.0466	-0.165	-0.0554	0.093	0.0598	0.0028	-0.0256
2	0.88	-0.021	0.392	-0.212	0.0191	-0.291	0.644	-0.209	0.0784	-0.197	0.0662
3	10	-1.6	0.142	-0.0831	0.0148	0.348	-0.294	0.0662	-0.122	0.118	-0.0295
4	135	-35	0.0798	-0.037	0.0023	0.0866	-0.106	0.0305	-0.0127	0.0169	-0.0051

The pressure absorption coefficient, in $(\text{bar.m})^{-1}$, of the j^{th} grey gas is given by

$$k_j = K1_j + K2_j \frac{p_w}{p_c} \tag{3.55}$$

In the previous models the emissivity factors $b_{j,i}$ are given directly in the tables. In this model we note the factors $c_{j,i}$ as they must be calculated with the tabulated C1, C2, C3 coefficients that verify a second order polynomial:

$$c_{j,i} = C1_{j,i} + C2_{j,i}\frac{p_w}{p_c} + C3_{j,i}\left(\frac{p_w}{p_c}\right)^2 \tag{3.56}$$

Then the temperature dependent weighting coefficients are calculated in a similar way to the other models, except that temperature is normalised by a reference value set which Johansson et al. defined as T_{ref} = 1200K:

$$a_j(T) = \sum_{i=1}^{3} c_{j,i}\left(\frac{T}{T_{ref}}\right)^{i-1} \tag{3.57}$$

As in the Cassol model, for the clear gas $k_5 \equiv 0$ and its weighting coefficient is also obtained from Eq. 3.54. One may note the Johansson approach could be of potential interest for fire simulations multi-step chemistry, although this remains out of scope of the present work. Under conditions of perfect combustion, methanol and methane fires yield a p_w/p_c ratio of 2, whereas heptane yields a p_w/p_c= 1.14, which is close enough to 1. If soot becomes the dominant radiation specie, grey gas and p_w/p_c considerations become less important as well. Cassol et al. pointed out that Johansson's slightly more complicated model adds a layer of error-inducing complexity. Their idea is to generate their own coefficients for pure CO_2 and pure H_2O, and rely on the principle of superposition for any mixture of the two [32].

These three sets of WSGG emissivity correlations were implemented in FireFOAM version 2.2.x. The WSGG implementations will hereafter be referred to as "Smith", "Cassol" and "Johansson" for clarity. The Smith and Cassol models were added for grey and banded solution methods. The Johansson model was added for banded solutions only. This total of five models will be the subject of a comparative study in the next chapters in various scenarios.

3.9. Exponential wide band (EWB) and "box" models

Originally formulated by Edwards [38], the EWB is a semi-empirical model attempting to represent the absorption spectrum with an exponentially increasing/decreasing shape around a band head. For symmetric bands the band head is at the centre, whereas asymmetric bands have an upper or a lower band head (Fig. 3-4). A box model, or stepwise-grey model, is a cruder band shape approximation that uses simply a rectangular box (Fig. 3-5). The width of the box is an equivalent band width noted $\Delta\eta_e$. A box model approximation can be obtain from any wide band model [7], but for the purpose of this work the EWB will be described first.

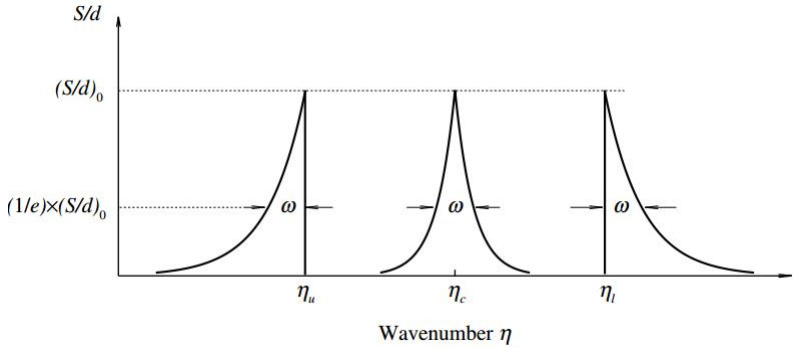

Fig. 3-4: Band shapes with the exponential wide band model (left: upper band head, centre: symmetric band head, right: lower band head) (reproduced from [7])

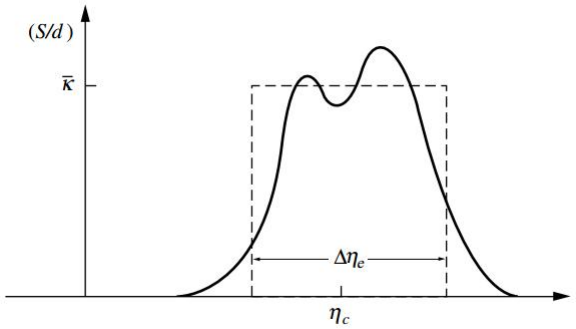

Fig. 3-5: Band shape with the box model (reproduced from [7])

3.9.1. Exponential wide band (EWB)

For this work the modern EWB formulation was used, such as described by Modest in Chapter 11 of [7]. The spectral locations will be expressed in wavenumbers η (cm^{-1}). The total band absorptance of a homogeneous, isothermal gas is defined by Eq. 3.58. In this formulation X is the mass path length (g/m^2), which replaces the usual L because the κ here is a mass absorption coefficient. Since we use mean beam lengths for our practical problems, we shall always define $X = \rho S$. For the rest of this section and unless specified otherwise, κ is a mass absorption coefficient calculated as $\kappa = \kappa_{linear}/\rho$ in units of $1/(g/m^2)$.

$$A \equiv \int_{band} \varepsilon_\eta d\eta = \int_0^\infty (1 - e^{-\kappa_\eta X}) d\eta \tag{3.58}$$

The idea of the EWB is that if ω is the bandwidth at the height 1/e of the maximum absorption (Fig. 3-4), then a non-dimensional band absorptance A^* can be expressed as a function of these three parameters:

$$A^* = A/\omega = A^*(\alpha, \beta, \tau_0) \tag{3.59}$$

Where α is the band integrated intensity (or area under the curve in Fig. 3-4), β is the band overlap parameter (units of pressure), and τ_0 is the optical thickness at the band's peak. α is in units of $cm^{-1}/(g/m^2)$, defined by:

$$\alpha \equiv \int_0^\infty \kappa_\eta d\eta \tag{3.60}$$

The three parameters are calculated from a number of sub-routines which use tabulated coefficients given for each gas species. For the purpose of this work only CO_2 and H_2O are considered, where most bands are symmetrical and correspond to a vibration-rotational transition mode (Table 3-4 and 3-5). The calculations for α, β and τ_0 are as follows. Wavelength subscripts are used for the two particular cases of H_2O at 71μm (pure rotational band) and 2.7μm (composed of three sub-bands with subscript n).

- Integrated band intensity α :

$$\alpha = \alpha_0 \frac{\Psi(T)}{\Psi(T_0)} \tag{3.61.a}$$

$$\alpha_{71\mu m} = 5.455\exp\left(-9\sqrt{T_0/T} - 1\right) \tag{3.61.b}$$

$$\alpha_{2.7\mu m} = \sum_{n=1}^{3} \alpha_n \tag{3.61.c}$$

$$\Psi(T) = \{1 - exp(-\sum_{k=1}^{m} u_k(T)\delta_k)\} \frac{\prod_{k=1}^{m} \sum_{v_k=v_{0,k}}^{\infty} \frac{(v_k+g_k+|\delta_k|-1)!}{(g_k-1)!v_k!} e^{-u_k(T)v_k}}{\prod_{k=1}^{m} \sum_{v_k=0}^{\infty} \frac{(v_k+g_k-1)!}{(g_k-1)!v_k!} e^{-u_k(T)v_k}} \tag{3.62}$$

$$u_k(T) = \frac{hc_0\eta_k}{k_B T} \tag{3.63}$$

Where T_0 = 100K and δ, v, g are quantum parameters, i.e. the step, energy level and degeneracy (from Table 3-4 and 3-5). The α_n in Eq. 3.61.c are calculated with Eq. 3.61.a.

- Overlap parameter β :

$$\beta = \beta^* P_e = \beta_0^* \sqrt{\frac{T_0}{T}} \frac{\Phi(T)}{\Phi(T_0)} P_e \tag{3.64.a}$$

$$\beta_{71\mu m} = 0.413\sqrt{T_0/T} P_{e,71\mu m} \tag{3.64.b}$$

$$\beta_{2.7\mu m} = \frac{1}{\alpha_{2.7\mu m}} \left[\sum_{n=1}^{3} \sqrt{\alpha_n \beta_n}\right]^2 \tag{3.64.c}$$

$$\Phi(T) = \frac{\left\{\prod_{k=1}^{m} \sum_{v_k=v_{0,k}}^{\infty} \sqrt{\frac{(v_k+g_k+|\delta_k|-1)!}{(g_k-1)!v_k!} e^{-u_k(T)v_k}}\right\}^2}{\prod_{k=1}^{m} \sum_{v_k=0}^{\infty} \frac{(v_k+g_k+|\delta_k|-1)!}{(g_k-1)!v_k!} e^{-u_k(T)v_k}} \tag{3.65}$$

$$P_e = \left[\frac{p_T}{p_0}\left(1 + (b-1)\frac{p_a}{p_T}\right)\right]^n \tag{3.66}$$

Where b, n, β_0^* are from Table 3-4 and 3-5. The β_n in Eq. 3.64.c are calculated with Eq. 3.64.a and the α_n with Eq. 3.61.a.

- Band head optical thickness τ_0 :

$$\tau_0 = \alpha X/\omega \tag{3.67}$$

$$\omega = \omega_0\sqrt{T/T_0} \tag{3.68}$$

Where ω_0 is from Table 3-4 and 3-5. Finally, the non-dimensional total band absorptance A^* (Eq. 3.59) is obtained from this four-region method:

$\beta \leq 1$	$A^* = \tau_0$ if $0 \leq \tau_0 \leq \beta$ (linear region) $A^* = 2\sqrt{\tau_0\beta} - \beta$ if $\beta \leq \tau_0 \leq \frac{1}{\beta}$ (square root region) $A^* = \ln(\tau_0\beta) + 2 - \beta$ if $1/\beta \leq \tau_0 < \infty$ (logarithmic region)
$\beta \geq 1$	$A^* = \tau_0$ if $0 \leq \tau_0 \leq 1$ (linear region) $A^* = \ln(\tau_0) + 1$ if $1 \leq \tau_0 \leq \infty$ (logarithmic region)

Table 3-4: Exponential wide band model coefficients for H_2O [7]

Location λ (μm)	Location η_c (cm^{-1})	Vibration quantum step δ_k	Pressure param. n	Pressure param. b	α_0 ($cm^{-1}/(g/m^2)$)	β_0^* (-)	ω_0 (cm^{-1})
71	140	(0,0,0)	1	$8.6\sqrt{T_0/T} + 0.5$	5.455	0.413	69.3
6.3	1600	(0,1,0)	1	$8.6\sqrt{T_0/T} + 0.5$	41.2	0.094	56.4
2.7	3760	(0,2,0) (1,0,0) (0,0,1)	1	$8.6\sqrt{T_0/T} + 0.5$	0.2 2.3 23.4	0.132	60.0
1.87	5350	(0,1,1)	1	$8.6\sqrt{T_0/T} + 0.5$	3.0	0.082	43.1
1.38	7250	(1,0,1)	1	$8.6\sqrt{T_0/T} + 0.5$	2.5	0.116	32.0

m = 3,η_k = (3652, 1595, 3756) cm^{-1};g_k = (1,1,1)

Table 3-5: Exponential wide band model coefficients for CO_2 [7]

Location λ (μm)	Location η_c or η_u (cm^{-1})	Vibration quantum step δ_k	Pressure param. n	Pressure param. b	α_0 ($cm^{-1}/(g/m^2)$)	β_0^* (-)	ω_0 (cm^{-1})
15	667	(0,1,0)	0.7	1.3	19.0	0.062	12.7
10.4	960	(-1,0,1)	0.8	1.3	2.47×10^{-9}	0.040	13.4
9.4	1060	(0,-2,1)	0.8	1.3	2.48×10^{-9}	0.119	10.1
4.3	2410 (upper)	(0,0,1)	0.8	1.3	110.0	0.247	11.2
2.7	3660	(1,0,1)	0.65	1.3	4.0	0.133	23.5
2.0	5200	(2,0,1)	0.65	1.3	0.060	0.393	34.5

$m = 3$, $\eta_k = (1351, 666, 2396)$ cm^{-1}, $g_k = (1,2,1)$

3.9.2. Box model

Once the total band absorptance A is obtained in each band, the box model parameters (equivalent bandwidth and band-averaged absorption coefficient) can be obtained from different methods. Modest proposed in [21] and [7] to evaluate the absorption coefficient at the optically thin limit. It follows from Eq. 3.58 that

$$A = \int_0^\infty (1 - e^{-\kappa_\eta X}) d\eta = \Delta\eta_e (1 - e^{-\bar{\kappa} X}) \tag{3.69}$$

Also, Eq. 3.60 leads to

$$\bar{\kappa} = \alpha / \Delta\eta_e \tag{3.70}$$

Substituting Eq. 3.70 in 3.69 yields:

$$A = \Delta\eta_e \left(1 - e^{-\alpha X / \Delta\eta_e}\right) \tag{3.71}$$

Since A, X and α are known, the box bandwidth $\Delta\eta_e$ can be obtained from Eq. 3.71 with e.g. a "while" loop where $\Delta\eta_e$ is incremented until it yields the correct A.

Alternatively, the absorption coefficient may also be taken at the mean beam length, which is the approach favoured in [43] or [64]. This is analogous to using Beer's law for the grey WSGG absorption coefficient (Eq. 3.40), except here the process is repeated in every band. The equivalent bandwidth is obtained from a four region method that is analogous to that of the total band absorptance.

$$\Delta\eta_e = \frac{A}{1-\tau} \tag{3.72}$$

$$\overline{\kappa} = -\ln(\tau)/S \tag{3.73}$$

Where τ is the band transmissivity given by:

$\beta \leq 1$	$\tau = 0.9$ if $0 \leq \tau_0 \leq \beta$ (linear region) $\tau = 0.5\left(1 + \frac{\beta}{A^*}\right)$ if $\beta \leq \tau_0 \leq \frac{1}{\beta}$ (square root region) $\tau = A^*$ if $1/\beta \leq \tau_0 < \infty$ (logarithmic region)
$\beta \geq 1$	$\tau = 0.9$ if $0 \leq \tau_0 \leq 1$ (linear region) $\tau = \frac{1}{A^*}$ if $1 \leq \tau_0 < \infty$ (logarithmic region)

These two different approaches to the box model were both implemented in FireFOAM for comparative purposes. For clarity, they will be henceforth referred to as the "Modest" box model (Eq. 3.70-3.71) and the "Beer" box model (Eq. 3.72-3.73).

Finally, we must evaluate the variation of the Planck function between in each band. The upper and lower band limits are easily obtained from the box model's bandwidth and the tabulated band head locations from Table 3-4 and 3-5, using wavenumber (cm^{-1}) to wavelength (μm) conversion factors:

$$\lambda_L = 10^4/\eta_U \quad ; \quad \lambda_U = 10^4/\eta_L \tag{3.74}$$

The fractional Planck function itself may be tabulated, or obtained from e.g. Siegel and Howell's correlation [77]. Plots of that function are shown in Fig. 3-6.

$$F(n,\lambda,T) = \frac{15}{\pi^4}\sum_{m=1}^{\infty}\frac{e^{-m\zeta}}{m^4}[6 + 6(m\zeta) + 3(m\zeta)^2 + (m\zeta)^3] \tag{3.75}$$

$$\zeta = \frac{C2}{n\lambda T} \tag{3.76}$$

Where C2 is a Planck constant and *n* the refraction index of the medium (as said before it will always be set to unity here). Then, from Eq. 3.74 it follows:

$$\Delta F = F(n,\lambda_U,T) - F(n,\lambda_L,T) \tag{3.77}$$

The non-scattering RTE for the j^{th} gas band thus takes the form:

$$\boldsymbol{s}.\nabla I_j = \bar{\kappa}_j \rho_j \left[\Delta F_j I_b(T) - I_j\right] \tag{3.78}$$

Which much resembles Eq. 3.48 for the banded WSGG, except that the individual intensities have a physical meaning, the weighting factor of the emission term is based on the real Planck function, and the mass absorption coefficient is multiplied by the gas density to become a linear absorption coefficient. Likewise to the WSGG though, the RTE must also be

solved for spectral windows. Since the sum of the fractional energies ΔF across the whole spectrum is necessarily equal to unity, all the windows before, after and between the gas bands may be grouped in a "clear gas" such that

$$\Delta F_{clear} = 1 - \sum_{j=1}^{J\ gas\ bands} \Delta F_j \tag{3.79}$$

For the boundary condition, ΔF_w simply replaces the WSGG weight a_w in Eq. 3.49. ΔF_w is calculated at the wall temperature, using the gas band limits:

$$\Delta F_w = F(n, \lambda_U, T_w) - F(n, \lambda_L, T_w) \tag{3.80}$$

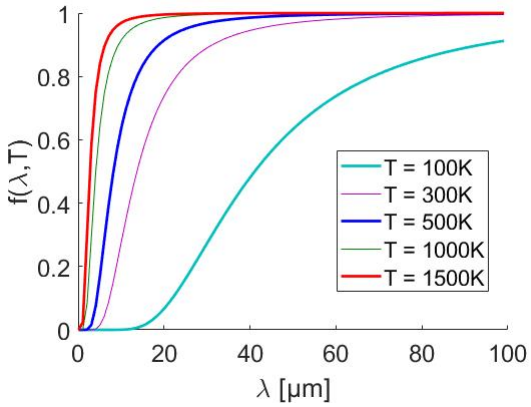

Fig. 3-6: Plots of the Planck fractional energy function, calculated with Eq. 3.75 for different temperatures

3.9.3. Band overlaps

The EWB coefficients of H_2O of Table 3-4 show a triple band overlap at the 2.7μm region. The properties of the three bands were combined into one using Eq. 3.61.c and 3.64.c. This particular case is relatively simple because all three bands have the same centre at 2.7μm and belong to one species. Whether other bands from a same species can overlap is not certain and should be investigated properly with our two box models. In gas mixtures bands from different species certainly overlap more or less easily, depending on pressure, temperature, path length, and how close such bands are on the spectrum. Such bands are difficult to combine into one because their heads have different locations. An easier approach is to consider the overlapped region as an extra band, which can be done by recalculating the absorption for the entire spectrum ($0 < \eta < \sim 8000$) from the individual $\bar{\kappa}_j$:

$$\kappa_\eta \approx \sum_{j=1}^{J} \bar{\kappa}_j \left[H\left(\eta - \eta_{c,j} + \frac{1}{2}\Delta\eta_{e,j}\right) - H\left(\eta - \eta_{c,j} - \frac{1}{2}\Delta\eta_{e,j}\right)\right] \tag{3.81}$$

For symmetric bands, and for the asymmetric CO_2 band with an upper head at 4.3μm (η_u = 2410 cm^{-1}):

$$\kappa_\eta \approx \bar{\kappa}_{4.3\mu m}\left[H\left(\eta - \eta_u + \Delta\eta_{e,4.3\mu m}\right) - H(\eta - \eta_u)\right] \tag{3.82}$$

Where H is Heaviside's unit step function:

$$\begin{cases} H(x) = 0 \; if \; x \leq 0 \\ H(x) = 1 \; if \; x > 0 \end{cases} \tag{3.83}$$

An absorption spectrum is thus generated with the "Beer" box model for an oxy-fuel combustion mixture type, with 35% H_2O, 65% CO_2, path length 9.3913m, T=1500K. The result (Fig. 3-7) is very similar to Marzouk and Huckaby's in the same conditions [64].

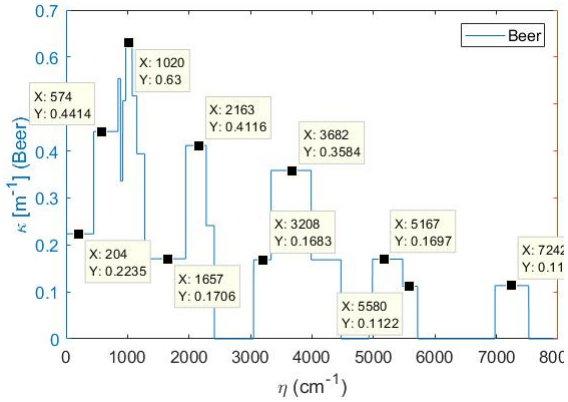

Fig. 3-7: "Beer" box model absorption spectrum for 35% H_2O, 65% CO_2, path length 9.4m, T=1500K

It is clear from Fig. 3-7 that with so many overlaps, there are many more absorption coefficients (22) than the initial 11 from Table 3-4 and 3-5. It is of course possible to compute the absorption calculations externally and input them manually in FireFOAM, but then if a fire simulation were considered the process would have to be repeated each time the temperature, mole fractions etc. are updated, which is impossible. On another hand, the code is structured so that the number of bands to solve is fixed for the entire simulation. Implementing a variable number of bands would be very tedious because absorption would have to be solved a first time so the number of overlaps is known, then another time with the extra bands, which would be too computer-intensive. Eleven bands are already much for CFD, never mind 22. Moreover, it would be extremely difficult to couple such a model with the non-grey liquid droplet radiation model (which has to work within the exact same band limits as the gas phase). For all these reasons, an exhaustive sensitivity study was carried out to determine the broadening of box model bandwidths in fire conditions. Once the always or frequently overlapping bands of CO_2 and H_2O were identified, we were able to combine several bands into one using fixed bandwidths, making sure these are reliable enough for the desired applications. This method will be discussed at length in Chapter 4, section 4-2.

3.9.4. Relevant simplifications for computational efficiency

The expressions of Eq. 3.62 and 3.65 are complicated. Even if repeated tests have shown that the infinite series converge quickly (~10 or 15 iterations with a very small criterion), it is preferable to seek faster expressions. As a matter of fact, with Eq. 3.62 the integrated band intensity of a strong band already simplifies to α_0. For all the rotation-vibration bands, Lallemant and Weber have proposed accurate fitting correlations in [47], listed below in Table 3-6. The calculations for α thus simplify to:

$$\alpha = \alpha_0 \frac{1-exp\left(-\sum_{k=1}^{m} u_k(T)\delta_k\right)}{1-exp\left(-\sum_{k=1}^{m} u_k(T_0)\delta_k\right)} \frac{\Psi'(S_k(T))}{\Psi'(S_k(T_0))} \tag{3.84}$$

$$S_k(T) = \left(1 - \mathrm{e}^{-u_k(T)}\right)^{-1} \tag{3.85}$$

With $u_k(T)$ from Eq. 3.63. Eq. 3.61.c is still required for the three H_2O bands at 2.7µm. For the overlap parameter β, Eq. 3.65 can be altogether bypassed as [47] provides a direct polynomial method. Conveniently, the 2.7µm region is already calculated as a single band, hence Eq. 3.64.c is no longer used. Thus for all vibration-rotational bands,

$$\beta \approx \beta_0^* \sqrt{T_0/T} P_e \sum_{l=0}^{4} a_l T^l \tag{3.86}$$

Where a_l are polynomial coefficients given in Table 3-7.

Table 3-6: Simplified correlations for Eq. 3.84

H_2O (η_k = 3652, 1595, 3756 cm^{-1})			**CO_2** (η_k = 1351, 666, 2396 cm^{-1})		
Location λ (µm)	Location η_c (cm^{-1})	$\Psi'(S_k)$	Location λ (µm)	Location η_c or η_u(cm^{-1})	$\Psi'(S_k)$
6.3	1600	S_2	15	667	$2S_2$
2.7	3760	$2(S_2)^2$ S_1 S_3	10.4	960	$e^{-u_1}(2-e^{-u_1})S_1S_3$
1.87	5350	S_2S_3	9.4	1060	$e^{-u_1}(2-e^{-u_1})S_1S_3$
1.38	7250	S_1S_3	4.3	2410 (upper)	S_3
			2.7	3660	S_1S_3
			2.0	5200	$2(S_1)^2S_3$

Table 3-7: Simplified correlations for Eq. 3.86

Gas	Loc.	a_0	a_1	a_2	a_3	a_4
H_2O	6.3	0.84230766	3.797542×10^{-4}	6.680344×10^{-7}	1.232428×10^{-9}	3.988783×10^{-14}
	2.7	1.5409553	7.483624×10^{-4}	3.480733×10^{-7}	2.212542×10^{-9}	1.589963×10^{-13}
	1.87	0.74454804	9.025019×10^{-4}	-2.695318×10^{-7}	1.884587×10^{-9}	7.466476×10^{-14}
	1.38	0.79549686	7.588211×10^{-4}	-4.698487×10^{-7}	1.655432×10^{-9}	1.032703×10^{-13}
CO_2	15	0.1961354	4.6026302×10^{-3}	-6.542622×10^{-7}	1.937692×10^{-8}	4.682619×10^{-15}
	10.4	-1.6560576	1.4951764×10^{-2}	-2.222106×10^{-5}	3.341932×10^{-8}	6.393986×10^{-13}
	9.4	-1.6428941	1.4896056×10^{-2}	-2.215055×10^{-5}	3.33859×10^{-8}	6.445583×10^{-13}
	4.3	-0.4652004	8.6506412×10^{-3}	-1.092158×10^{-5}	2.418113×10^{-8}	6.129179×10^{-14}
	2.7	-1.5631418	1.4952999×10^{-2}	-2.401862×10^{-5}	3.807809×10^{-8}	1.421920×10^{-13}
	2.0	-2.3330982	1.9693219×10^{-2}	-3.481327×10^{-5}	5.023159×10^{-8}	7.235694×10^{-15}

3.9.5. Parameter scaling for inhomogeneous path lengths

This relatively straightforward approach relies on arithmetic averages of temperature and gas mole fraction and related quantities (density, partial pressure...), which are used for the following calculations:

$$\tilde{\alpha} = \alpha(\tilde{T}) = \alpha_0 \frac{\Psi(\tilde{T})}{\Psi(T_0)} \tag{3.87}$$

$$\tilde{\omega} = \omega(\tilde{T}) = \omega_0 \sqrt{\frac{\tilde{T}}{T_0}} \tag{3.88}$$

$$\tilde{\beta} = \beta(\tilde{T}, \tilde{P_e}) = \beta_0 \tilde{P_e} \sqrt{\frac{T_0}{\tilde{T}}} \frac{\Phi(\tilde{T})}{\Phi(T_0)} \tag{3.89}$$

$$\tilde{P_e} = \left[\frac{p}{p_0}\left(1 + (\tilde{b} - 1)\frac{\widetilde{p_a}}{p}\right)\right]^n \tag{3.90}$$

$$\tilde{b} = \begin{cases} cst = b, \text{ for CO2} \\ 8.6\sqrt{\frac{T_0}{\tilde{T}}} + 0.5, \text{ for H2O} \end{cases} \tag{3.91}$$

$$\tilde{\tau_0} = \tilde{\alpha}\widetilde{X_a}/\tilde{\omega} \tag{3.92}$$

One may note that for the fixed bands box model most of these relations are redundant and only Eq. 3.87 remains. Other averaging techniques may be considered in the future, but then the use of the uncorrelated solution method in 3D problems (and perhaps the use of mean beam length too) forbids rigorous integrations over lines of sight.

3.10. Radiative properties of soot

Determining soot radiative properties can be seen as a particular case of the Mie theory in the small size parameter limit (Rayleigh theory). If the soot particles are very small indeed, the soot absorption coefficient does not depend on particle size distribution but only on wavelength and the total volume occupied by all particles per unit volume [7], indeed the soot volume fraction noted *fv*. In that case the spectral absorption coefficient of the soot phase is written:

$$\kappa_{s,\lambda} = \frac{36\pi nk}{(n^2-k^2+2)^2+4n^2k^2}\frac{fv}{\lambda} = \frac{C_0 fv}{\lambda} \tag{3.93}$$

Where *n* and *k* are wavelength-dependent and define the complex index of refraction $m = n - ik$. Unlike molecular gases, soot has a continuous absorption spectrum which facilitates spectral integration for grey approximations [17]. A Planck-mean soot absorption coefficient is often used for in moderately sooty fires, where soot is an emitter. Spectral-averaged values of *n* and *k* are commonly defined as $\bar{n} = 1.57$ and $\bar{k} = 0.56$ [78] which yields $C_0 = 4.89$. The spectral-integrated sooty absorption coefficient is then expressed as a function of the second Planck constant, $C_2 = 0.014388$ m.K:

$$\kappa_s = \frac{3.6 fv C_0 T}{C_2} = 1226.\, fv.T \tag{3.94}$$

The soot volume fraction *fv* may be expressed as $fv = \bar{\rho}\tilde{Y}_s/\rho_s$ where $\rho_s = 1800$ kg/m^3 is the soot density. For fires where soot is both emitting and absorbing (cold soot), this grey approach usually no longer holds. Toluene pool fires are such a case, where cold soot tends to settle at the bottom and act as a heat sink [4].

3.11. Turbulence-radiation interaction (TRI)

Following the recommendations from various sources such as [18,19,34,52,61], TRI is taken into account so that radiation calculations are performed from an estimated turbulent flame sheet temperature T_f rather than the cell temperature *T*. The works cited above emphasise the importance of TRI with regards to soot modelling, however methanol flames are soot-free and here radiation is thus only driven by the temperature of the gas phase. As these sources state, in optically-thin flames only the temperature self-correlation is significant, and a first order approximation is usually sufficient, i.e.

$$T_f{}^4 = T^4\left(1 + 6C_{TRI}\frac{T''^2}{T^2}\right) \tag{3.95}$$

This temperature is used both in the emission term of the RTE and absorption calculations. The subgrid temperature fluctuation is estimated similarly to Chaterjee et al.'s recent work [18] with FireFOAM, i.e.:

$$T''^2 = C\Delta^2\left|\vec{\nabla}T\right|^2 \tag{3.96}$$

The resolved temperature fluctuation, *T'*, is calculated by FireFOAM as the difference between the instant and time-averaged temperature. As in [18], the RMS temperature is thus $T_{rms} = T'' + T'$.

3.12. Combustion, soot and turbulence models in FireFoam

Outside the scope of pure gas radiation, some other FireFOAM submodels were used in this work without modification from this author. The combustion model henceforth used for pool fire simulations is based on the eddy dissipation concept (EDC) of Magnussen and Hjertager [79], which was extended for LES and implemented in FireFOAM by Chen et al. in [23,80]. The model uses the concept of energy cascade from the integral length scale (largest structures containing most of the kinetic energy) down to the Kolmogorov scale of the smallest eddies. Fig. 3-8 summarises the concept, where U_n, L_n and ω_n are the velocity scale, length scale and strain rate of the n^{th} structure level. Assuming that the LES filter width usually falls between these two scales, the total kinetic energy and its dissipation rate may be derived from subgrid-scale quantities [23].

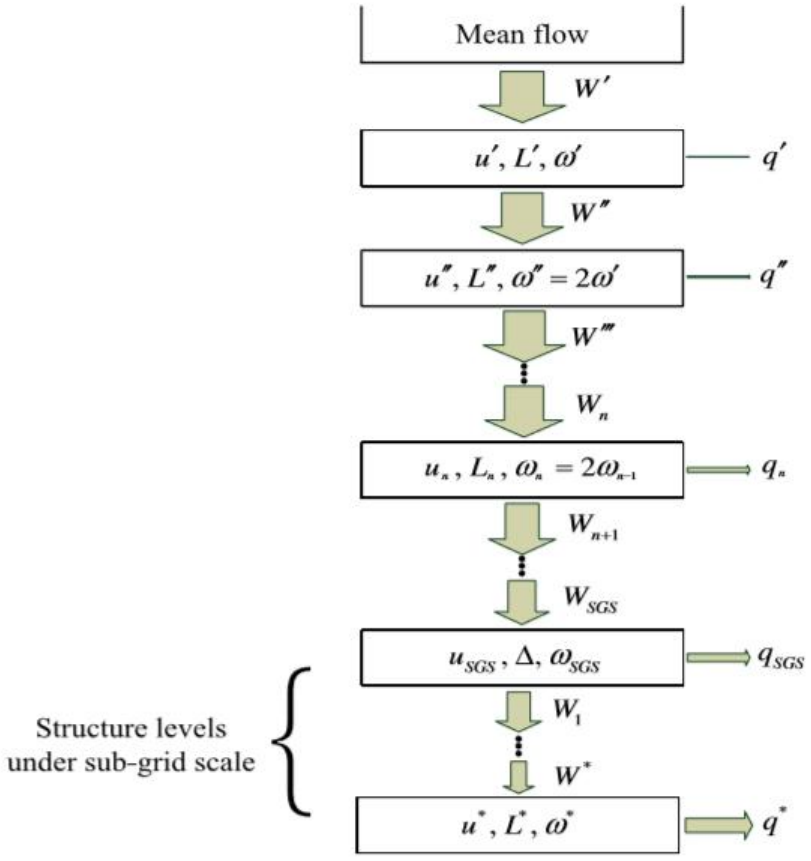

Fig. 3-8: Turbulent energy cascade in the LES framework (reproduced from [23])

The soot model, based on the laminar smoke point soot model, was also extended for LES and implemented by Chen [59,80], who used the partially stirred reactor (PaSR) concept to relate the filtered soot formation rate to the soot chemical time scale, which is assumed to be proportional to the laminar smoke point height (SPH) of the fuel [59]. The combustion and soot models were later upgraded by Wang et al. in [81,82]. The governing equations for the LES-filtered soot formation rate and soot oxidation rate are respectively:

$$\bar{\omega}_{s,f} = \begin{cases} \frac{\tau_{c,s}}{\tau_{c,s}+\tau_{mix}} \frac{4.4E-6}{L_{sp}} \bar{\rho}^2 \tilde{Y}_{fu} \tilde{T}^{2.25} \exp\left(-\frac{2000}{\tilde{T}}\right) \; if \; 0 \leq \tilde{Y}_{fu} - \frac{\tilde{Y}_{O_2}}{s} \leq \frac{1.5Y_{O_2}^0}{s} \\ 0, \; else \end{cases} \tag{3.97}$$

$$\bar{\omega}_{s,o} = \begin{cases} \left\{ \bar{\rho} \tilde{Y}_s \dot{m}^* \frac{\gamma\chi}{1-\gamma\chi}, if \; \tilde{Y}_{fu} - \frac{\tilde{Y}_{O_2}}{s} \leq 0 \; and \; \tilde{T} \geq 1300K \right. \\ 0, else \end{cases} \tag{3.98}$$

Where χ, γ, τ_{cs} and τ_{mix} are respectively the reacting fraction of fine structures, the mass fraction of fine structures, the chemical time scale of and the turbulent mixing time scale for soot formation [59].

For the simulated pool fires, the pressure-implicit split operator (PISO) algorithm was used, which is OpenFOAM's iterative procedure for solving the equations of velocity and pressure in transient problems [20]. More recently, the liquid phase radiation (Mie theory) model was implemented by FM Global (not yet published at this time of writing). A common code structure (the "Binary Absorption Emission" class) was created specifically for the coupling of the gas box model and the liquid radiation model, hence a succinct description of Mie theory will be given in Chapter 6.

3.13. Summary

This author's original modelling contributions mostly reside with the box model, since the WSGG are basically "ready to use" models and thus do not offer much freedom for custom modification. In the paragraphs above the exponential wide band model description was similar to that of other literature works, but in the next chapter the "traditional" EWB and box model implementations will undergo significant changes while addressing the issues of gas inhomogeneity and band overlap in a CPU-efficient manner. The modification of the fvDOM class described above came as very helpful, as the the pre-existing Blackbody class (tabulated Planck function with linear interpolation) could not represent the non-physical WSGG weights, and also as the banded treatment of radiant fluxes eventually resolved a long running issue with reflective boundaries.

Chapter 4 - Results and discussion (pure radiation cases)

A large part of this chapter will be dedicated to the validation of the new gas radiation models added to FireFOAM, and also the modifications added to the pre-existing code (see previous chapter). To that effect repeated tests were carried out with a series of test case scenarios with static, non-reactive media where only radiation calculations are performed. These scenarios mostly come from the radiation studies by Coelho [34], Goutiere et al. [35] and Bressloff [36], who also provided useful benchmark data from more sophisticated radiation models. The 1D scenarios of [36] only consider line-of-sight solutions along a 1m gas slab, and are thus ray effect-free. Also, the soot and gas mixtures constitute interesting case studies for fire scenarios. The 2D case of [35] is a 1m x 0.5m rectangular box alternatively filled with a grey gas, pure CO_2, pure H_2O or a mixture of both species, all at relatively small concentrations. The individual species scenarios will help assess the box models which deal with one species and band at a time, which will be compared against the mixture variant. The 3D cases of [36] (also [84]) is a larger rectangular enclosure of size 2m x 2m x 4m, filled with pure H_2O at atmospheric pressure. Although not typical of fire conditions, this scenario will help understand the behaviour of each model at larger (linear, mass, pressure) path lengths, and highlight the errors induced by mean beam lengths. All these scenarios will come with homogeneous or inhomogeneous, isothermal or non-isothermal variants to provide a comprehensive view of the capabilities of the new gas radiation models. The results will come in the form of comparative studies, at the end of which conclusions will be drawn on the justification of using one model instead of another. These test cases will also help validate our own modified box model, which will be tested extensively. A full sensitivity study of box model bandwidths relative to path lengths will be provided, which to our best knowledge has not been done before in such an exhaustive way. After the static pure radiation scenarios, the FireFOAM implementations of WSGG and box models will be assessed in simulated and synthetic pool fires. This section will answer one core question for this work - whether the newer WSGG correlations of [32,33], developed for oxy-fuel combustion applications, bring any improvement over those of [29] in fully coupled fire simulations. Such a comparative study has been scarcely overtaken in the past, as radiation studies in fires usually favour the decoupled approach, which is much less computational-intensive. High angular resolutions of several hundred solid angles will be used and the CPU times reported. The new box model will join the WSGG comparisons.

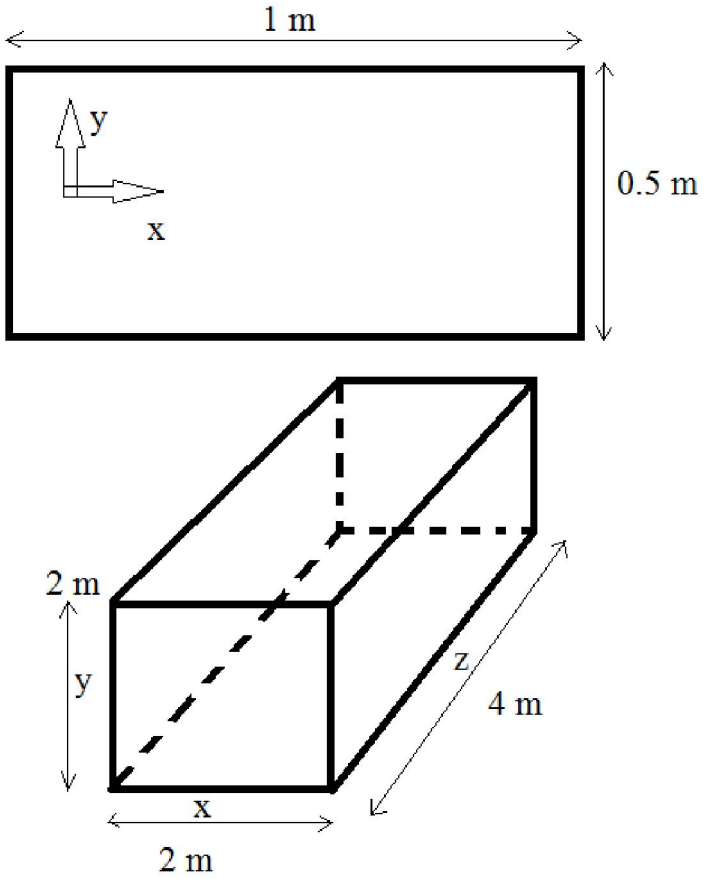

Fig. 4-1: Sketch of 2D and 3D geometries employed in [35] and [34] respectively

4.1. Investigation of the weighted-sum-of-grey-gases (WSGG) in static media (pure radiation only cases)

An investigation is carried out in this section to assess the accuracy of the implemented WSGG approaches into FireFOAM for radiation only, without flow dynamics or combustion. Black-walled enclosures are considered where the emitter is a hot gas or a hot surface. In sections 4.1.1 and 4.1.2 the accuracy of the finite volume (FVM) radiation solver will be tested independently from any gas absorption/emission model. In 4.1.1, an arbitrary grey gas in a 2D enclosure will be considered to identify the sensitive parameters of the FVM solver. In 4.1.2, the FVM's sensitivity to angular discretisation (ray effects) is investigated in a 3D cylinder, a geometry typical of pool fire simulations. In this scenario, reproduced from [83], a hot surface radiates to the adjacent cold walls through a non-participating medium. The radiant heat flux was solved in [83] with an exact ray tracing method (RTM) to which the FireFOAM solution is compared with an increasing number of solid angles, which serves as a calibration for subsequent FireFOAM pool fire simulations. The rest of this section will be a discussion of the five new WSGG implementations ("Grey Smith", "Grey Cassol", "Banded Smith", "Banded Cassol", "Banded Johansson") in homogeneous media (section 4.1.3) and inhomogeneous media (section 4.1.4). The 3D, 2D and 1D case scenarios are taken from [34-36]. The interest is to compare our FireFOAM solutions with the WSGG-FVM combination

against the narrow band models (SNB or SNBCK) employed in these papers, which are thus used as benchmarks. Their RTE solving methods were the discrete transfer (DTM) [34,36] or the ray tracing (RTM) [34,35], although the more approximate discrete ordinates (DOM) was also used in [34,35]. Sections 4.1.3 and 4.1.4 shall start with line-of-sight solutions in the 1D scenarios of [36], then the radiant heat fluxes and source terms will be discussed in the 2D scenarios of [35], and then the 3D scenarios of [34].

4.1.1. Grey gas in a 2D enclosure

This case scenario is from Goutiere et al. [35]. A grey gas of uniform absorption coefficient κ = 0.5 m^{-1} fills a rectangular, 1m x 0.5m enclosure with a 61 x 31 uniform Cartesian mesh and cold black boundaries. The RTM solution of [35] (considered exact) is compared against FireFOAM solutions whose angular resolution is increased until the solutions converge with one another. The incident radiative heat flux and the radiative source term are sampled along four lines, i.e. (x ,y = 0) and (x = 1, y) for the fluxes ; (x, y = 0.5) and (x = 0.5, y) for the source terms. It turns out the various convergence criteria tested (from 10^{-3} to 10^{-6}) had no visible effect on the FireFOAM solutions, probably because this form of the RTE is a simple ODE and the quality of the solution is bound by the limitations of the FVM itself. Convergence on each directional RTE is reached after the first or second iteration. The only parameter that has any effect is the discretisation of the azimuthal angle φ in the XY plane, as seen on Fig. 4-1-1. Four discretisation were used (4, 8, 16 and 24 solid angles).

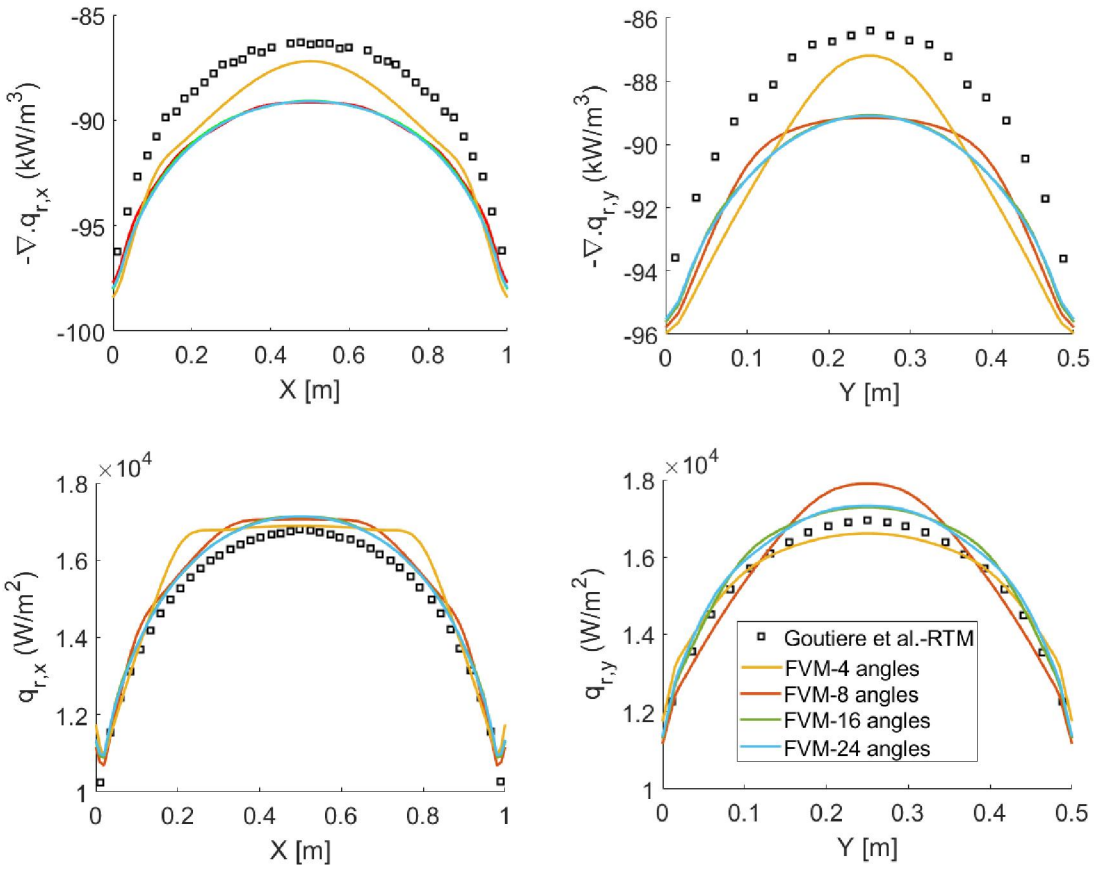

Fig. 4-1-1: Radiative source term along (x, y = 0.25) and (x = 0.5, y) (top), incident flux along (x, y = 0.5) and (x = 1, y) (bottom) for the 2D grey gas case of [35], FireFOAM-FVM vs RTM of [35]

The solutions with 16 and 24 angles are visually undistinguishable, indicating that 16 angles are enough for this scenario. The relative differences between FVM and RTM seem large on Fig. 4-1-1, but they are in fact around 3% or less (Table 4-1-1). The coarsest solution with 4 solid angles occasionally appears closer to the RTM than the others, but it is probably coincidental. It also exhibits a 'square' behaviour (flux along x) that cannot be considered as physical. It is clear that the FVM solution cannot be improved on by adding any more angles - some incompressible error will have to be reckoned with for the rest of this work. Besides, with a uniform grey gas the solution is independent from the spatial discretisation hence no numerical smearing effect can be at play here.

Table 4-1-1: Midfield source terms and fluxes for the grey case with relative errors

	$-\mathrm{div}(q_r)$ (kW/m^3) x = 0.5, y = 0.25	$q_{r,x}$ (kW/m^2) x = 0.5, y = 0	$q_{r,y}$ (kW/m^2) x = 1, y = 0.25
RTM (Goutiere et al. [35])	-86.39	16.79	16.95
FireFOAM-FVM (16 angles)	-89.10	17.13	17.32
Error = $\frac{\lvert FV-RT\rvert}{\lvert RT\rvert}$	3.1%	2.0%	2.2%

4.1.2. Hot surface emitting through transparent gas in a 3D cylinder

4.1.2.1. Wide emitting surface

The angular sensitivity of FireFOAM's FVM is assessed for a 3D geometry based on Joseph's case scenario [83]. This test case is important to assess the ray effects in the FVM solver used in the present study. A cylinder of radius 1m and height 2m is filled with a uniformly transparent gas (κ = 0 m^{-1}), allowing free energy propagation from the bottom surface (3.14 m²) emitting at 700K towards the adjacent cold black walls (Fig. 4-1-2a). The radiative flux is taken on the side wall, at three heights (10cm, 1m and 1.90m), circumferentially along the azimuthal angle φ (Fig. 4-1-2b). Joseph used a RTM with a great number of rays (200,000) for maximal accuracy, and an unstructured grid of 26,000 tetrahedra. In the present case a structured grid is considered instead, since the O-grid structure is usual for simulating pool fires with FireFOAM [18, 23]. Ray effects affect the radiant flux differently depending on the mesh grid size, as coarse grids may indeed compensate ray effects by numerical smearing or false scattering [25]. Hence four different grids were studied: one coarse (28 cells across the radius, 25 vertically), one refined radially

(84x25), one refined axially (28x100) and one refined in both directions (84x100) (labelled a, b, c, d).

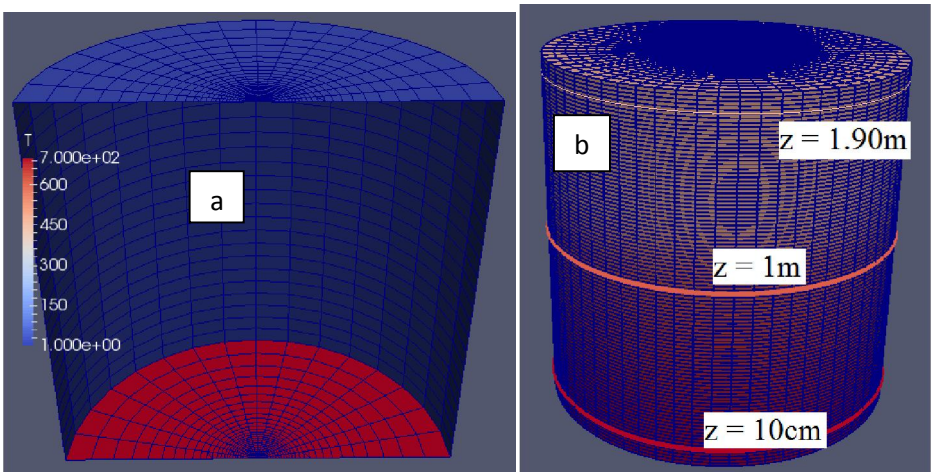

Fig. 4-1-2: View of the transparent cylinder mesh and temperature field (a), locations of the radiative flux line plots (b) (z = 10cm, 1m, 1.90m).

The radiative flux was found to be relatively much less sensitive to the discretisation of the azimuthal angle φ than that of the polar angle θ (between the radial plane xy and the axis z), therefore the dependence along φ is not considered at this stage. A large number of φ divisions (20) is considered to almost completely eliminate that dependence, so the results are simpler to read by showing just the dependence on θ and the grid size. Joseph's RTM solution is used as the benchmark for relative error calculations (Table 4-1-2, 4-1-3, 4-1-4).

Table 4-1-2: Relative errors (%) from FireFOAM'sFVM solutions vs. RTM of [83] for the net radiative flux at elevation z = 10cm.

Error (%) = $\frac{\lvert FV-RT\rvert}{\lvert RT\rvert}$	Mesh grid a): 28(r) x 25(h) cells	Mesh grid b): 84(r) x 25(h) cells	Mesh grid c): 28(r) x 100(h) cells	Mesh grid d): 84(r) x 100(h) cells
20 x 2 angles	8.8	9.7	9.0	10.0
20 x 3 angles	57.0	57.0	57.0	57.0
20 x 4 angles	6.9	9.1	7.4	9.8
20 x 5 angles	33.1	32.7	33.0	32.5
20 x 6 angles	4.2	8.1	5.0	9.1
20 x 7 angles	22.1	21.2	21.9	21.0
20 x 8 angles	1.9	7.1	2.8	8.4
20 x 9 angles	16.1	14.7	15.8	14.4
20 x 10 angles	0.1	5.9	1.0	7.9

Table 4-1-3: Relative errors (%) from FireFOAM'sFVM solutions vs. RTM of [83] for the net radiative flux at elevation z = 1m.

Error (%) = $\frac{\lvert FV-RT\rvert}{\lvert RT\rvert}$	Mesh grid a): 28(r) x 25(h) cells	Mesh grid b): 84(r) x 25(h) cells	Mesh grid c): 28(r) x 100(h) cells	Mesh grid d): 84(r) x 100(h) cells
20 x 2 angles	40.7	48.8	47.1	83.0
20 x 3 angles	0.0	2.4	1.8	4.2
20 x 4 angles	21.9	36.8	25.6	48.8
20 x 5 angles	10.7	17.0	15.0	31.1
20 x 6 angles	4.8	3.9	3.1	0.8
20 x 7 angles	1.4	7.1	1.5	25.6
20 x 8 angles	0.4	4.0	3.1	15.2
20 x 9 angles	1.9	4.4	0.9	2.4
20 x 10 angles	0.4	1.7	0.9	6.9

Table 4-1-4: Relative errors (%) from FireFOAM'sFVM solutions vs. RTM of [83] for the net radiative flux at elevation z = 1.90m.

Error (%) = $\frac{\lvert FV-RT\rvert}{\lvert RT\rvert}$	Mesh grid a): 28(r) x 25(h) cells	Mesh grid b): 84(r) x 25(h) cells	Mesh grid c): 28(r) x 100(h) cells	Mesh grid d): 84(r) x 100(h) cells
20 x 2 angles	75.8	93.6	86.5	101.1
20 x 3 angles	46.8	53.6	56.2	83.9
20 x 4 angles	6.4	8.5	9.9	13.5
20 x 5 angles	15.5	27.6	21.8	34.4
20 x 6 angles	4.5	2.2	2.9	24.9
20 x 7 angles	8.6	11.1	13.0	29.4
20 x 8 angles	4.4	1.2	4.9	4.9
20 x 9 angles	4.0	2.8	2.4	19.9
20 x 10 angles	5.1	2.1	5.3	3.3

At z = 10cm, close to the emitting source, a clear difference is made by discretising θ in even or odd numbers (Table 4-1-2). Odd numbers always produce much more error, as high as 57% with 3 angles and down to around 15% with 9 angles. With even numbers the relative error is never higher than 10% with 2 angles. When the angular discretisation increases the error levels converge towards zero, but differently between the mesh grids. The mesh refinement along the axis (grid c) produces only a marginal increase of error, but refinements in the radial plane have much more impact (grids b and d). The effect is more pronounced at higher angular resolution. For the fine mesh (d) the angular refinement 20x10 leaves a non-negligible error of 8%. Mid-height at z = 1m, the odd-versus-even number trend is less clear (Table 4-1-3) and the evolution against angular refinement is "saw-tooth"-like. However, overall the errors do decline sharply past the three refinements, suggesting that further refinements may not bring large improvement. The angular mesh 20x3 seems to yield small errors (4% and less) for every grid mesh, but it cannot be deemed usable because of the large

error back at z = 10cm (57%), nor the 20x9 angular mesh for the same reason. The 20x10 angular mesh is the safest option, yielding a maximal error of 7% with mesh (d) and negligible with the others. Finally at the highest location z = 1.90m (Table 4-1-4), the data again shows that an even number of azimuthal angles is the safe choice. Up to 6 angles the error in the fine mesh (d) is unacceptable at 25%, but with 8 or 10 angles it drops to reasonable levels (3-5%).

4.1.2.2. Smaller emitting surface

Although the above gives an idea of ray effects in FireFOAM, the case set up can be modified to suit pool fire conditions some more, to further test the convergence on the radiative flux. To do so, we shall take the finer mesh grid (d) and reduce the radius of the emitting surface from 1m to 15cm (radius of often-studied pool fires, see Chapter 2). The emitted energy now travels a longer distance from the bottom-centre to the side wall, which increases ray effects. We now consider the side wall flux along a ring (0 to 2π) at a height z = 1m (Fig. 4-1-3).

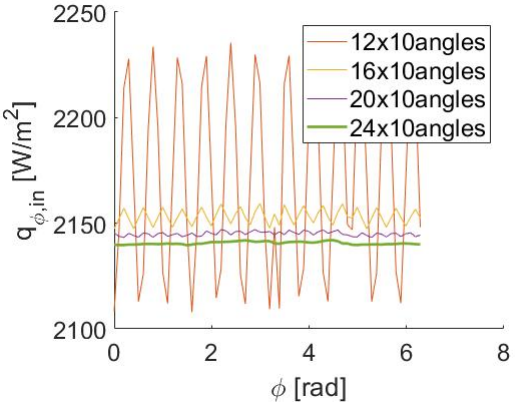

Fig. 4-1-3: Evolution of the incident radiative flux along the cylinder circumference, at height z = 1m above the emitting region (modified case with $R_{emission}$ = 15cm). Showing dependence on discretisation of azimuthal angle φ.

The number of azimuthal angles in a 3D geometry is equal to 4x$N\varphi$. Here, "12x10 angles" means that $N\varphi$ = 3 and there are 12 divisions between 0 and 2π (and 10 divisions vertically). Fig. 4-1-3 shows strong ray effect fluctuations with the 12x10 scheme (the 8x10 scheme yielded too much fluctuation to be shown). However the differences between the schemes fade rapidly with the resolution increase, as with the 16x10 scheme the fluctuations become much smaller, and negligible by the 24x10 scheme. If computational demands prevent using that many polar angles, an averaging technique may be used along φ, if the standard deviation is sensible (not like in e.g. the 12x10 plot). Let us assume that the azimuthal dependence is completely removed with 24 angles, so we can sample the vertical evolution of the flux along the side wall at any azimuthal location. Fig. 4-1-4 shows this vertical evolution for four polar discretisations.

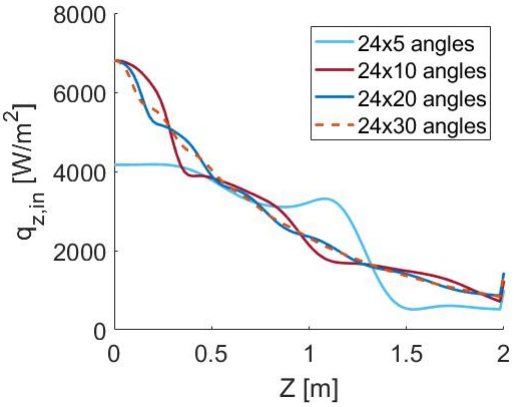

Fig. 4-1-4: Evolution of the incident radiative flux vertically along the cylinder's side wall at R = 1m for the modified emission surface case. Showing dependence on discretisation of polar angle θ.

Fig. 4-1-4 shows that the convergence towards the complete removal of ray effect fluctuations is slower in the vertical direction, which is due to the aspect ratio of the geometry of 2:1 along the cylinder axis. Using just 5 angles for θ leads to poor performance. 10 or 20 angles improve the smoothness but it is not until 30 angles that the flux shape is almost smooth. Note that along the centreline, this mesh has a uniform cell resolution of 6mm, which is close to the typical cell size of the pool fires studied in Chapter 5. This cylinder has a height of 2m, which may contain a fire of height around 50cm, therefore, the fact that the radiation source is not flat like in this example may lead to the assumption that 20 azimuthal directions for a cylinder this size should be acceptable with regards to ray effects. By extension, for a cylinder height of e.g. 4m containing a flame of 1m or more in height, no less than 30 directions may be used (if the cell size is unchanged).

To summarise and conclude this section, we may reasonably assume that the FVM solver has an intrinsic error of about 3% on the radiative flux and its divergence, that is independent of ray effects and cannot be reduced (grey gas case, section 4.1.1). As for the ray effects, which do happen when the flux is sampled at a distant location from the source, we have established that for the cylindrical geometry of a 30cm pool fire, of about 1m in radius and 2m in height might require an angular mesh of at least 16x20 solid angles and at least 16x30 if the height is doubled (all for a cell size of about 6mm).

4.1.3. Homogeneous gases

Homogeneous gases rigorously remove the necessity of integrating the optical depth over the path length in the general expression of transmissivity (Eq. 3.28), which also removes grid dependency. It is thus an ideal way of assessing the accuracy of a gas absorption model in detail, especially in a 1D scenario, since the two remaining sources of possible error are the non-correlated RTE solution along the line of sight and the modelling of non-grey absorption/emission. An extra source of error is expected to affect the grey WSGG models that use mean beam lengths, to different degrees between the 1D, 2D and 3D cases investigated here. In particular, the non-cubic 2D and 3D geometries will be expected to

emphasise the MBL issue, which is why the source terms and radiant fluxes will be always evaluated vertically and horizontally.

4.1.3.1. One-dimensional gas mixture with soot loadings

A 1 metre thick slab of gas is considered in line-of-sight RTE solutions, as per Bressloff's test case in [36]. The homogeneous gas mixture contains 8% of CO_2 and 16% of H_2O in mole fractions. Temperature is isothermal at 1000K and boundaries are cold and black. Starting with no soot, uniform soot loadings are added successively (0.1, 1 and 10ppm). FireFOAM solves the RTE in a single direction (left to right) for the five WSGG implementations. Bressloff's most accurate model, the RADCAL-based DBT-SNB (differential banded treatment-statistical narrow band), was coupled with an exact (correlated) RTE solution in [36]. That solution is also used as benchmark here. For a homogeneous path the absorption coefficient is spatially uniform, but unlike the uncorrelated method where only the last cell is considered, the correlated transmissivity varies along the path taken from the origin. For grey WSGG calculations the mean beam length is S = 1m x 1.76 = 1.76m, hence the pressure-path length of the gas phase is also relatively small at 0.42 atm.m and remains well within validity limits of all WSGG models (see Chapter 3). The results for the four case variants are shown in Fig. 4-1-5.

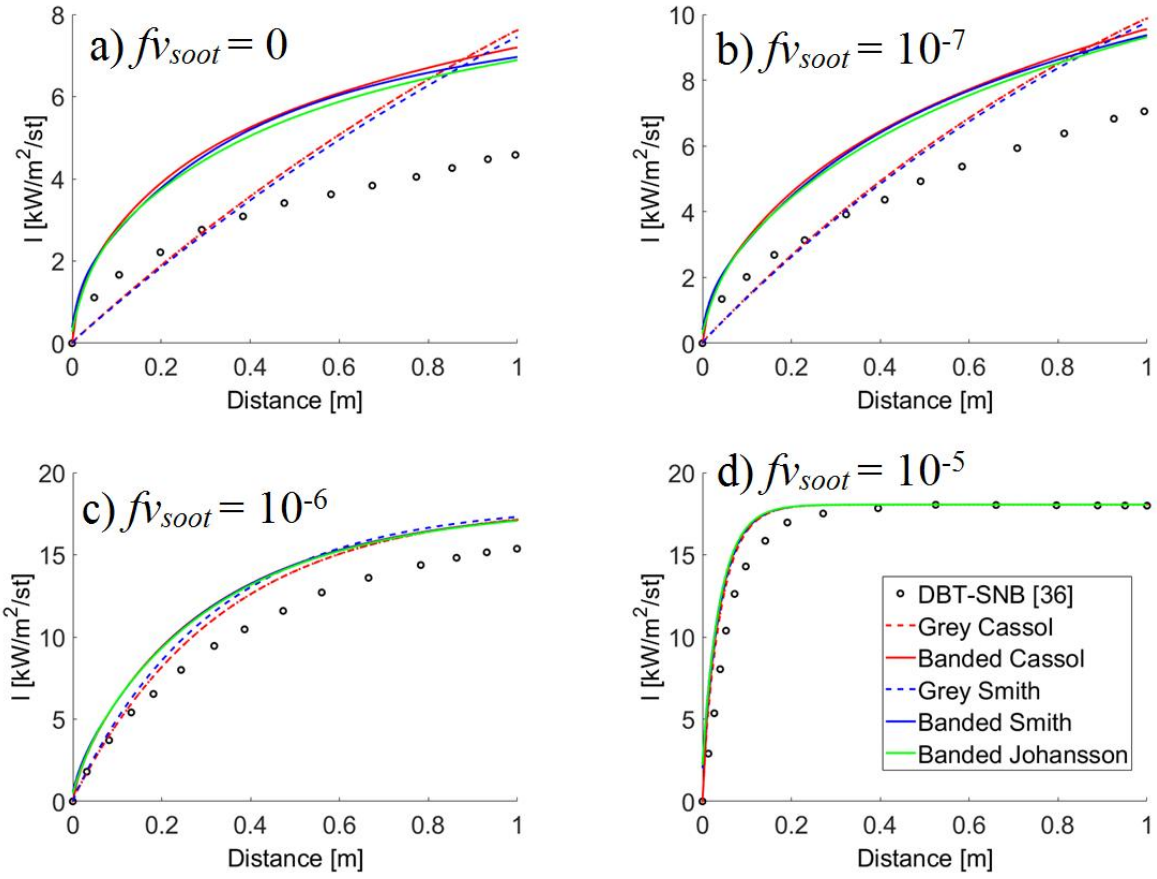

Fig. 4-1-5: Comparison of FireFOAM-WSGG line-of-sight solutions with DBT-SNB from [36] for different soot volume fractions (isothermal & homogeneous gas)

For non or low sooty mixtures, the grey WSGG solutions are poor and display almost straight line profiles (Fig. 4-1-5-a and 4-1-5-b) that disagree qualitatively with the other models. The banded WSGG solutions do manage a qualitative agreement, but all of them overpredict the intensity at the slab's end by more than 50% relative to the DBT-SNB. Besides, there are no significant differences between the Smith, Cassol or Johansson models. When the soot concentration increases, a convergence of behaviours is seen between grey and banded WSGG models (Fig. 4-1-5-c and 4-1-5-d). In the last case (Fig. 4-1-5-d) the soot absorption coefficient is κ_{soot} = 1226 x10^{-5} x 1000 = 12.26 m^{-1}. As indicated by the asymptotic behaviour in Fig. 4-1-5-d, the whole spectrum is already thick at the mean beam length (κS = 21.6) with or without the gas phase, hence the lack of differences between models. This drives to the conclusion that the large errors of the non or little sooty cases are due to the uncorrelated nature of the FVM solution, rather than the WSGG models.

4.1.3.2. Non-isothermal mixture in 2D enclosure

This case scenario is from Goutiere et al. [35] and uses the same boundaries, geometry and mesh as described in section 4.1.1. The rectangular enclosure is now filled with a gas mixture of uniform mole fractions (10% CO_2 and 20% H_2O), but the temperature follows a spatial distribution as per Eq. 4.1.1 and Fig. 4-1-6. This distribution, axisymmetric along (x, y = 0.25), is meant to reproduce furnace conditions [35]. The bounding cells are set to 400K but there is a 1800K peak at x = 0.1, y = 0.25m, hence a very abrupt $\Delta T/\Delta x$ = 140K/cm in that region. The mean beam length for grey solutions is determined from the enclosure's dimensions as $S = 3.6V/A$ = 0.6m, hence the pressure path length pS = (0.2 + 0.1)x0.6 = 0.18 atm.m meets the WSGG validity criteria. Following the grey gas study of section 4.1.1 the FireFOAM solutions use 16 solid angles. The benchmark is the SNB solution of [35] which was coupled with a RTM solver using the correlated approach.

$$y_0 = \frac{|0.25-y|}{0.25},\ T(x,y) = \begin{cases} (14000x - 400)(1 - 3y_0^2 + 2y_0^3) + 800 & \text{if x} < 0.1 \\ \frac{-10000}{9}(x-1)(1 - 3y_0^2 + 2y_0^3) + 800 & \text{if x} > 0.1 \end{cases} \quad (4.1.1)$$

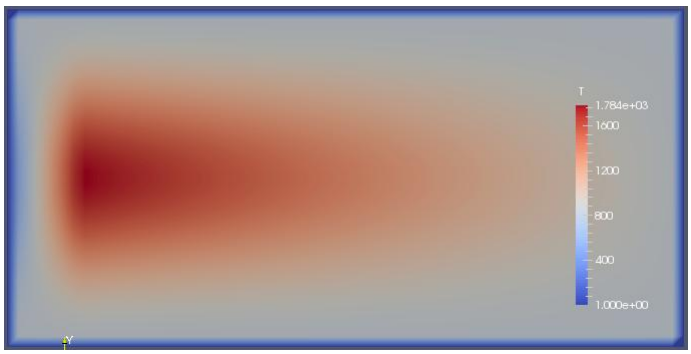

Fig. 4-1-6: Temperature field from Eq. 4.1.1 in 1m x 0.5m enclosure of [35]

The horizontal source term along the symmetry axis (Fig. 4-1-7-a) is the most delicate to represent as it has the strong temperature gradient between $x = 0$ and $x = 0.1$m. The two grey WSGG models strongly underpredict at $x = 0$ with a relative error $\left|\frac{WSGG-SNB}{SNB}\right|$ of 81% but improve moving away from the wall. The errors at the bottom peak at $x = 0.11$ are of 28% (Grey Cassol) and 17% (Grey Smith) are acceptable. The banded models perform well all along the axis. The Johansson and Cassol curves are almost confounded and provide the best overall match with SNB, but the Smith model better predicts the peak with a near-exact match. Both the grey and banded Smith WSGG tend to increase the radiative output in this kind of mixture ($p_w/p_c = 2$). Away from the hot zone, the vertical source term curves along ($x = 0.5$, y) the grey models are again very close (and poor) at the walls (Fig. 4-1-7-b). With its weaker output the Grey Cassol model overpredicts less the peak at $y = 0.25$ (16%) than the Grey Smith (23%). The banded models perform slightly less well near the walls than in the horizontal direction with relative errors of ~45%. At the peak the errors are between 7% (Banded Johansson) and 19% (Banded Smith). There is only a 10kW/m^3 difference between the Cassol and Johansson models, which are otherwise similar. The fluxes show similar trends. The horizontal flux along at $y = 0$ shows all models overpredict to a degree (Fig. 4-1-7-c). At the wall at $x = 0$ there is a relative error of up to 37% from the grey models, and 13% for the banded, both from the Smith model. The banded Cassol and Johansson models perform well at the boundaries. The flux peaks around x = 0.24m. The maximum relative error there is from the grey Smith model (32%), and the best performance is from the banded Johansson (5%). The banded Smith model yields 21% and the banded Cassol 10%. Finally, at the furthest wall from the hot zone (Fig. 4-1-7-d), the trends accentuate. All three banded models are very close to one another, with the Johansson slightly better. The relative errors never exceed 8%, despite some fluctuations appearing around $y = 0.14$m and $y = 0.37$m that are most likely from some residual ray effects (which did not appear in the grey case with the same discretisation). The two grey models perform quite poorly and seem to enhance these fluctuations, causing relative errors of up to 50%. Overall, as a summary, the most consistently well-performing model is the banded Johansson, followed closely by the banded Cassol WSGG. The Smith correlations seem to overpredict the radiative output for this particular p_w/p_c. Despite the very strong temperature gradient the banded WSGG models do quite well. The grey gas pressure-absorption coefficients are temperature independent, which could have posed an issue, but the temperature dependent weights seem to compensate that, perhaps because they are very sensitive to temperature changes, as stated by Goutiere et al. [35]. Somehow, even the grey models are not that off with such strong gradients. The bulk of their errors come mostly from their "flat" behaviour at the boundaries, which is no doubt a consequence of the use of the mean beam length. Middle-field errors are actually acceptable, because this is where the mean beam length approximation is most relevant.

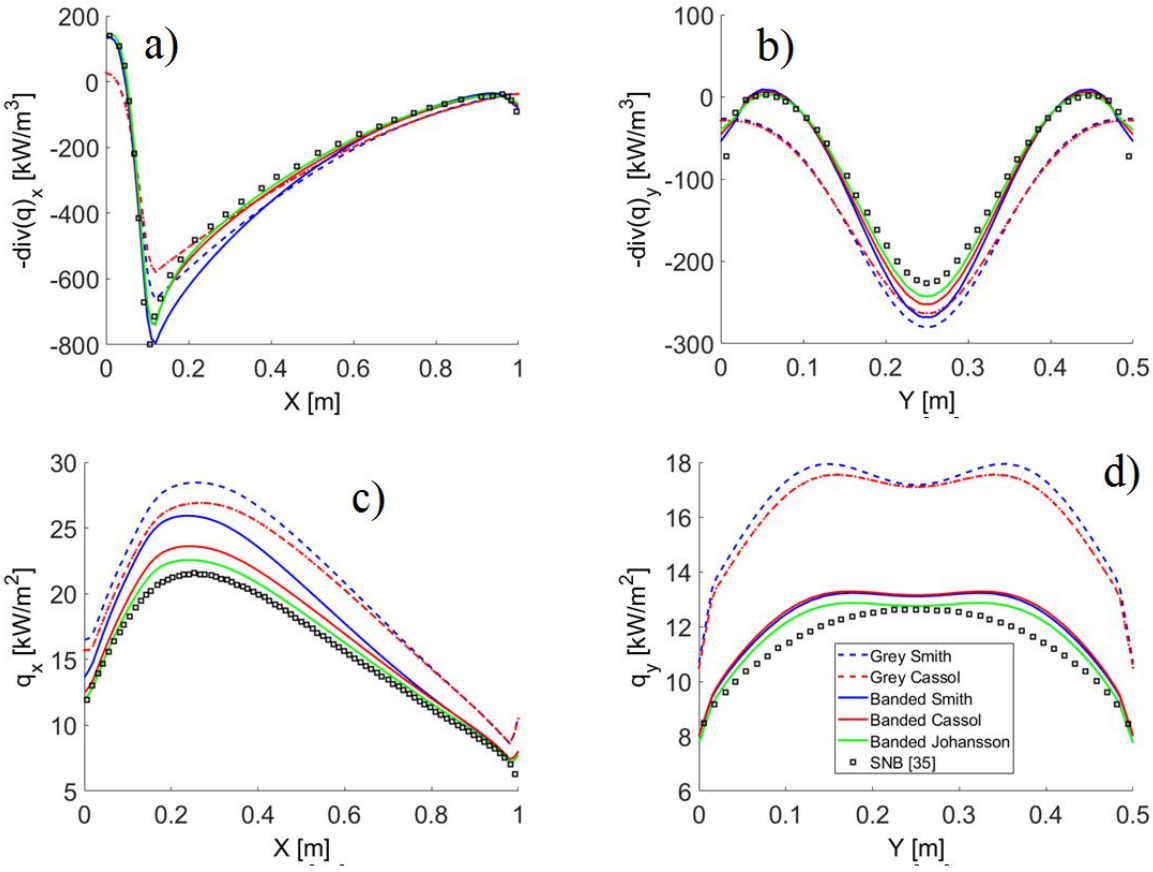

Fig. 4-1-7: (a), (b) Radiative source term along (x, y = 0.25) and (x = 0.5, y), (c), (d) incident flux along (x, y = 0.5) and (x = 1, y) for the non-isothermal 2D enclosure of [35], FireFOAM-WSGG vs SNB of [35]

4.1.3.3. Pure H_2O in 3D enclosure

A rectangular enclosure of dimensions 2m x 2m x 4m contains a homogeneous water vapour phase with $p_w = p_T = 1$ atm, as per the first test case of Coelho [34]. All walls are black at 300K and the gas is isothermal at 1000K. We use the same uniform mesh grid of 11 x 11 x 16 cells and solve the RTE for the same 128 directions as in [34]. For the benchmark, Coelho used the results of Liu [84], who coupled a SNB model with a RTM solver, which is thus the benchmark for this work too. Coelho also performed WSGG calculations with grey and banded implementations of Smith WSGG, coupled with a DOM and a DTM consecutively, pointing out negligible differences between the two. Those DOM-WSGG results were not reproduced here to avoid confusion but they are discussed below. Our FireFOAM calculations are done with the Smith (p_w = 1atm) and Cassol models only, as the Johansson WSGG can handle only mixtures. The mean beam length for grey solutions is the spectral averaged $S = 3.6V/A$ = 1.44m, hence the pressure-path length pS = 1.44 atm.m.

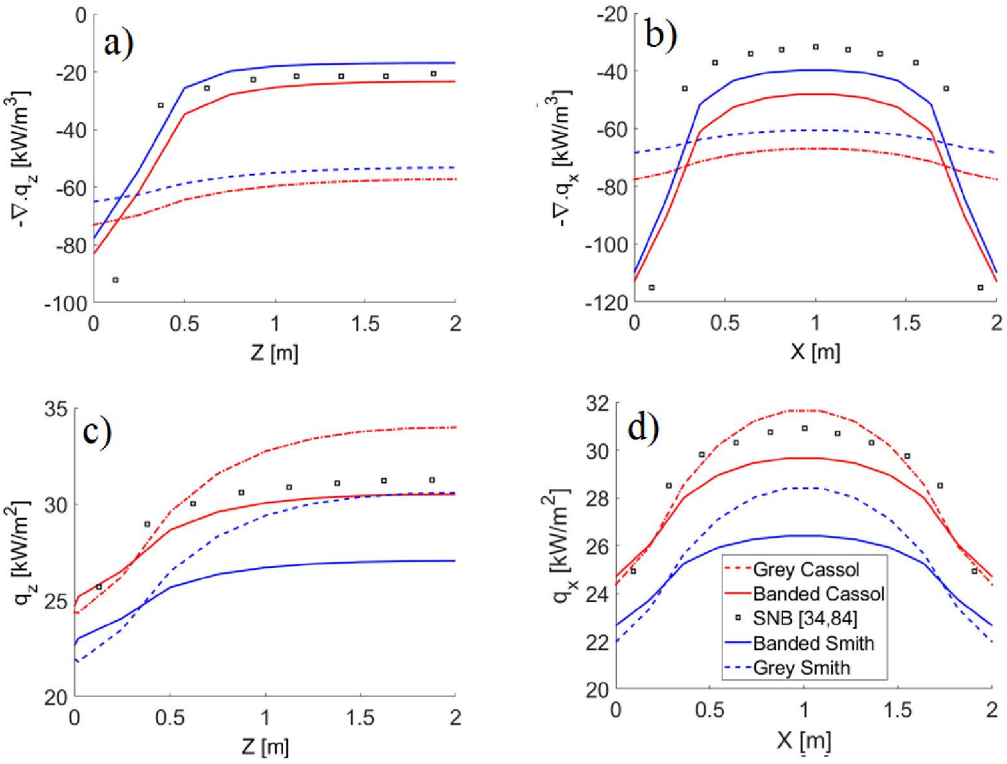

Fig. 4-1-8: (a), (b) Radiative source term along (x = 1m, y = 1m, z) and (x, y = 1, z = 0.375m) ; (c), (d) incident flux along (x = 2m, y = 1m, z) and (x, y = 1m, z = 4m) for the 3D enclosure of [34], FireFOAM-WSGG vs SNB of [34,84]

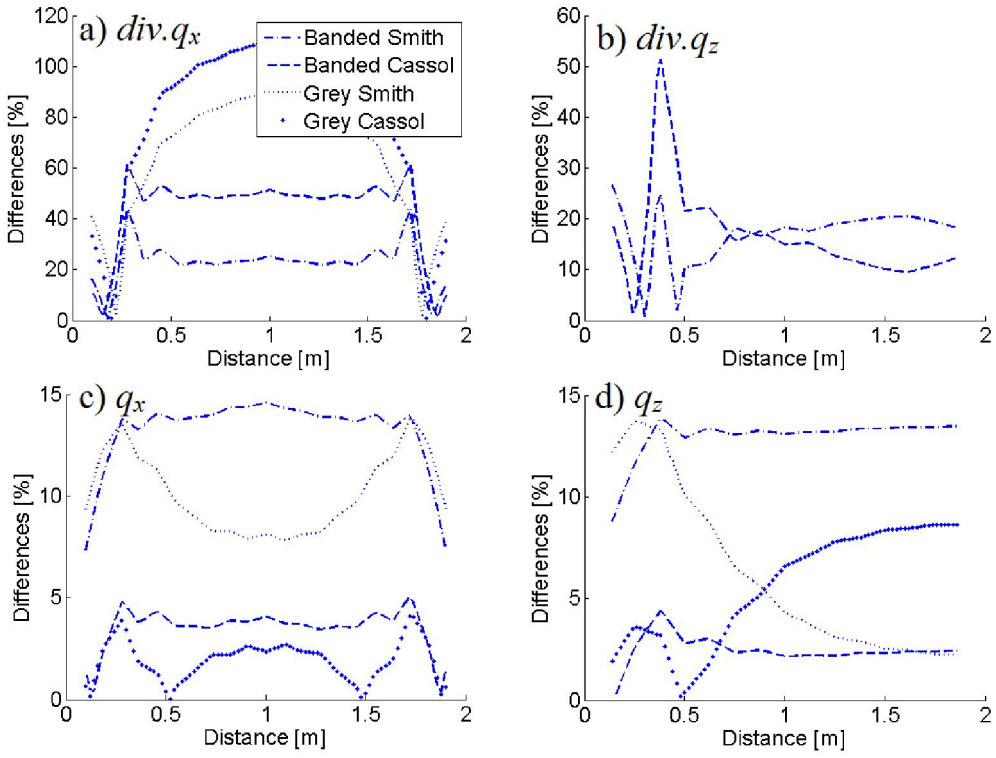

Fig. 4-1-9: Errors of FireFOAM-WSGG relative to SNB [34,84], on the radiant source term (a, b) and flux (c, d) from Fig. 4-1-8

Source terms and fluxes are plotted along the z and x axes, i.e. (x = 1m, y = 1m, z) and (x, y = 1, z = 0.375m) for the source terms, (x = 2m, y = 1m, z) and (x, y = 1m, z = 4m) for the fluxes (Fig. 4-1-8). The respective errors relative to the SNB benchmark are in Fig. 4-1-9. Overall the FireFOAM-WSGG results are quite consistent with the DOM-WSGG calculations reported in [34]. Both the grey Smith and grey Cassol WSGG yield near-flat source term lines (Fig. 4-1-8-a, 4-1-8-b), similar to Coelho's grey WSGG that use the domain-based mean beam length. The relative errors reach above 100% along x (Fig. 4-1-9-a) and are too high to be shown on Fig. 4-1-9-b. The banded models much improve the source term both at the boundaries and midfield. The banded Smith WSGG is significantly better than the banded Cassol in that respect, as the bulk of the relative error is more or less around 20% between both directions. The Cassol model yields errors that are mostly up to 50%. For the flux, it seems the driving parameter is not so much the banded vs grey solution as the WSGG model itself. The relative errors of the grey and banded Cassol models are mostly under 5% (Fig. 4-1-9-c, 4-1-9-d). The banded Smith yields a consistent average of ~13%, whereas the grey Smith occasionally drops below 10%. Overall this is quite consistent with the Smith WSGG errors of 10% on the flux and 30% on the source term reported in [34]. The differences between the Smith and Cassol WSGG models may be explained by the fact that Cassol et al. generated one set of coefficients for any mole fraction of H_2O, whereas Smith et al. had two sets for H_2O, an approach perhaps better suited to that gas. A preliminary run using the Smith p_w -> 0 set showed source terms differences of 50% from the Smith p_w = 1 atm set, although the grey gas absorption coefficients k_j differ by only about 10% between these two sets.

4.1.4. Inhomogeneous gases

For any WSGG model, the absorption coefficient is calculated in each cell where temperature and gas concentration are treated as uniform. The uncorrelated FVM only considers the history of radiant intensity from the previous cell along a line of sight, thus the homogeneous treatment of transmissivity in each cell is somewhat accurate, although perhaps at the cost of a grid dependence. The inhomogeneous variants of the scenarios investigated above thus serve to evaluate how well such approximations hold, each time reproducing the same grids as specified in the references, to maintain coherence in the comparisons with those works' benchmark data. For a grey WSGG, the approach certainly cannot be expected to be rigorous, because the mean beam length S is still evaluated from the whole (inhomogeneous) domain, not the quasi-homogeneous computational cell (cell-based mean beam lengths reportedly only work in optically opaque or very thick media, which were never encountered in this work's context [7]). However, the next sections may show that the locally-computed absorption coefficient may perhaps be able to rectify the optical depth κS in each cell.

4.1.4.1. One-dimensional gas mixture with soot loadings

The 1m slab of section 4.1.3.1 and [36] is now inhomogeneous in temperature, and gas-soot concentrations. One distribution ("gas A") is bell-shaped, the other ("gas B") is reverse-bell shaped (Fig. 4-1-10-a, 4-1-10-b). Each gas type has two soot distributions, weaker or stronger in concentration (Fig. 4-1-10-c, 4-1-10-d). The field equations are given in Table 4-

1-5. As previously, p_w/p_c = 2, and we calculate the line-of-sight intensities with the five FireFOAM-WSGG models and compare against the exact DBT-SNB solution of Bressloff [36]. The results for the six scenarios (two non-sooty and four sooty) are presented in Fig. 4-1-11.

Table 4-1-5: Temperature, gas and soot distributions for the 1D slab from [36]

Gas	Temperature (K)	CO_2 partial press. (atm)	Soot volume fraction (-)	Soot
A	$4000x(L-x)+800$ (4.1.2)	$0.4x(L-x)+0.06$ (4.1.3)	$(40x(L-x)+6)10^{-7}$ (4.1.4.a) $(40x(L-x)+6)10^{-8}$ (4.1.4.b)	As Bs
B	$4000x(x-L)+1800$ (4.1.5)	$0.4x(x-L)+0.16$ (4.1.6)	$(4x(x-L)+1.6)10^{-6}$ (4.1.7.a) $(4x(x-L)+1.6)10^{-7}$ (4.1.7.b)	Cs Ds

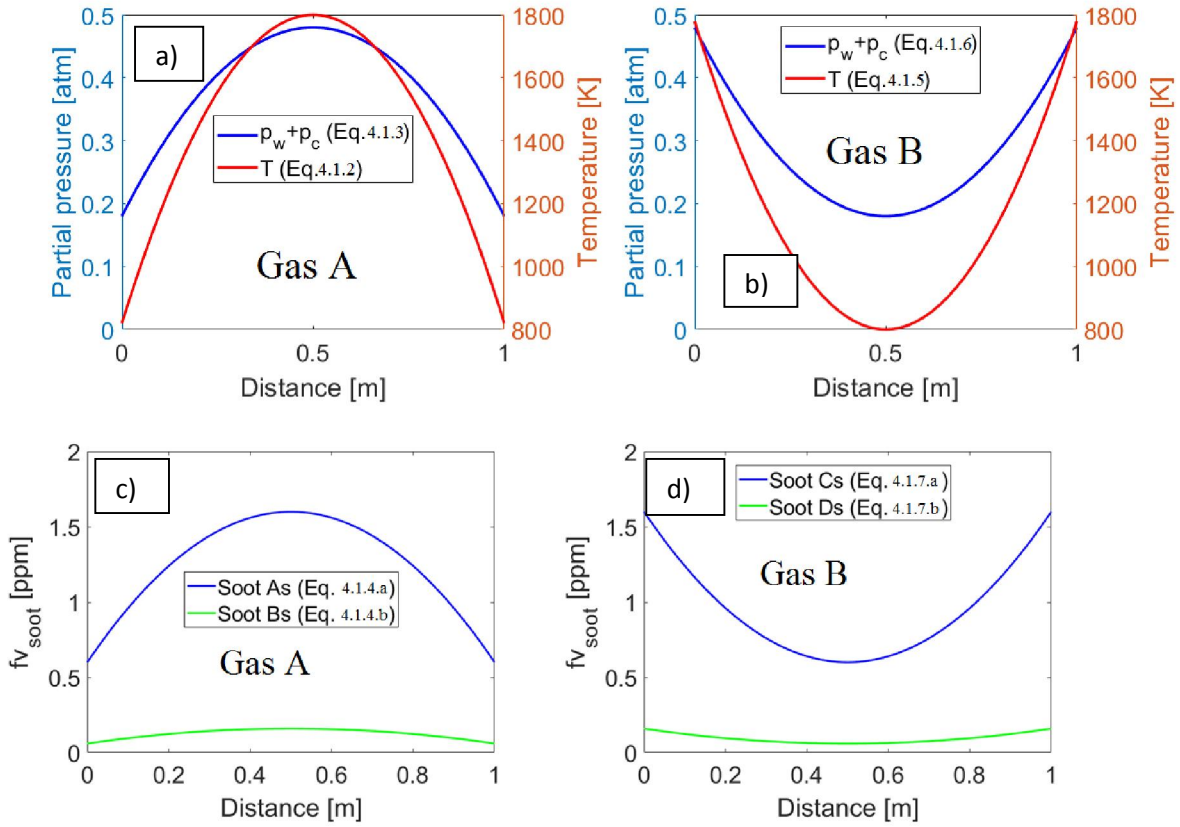

Fig. 4-1-10: Gas pressures and temperatures (a, b), soot distributions (c, d) for inhomogeneous 1D slab from [36]

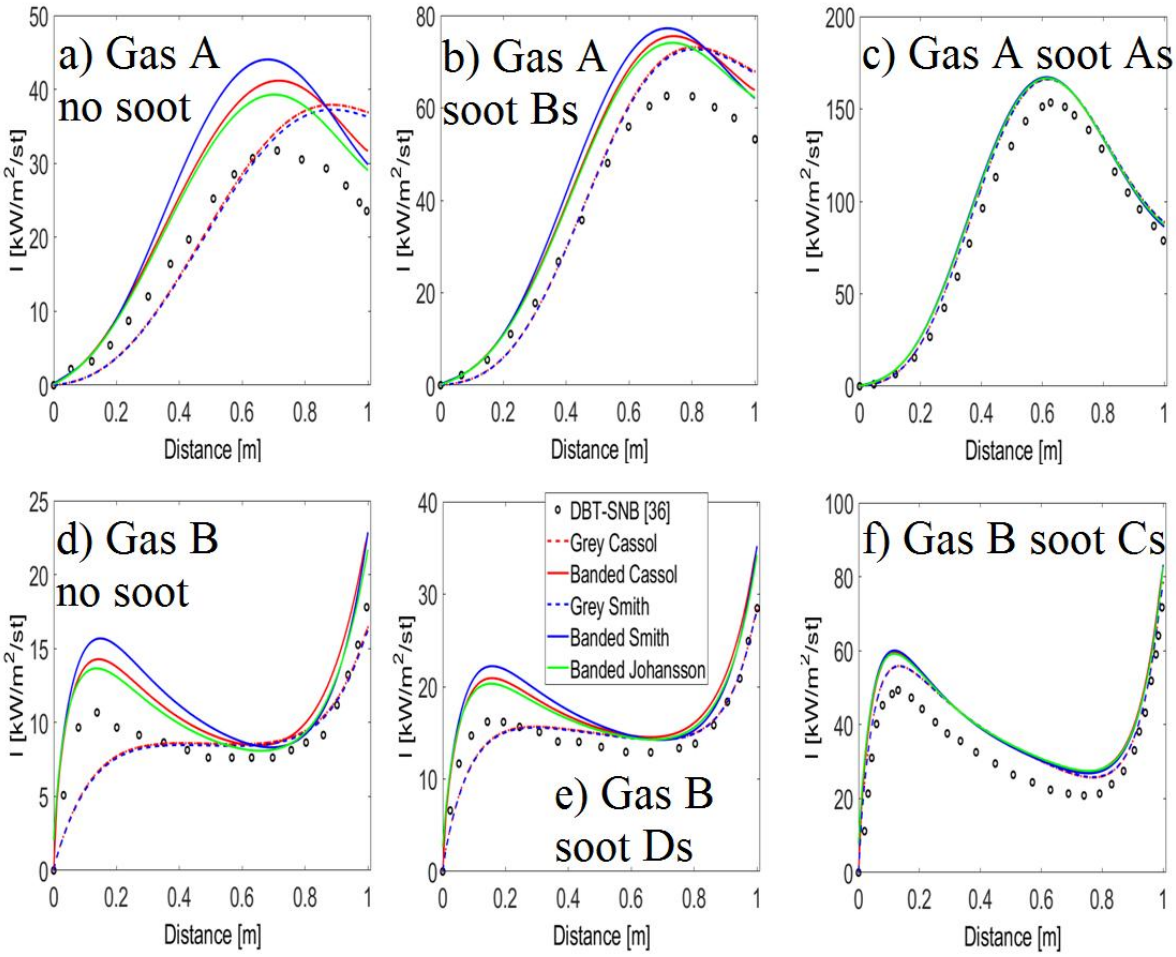

Fig. 4-1-11: Comparison of FireFOAM-WSGG line-of-sight solutions with DBT-SNB from [36] for different soot volume loadings (non-isothermal, inhomogeneous)

The grey solutions are just as off as previously but the inhomogeneities bring out contrasts between the banded WSGG solutions. For Gas A where temperature and concentration peak in the middle (Figs. 4-1-11-a, 4-1-11-b and 4-1-11-c), the Johansson model clearly outperforms the other two, as in the non-sooty variant the error relative to DBT-SNB peaks at 27% (32% and 42% for Cassol and Smith respectively). Then again, once soot is introduced, the peak differences become smaller both between the WSGGs, and between the WSGGs and the DBT-SNB (in the 18-23% range for the weaker sooty variant of Gas A (Fig. 4-1-11-b) and around 8% for all WSGGs for the sootier variant (Fig. 4-1-11-c). With Gas B, it is very much the same picture (Fig. 4-1-11-d, 4-1-11-e, 4-1-11-f) where the gradients are located at the start and at the end of the optical path. Without soot, the largest differences are near the start (Fig. 4-1-11-d) and they are quantitatively almost identical to that of Fig. 4-1-11-a. For the weakly sooty variant (Fig. 4-1-11-e) the differences are a little more important than in Fig. 4-1-11-b (25 to 35%), again with the Johansson WSGG performing best. The sootier variant of Gas B (Fig. 4-1-11-f) is the only time where a grey WSGG outperforms a banded formulation (14% vs. 20%).

The WSGGs combined with the uncorrelated FVM solver give better results in inhomogeneous media than in homogeneous scenarios. Most of the time, the banded

treatment clearly improved the predictions, but with relative errors never smaller than 14% in "grey" media (soot-dominated), or never smaller than 27% in non-grey media (gas-dominated), the overall performance is far from outstanding. However let us bear in mind that these are line-of-sight solutions; for practical CFD applications the radiant source term and the heat flux are more important and involve multiple directions.

4.1.4.2. Pure CO_2 or pure H_2O in 2D enclosure

This case is a variant of section 4.1.3.2 based on [35]. Inhomogeneous, non-isothermal CO_2 and H_2O phases are tested separately with relatively small concentrations typical of fires. The equations for the temperature and concentration fields are:

$$T(x,y) = T_0[0.3333(1-2|x-0.5|)(1-4|y-0.25|)+1] \quad (4.1.8)$$

$$c(x,y) = c_0[4(1-2|x-0.5|)(1-4|y-0.25|)+1] \quad (4.1.9)$$

Where T_0 = 1200K and c_0 = 0.02 for CO_2 and 0.04 for H_2O. The temperature varies between 1200 and 1600K as per Fig. 4-1-12. The partial pressures have the same spatial distribution and vary between 0.02 and 0.10 for CO_2 and 0.04 and 0.20 for H_2O [35].

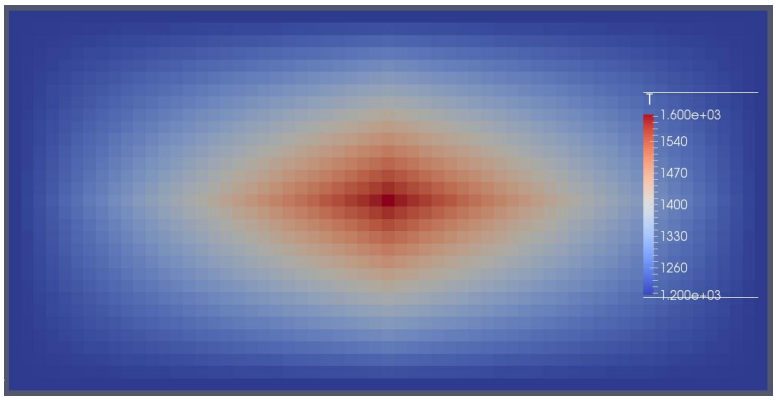

Fig. 4-1-12: Temperature field from Eq. 4.1.8 in 1m x 0.5m enclosure of [35]

As in section 4.1.3.2, the source term is sampled along the horizontal and vertical median axes, and the flux is taken horizontally at the bottom wall and vertically at the right hand side wall. The benchmark data is again the SNB-RTM of [35]. The Johansson WSGG is left out since the gas are not mixtures so only the Smith and Cassol WSGG models are shown in Fig. 4-1-13 (CO_2) and 4-1-15 (H_2O), with corresponding relative errors in Fig. 4-1-14 (CO_2) and 4-1-16 (H_2O). For CO_2, the grey models are in large error typically by the boundaries (~40%), and quarter-way and three-quarter way along the line (20-25%). The midfield peaks are however below 20% in error, thus not too different from a banded WSGG. The latter are again better in all areas (mostly under 10%). The grey models are better with the radiant fluxes, although still 2-3 times more in error than the banded WSGG. The grey WSGG also appear sensitive to gas field gradients, which are sharper in the *y* direction, hence largely increasing the errors. The banded WSGG also have that trend but to a much lesser extent as flux errors remain under 10% in both directions. For the H_2O case the picture is slightly different. The grey and banded Cassol models yield large flux errors in both directions (30%

banded, 30-45% grey), whereas the errors from Smith models are mostly under 15%. For the source terms, the grey and banded Cassol both yield 25-30% errors near the walls, versus 10-15% for both Smith models at the same locations. This situation reminds of the H_2O only gas case of the homogeneous 3D case of section 4.1.3.3., therefore the same explanation about P_w ->0 and P_w= 1 coefficients may be advanced here. On a better note all models very neatly reproduce the midfield peak of the source term.

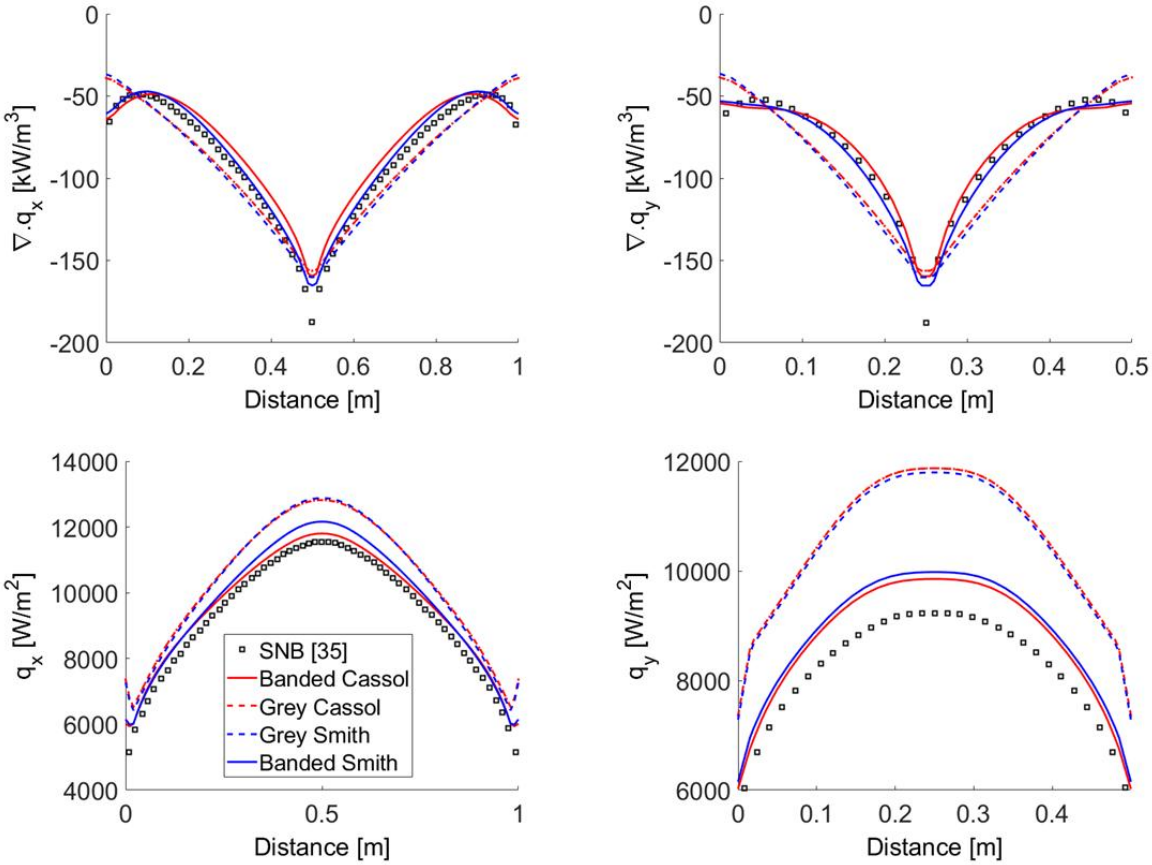

Fig. 4-1-13: FireFOAM-WSGG vs SNB of [35] in 2D inhomogeneous and non-isothermal CO_2 case of [35], (a), (b) radiative source term along (x, y = 0.25) and (x = 0.5, y), (c), (d) incident flux along (x, y = 0.5) and (x = 1, y)

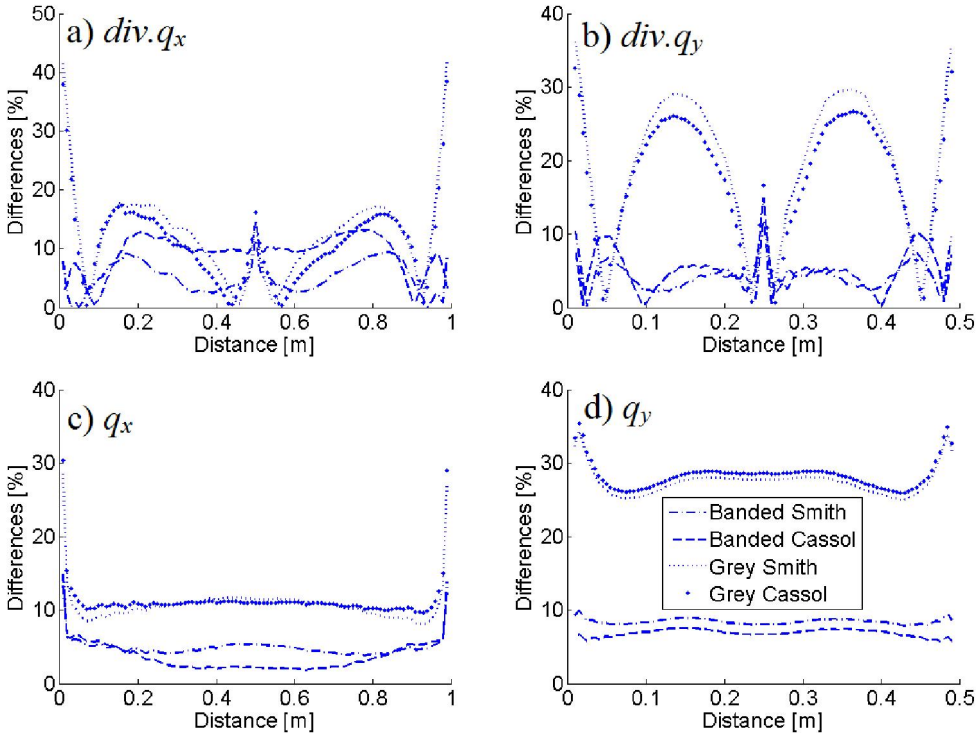

Fig. 4-1-14: Errors of FireFOAM-WSGG relative to SNB [35], on the radiant source term (a, b) and flux (c, d) from Fig. 4-1-13

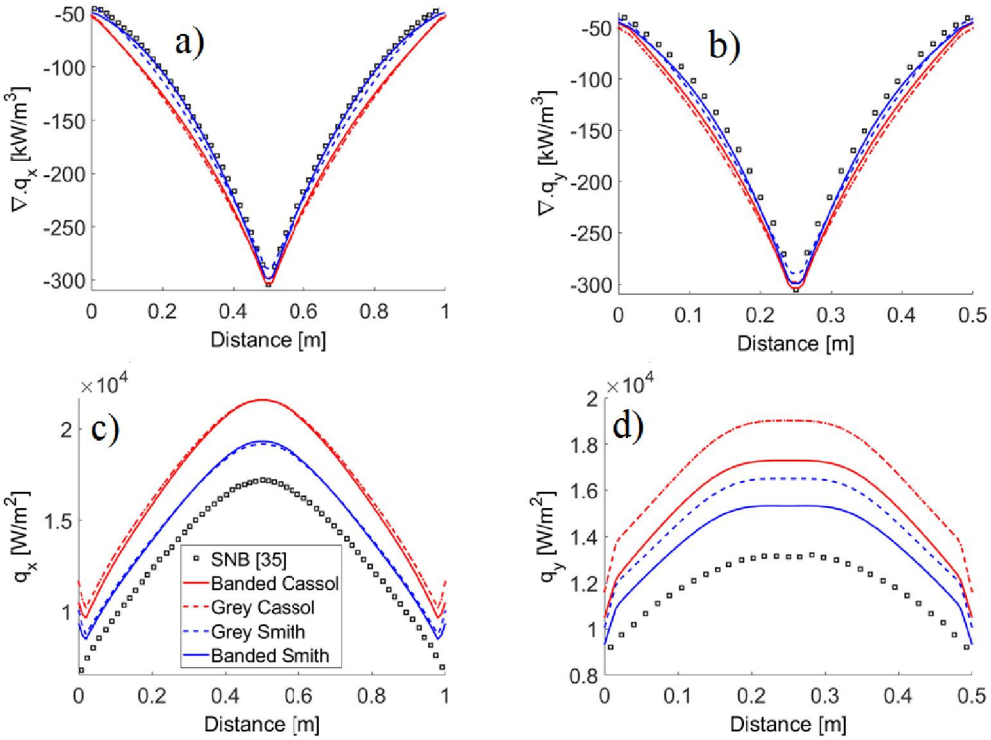

Fig. 4-1-15: FireFOAM-WSGG vs SNB of [35] in 2D inhomogeneous and non-isothermal H_2O case of [35], (a), (b) radiative source term along (x, y = 0.25) and (x = 0.5, y), (c), (d) incident flux along (x, y = 0.5) and (x = 1, y)

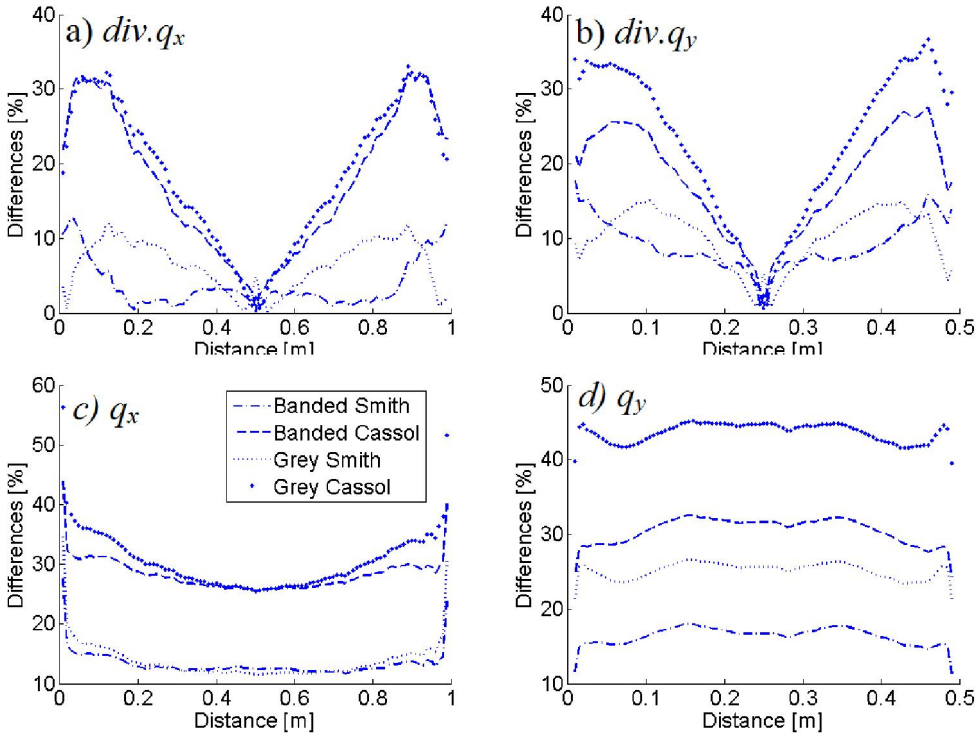

Fig. 4-1-16: Errors of FireFOAM-WSGG relative to SNB [35], on the radiant source term (a, b) and flux (c, d) from Fig. 4-1-15

4.1.4.3. Pure H_2O in 3D enclosure

This is the second test case in Coelho's paper [34] and parameters are similar to the first uniform case (mean beam length, isothermal temperature, angular discretisation, etc). The grid resolution along z increases from 16 to 25 cells, and the mole fraction of H_2O varies as per $z(1-z/4)$, which makes a "scooped" distribution (parabola in reverse) centred at z = 2m, so that $0 < p_w < 1$. Temperature, however, remains isothermal at 1000K (boundaries black and still at 300K). The source term along z is taken at (1m, 1m, z), respectively (x, 1m, 0.24m) along x, and the flux along z is taken at (2m, 1m, z), respectively (x, 1m, 4m) along x (Fig. 4-1-17). The corresponding relative errors with the benchmark solution are in Fig. 4-1-18. This scenario is in some way the opposite of that of section 4.1.3.2, where temperature varied but gas concentrations stayed uniform. With WSGG models, only the emission term is temperature dependent, whereas the optical thickness depends only on gas mole fractions (pressure-absorption coefficients in $(atm.m)^{-1}$), thus we can assume this explains why the grey treatment of the inhomogeneous but isothermal medium leads to completely off source terms along the direction of the concentration gradient (Fig. 4-1-17-a). In the other direction (Fig. 4-1-17-b), the optical path is homogeneous and isothermal, hence the grey WSGG models adopt the exact same "flat" behaviour as they did in the isothermal and homogeneous case of section 4.1.3.3. It should be stressed that an isothermal/inhomogeneous scenario is unlikely to occur in a fire, where temperature and mole fraction normally evolve together, in which case a grey WSGG can yield acceptable errors (see inhomogeneous, non-isothermal 2D case). The banded models, on another hand, manage to qualitatively reproduce the source term in the gradient direction, maintaining relative errors of 25-30%. Along x, deviations are mostly

below 10% - oddly enough this is 20 to 40% better than in the uniform variant of section 4.1.3.3. Flux differences are all well below 15%, which is consistent with previous tests.

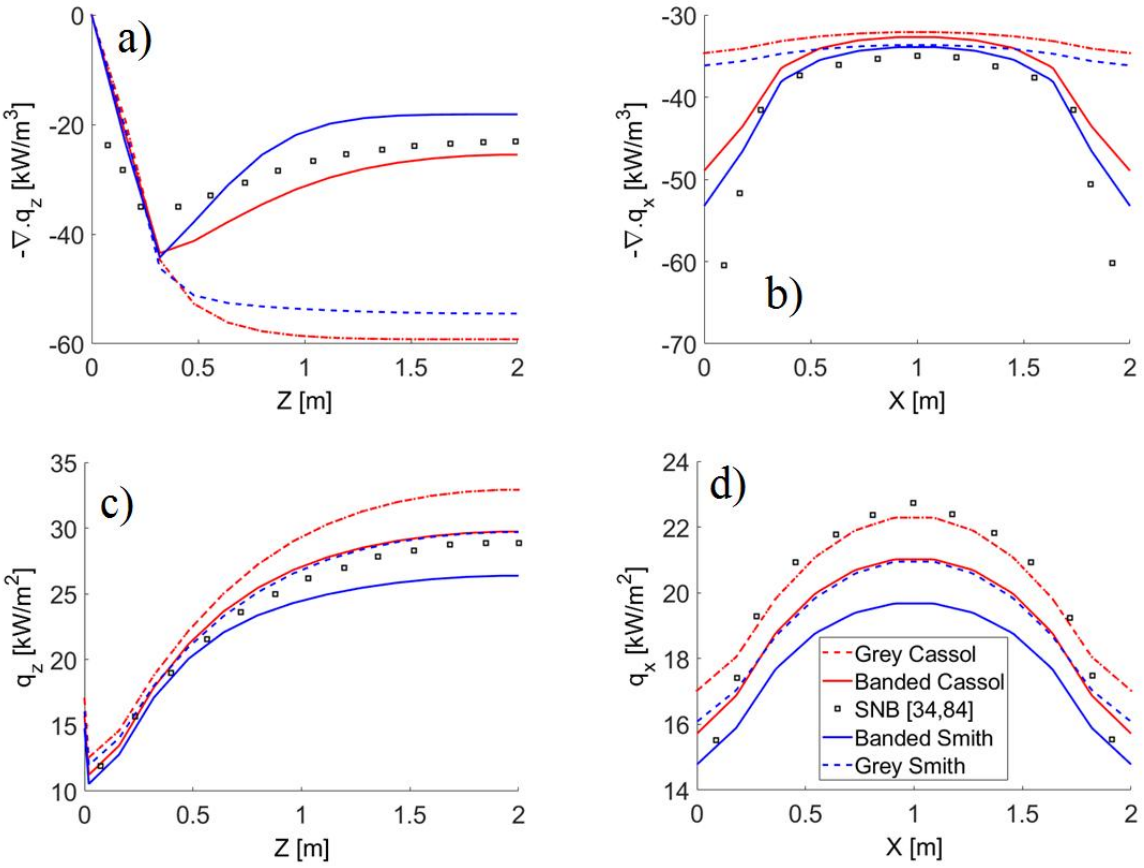

Fig. 4-1-17: (a), (b) Radiative source term along (x = 1m, y = 1m, z) and (x, y = 1, z = 0.24m) ; (c), (d) incident flux along (x = 2m, y = 1m, z) and (x, y = 1m, z = 4m) for the inhomogeneous 3D gas of [34], FireFOAM-WSGG vs SNB of [34,84]

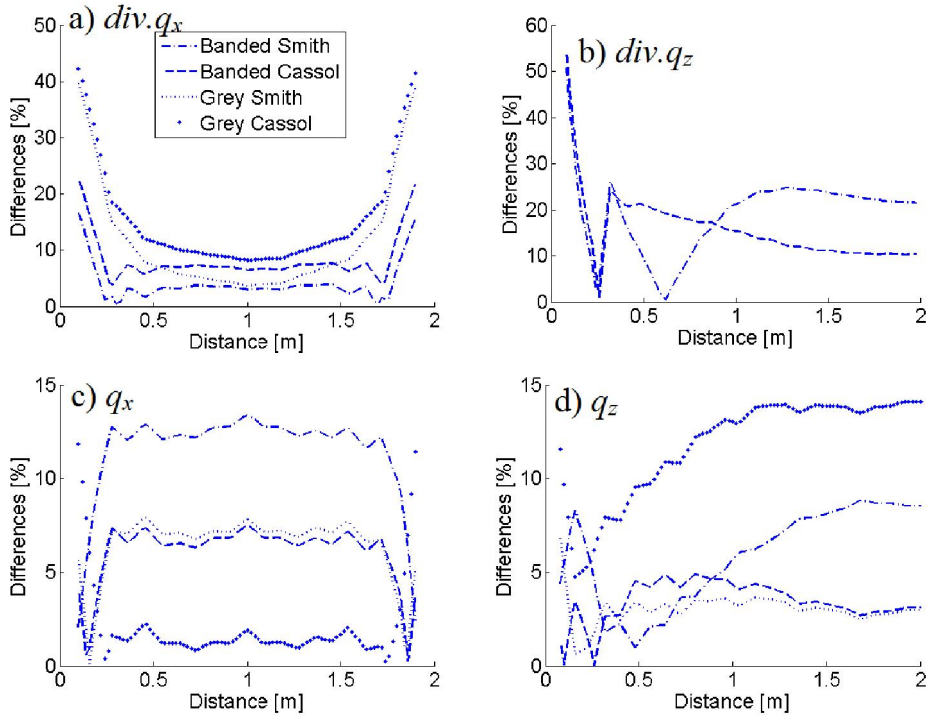

Fig. 4-1-18: Errors of FireFOAM-WSGG relative to SNB [34,84], on the radiant source term (a, b) and flux (c, d) from Fig. 4-1-17

4.1.5. Summary

Based on the results from this section, we can estimate that for fire applications the errors from WSGG modelling in inhomogeneous media should be around 20% for radiant source terms and 10% for radiant fluxes. Using a banded model would tend to decrease these errors by possibly 5%, but most likely never more than that. Overall we saw less error in inhomogeneous, non-isothermal media than in homogeneous and isothermal media with the banded WSGG models, especially in the line of sight solutions of the 1D case, which perhaps has to do with the uncorrelated RTE solution method and the independence from mean beam length. In the same conditions we saw that the grey models are not necessarily completely unreliable. As mentioned at the beginning of this section, the local computations of the grey absorption coefficient can sometimes partially compensate the inaccuracy of a mean beam length based on the entire inhomogeneous domain, provided that temperature and gas concentration vary together and without very sharp gradients. This explains why the performance of grey models is always the worst near the boundaries, when those are cold and immediately adjacent to a hot gas. In the case of a pool fire, we assume the effects of grey approximations would thus mostly be felt near the burner surface, potentially resulting in poor prediction of the radiant heat flux in that area. Radiant fluxes to distant boundaries, however, could be better captured since the decay of temperature and gas mole fraction is slow and smooth between the flame zone and the distant cold boundary. Otherwise, our estimation for the intrinsic finite volume method error would be about 3% based on the grey gas test, that is if there are no ray effects. That later issue is better left as a separate problem. The pre-

calibration performed in the transparent cylinder case provided at-first-sight guidelines which may be tailored to specific fire size, which will be considered in Chapter 5.

4.2. The exponential wide band-box model

4.2.1. Introduction

The box model based on the exponential wide band (EWB), or stepwise-grey EWB model, was retained as a solution to the problem of dual-phase radiation from gas and liquid droplets found in fire suppression simulations. The first two FireFOAM box model implementations, henceforth designated as "Modest" and "Beer" (Chapter 3), used on-the-fly calculations of the equivalent bandwidths. As it turned out that FM Global's implementation of the Mie theory model for liquid phase radiation was based on fixed band limits, that same approach was retained for a third version of the box model. However, removing bandwidth calculations left questions about the box model's sensitivity to path length or mean beam length (a key parameter in EWB calculations), as well as the approach's capability in a wide range of scenarios. This section will address these questions with as much detail as possible. Firstly, in section 4.2.2, the two variable band limit models will be assessed with the test case battery of section 4.1, where WSGG models were assessed in static, homogeneous or inhomogeneous media. In section 4.2.3, the dependence of box model bandwidth on path length is investigated to the fullest extent. In Section 4.2.4, a range of path lengths applicable to fires will be determined. In section 4.2.5 the strength of each band will be assessed. The findings from sections 4.2.3, 4.2.4 and 4.2.5 will be used in section 4.2.6 to reformulate the box model for fixed band limits, which will be going through the same static test cases in the next sub-sections (this discussion was kept separate from the variable band box models for clarity). Lastly, in section 4.2.7, we will propose and test a scaling technique specially developed for fire simulations and discuss the box model aspects of spectral modelling in methanol and heptane pool fires (the actual simulations will be discussed in Chapter 5 for clarity).

4.2.2. Variable band models in static media

4.2.2.1. Non-overlapping bands, single gas species, homogeneous media

The advantage of starting with a single absorbing gas specie is that gas absorption/emission bands are less likely to overlap, due to the spectrum being less populated. Homogeneous scenarios are considered first, then inhomogeneous to assess the relevance of the scaled temperatures and CO_2-H_2O mole fractions. Each time, box model absorption spectra from both models (Beer and Modest) are quantified. The main point of discussing these two models in details to understand how taking the absorption coefficient at the optically thin limit (Modest model) or the mean beam length (Beer model) on a few (but key) isolated bands can drastically change the total radiative properties (source term and flux) in a

wide range of scenarios. After the homogeneous and inhomogeneous non-overlapping scenarios are reviewed, a mixture case will be investigated to assess how much band overlaps between species are a source of error to total radiative property prediction. Once the Beer and Modest models are properly analysed in a wide range of scenarios (this section), then more widely evaluated in a full-on sensitivity analysis (next section), it will be possible to move on to a box model with fixed band limits.

4.2.2.1.1. 2D pure CO_2

A scenario studied by Goutiere et al [35] is considered here. A 2D rectangular enclosure (1m x 0.5m) contains a homogeneous CO_2 gas phase at a mole fraction of 10% and uniform temperature 1000K. The boundary field is cold (T_w = 0K) and black (ε_w = 1). The mesh is uniform with 61 x 31 cells as per specifications of Goutiere et al. [35]. The mean beam length calculated as $S = 3.6V/A$ yields 0.6m, hence the mass path length X = 35.93 g/m^2 (pressure path length pS = 0.067 atm.m). As shown in Fig. 4-2-1, the resulting bandwidths from Beer and Modest box models are quite similar, which means that with CO_2 the bandwidths do not vary much whether taken at the optically thin limit or the mean beam length. The bands are too distant from one another and too narrow to cause any overlaps. Only the absorption coefficients (box heights) vary significantly between the models, at the strong bands 667 and 2410 cm^{-1}. Table 4-2-1 quantifies the bandwidths and absorption coefficients.

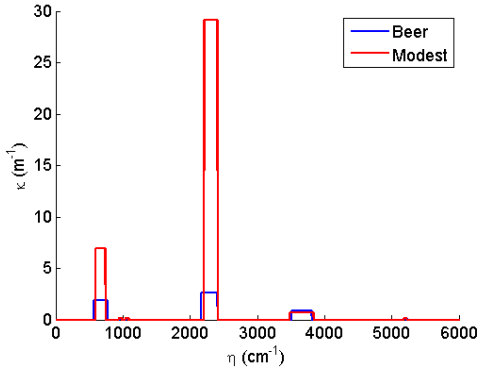

Fig. 4-2-1: Absorption spectrum of CO_2 at X = 35.93 g/m^2

Table 4-2-1: Absorption coefficients, bandwidths and emissivities of CO_2 at X = 35.93 g/m^2

	Beer			Modest		
Band (cm^{-1})	κ (m^{-1})	$\Delta\eta_e$ (cm^{-1})	ε	κ (m^{-1})	$\Delta\eta_e$ (cm^{-1})	ε
667	1.92	200.49	0.02	6.97	146.24	0.02
960	0.16	30.57	0.00	0.10	45.72	0.00
1060	0.16	30.94	0.00	0.10	46.91	0.00
2410	2.60	245.33	0.06	29.14	202.40	0.06
3660	0.91	299.47	0.02	0.72	357.14	0.02
5200	0.16	30.31	0.00	0.10	44.93	0.00
		Total ε	**0.10**		**Total ε**	**0.10**

Both Fig. 4-2-1 and Table 4-2-1 show that the 960 and 1060 cm^{-1} bands are quasi-windows, with very small emissivities/absorption. With the Modest model the 667 and 2410cm^{-1} bands are optically intermediate or thick (κS = 4.7 and 19.5 respectively) whereas with the Beer model these bands are merely in the intermediate regime (1.3 and 1.7). All other bands are treated similarly by both models. However subtle the differences may seem, they do make a very clear difference on the heat flux and flux divergence as seen in Fig. 4-2-2. The way the two box models differ in their renditions of the source term in both directions (Fig. 4-2-2-a, 4-2-2-b) are very reminiscent of the banded and grey WSGG models in the same scenarios. This is no coincidence, as the grey WSGG averages the absorption coefficient over a mean beam length like the Beer box model (although the latter does that in each band). With the banded WSGG formulation absorption coefficients are taken at the optically thin limit, which is analogous to the Modest box model. Such considerations are responsible for the poor performance of the Beer model near the walls, which are at the optically thin limit, whereas the Modest model does reproduce the source term adequately. In midfield regions (x = 0.5m, y = 0.25m), the Modest source term deviates by 33% from Goutiere's SNB solution [35]. The Beer source term is almost half the SNB value. Both models tend to overestimate the radiant heat flux. The midfield differences with SNB are 7% (Modest) and 10% (Beer) along x, 8% (both models) along y; a rather good performance in line with previous WSGG results

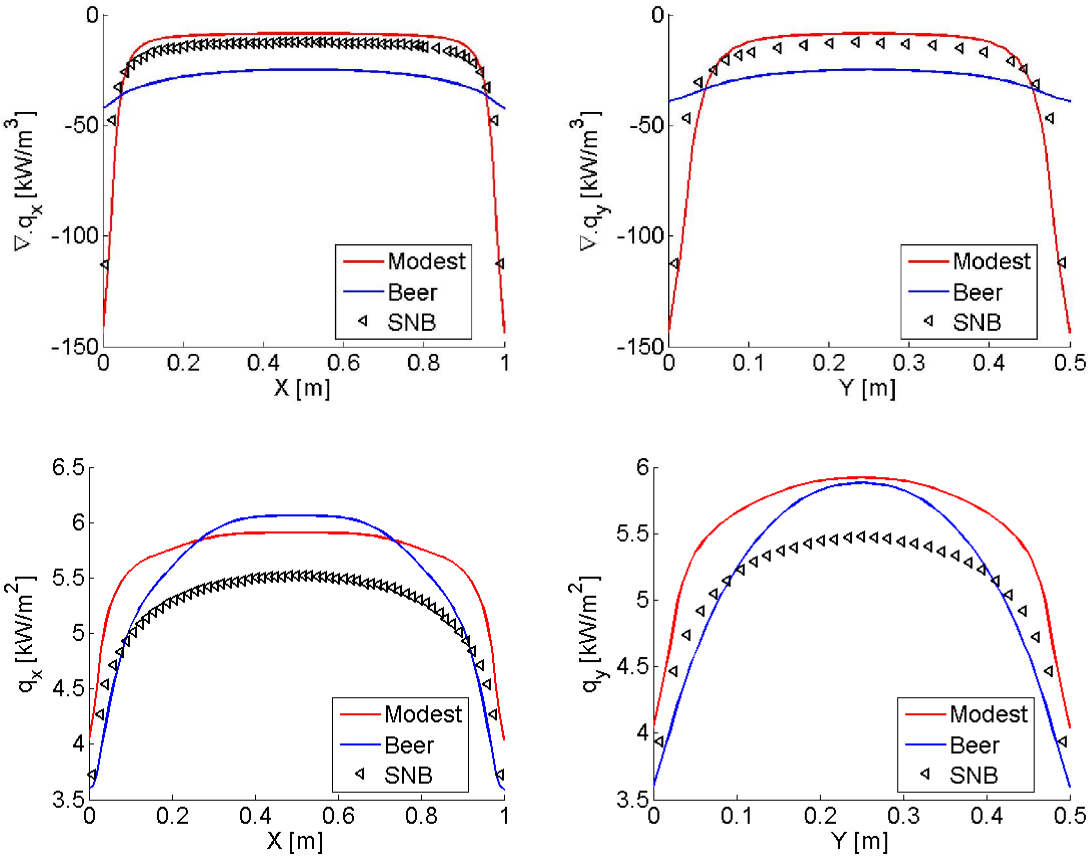

Fig. 4-2-2: Comparison of box models vs SNB of [35], source term along x and y (top), heat flux along x and y (bottom) for CO_2 at X = 35.93 g/m^2

4.2.2.1.2. 2D pure H_2O

The same enclosure filled with 20% of H_2O shows similar overall trends but highlights differences between box models in a more obvious way than with CO_2, as visible on Fig. 4-2-3. The mass path length is $X = 29.39$ g/m^2, pressure path length is $pS = 0.134$ atm.m.

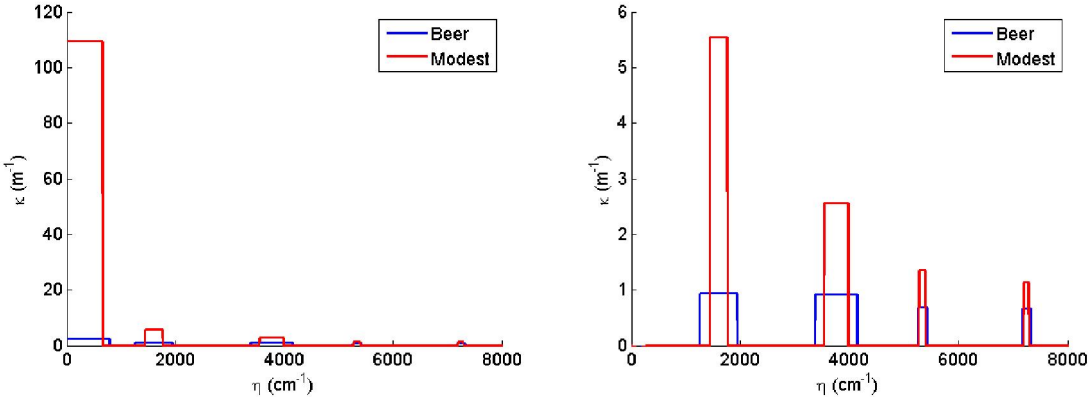

Fig. 4-2-3: Box model absorption spectra of H_2O at $X = 29.39$ g/m^2, with (left) and without (right) the pure rotational 140 cm^{-1}band

Table 4-2-2: Box model absorption coefficients, bandwidths and emissivities of H_2O at $X = 29.39$ g/m^2

	Beer			Modest		
Band (cm^{-1})	κ (m^{-1})	$\Delta\eta_e$ (cm^{-1})	ε	κ (m^{-1})	$\Delta\eta_e$ (cm^{-1})	ε
140	2.44	778.51	0.04	109.50	654.24	0.03
1600	0.93	688.88	0.09	5.54	326.11	0.10
3760	0.92	763.81	0.06	2.55	429.07	0.06
5350	0.69	175.91	0.00	1.35	108.77	0.00
7250	0.65	147.14	0.00	1.14	97.36	0.00
		Total ε	**0.19**		**Total ε**	**0.18**

The Modest model yields a large absorption coefficient of 109 m^{-1} at 140 cm^{-1} (pure rotational band, Fig. 4-2-3-a). This band, whose importance increases when temperature decreases (as shown by Modak [16]), has its head in the far-infrared, and hence if the band is not too wide the corresponding blackbody energy fraction will be small, which reduces its emissivity. In the present case the emissivity makes for about 18-19% of the total emissivity, which holds well with Modak's data, so it is clear that the 140cm^{-1} band should not be neglected, although the main emitter remains the 1600cm^{-1} band (Table 4-2-2). Fig. 4-2-4 below compares the source terms and flux from both box models, including and excluding the 140cm^{-1} band.

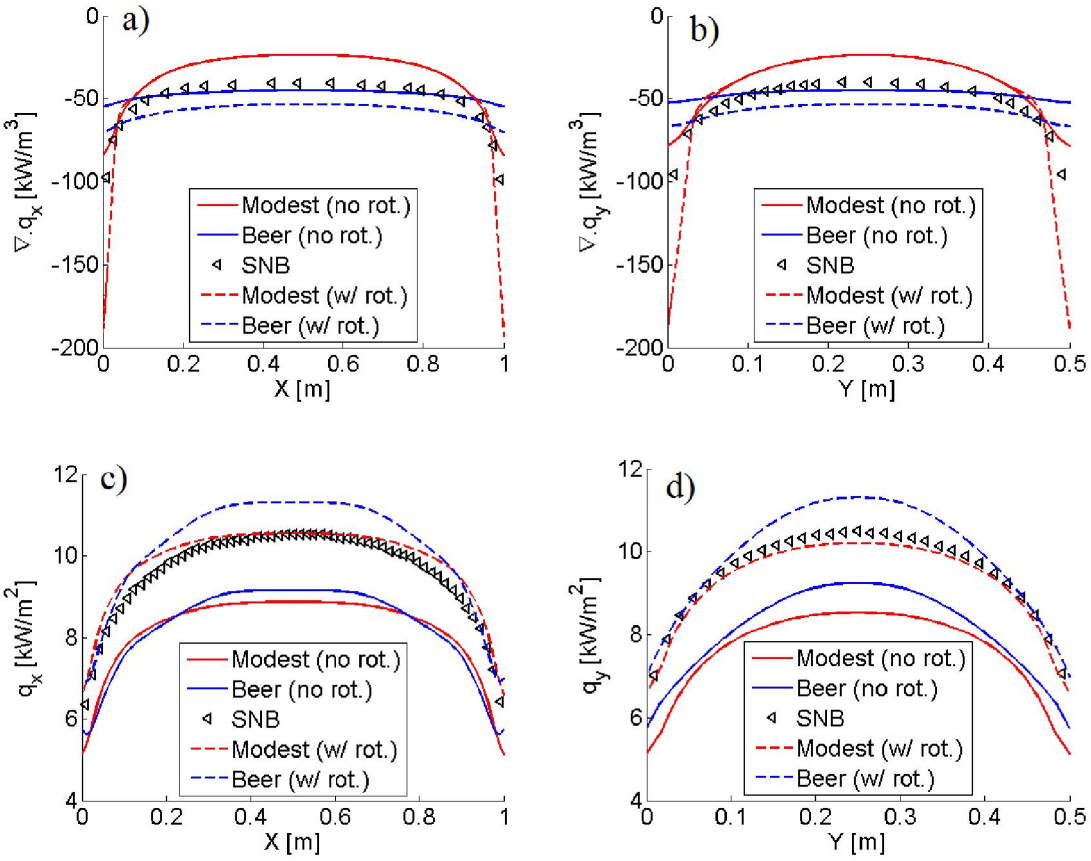

Fig. 4-2-4: Source term along *x* and *y* (top), heat flux along *x* and *y* (bottom) for pure H_2O with $X = 35.93$ g/m^2, with and without the 140 cm^{-1} band

Excluding the rotational band, the source term and heat flux show trends consistent with the CO_2 case. The same effects are visible at the boundaries, and at midfield the Modest source term is overpredicted and the Beer one is underpredicted with respect to the more accurate statistical narrow band (SNB) solution of [35] (Fig. 4-2-4-a, 4-2-4-b, solid lines). Unlike in CO_2 however, the error is larger with Modest (42%) and smaller with Beer (10%). Without the rotational band the heat fluxes are clearly under predicted by either model, which is not surprising considering that nearly 20% of the total emissivity is missing. With the inclusion of the 140cm^{-1} band, the Modest flux matches the SNB very closely (Fig. 4-2-4-c, 4-2-4-d, solid lines), while the Beer flux becomes slightly over estimated (by 7%). The effect on the source term is more subtle. The Modest profile is unaffected midfield, but is quite different around the boundaries, as it plummets towards the far negative range much quicker than without the 140cm^{-1} band (Fig. 4-2-4-a, 4-2-4-b, dashed red lines). The Beer source term, on the other hand, remains the same, although it is quantitatively smaller (Fig. 4-2-4-a, 4-2-4-b, dashed blue lines). It seems clear that in this scenario that the optically thick 140cm^{-1} band only affects the extremities of the optical path, hence why the incident radiation fluxes are so drastically affected.

4.2.2.1.3. 3D pure H_2O

This 2 x 2 x 4 metres enclosure, based on Coelho's first test case [34], contains gaseous H_2O at 1 atm and 1000K between cool black walls at 300K. The mesh is a uniform 11 x 11 x 16 grid, solved for 128 angular directions. The mean beam length is S = 3.6V/A = 1.44m, hence the mass path length X = 315.87 g/m^2 and the pressure path length pS = 1.44 atm.m. These path lengths are far higher than previously, which has vast effects on all results. Fig. 4-2-5 and Table 4-2-3 below show the absorption spectra. With the Beer model the 140cm^{-1} band is so broadened that it overlaps very shortly with the 1600cm^{-1} band. All Beer bands are optically intermediate (kS ~1 or 2), unlike previous examples where the dominant behaviour was optically thin. With the Modest model, all bands (weak and strong) are either thick or at least intermediate, which means that for the most part they are saturated (i.e. optically opaque with $\kappa S >> 1$, consequently the line-of-sight intensity is strongly asymptotic, hence it is mostly constant along the optical path). The 140cm^{-1} band's contribution to total emissivity is slightly less than in earlier scenarios (16%) despite the enormous absorption coefficient (342 m^{-1}), which is not surprising since the transmissivity $exp(-\kappa S)$ is converging towards zero.

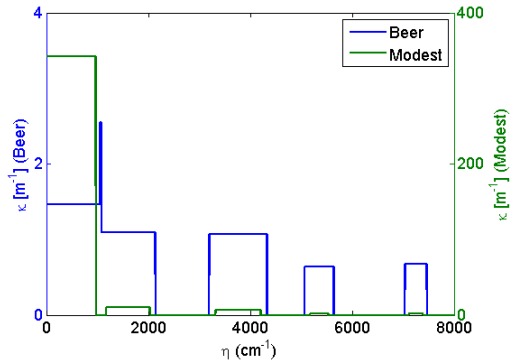

Fig. 4-2-5: Box model absorption spectra of H_2O at X = 316 g/m^2

Table 4-2-3: Absorption coefficients, bandwidths and emissivities of H_2O at X = 316 g/m^2

	Beer			Modest		
Band (cm^{-1})	**κ (m^{-1})**	**$\Delta\eta_e$ (cm^{-1})**	**ε**	**κ (m^{-1})**	**$\Delta\eta_e$ (cm^{-1})**	**ε**
140	1.46	1078.04	0.09	341.63	964.12	0.08
1600	1.09	1080.08	0.25	10.57	854.70	0.25
3760	1.07	1125.30	0.14	6.19	883.79	0.14
5350	0.63	567.35	0.02	2.05	358.38	0.02
7250	0.67	429.87	0.00	1.95	283.93	0.00
		Total ε	**0.50**		**Total ε**	**0.49**

As usual the source term is extracted horizontally and vertically along x and z, however the line along x is not central but close to a wall, i.e. x, y = 1, z = 0.375m. The z line is axisymmetric, i.e. x = 1, y = 1, z. It can be seen in Fig. 4-2-6 that the Modest approach is showing its limits at such a high mass path length of H_2O. Because the absorption coefficient is taken at the optically thin limit, all bands saturate too quickly (Table 4-2-3 above), which is fine if the bandwidths are not so sensitive to pressure-induced broadening (as in e.g. CO_2) but inappropriate here. This results in a next to null source term along the x and z lines from the

Modest model. Since source term = emission term - absorption term, where the emission term is proportional to blackbody fraction multiplied by the absorption coefficient, with such high absorption coefficients the emission term is so large it almost cancels out the absorption term. Should one experiment with enlarged Modest bandwidths, the subsequent reduction in absorption coefficients would still not be enough to decrease the emission term massively. Hence the better approach here is the Beer model and its smaller absorption coefficients that prevent the opacity of all bands. This is however only working at the mean beam length, as near the boundaries the Beer absorption coefficients are too small again, whereas the Modest source term neatly matches the SNB data in both directions (Fig. 4-2-6-a, 4-2-6-b). As for the fluxes (Fig.4-2-6-c, 4-2-6-d), the "square" profiles of the Modest model are another illustration of the same issue: a good match is achieved near the boundaries, then the profile suddenly becomes flat around the middle, which is the result of every band intensity getting infinitely thick at some one third of their optical paths (this will be discussed in more detail in the 1D mixture case further down, as line of sight analysis is difficult in a 3D geometry with many angular directions). The Beer model is again better at matching the SNB flux shapes along both directions, with midfield relative errors of 4% (along x) and 2% (along z). However, with very high differences in the source term (67% along *x*, 58% along *z*) the agreement can be only described as qualitative. It is not believed that the very short wavenumber interval where the 140 and 1600cm^{-1} bands overlap (Fig. 4-2-5, solid blue line) could cause such errors, this is rather an intrinsic model limitation. One may observe that the Beer model's performance in this test case is very similar to some of the WSGG implementations from either Coelho or the present author.

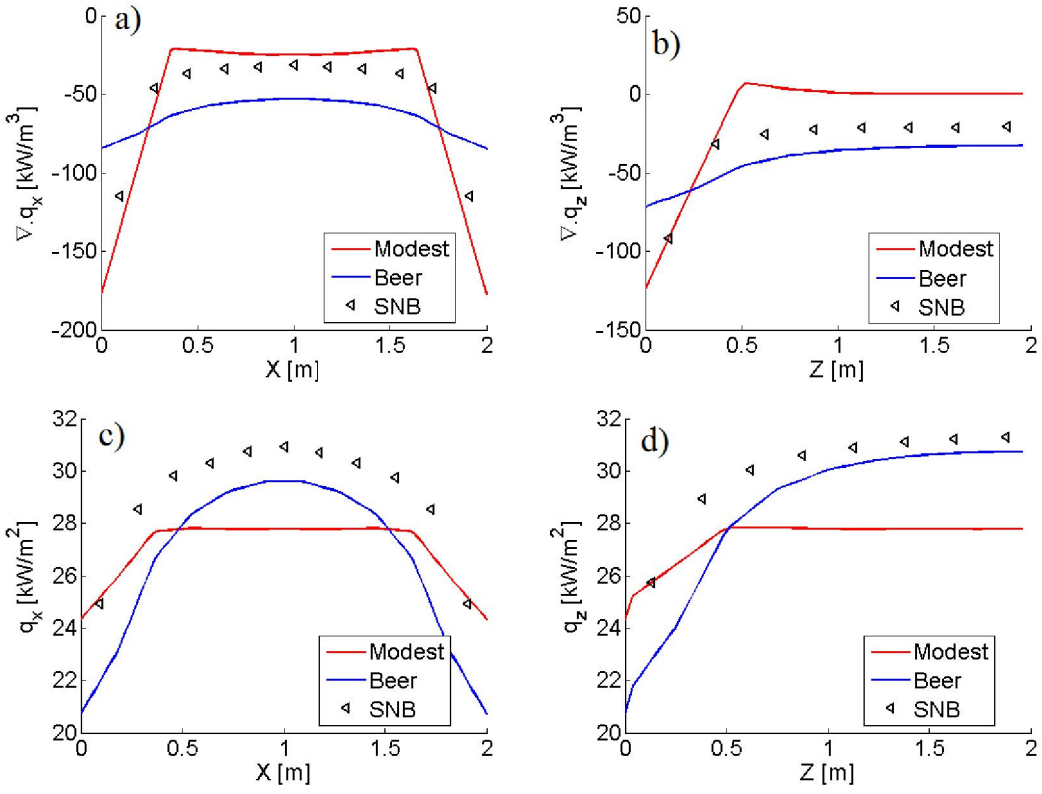

Fig. 4-2-6: Comparison of box models vs SNB of [34,84], source term along *x* and *z* (top), heat flux along *x* and *z* (bottom) for pure H_2O with $X = 316$ g/m^2

4.2.2.2. Non-overlapping bands, single gas specie, inhomogeneous media

Throughout the rest of this section and onwards, all box models are required to use a scaled temperature and partial pressure or mole fraction to satisfy the equation of absorptance in a homogeneous medium. Arithmetic averaging is used to that effect, since it is the numerical equivalent of analytically integrating the optical thickness κS over an inhomogeneous path length. The whole computational domain has to be considered for the averaging (if the participating medium fills the geometry), since it is not possible to replicate the analytical integration along a line of sight, other than in a 1D setup. Three scenarios are investigated here, still without gas mixtures to ensure no band overlaps occur. The inhomogeneous CO_2 or H_2O scenarios Goutiere et al. [35], previously used for the WSGG tests in 4.1.42, are thus revisited here with the box model. Centreline evolutions of temperature and CO_2 and H_2O mole fractions are as in Fig. 4-2-7-a, and the corresponding mass path lengths are visible in Fig. 4-2-7-b. The averaged mass path lengths of CO_2 and H_2O are 10.1 and 9.3 g/m^2, respectively corresponding to the pressure path lengths 0.025 atm.m and 0.056 atm.m. These are smaller values than in the homogeneous variants: the mass path lengths are less than halved and the pressure path lengths are nearly one order of magnitude smaller than the homogeneous cases. The scaled temperature is higher, however, at 1295K instead of 1000K previously. The mass path lengths gradients are relatively smooth, with the averaged values roughly centred between the minima and maxima.

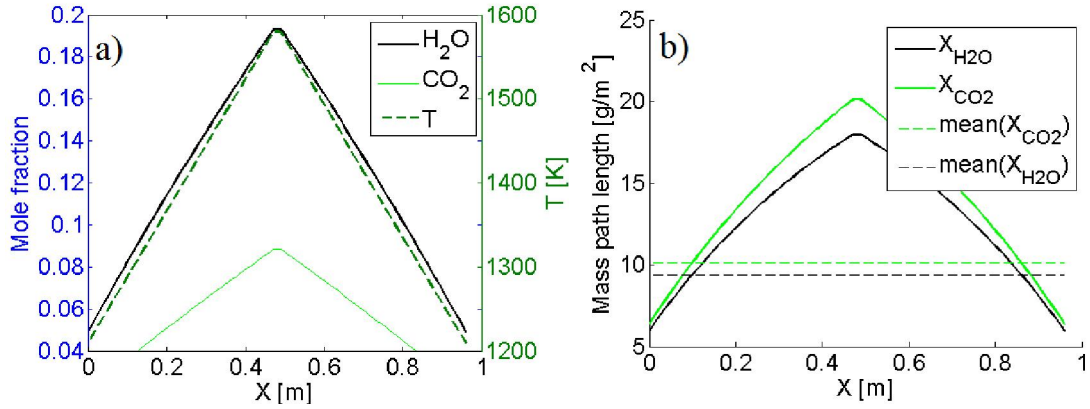

Fig. 4-2-7: For the inhomogeneous CO_2 and H_2O cases from Goutiere et al. [35], (a) centreline distribution of temperature and mole fractions and (b) centreline mass path lengths (b) with scaled values

For Coelho's second test case [34], the box's dimensions are unchanged (2m x 2m x 4m) but the mesh is now a 11 x 11 x 25 grid (11 x 11 x 16 previously). The angular resolution (128 directions) is unchanged (see WSGG section 4.1.4.3). The mole fraction or partial pressure of H_2O follows a vertical distribution across the centreline of z axis shown in Fig. 4-2-8. Since the temperature is still uniform at 1000K, the resulting mass path length rises and falls sharply to a still-high maximum (> 300 g/m^2), indeed a very different scenario from the Goutiere case above. The scaled partial pressure and mass path length are closer to peak values as well.

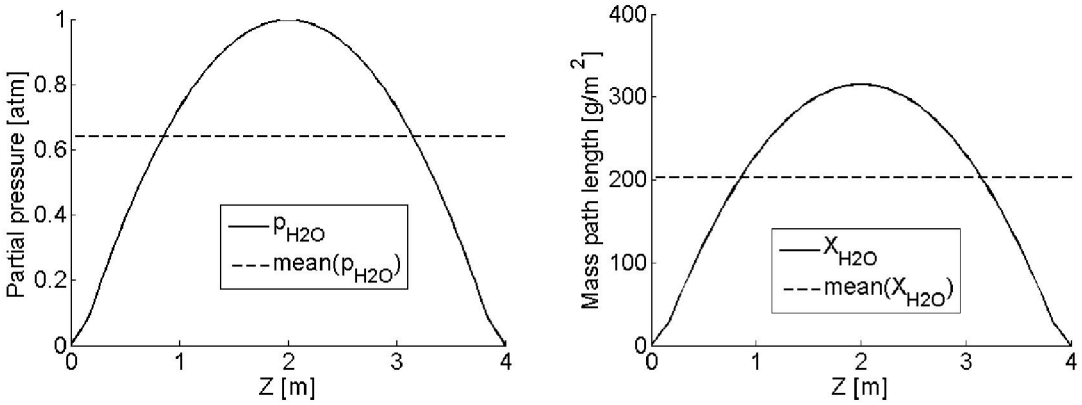

Fig. 4-2-8: Inhomogeneous test case from Coelho [34]: distribution of partial pressure of H_2O (a) and the corresponding mass path length (b) along the centreline

4.2.2.2.1. 2D pure CO_2

The spectrum of the inhomogeneous 2D CO_2 case of Fig. 4-2-9 is for scaled temperature 1295K and scaled mole fraction 0.037 (the mean beam length remains S = 0.67m as with the homogeneous variant). The mass path length being less than a third that of the homogeneous case, and the bandwidths appear narrower.

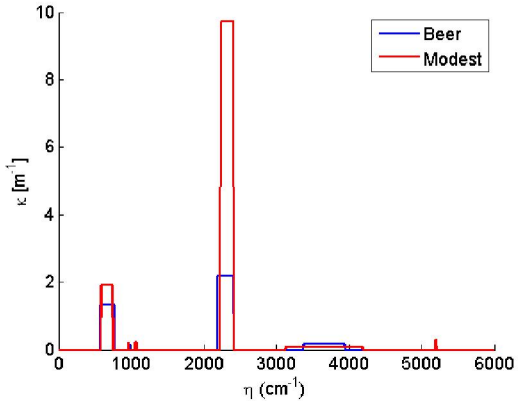

Fig. 4-2-9: Box model absorption spectra of CO_2 at X = 10.1 g/m^2

The total emissivities (0.06) are 40% smaller than in the homogeneous case. The absorption coefficients of 0.16 m^{-1} in weaker bands are due to transmissivities being not allowed to be higher than 0.9, as per recommendations of Lallemant and Weber [47].

Table 4-2-4:Absorption coefficients, bandwidths and emissivities of CO_2 at $X = 10.1$ g/m^2

	Beer			Modest		
Band (cm^{-1})	κ (m^{-1})	$\Delta\eta_e$ (cm^{-1})	E	κ (m^{-1})	$\Delta\eta_e$ (cm^{-1})	E
667	1.33	189.07	0.01	1.90	154.97	0.01
960	0.16	13.36	0.00	0.23	8.51	0.00
1060	0.16	13.54	0.00	0.23	8.73	0.00
2410	2.19	227.48	0.04	9.73	175.33	0.04
3660	0.16	566.21	0.01	0.08	1056.71	0.01
5200	0.16	11.06	0.00	0.28	5.80	0.00
		Total ε	**0.06**		**Total ε**	**0.06**

The scaling of inhomogeneities appears sensible for both box models. For the source term at midfield, where gradients are the sharpest, the Modest model performs well in both directions with a relative difference with SNB of 16% (Fig. 4-2-10-a, 4-2-10-b).This is better than in the homogeneous case, probably because of the smaller mass path length and smaller absorption coefficients resulting in an optically thinner medium across all bands, a scenario the Modest model seems to be handling well. However it underestimates the heat flux by 15% along x and 7% along y, whereas the Beer model renders a nearly exact match in both directions (Fig. 4-2-10-c, 4-2-10-d). These differences are not dissimilar to the homogeneous and isothermal variant, and are due to the mass path length averaging. An alternative method would without doubt yield visibly different results, as it did during trial runs where minimum and maximum values were tested as well as the average.

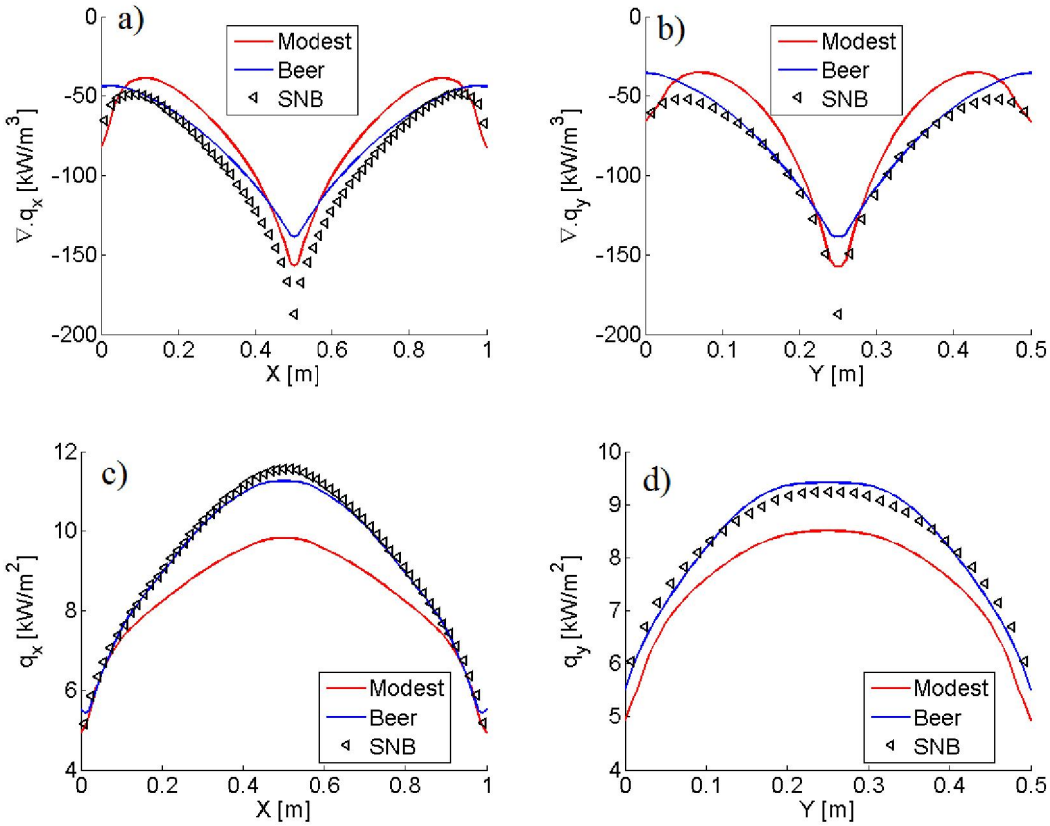

Fig. 4-2-10: Comparison of box models vs SNB of [35], source term along *x* and *y* (top), heat flux along *x* and *y* (bottom) for pure inhomogeneous CO_2 with X_{ave} = 10.1 g/m^2

4.2.2.2.2. 2D pure H_2O

For the inhomogeneous, non-isothermal H_2O variant, the average temperature is still 1295K and the average mole fraction is 0.084. The spectrum is as per Fig. 4-2-11 and Table 4-2-5. Comparing this spectrum with the one from the homogeneous case yields contrasted behaviours. The Modest model, with the smaller mass path length of the inhomogeneous case, yields smaller absorption coefficients and slightly broader bandwidths in the important bands (1600, 3760cm^{-1}). For weaker bands (5350, 7250cm^{-1}) the same behaviour is observed with a greater sensitivity. The Beer model is the other way around: the strong bands have narrower bandwidths in the inhomogeneous case, but the weaker bands get wider (absorption coefficients are all smaller to various extents).

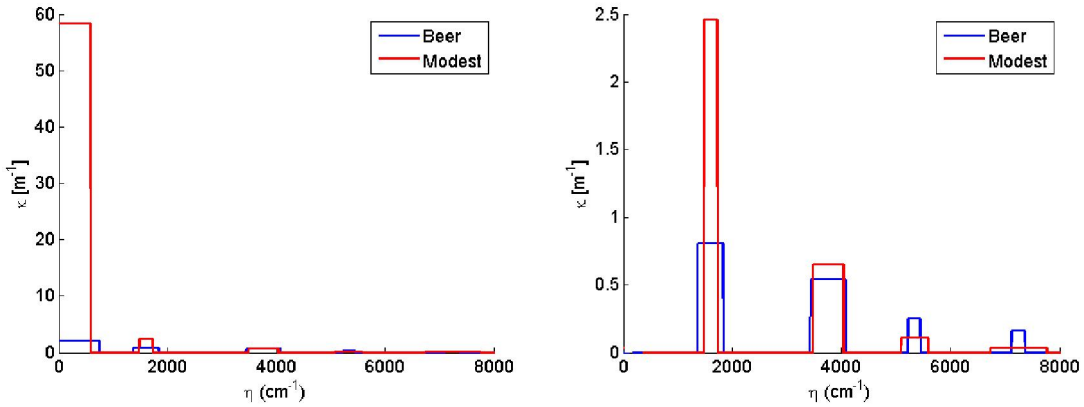

Fig. 4-2-11: Absorption spectrum of H_2O with X = 9.3 g/m^2, with (left) and without(right) the pure rotational 140 cm^{-1}band

Table 4-2-5: Absorption coefficients, bandwidths and emissivities of H_2O at X = 9.3 g/m^2

	Beer			Modest		
Band (cm^{-1})	**κ (m^{-1})**	**$\Delta\eta_e$ (cm^{-1})**	**E**	**κ (m^{-1})**	**$\Delta\eta_e$ (cm^{-1})**	**ε**
140	2.03	737.59	0.02	58.25	584.45	0.01
1600	0.80	463.82	0.04	2.46	239.15	0.04
3760	0.54	641.46	0.04	0.65	551.24	0.04
5350	0.25	223.38	0.00	0.11	490.22	0.00
7250	0.16	245.70	0.00	0.04	1024.66	0.00
		Total ε	**0.09**		**Total ε**	**0.09**

Larger errors are seen with H_2O than with CO_2, reflecting the increased sensitivity to mass path length, hence the scaling of it. Without the pure rotational 140cm^{-1} band, both models yield an underpredicted source term in both directions (Fig. 4-2-12-a, 4-2-12-b) and the heat flux is also systematically underestimated, which confirms the trend of the homogeneous case. With the rotational band included, the underprediction is compensated (Fig. 4-2-12-c, 4-2-12-d) and fluxes return to normal values, although the Beer model overestimates the flux

along *y*. Source terms are somewhat improved in the middle but a strange boundary effect appears in the Modest model's profiles, with a sharp plummeting by the walls. Since the 140cm^{-1} band seems to affect boundary surroundings, it may suggest that its absorption is too strong, or the bandwidth may be too narrow. The sensitivity analysis in the next section will highlight this band's different behaviours from the other rotational-vibrational bands. Indeed, bandwidths can get very wide, which results in a negative wavenumber lower limit, which is of course not physical. The negative range is hence truncated, but then the blackbody energy fraction may be subsequently wrong. Elsewhere, midfield relative differences with SNB are in the usual range, i.e. 33% for the source term and between 4 and 15% for fluxes depending on models.

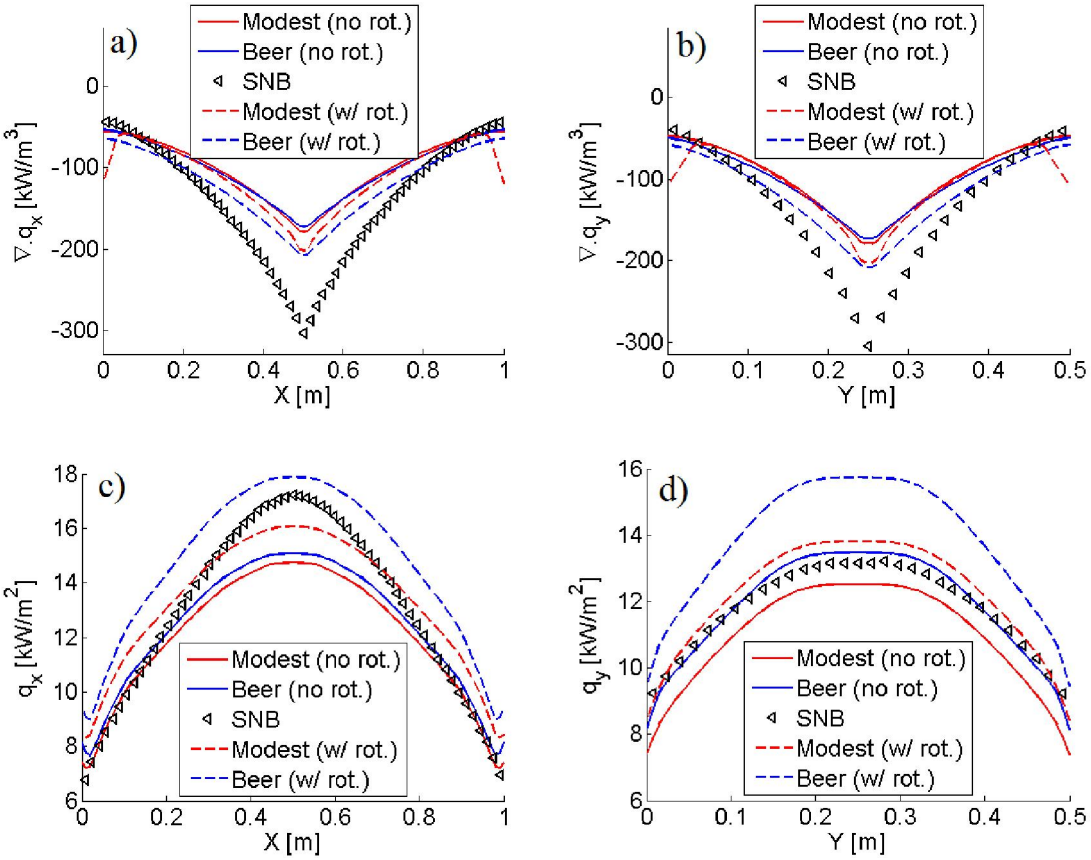

Fig. 4-2-12: Comparison of box models vs SNB of [35], source term along *x* and *y* (top), heat flux along *x* and *y* (bottom) for pure inhomogeneous H_2O with X_{ave} = 9.3 g/m^2

4.2.2.2.3. 3D pure H_2O

The spectrum of the pure H_2O phase is as Fig. 4-2-13 and Table 4-2-6. The scaled mass path length, at 202 g/m^2, does not cause any overlaps from band broadening as was the case with the homogeneous case at 316 g/m^2. Otherwise the same comments can apply here: all bands from the Modest model are too opaque, with narrower bandwidths than with the Beer model.

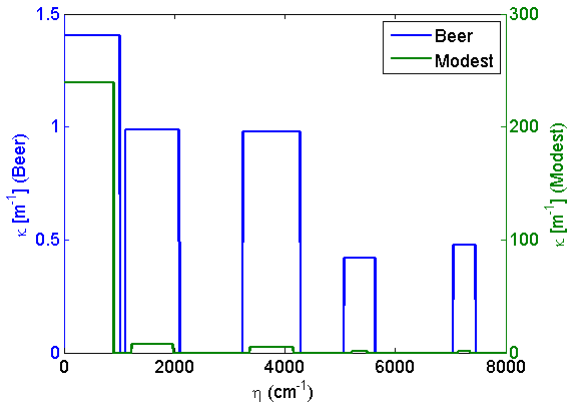

Fig. 4-2-13: Box model absorption spectra of H_2O at $X = 202$ g/m^2

Table 4-2-6: Absorption coefficients, bandwidths and emissivities of H_2O at $X = 202$ g/m^2

	Beer			Modest		
Band (cm^{-1})	**κ (m^{-1})**	**$\Delta\eta_e$ (cm^{-1})**	**E**	**κ (m^{-1})**	**$\Delta\eta_e$ (cm^{-1})**	**ε**
140	1.40	1009.91	0.08	238.81	894.52	0.07
1600	0.99	972.85	0.21	7.84	737.62	0.22
3760	0.98	1027.67	0.12	4.50	777.68	0.12
5350	0.42	549.90	0.01	1.73	271.91	0.01
7250	0.48	404.78	0.00	1.58	224.21	0.00
		Total ε	**0.43**		**Total ε**	**0.42**

Source terms and fluxes (Fig. 4-2-14) are taken at the same location as in the homogeneous case, except the source term along x is taken a little closer to the wall, i.e. along x, $y = 1$, $z = 0.24$m. The description of model performance is again very much the same as in the homogeneous case, hence there is no point discussing the Modest model here again. For the Beer model, the major difference with the homogeneous case comes from the scaled parameters which are not working particularly well and causing more relative errors from the SNB solution. Bearing in mind that the inhomogeneity is distributed only along the z axis, the Beer model behaves exactly like in the homogeneous case, but predictions are either too high or too low because of using an averaged mole fraction that is far from both the minimal and maximal values. Indeed the mole fraction varies between 0 and 1 (i.e. the gas goes from infinitely diluted to fully saturating across a distance of 2 metres), whereas in the 2D case above the variation is much more moderate. Hence the flux along z (Fig. 4-2-14-d) is partly overpredicted and partly underpredicted, whereas in the x direction (along which the path length is homogeneous, Fig. 4-2-14-c) the flux is entirely overpredicted. But with relative errors to SNB of 7% and 13% in the midfield, the match remains very reasonable considered the extreme mole fraction or partial pressure variation. For the source term, the Beer model profiles happen to reduce the relative errors from the homogeneous case, with midfield values of 50% and 33% along x and z respectively (Fig. 4-2-14-a, 4-2-14-b). But in any case the effect of the inhomogeneity along z is not reproduced near the boundary around $z = 0.1$m (Fig. 4-2-14-b).

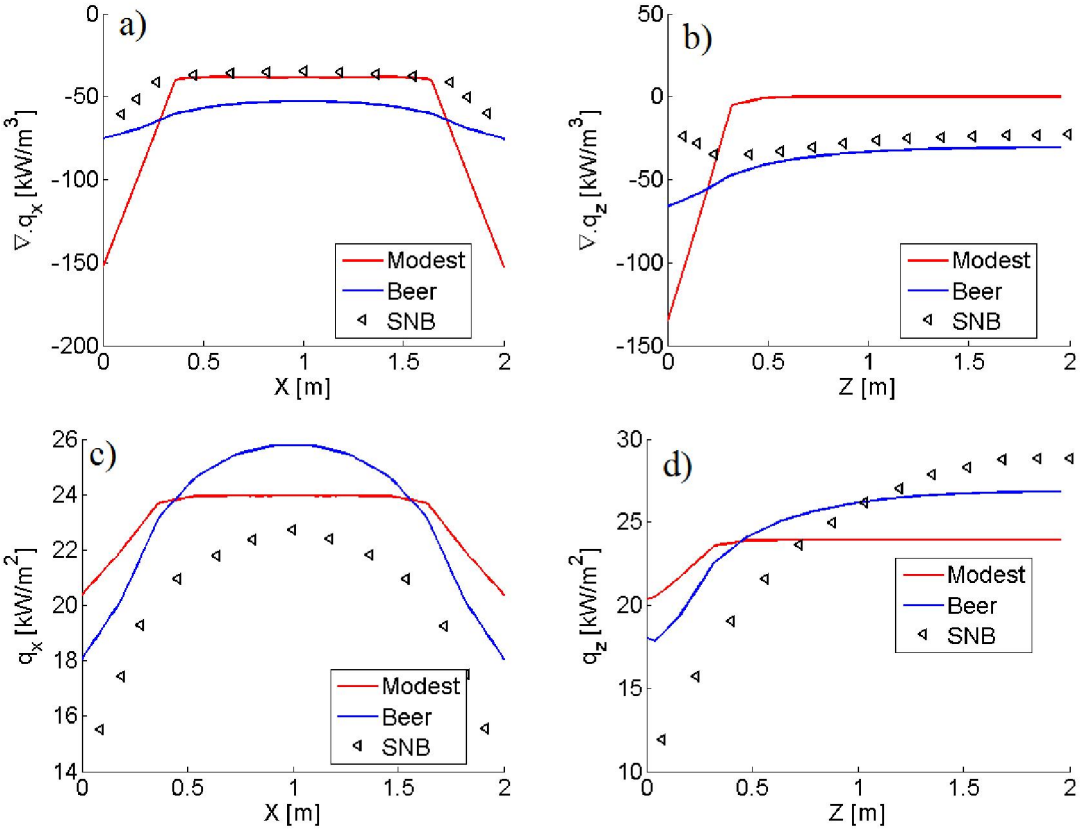

Fig. 4-2-14: source term along *x* and *z* (top), heat flux along *x* and *z* (bottom) for pure H_2O with X_{ave} = 202 g/m^2

4.2.2.3. Overlapping bands, mixtures of two absorbing gas species

It was seen previously that only at mass path lengths above 300 g/m^2 can box model bandwidths get broad enough to cause overlaps within one same species (actually, only in H_2O since CO_2 is not as sensitive). This subsection thus investigates mixtures of CO_2 and H_2O at smaller mass path lengths more typical of fire conditions. The scenario is from Bressloff's paper [36], where a homogeneous hot gas mixture at atmospheric total pressure is confined between two infinite and parallel walls 1 metre apart. The mean beam length is S = 1 x 1.76 = 1.76m. In this test case the interest is in line of sight solutions of the RTE, i.e. the directional total radiative intensity, for which exact solutions are available. To that effect Bressloff employed a differential banded transmissivity-statistical narrow band (DBT-SNB) solution, reproduced here for benchmarking. Unlike the uncorrelated finite volume method of FireFOAM, in the DBT-SNB emission and absorption are correlated by the transmissivity differences along an optical path. Also the transmissivities are calculated for narrow spectral intervals with a parameter scaling approach to account for inhomogeneities [36]. Since this subsection evidences the errors introduced by band overlaps as yielded by the Modest and Beer models, there is no point in investigating inhomogeneous mixtures since the errors can

only increase from there. These scenarios will be analysed with the fixed bands box model, the goal of which is to remove the overlaps (see section 4.2.6).

4.2.2.3.1. 1D homogeneous gas mixture

The mixture is at 1000K, with CO_2 and H_2O mole fractions of respectively 8% and 16% throughout, hence the respective mass path lengths X_{CO2} = 65.6 g/m^2 and X_{H2O} = 80.1 g/m^2 and the pressure path lengths pS_{CO2}= 0.141 atm.m and pS_{H2O} = 0.282 atm.m. The resulting absorption spectrum is as per Fig. 4-2-15 and Table 4-2-7 below.

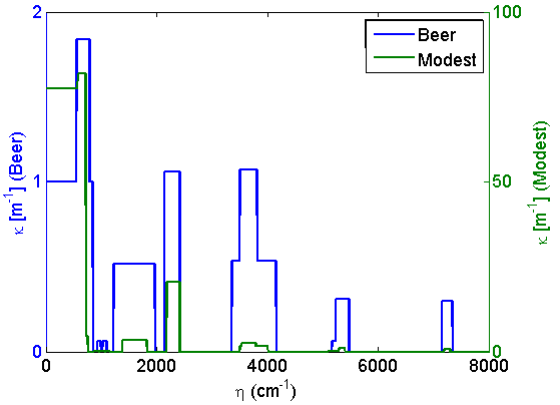

Fig. 4-2-15: Box model absorption spectra of CO_2-H_2O mixture with X_{CO2} = 65.6 g/m^2 and X_{H2O} = 80.1 g/m^2

Table 4-2-7: Absorption coefficients, bandwidths and emissivities of CO_2-H_2O mixture with X_{CO2} = 65.6 g/m^2 and X_{H2O} = 80.1 g/m^2, before overlap correction

	Beer			Modest		
Band (cm^{-1})	κ (m^{-1})	Δηe (cm^{-1})	ε (%)	κ (m^{-1})	Δηe (cm^{-1})	ε (%)
140	1.00	1406.93	12	77.32	1165.23	10
667	0.84	226.83	6	4.67	174.68	6
960	0.06	64.25	0	0.02	204.32	0
1060	0.06	65.01	0	0.02	209.19	0
1600	0.51	740.23	34	3.27	441.87	35
2410	1.06	270.61	18	20.63	228.70	18
3660	0.54	313.27	8	0.82	251.52	9
3760	0.53	795.98	20	1.72	508.33	20
5200	0.06	63.69	0	0.02	200.72	0
5350	0.31	236.17	1	0.97	120.69	1
7250	0.30	195.11	0	0.87	102.40	0
		Total ε	**0.39**		**Total ε**	**0.38**

Table 4-2-7 shows that with the Modest model there are only two optically thick bands, i.e. the 140cm^{-1} (κS = 136) of H_2O and the 2410cm^{-1} of CO_2 (κS = 36). Some other bands are intermediately thick, e.g. the 667cm^{-1} of CO_2 (κS = 8.2) and the 1600cm^{-1} of H_2O (κS = 5.7),

but everything else is optically thin. With the Beer model, the 140cm^{-1} and the 2410cm^{-1} barely qualify as optically intermediate. Fig. 4-2-16 compares the directional intensities of each bands for each model. The optically thin behaviour of the Beer model is obvious with all the intensity lines being almost like linear functions of path length. With the Modest model, the two thick bands display a quick curvature early along the path, followed by the asymptotic behaviour induced by the saturation of the transmissivity term *exp(-κS)* (Fig. 4-2-16 left, blue and red solid lines). With the Beer model these same bands show very little curvature (Fig. 4-2-16 right, same lines). One may note that the thickest bands are not necessarily the strongest, i.e. the 1600cm^{-1} band clearly dominates the spectrum in both models while belonging in the intermediate regime of thickness. The 3660 and 3760cm^{-1} bands are just about intermediately thick as well but they are far from negligible (Fig. 4-2-16, dashed lines). The band that might really make a difference between the Modest and Beer models is the 2410cm^{-1} of CO_2 which is the second strongest band in both models but has very different shapes (Fig. 4-2-16, solid magenta lines). This is because the Planck function of blackbody intensity hits a peak in the intermediate wavenumber range, preceded and followed by sharp gradients, hence the relatively large blackbody fractions make for large emissivities. Another useful information to retain from Fig. 4-2-16 is that optically thick bands, because they thicken so quickly, are going to strongly affect the beginning of the path, whereas the thin bands do not get as strong until they reach the end of the path. Also, should another beam come from the opposite direction, then the resulting total intensity (hence the incident radiation *G*) adopts a bell-like shape, that is more squared if the optically thick bands are stronger, and more curvy if the thin bands dominate. Hence, if the decay near the boundaries is not very pronounced, it is because the absorption coefficients are weak, hence an optically thin-type of behaviour. This explains much of the different source term and flux profiles observed in the previous subsections: the Beer model has smaller absorption coefficients than the Modest model in any band, hence why the source term's near-boundary decay is never captured.

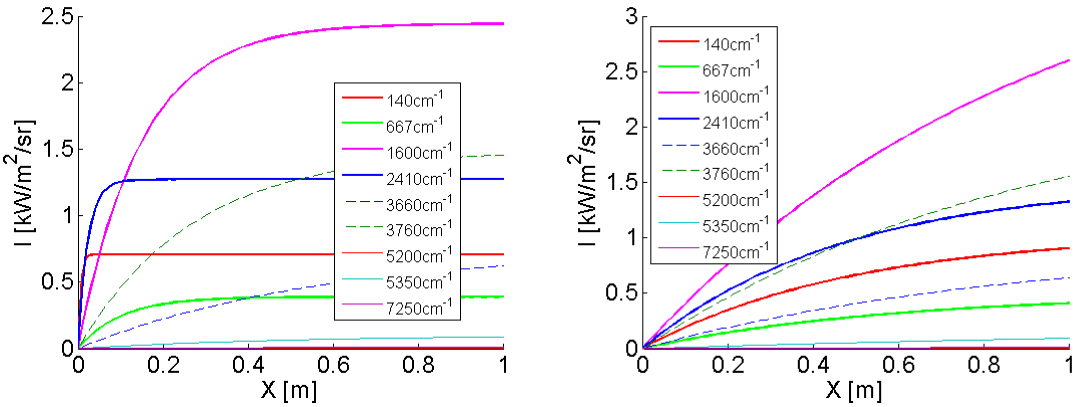

Fig. 4-2-16: Line of sight intensity of each band from Modest (left) and Beer (right) models, for CO_2-H_2O mixture with X_{CO2} = 65.6 g/m^2 and X_{H2O} = 80.1 g/m^2

It is shown that the Modest model treats the 2410cm^{-1} band as thick, whereas in the Beer model it is intermediate. Since the total directional intensity is the addition of all these bands intensities the end result is evident in Fig. 4-2-17. One clearly recognises the shape of the dominant 1600cm^{-1} band in either model, but the optically thick treatment of the Modest

model on just two bands is sufficient to significantly change the shape of the total intensity. As glimpsed earlier in the 3D pure H_2O scenarios, which showcased the consequences of band oversaturation, the accuracy of a box model crucially boils down to just how well the optical thickness of each band is represented. Furthermore, we may observe that in these line of sight calculations, the optical depth along the path is a constant of position. Rigorously speaking this is not accurate: the product κS should vary with distance along the line of sight, not only because S is proportional to that distance, but because κ itself is calculated from S. But because we define S as a constant mean beam length, an error is thus unavoidably introduced in intensity calculations. In the context of this work, a test was run for this particular case where S was calculated in each cell as an incremented function of position, during the absorption calculation routine of the Modest model. The result was that at the end of the path (x = 1m), the error of the total intensity relative to the DBT-SNB solution was decreased from 53% (present case, Fig. 4-2-17) to just 20%. Since this test was basically a one-off recreation of the correlated RTE solution, the rest of the error could only come from purely the box model's absorption coefficients. Unfortunately this solution technique (variable path length) can only work in a 1D scenario, but it does explain why the WSGG errors were also so high in the same scenario (section 4.1.3.1).

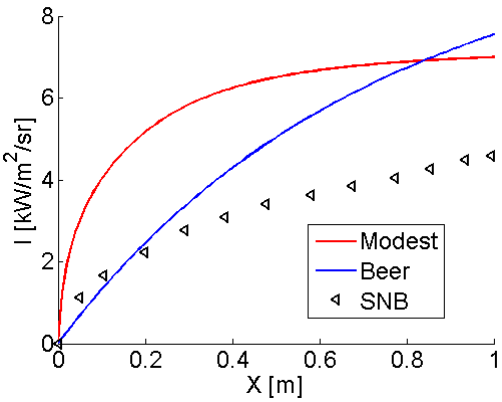

Fig. 4-2-17: Line of sight total intensities for CO_2-H_2O mixture with X_{CO2} = 65.6 g/m^2 and X_{H2O} = 80.1 g/m^2

On another hand, there is another significant source of error that can be addressed in a practical way indeed. Looking back at Fig. 4-2-15 it is clear that some of the bands are overlapping between the two species with both models, most notably: the 140 cm^{-1} of H_2O with the 667 cm^{-1} of CO_2, the 3660 cm^{-1} of CO_2 with the 3760 cm^{-1} of H_2O and the 5200 cm^{-1} of CO_2 with the 5350 cm^{-1} of H_2O. The distribution of the absorption coefficients in Fig. 4-2-15 is also different from the values in Table 4-2-7. Indeed, where overlaps occur, absorption coefficients are added, creating extra stepwise-grey regions (hence more bands) that FireFOAM should be taking into account, but is difficult to implement as it would firstly involve retroactive modification of the number of bands, then a full recalculation of all absorption coefficients over bands whose limits should be fixed. The overlap problem must however be dealt with, since it is very likely to be a source of error because the blackbody energy fractions that weigh the emission term of the RTE are picking up the same parts of the spectrum where two bands overlap. A way to address the issue is to consider the spectra from

Fig. 4-2-15 and manually input the absorption coefficients and bandwidths into the code. This is done by ignoring the initial band limits, and matching each value of κ with the respective interval so that overlaps are eliminated. In this case (Fig. 4-2-15) κ takes 13 values, hence there are 13 non-overlapping bands. The new values for both Beer and Modest models are given in Table 4-2-8.

Table 4-2-8: Absorption coefficients, bandwidths and emissivities of CO_2-H_2O mixture with X_{CO2} = 65.6 g/m^2 and X_{H2O} = 80.1 g/m^2, after manual overlap correction

Beer			Modest		
Band limits(cm^{-1})	κ (m^{-1})	ε (%)	Band limits(cm^{-1})	κ (m^{-1})	ε (%)
0 - 553	1.001	5	0 - 579	77.32	7
553 - 780	1.836	8	579 - 722	81.98	5
780 - 843	1.001	2	722 - 754	4.66	1
928 - 992	0.05986	0	858 - 955	0.02	0
1028 - 1092	0.05986	0	955 - 1062	0.04	0
1230 - 1970	0.5138	37	1062 - 1164	0.02	0
2140 - 2410	1.06	20	1380 - 1820	3.27	40
3363 - 3503	0.5319	5	2182 - 2410	20.63	21
3503 - 3816	1.071	13	3506 - 3534	1.72	1
3816 - 4157	0.5319	8	3534 - 3785	2.54	13
5169 - 5231	0.05986	0	3785 - 4014	1.72	10
5231 - 5468	0.3088	1	5100 - 5289	0.02	0
7153 - 7347	0.3005	0	5289 - 5300	0.99	0
			5300 - 5410	0.97	1
			7199 - 7301	0.87	0
	Total ε	**0.35**		**Total ε**	**0.33**

One may note, crucially, that the total emissivities from the overlap-corrected models are 10-13% lower than previously, which does make an impact on the line-of-sight intensity (which for a homogeneous or scaled optical path is proportional to emissivity), as visible in Fig. 4-2-18.

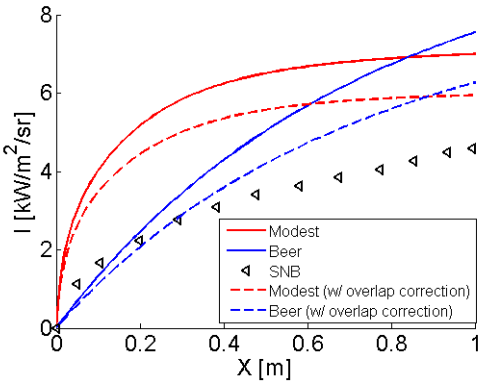

Fig. 4-2-18: Evolution of line-of-sight radiant intensity in CO_2-H_2O mixture with X_{CO2} = 65.6 g/m^2 and X_{H2O} = 80.1 g/m^2

At the end of the slab (x = 1m), we saw earlier that the non-corrected Modest model is in error of 53% relative to Bressloff's SNB-DBT solution, respectively 63% for the non-corrected Beer model. With the application of the overlap-corrections, these errors are nearly halved (Modest 30%, Beer 37%). Clearly, the overlap problem cannot be neglected. Increasing the number of bands manually is however impractical - from a computational cost point of view, but also because the number of bands may be completely different with every scenario. Rather, it is preferable to keep a smaller number of bands, and lump together the bands that are likely to overlap in a large number of configurations. This requires a full understanding of how bandwidths vary with path length, hence an exhaustive sensitivity study is carried out in the next section.

4.2.3. Bandwidth sensitivity study with the variable band box models

Although the exponential wide band (EWB) model is based on calculations involving a mass path length (X, g/m^2), a full-on sensitivity analysis of box model bandwidths ($\Delta\eta_e$, cm^{-1}) relative to X is difficult to understand, firstly because behaviours are as a whole complicated and wavenumber-sensitive, and secondly because the same X obtained from various combinations of T, S and p may result in different $\Delta\eta_e$. It is easier to break down the sensitivity analysis for two parameters, pressure path length (pS, atm.m) and temperature T. In Fig. 4-2-19 through Fig. 4-2-40 below, the evolution of $\Delta\eta_e$ against pS is shown for each band at temperatures ranging from 800K to 2000K, evidencing some trends, notwithstanding the pure rotational band of H_2O at 140cm^{-1}, whose spectral calculations are very simple, yielding an equally simple behaviour compared with the rotational-vibrational bands. The box model bandwidths were generated for a three-dimensional array, combining the variables temperature (varying between 600 and 2400K), path length (from 10^{-2} to 10^2 metres) and mole fraction or partial pressure (0.1 to 1 atm).

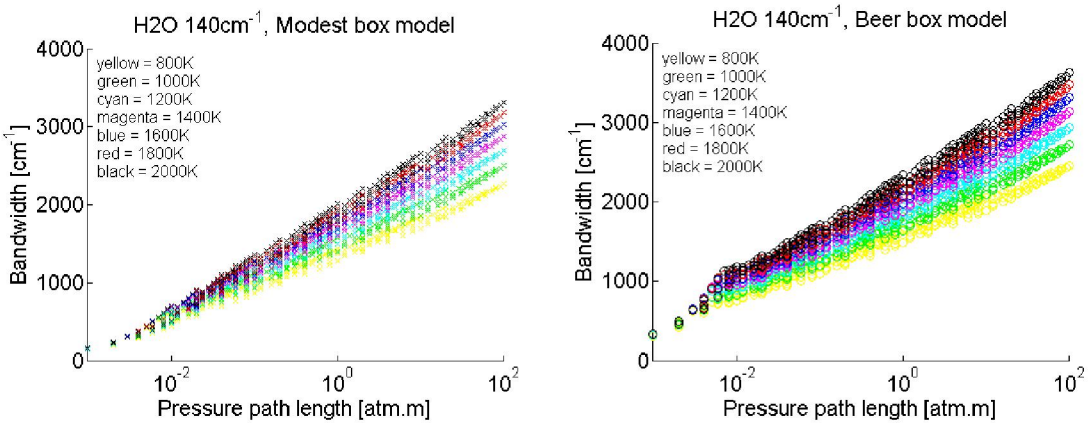

Fig. 4-2-19 & 4-2-20: Modest and Beer model bandwidths vs. pressure path length at 140 cm^{-1}

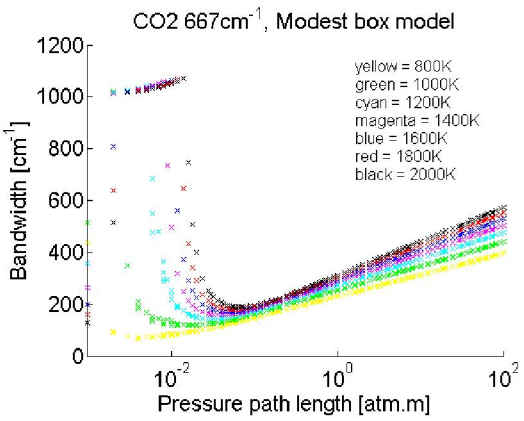

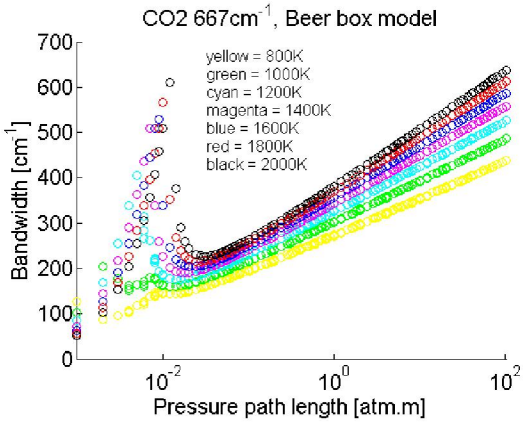

Fig. 4-2-21 & 4-2-22: Modest and Beer model bandwidths vs. pressure path length at 667 cm^{-1}

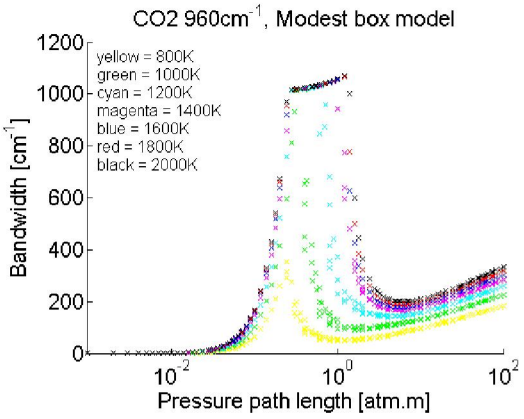

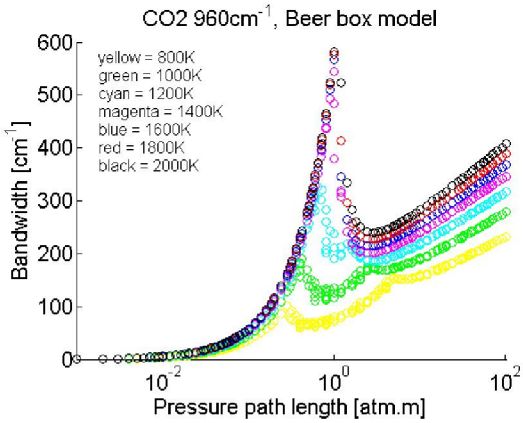

Fig. 4-2-23 & 4-2-24: Modest and Beer model bandwidths vs. pressure path length at 960 cm^{-1}

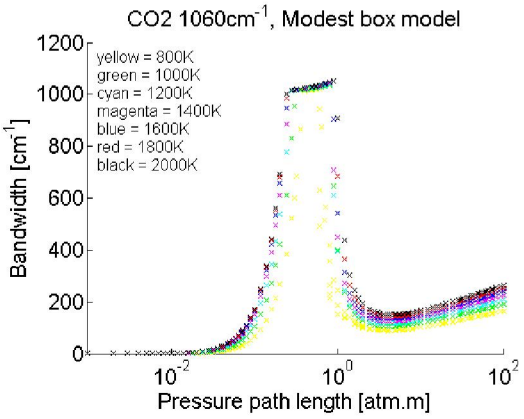

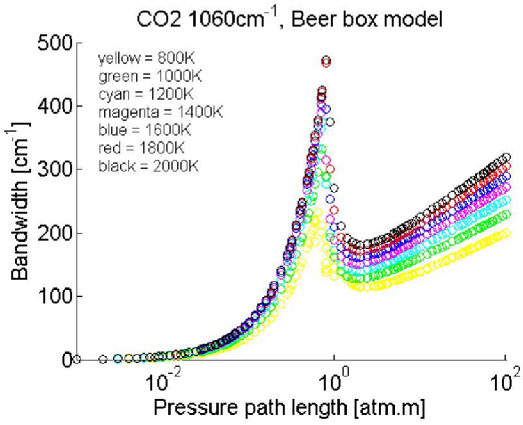

Fig. 4-2-25 & 4-2-26: Modest and Beer model bandwidths vs. pressure path length at 1060 cm^{-1}

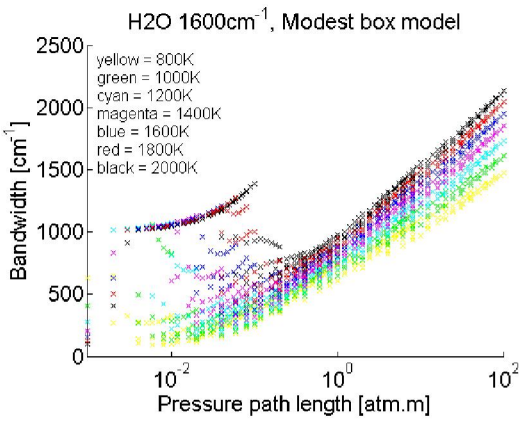

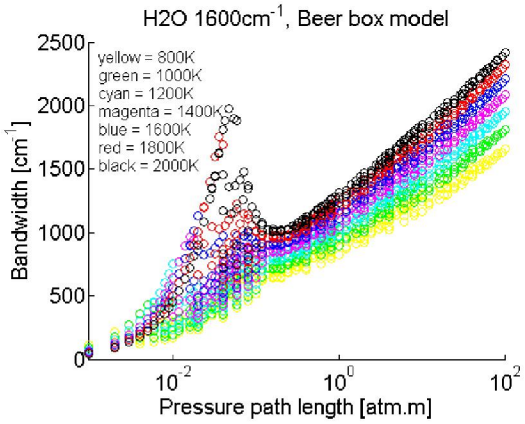

Fig. 4-2-27& 4-2-28: Modest and Beer model bandwidths vs. pressure path length at 1600 cm^{-1}

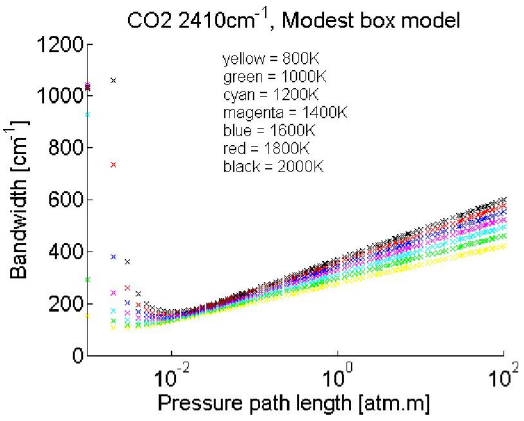

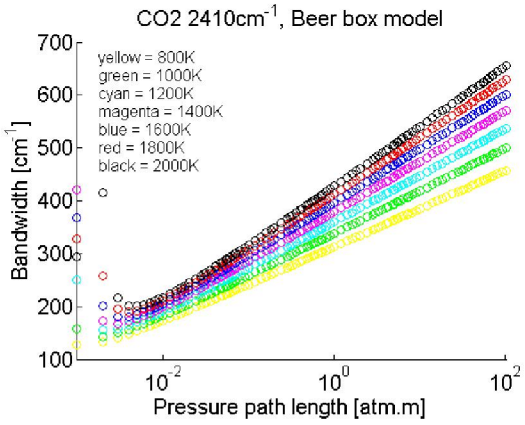

Fig. 4-2-29 & 4-2-30: Modest and Beer model bandwidths vs. pressure path length at 2410 cm^{-1}

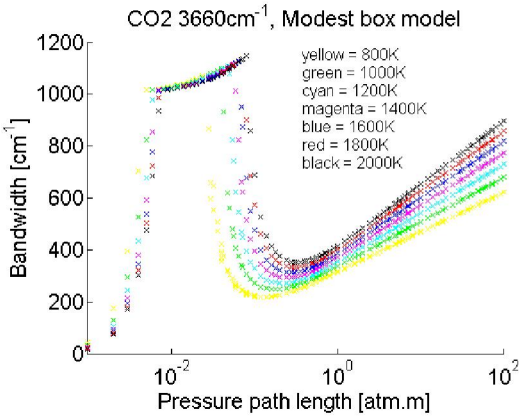

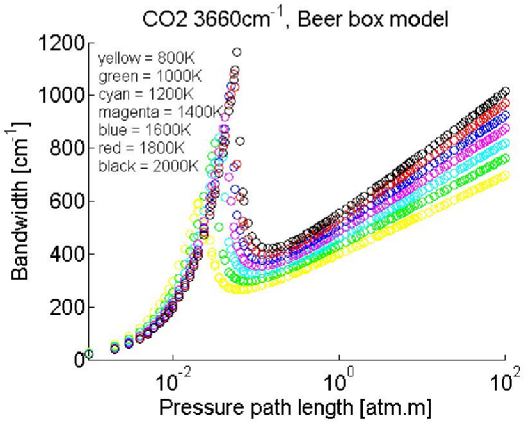

Fig. 4-2-31& 4-2-32: Modest and Beer model bandwidths vs. pressure path length at 3660 cm^{-1}

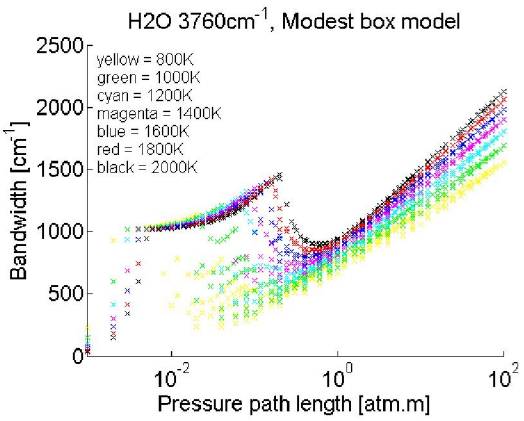

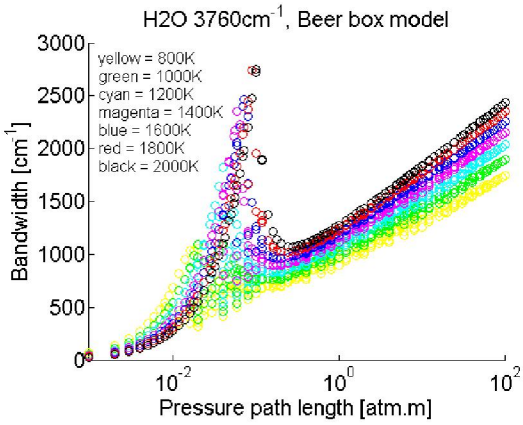

Fig. 4-2-33 & 4-2-34: Modest and Beer model bandwidths vs. pressure path length at 3760 cm^{-1}

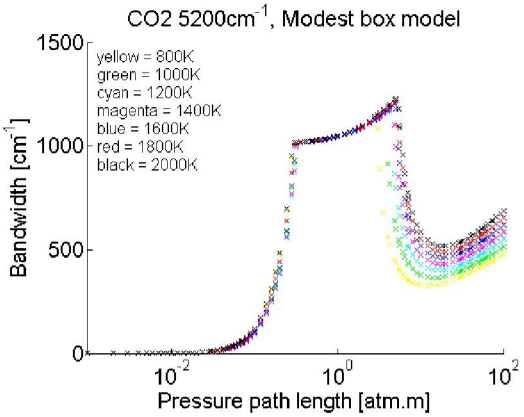

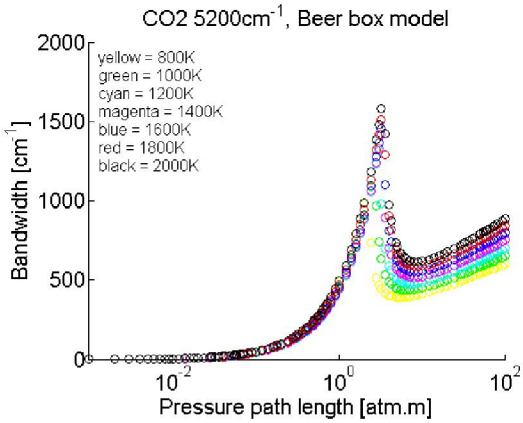

Fig. 4-2-35 & 4-2-36: Modest and Beer model bandwidths vs. pressure path length at 5200 cm^{-1}

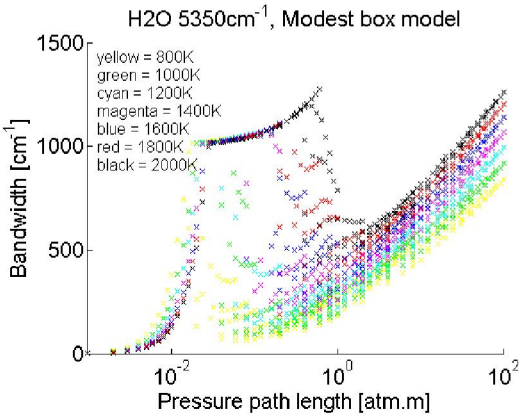

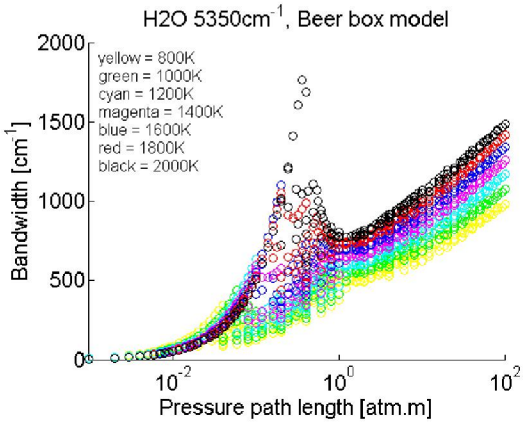

Fig. 4-2-37& 4-2-38: Modest and Beer model bandwidths vs. pressure path length at 5350 cm^{-1}

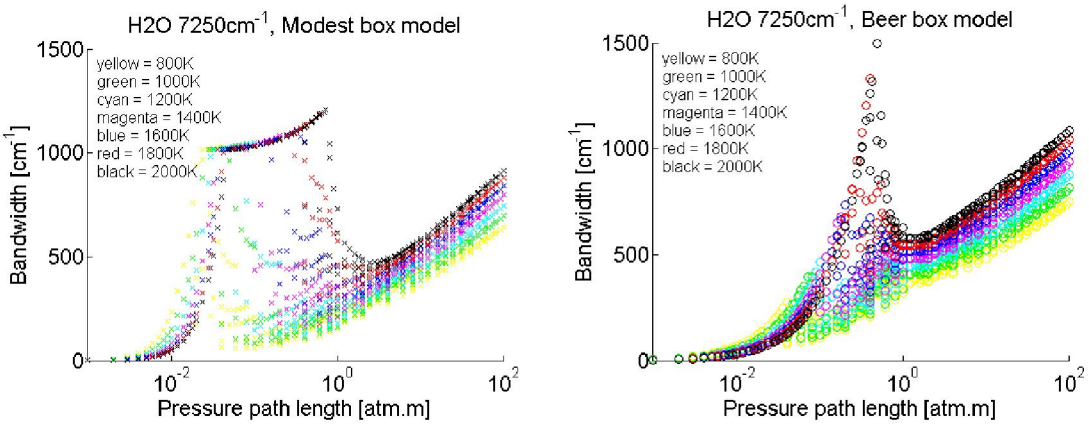

Fig. 4-2-39 & 4-2-40: Modest and Beer model bandwidths vs. pressure path length at 7250 cm^{-1}

Fig. 4-2-19 to 4-2-40: Box model bandwidth as a function of pressure-path length for different temperature, comparing Modest and Beer models in each CO_2 and H_2O band

Firstly, CO_2 bandwidths have a regular dependency on pS, that is, at a given T, one value of pS matches one value of $\Delta\eta_e$. This is clearly not the case with H_2O, where multiple $\Delta\eta_e$ are seen for one same pS, meaning H_2O bands are independently sensitive to p and S. In other words, CO_2 bands and absorption coefficients have two degrees of freedom, and H_2O bands have three. Secondly, all rotational-vibrational bands show overall consistency in the way their $\Delta\eta_e$ peaks, especially at higher temperatures. In both Modest and Beer models, $\Delta\eta_e$ rises and falls sharply, the difference being that with the Modest model the peak plateaus over relatively large pS range, whereas with the Beer model the peak is very local. The peaks happen at different pS across the spectrum, for each species, and their displacements may be correlated to band strength, spectral position or both. What is more relevant to this work is what kind of bandwidth one may expect from these models in a fire scenario, or even a fire suppression scenario, and whether or not these bandwidths may cause error-inducing overlaps. The following is an analysis of the range of temperature and pressure path lengths found in four different pool fires.

4.2.4. Estimation of mass path length range for pool fires

Data from large eddy simulations of four pool fires is considered below to get an estimation of the relevant path length range for pool fires. These fires are the 30cm heptane fire (heat release rate 116kW) of Klassen and Gore [4], the 28cm methane fire (53kW) of McCaffrey [86], and the methanol fires of Klassen and Gore (30cm - 20 kW and 100cm - 252kW). The pressure and mass path lengths were calculated from FireFOAM mass fractions and temperatures extracted along the axial centreline. Unlike the radiation field, mass fractions and temperatures are not expectable to vary significantly between simulations employing different gas radiation models (for these runs a WSGG was used).

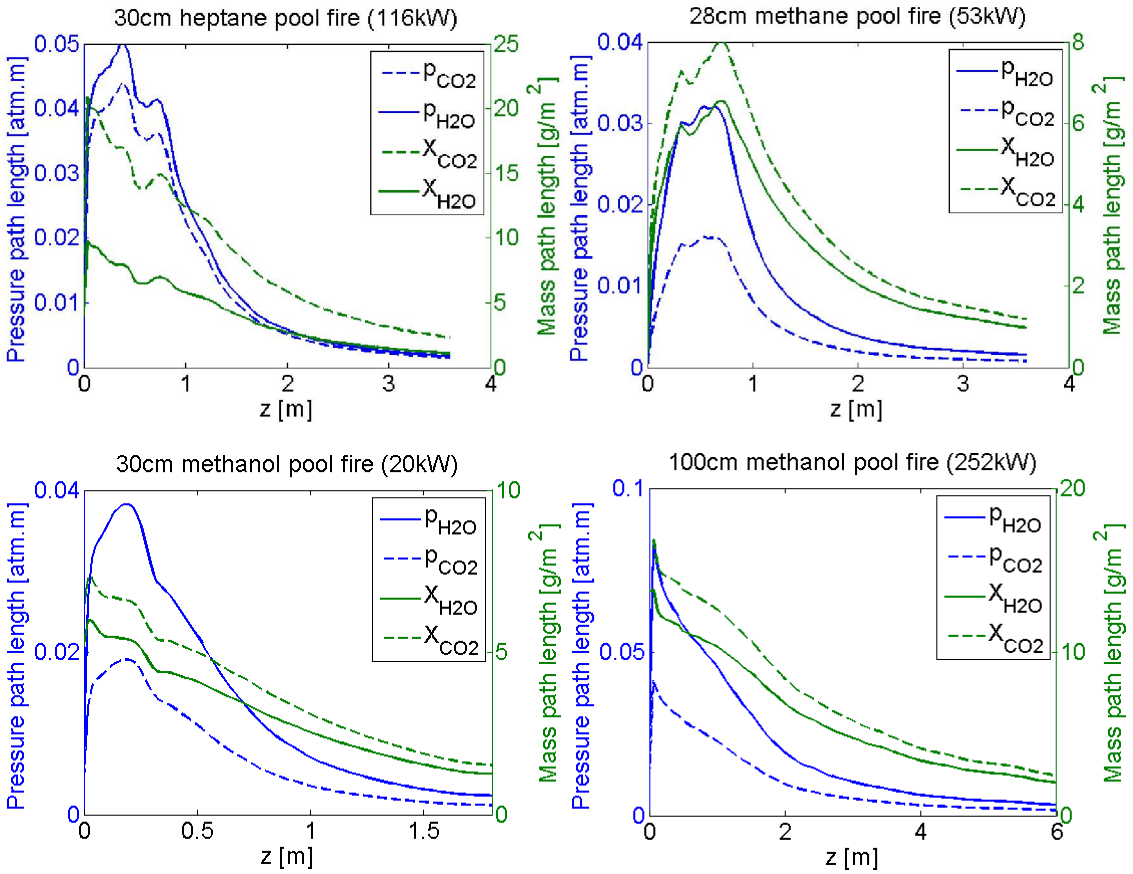

Fig. 4-2-41: Centreline distributions of pressure path length (blue) and mass path length (green) in four pool fires of different fuels, heat release rates and diameters

It is plain from Fig. 4-2-41 that no pressure-path length ever reaches 0.1 atm.m, regardless of the size, fuel or heat release rate. Should one seek averaged values for a Curtis-Godson type scaling approach, those should be even lower. The mass path lengths, which include temperature information, do show somewhat increased values at higher heat release rates but these are rather mild compared with the increase of heat release rate (e.g. from 20kW to 252kW for the methanol fire). Hence, it is with relative confidence that one may dismiss box model bandwidths from any pressure path length above 0.1 atm.m. One reason for this is that partial pressures are defined by the mole fractions in the single-step chemistry equation and fires develop in atmospheric conditions, hence in fires such as the ones above the products of combustion cannot be expected to saturate the environment (soot, however, is likely to do so, but soot radiation is altogether independent of gas radiation, indeed of path length too). On another hand there is the calculation method of mean beam length. Geometric flame properties can be considered to obtain S, if flame height is known *a priori*, so the $S = 3.6V/A$ formula may be applied (in the present case, measured flame heights are available from Klassen and Gore's experiments [4], reasonably well matched by fellow FireFOAM developers [18,23]). Indeed, the time averaged flame temperature profiles of the examples above all share a roughly conic shape, with a wider disc base at the pool surface and vertically necking more or less sharply. But as it turns out, large fires like the 100cm methanol do not yield a large S, which also explains why the pressure path lengths remain quite small. On another hand, since the mean beam length is in essence a length scale, another method to

calculate S is to use the integral length scale as S. This method has the advantage of only requiring knowledge of the total heat release rate, thus:

$$L = \left(\frac{Q}{C_p \rho T \sqrt{g}}\right)^{0.4} \tag{4.2.1}$$

Where Q is the heat release rate in kW and the denominator term corresponds to far field specific heat, density and temperature (i.e. room air). The integral length scale is plotted against the heat release rate in Fig. 4-2-42. The mean beam lengths based on geometric approximations of the flame shape, whether conical or cylindrical, generally yield smaller mean beam lengths than with the integral length scale method. In any case, the mean beam length is a rather weak function of heat release rate, and one should not expect path lengths larger than 1 metre from atmospheric pool fires smaller than 1 megawatt.

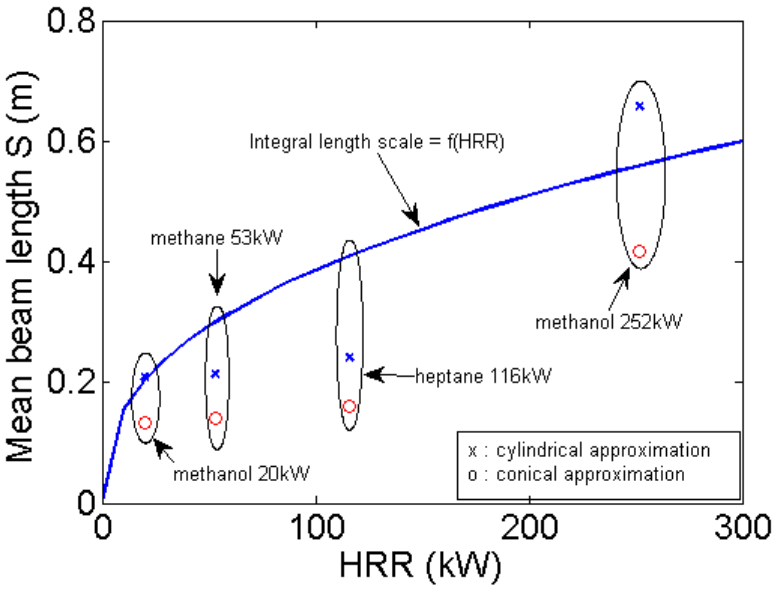

Fig. 4-2-42: Comparing different methods for mean beam length calculations in pool fires, i.e. the integral length scale (solid line, Eq. 4.2.1), the cylindrical approximation ('x' symbols) and the conical approximation ('o' symbols)

With a pressure path length range hence reasonably defined between roughly 10^{-2} and 10^{-1} atm.m, looking at the bandwidth data from Fig. 4-2-19 through Fig. 4-2-40 yields the ranges listed in Table 4-2-9 below.

Table 4-2-9: Visual estimation of box model bandwidths for pressure path lengths between 10^{-2} and 10^{-1}atm.m

Specie	Band head locations (cm^{-1})	Modest $\Delta\eta_e$ (cm^{-1})	Beer $\Delta\eta_e$ (cm^{-1})
H_2O	140	540	640
CO_2	667	170	200
CO_2	960	50	5-30
CO_2	1060	100	5-30
H_2O	1600	440	500
CO_2	2410	200	200
CO_2	3660	200-1000	200-800
H_2O	3760	200-800	750
CO_2	5200	0-100	5-40
H_2O	5350	0-200	100-200
H_2O	7250	0-1000	50-400

For some bands like the 3660 or 7250cm^{-1} the bandwidths can be quite irregular, covering an array of temperatures. Then again, the 3660cm^{-1} band of CO_2 is very close to the 3760cm^{-1}, hence these two can be expected to overlap in almost any CO_2-H_2O mixture. Lumping them together into one single band combining the lower limit of the 3660cm^{-1}, the upper limit of the 3760cm^{-1} and the integrated band intensities (α, in $cm^{-1}/(g/m^2)$) of both will save computational time. Bearing in mind that three H_2O bands are present at the 3760cm^{-1} location, this amounts to a quadruple band overlap (three H_2O and one CO_2), where the respective α_i of each species is weighted by the partial density (g/m^3). The properties of four bands combined into one may potentially save massive computational time. The same method can be applied to the 5200 and 5350cm^{-1} bands of CO_2 and H_2O respectively. One may note that the overlapping CO_2 bands, at both these locations, are relatively weak. Their contribution to the combined bands is less in terms of absorption coefficient than bandwidth. The two "hot bands" of CO_2 at 960 and 1060cm^{-1} can broaden to very large extents, but because their integrated intensities α are so low (~10^{-9} $cm^{-1}/(g/m^2)$), they can pass as windows and may as well be neglected altogether, saving some more computational time. The pure rotational band of H_2O at 140cm^{-1} poses a particular issue. Unlike the other bands, the bandwidth broadens indefinitely with pressure path length and thus can eventually swallow a large portion of the spectrum including the first three bands of CO_2. But since the relevant range of pS is between 10^{-2} and 10^{-1}atm.m, the broadening remains contained, and the only potential overlap may occur with the first CO_2 band at 667cm^{-1}. Both these bands are important and combining their properties is more difficult than with the other CO_2-H_2O combinations. The 140cm^{-1} has its head in the far infrared but with a large broadening it can pick up a significant blackbody energy fraction. Also, the absorption coefficient is usually one or two orders of magnitude larger than other bands. The 667cm^{-1} band has much smaller

absorption coefficients but is weighted by larger blackbody energy fractions because blackbody energy rises very sharply in this region. Since there is uncertainty with the strategy to adopt, a default configuration may be to leave the two bands separate for scenarios involving mixture. The 140cm^{-1} band hence stops where the 667cm^{-1} band typically starts, that is around ~600cm^{-1}. Since the overlap region is narrow according to Table 4-2-9 (with the Modest model, well under 50cm^{-1}), the strategy of keeping the two bands separate seems appropriate and may work also in non-mixture scenarios without requiring manual changes in either the source code or input data. In any case however, the work from the previous section has evidenced that the pure rotational band should not be neglected because it contributes to total emissivity no less than 20% at 1000K, and up to 80% at 600K according to Modak's data [16] (also confirmed in this work). Since in pool fires and inhomogeneous media an average temperature must be used, it is very much likely to be below 1000K hence the importance of that band. Another consideration to account for is the fact that strong bands tend to narrow down with decreased mass path lengths (i.e. either temperature increase or mole fraction decrease), hence only the bands whose heads are closest to one another may be eligible for possible overlaps.

4.2.5. Estimation of band strengths (full emissivity data)

The band-by-band analysis of section 4.2.2.3.1 (1D homogeneous mixture) offered some insight on the individual strength of each band as calculated by the box model, as well as the information found in Tables 4-2-1 to 4-2-8, where it was seen that some bands contribute very little to total emissivity. Since CPU time is always a concern, the sensitivity analysis that was carried out on Fig. 4-2-19 to 4-2-40 for bandwidths has been reproduced for band emissivities in Fig. 4-2-43 to 4-2-53 below, in order to dismiss the weaker bands safely from future calculations. Even though all bands broaden to very large extents at certain pressure-path lengths, the band strength is a combination of bandwidth (which determines the blackbody energy fraction) and the absorption coefficient. The band emissivity combines both parameters, since it can be defined as follows along a homogeneous optical path:

$$\varepsilon = \Delta F\left(1 - exp(-\kappa X)\right) \qquad (4.2.2.a)$$

Where

$$\Delta F = F(T, \lambda_+) - F(T, \lambda_-) \qquad (4.2.2.b)$$

ΔF is the difference between fractional blackbody energies at the band limits. It can be seen from Fig. 4-2-43 to 4-2-53 that up to 2410cm^{-1}, all band emissivities decrease with temperature. After 3660cm^{-1} the trend is reversed. Emissivity always increases with pressure-path length. The hierarchy can vary at intermediate pressure path lengths, but at 1000K, the strongest bands visibly identify as - in decreasing order - 1600, 3760, 2410, 140, 3660 cm^{-1}. The 667 and 5350 cm^{-1} are relatively less important although non-negligible. The 960, 1060 and 7250cm^{-1} bands, at last, contribute very little. Clearly, the pure rotational band of H_2O at 140cm^{-1} should not be neglected, especially considering that averaged temperatures in a flame tend to be much lower than the local maximum.

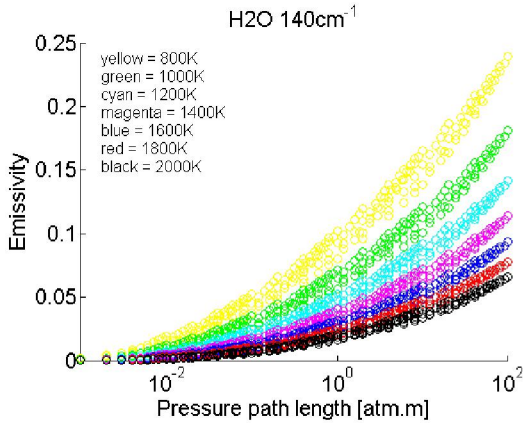

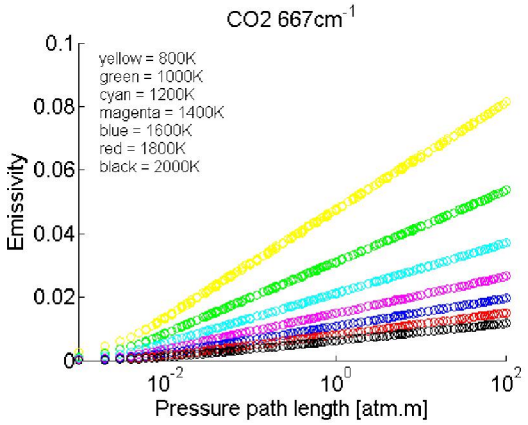

Fig. 4-2-43 & 4-2-44: Band emissivity vs. pressure path length at 140 and 667 cm^{-1}

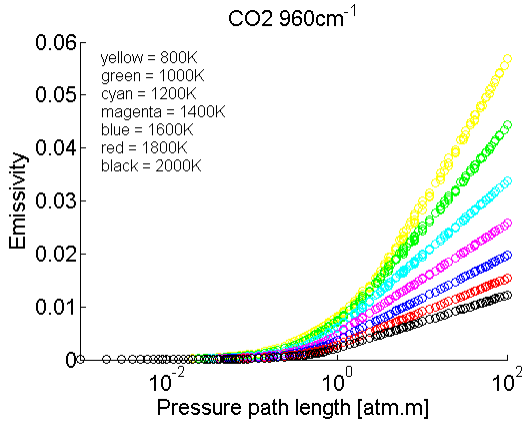

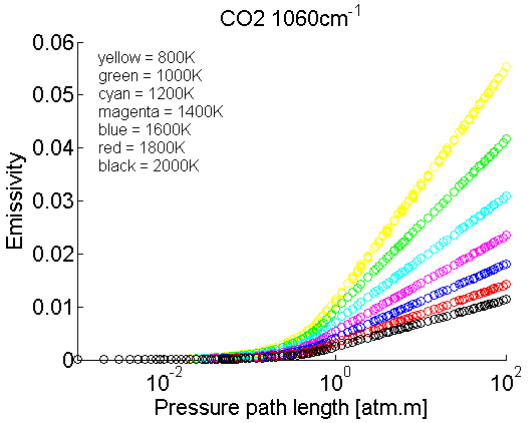

Fig. 4-2-45 & 4-2-46: Band emissivity vs. pressure path length at 960 and 1060 cm^{-1}

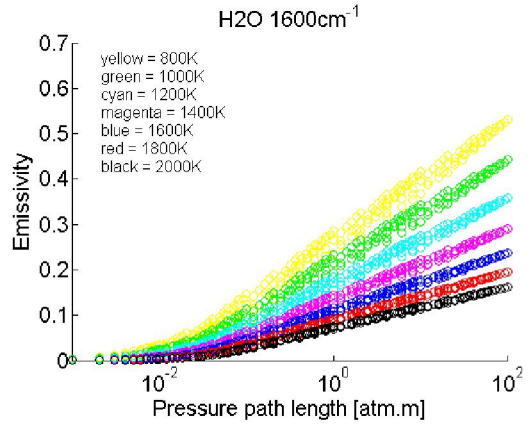

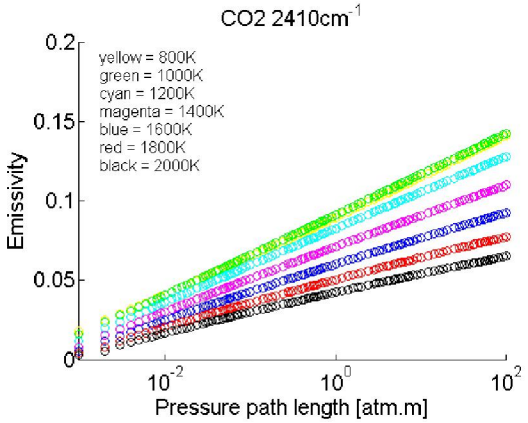

Fig. 4-2-47 & 4-2-48: Band emissivity vs. pressure path length at 1600 and 2410 cm^{-1}

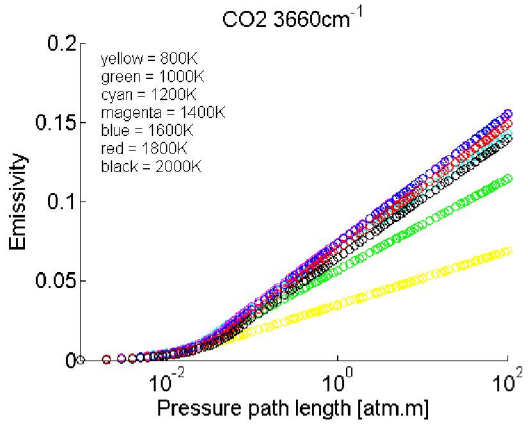

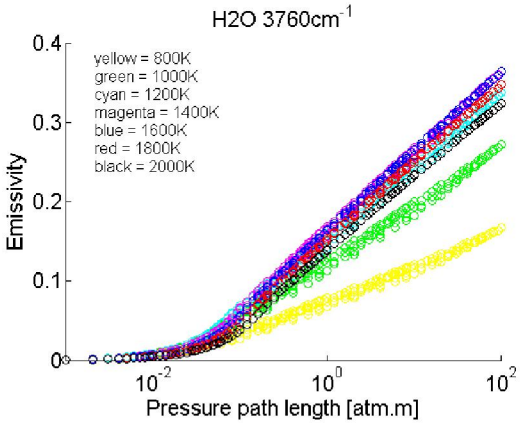

Fig. 4-2-49 & 4-2-50: Band emissivity vs. pressure path length at 3660 and 3670 cm^{-1}

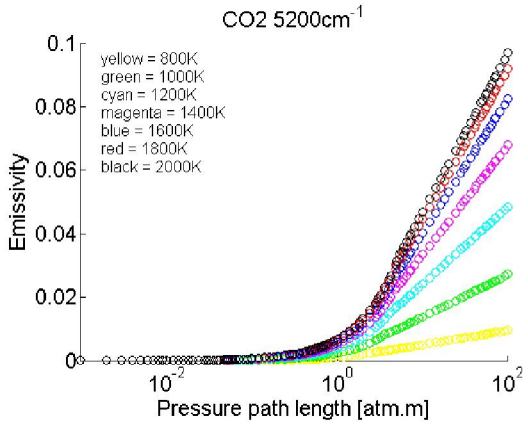

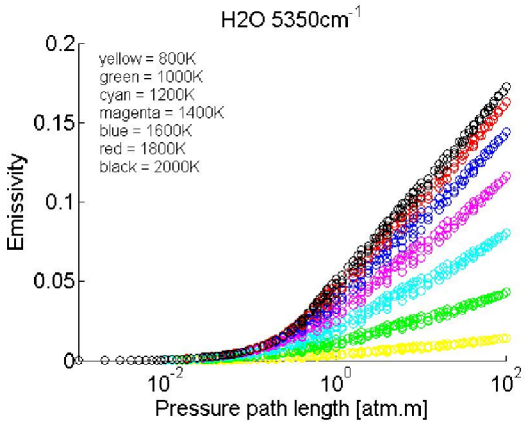

Fig. 4-2-51 & 4-2-52: Band emissivity vs. pressure path length at 5200 and 5350 cm^{-1}

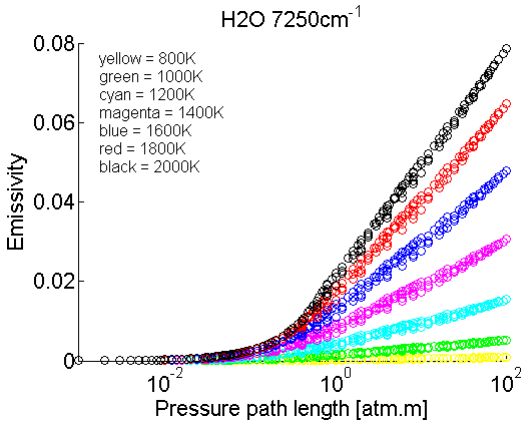

Fig. 4-2-53: Band emissivity vs. pressure path length at 7250 cm^{-1}

Fig.4-2-43 to 4-2-53: Box model band emissivities as a function of pressure-path length for different temperatures

4.2.6. Modest-based fixed bands box model in static media

As a result of the discussion above, after eliminating the weak bands, grouping the overlapping ones and considering a reasonable bandwidth that may work for the relevant range of pressure or mass path length; the fixed bands model comes as defined in Table 4-2-10. The Modest approach was preferred over the Beer model for two reasons. Firstly, we saw that pool fire mass path lengths are in the 5-20 g/m^2 range, which is a good order of magnitude lower than the 200-300 g/m^2 range of the Coelho cases where Modest absorption coefficients are so high that nearly all bands have strongly asymptotic intensities, leading to large errors. Since that risk is unlikely, the Modest model may as well be used for its better rendition of source terms. Secondly, once bandwidths are known, the Modest model's absorption coefficient is directly proportional to species density and the integrated band intensity α, which is indeed a relatively simple calculation routine since the whole EWB procedure that yields the band absorptance can be altogether ditched, as well as the requirement of inputting a mean beam length (analogous to the banded WSGG implementation). With the Beer model, however, such a simplification is not possible: the absorption coefficient is a function of transmissivity, itself a function of bandwidth and absorptance - hence the EWB absorptance routine would have to be kept in the code. Also, it is unclear how theoretically sound it would be to back-calculate the absorptance independently from the bandwidth. For the present implementation, thus based on Modest's model, the band heads chosen for the overlapping bands are that of H_2O (3760, 5350cm^{-1}) since they are about 2 times stronger than the CO_2 bands they overlap with, according to the emissivity charts of the previous section.

In terms of CPU savings, an early (and since then deleted) implementation of the box model featured cell-based absorption calculations, meaning that likewise to the WSGG absorption is calculated locally. This was tested with a 30cm methanol pool fire simulation that took 2 to 3 weeks to run, whereas the same simulation with a WSGG would have taken a few days - clearly this was not an option for fire simulations. The most important modification at this stage was to use the Curtis-Godson-type to restrict absorption calculations to one for the whole domain. Past that stage, the main advantage of the fixed bands version is going to be with the reduced number of bands. It is true that thanks to a simplified absorption calculation routine, some CPU gain is to be expected from the new version, but that is difficult to quantify with certainty because the total FireFOAM running times for the pure radiation cases are very fast (a few seconds or even less than a second), and that includes absorption calculations, RTE solutions and energy equation solution. To answer this question, a test run was done with the regular Modest box model and the fixed bands model with a medium-size pool fire. Both simulations identical parameters (including the same number of bands) so the only difference in CPU time should come from the absorption calculation. Over a CPU runtime of about 10-12 hours, the fixed bands model turned out to be ~7% quicker. But clearly, the fact that the fixed bands model calculates 7 absorption coefficients (instead of 13 with the original box model) is the most determinant. In fire simulations that use hundreds of solid angles, this is a crucial detail because the number of RTE solutions per solver iteration is equal to the product of the number of bands and the number of solid angles, hence this can mean an economy of thousands of solved RTE's. Besides, as explained earlier, with a

variable band limits model it is not possible to anticipate band overlaps that may occur every time absorption is updated in a simulation. The fixed bands model was corrected to that intent and is thus safer to use here.

Table 4-2-10: Band limits of the Modest-based fixed bands box model

Band head (cm^{-1})	Gas species	Wavelength range (μm)	Wavenumber range (cm^{-1})
7250	H_2O	1.3695-1.3893	7198-7302
5350	H_2O, CO_2	1.8481-1.8907	5289-5411
3760	H_2O, CO_2	2.4907-2.8531	3505-4015
2410	CO_2	4.1494-4.5851	2181-2410
1600	H_2O	5.4885-7.2569	1378-1822
667	CO_2	13.3156-17.1821	582-751
140 (for mixtures)	H_2O	17.1821 - ∞	0 - 582
140 (H_2O only)	H_2O	10.3735 - ∞	0 - 964

As stated above, fixing the band limits has heavy consequences on the structure of the code. Band width calculations are no longer necessary, which makes the following functions redundant: equivalent bandwidth ($\Delta\eta_e$), band absorptance (A), band equivalent pressure (P_e), optical depth at band head (τ_0), pressure broadening parameter (β). The only remaining functions related to the EWB model are the density integrated band intensity ($\rho\alpha$), and one of the two non-dimensional functions of temperature that calculate vibration-rotational energy transitions (Ψ). The absorption coefficient is thus essentially temperature-dependent, with a pressure dependency implicitly remaining in the density ρ. The box model mathematics hence reduce to:

$$\alpha(T) = \alpha_0 \frac{\Psi(T)}{\Psi(T_0)} \tag{4.2.3}$$

$$\kappa = \frac{\rho\alpha}{\eta_U - \eta_L} \tag{4.2.4}$$

Where, as before, the temperature T is an arithmetic average, and Ψ is obtained from the simplified correlations from Lallemant and Weber [47]. In Eq. 4.2.4 the calculation of the density-integrated intensity $\rho\alpha$ may vary, depending on whether gas bands overlap or not. ρ is just the average density of one species if no overlaps. If overlaps occur, then

$$\rho\alpha = \sum_i \sum_k \rho_i \alpha_{i,k} \tag{4.2.5}$$

Where *i* is the species subscript and *k* the index of the overlapping band. Elsewhere, the energy fractions calculations for the gas phase remain unchanged (except they are now done with fixed band limits).

4.2.6.1. Homogeneous media

4.2.6.1.1. 2D pure CO_2

The fixed bands box model based on the Modest variant is tested in the 1m x 0.5m rectangular enclosure of Goutiere et al. [35] filled with a homogeneous, isothermal CO_2 phase at mole fraction 10% and temperature 1000K (mass path length 35.9 g/m^2). Although the fixed bands model is for CO_2-H_2O mixtures, the bands "hidden" in the overlap calculations are still there since each phase is weighted by its respective density. All CO_2 bandwidths are however in close agreement with the earlier Modest model, hence the spectrum is very much the same (Fig. 4-2-54, Table 4-2-11), except for the 3660cm^{-1} band, which takes the band head at 3760cm^{-1} (the neighbouring H_2O band in a mixture). This slight displacement does not make any noticeable difference on that band's emissivity (always 0.02 with any box model variant), because this band is always broad but not optically thick. The same comment applies to the 5200cm^{-1} band, which in the fixed bands model is stretched to around ten times the width of the other box models, hence reducing the absorption coefficient by almost tenfold too. The emissivity is negligible with any box model, hence the change in bandwidth is inconsequential. The important CO_2 667cm^{-1} and 2410cm^{-1} bands remain overlap-free in the fixed bands model, and are hence very close to the regular Modest.

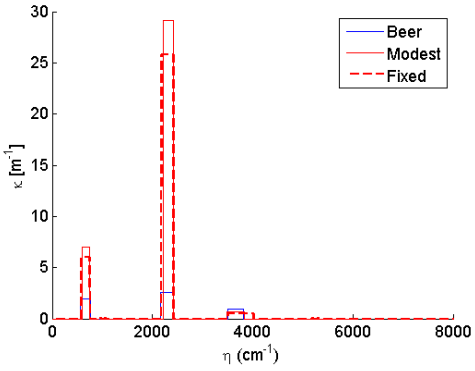

Fig. 4-2-54: Box model absorption spectra of pure CO_2 with X = 35.9 g/m^2

Table 4-2-11: Absorption coefficients, bandwidths and emissivities for pure CO_2 with X = 35.9 g/m^2

	Fixed bands model		
Band (cm^{-1})	**κ (m^{-1})**	**$\Delta\eta_e$ (cm^{-1})**	**ε**
667	6.03	169.00	0.02
2410	25.76	229.01	0.07
3660	0.50	509.98	0.02
5200	0.04	121.92	0.00
		Total ε	**0.11**

The fixed bands spectrum similar to the Modest model translates to rather similar overall performance, with source terms in error of 26% midfield relative to the SNB solution (the variable Modest model yielded 33%) (Fig. 4-2-55-a, 4-2-55-b), respectively 18% for the heat flux (around 10% for the variable Modest model) (Fig. 4-2-55-c, 4-2-55-d). These differences are explained by the slightly increased total emissivity of the fixed bands model (0.11 instead of 0.10 previously).

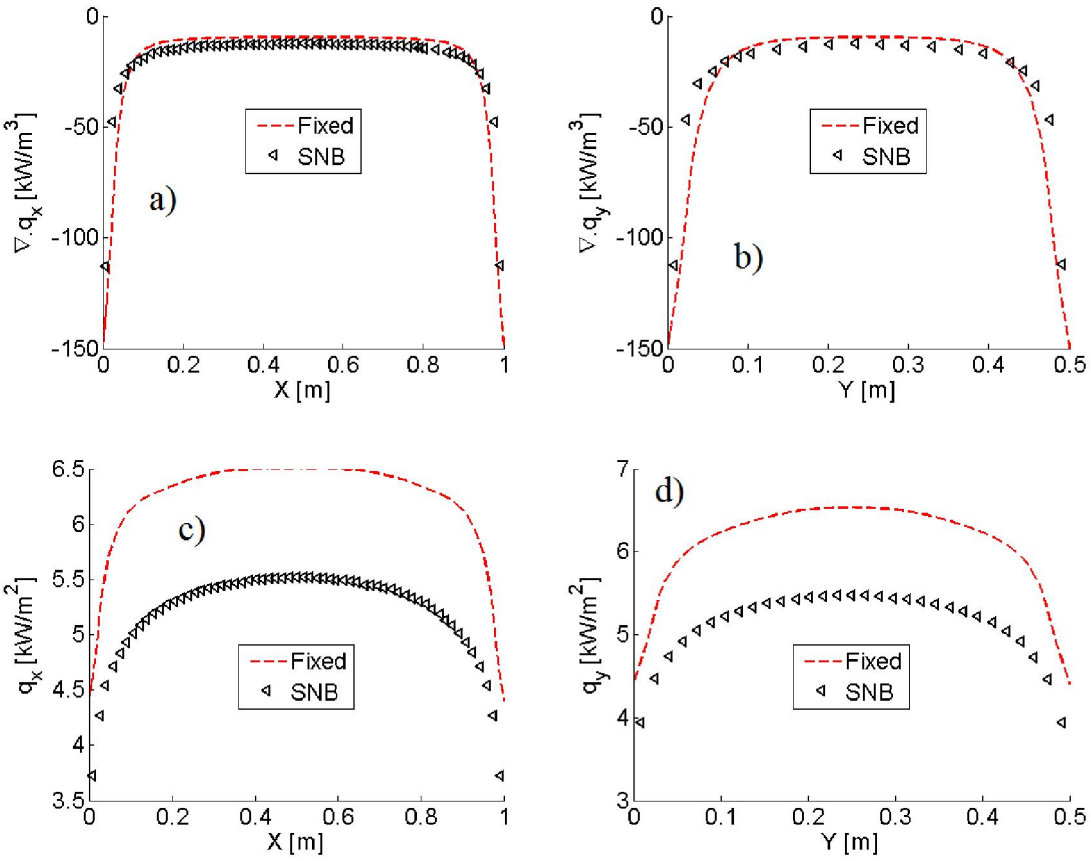

Fig. 4-2-55: Box model vs. SNB from [35], source term along *x* and *y* (top), heat flux along *x* and *y* (bottom) for CO_2 at $X = 35.93$ g/m^2

4.2.6.1.2. 2D pure H_2O

With the H_2O variant, the upper limit of the pure rotational 140cm^{-1} band is fixed at 964cm^{-1}. This value was obtained from the sensitivity analysis discussed previously, accordingly with the relevant range described for fires. This band is symmetrical around the 140cm^{-1} head, but large bandwidths can make the lower limit go negative, which is not physical. In the variable limit models the negative range is truncated, to the extent that almost half the calculated bandwidth is not taken into account, resulting in low band emissivities (e.g. for this scenario, 0.03 or 0.04, see Table 4-2-2 in section 1). This arbitrary truncation may be responsible for the seemingly abnormal underestimation of the source term with the variable band limit models seen previously. With the fixed model the bandwidth is kept whole, with limits going from $\eta_L = 0$ to $\eta_U = \Delta\eta_e$, rather than $\eta_U = 140 + \Delta\eta_e/2$. This results in a more than

doubled band emissivity for the fixed bands model, as can be seen from Table 4-2-12 and Fig. 4-2-56. Elsewhere, the emissivity of the important 1600cm^{-1} band is slightly increased from the regular Modest model (0.12 instead 0.10) due to the 35% larger bandwidth, indeed the blackbody fraction is sensitive in that region and its increase has more effect on emissivity than the slight decrease in the absorption coefficient. The other band emissivities are rather similar to the regular Modest model, but the total emissivity now increases to a significant 0.27 (0.18 and 0.19 with the Modest and Beer models previously).

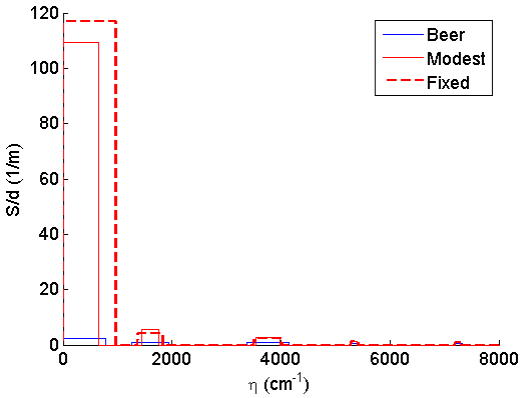

Fig. 4-2-56: Absorption spectrum of pure H_2O with X = 29.4 g/m^2, with (left) and without (right) the pure rotational band 140cm^{-1}

Table 4-2-12: Absorption coefficients, bandwidths and emissivities for pure H_2O with X = 29.4 g/m^2

	Fixed bands model		
Band (cm^{-1})	κ (m^{-1})	$\Delta\eta_e$ (cm^{-1})	ε
140	116.82	963.98	0.08
1600	4.07	443.99	0.12
3760	2.23	509.98	0.06
5350	1.21	121.92	0.00
7250	1.06	104.07	0.00
		Total ε	**0.27**

The results of these spectral changes are very visible on the source term. Previously, the Beer model yielded an acceptable match at the mean beam length, but was very off near the boundaries, whereas the Modest model would perform the other way around, yielding a 42% relative error at the mean beam length (midfield location). The fixed bands model very much improves the source term midfield from the regular Modest model, while retaining the boundary effects, and this time the relative error with SNB is down to 13% midfield in both directions (Fig. 4-2-57-a, 4-2-57-b). The heat fluxes are very good as well, with maximal relative differences of just 5% horizontally (Fig. 4-2-57-c) and a near-perfect match vertically (Fig. 4-2-57-d).

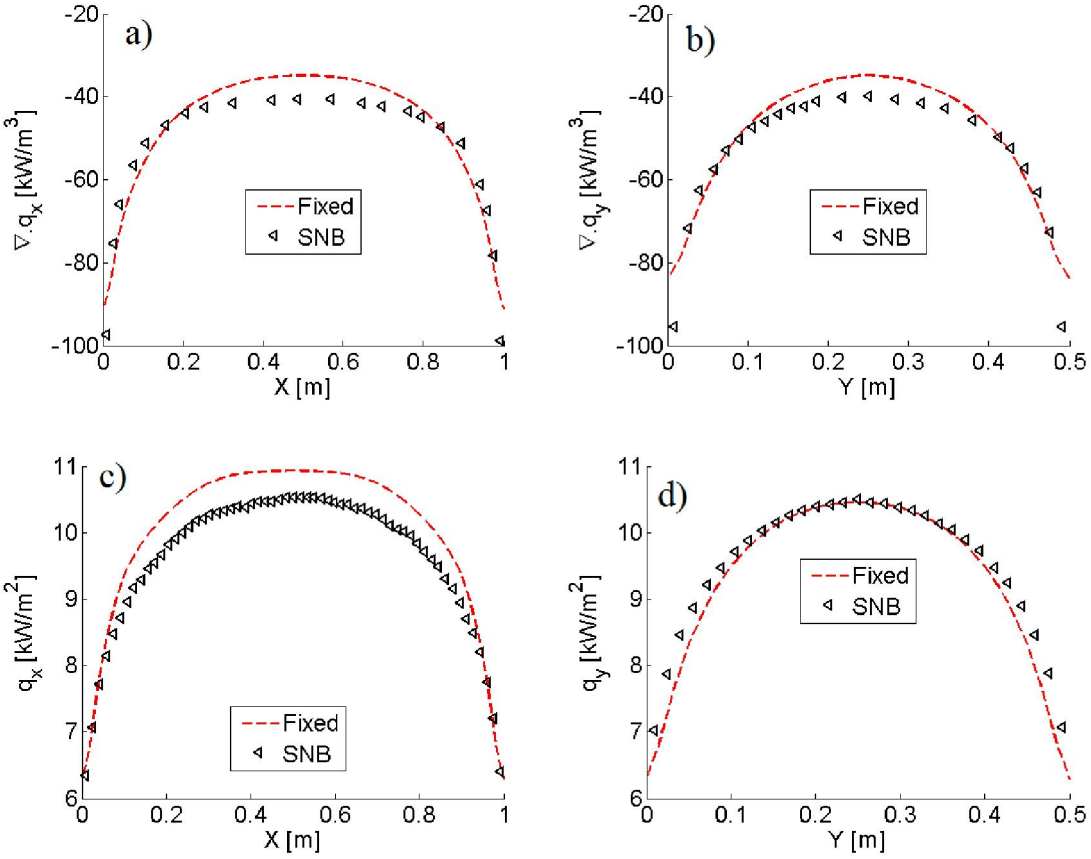

Fig. 4-2-57: Box model vs SNB from [35], source term along *x* and *y* (top), heat flux along *x* and *y* (bottom) for H_2O at $X = 29.4$ g/m^2

4.2.6.1.3. 3D pure H_2O

The next scenario, involving the 2 x 2 x 4m box enclosure of Coelho [34], paints a similar picture to that of section 1 with the variable limit models. What is new here is that the fixed bands model has different bandwidths to the regular Modest model (Fig. 4-2-58, Table 4-2-13), but the core issue is the same: the absorption coefficients are too high, causing optical thicknesses to tend towards infinity, hence transmissivity towards zero. No matter how one may broaden the fixed band limits, the absorption coefficients will not decrease enough. This is purely an intrinsic limitation of the approach (over which the Beer model is preferred). Actually, the fixed band limits are narrower than the regular Modest model's, hence all absorption coefficients are increased which can only make the oversaturation worse.

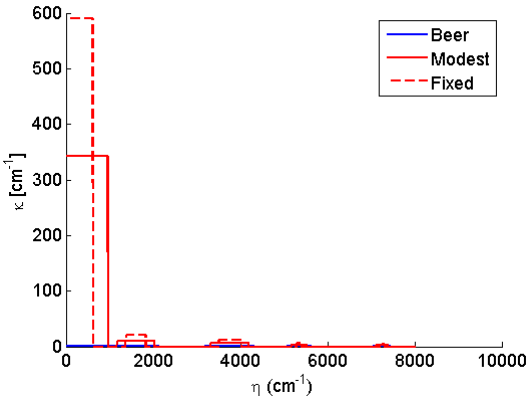

Fig. 4-2-58: Absorption spectrum of pure H_2O with $X = 316$ g/m^2

Table 4-2-13: Absorption coefficients, bandwidths and emissivities for pure H_2O with $X = 316$ g/m^2

	Fixed bands model		
Band (cm^{-1})	**κ (m^{-1})**	**$\Delta\eta_e$ (cm^{-1})**	**ε**
140	584.12	963.98	0.08
1600	20.36	443.99	0.13
3760	11.16	509.98	0.08
5350	6.03	121.92	0.01
7250	5.32	104.07	0.00
		Total ε	**0.30**

As one may notice, the total emissivity at 0.30 is nearly half that of the variable band models (0.50), because here the bands are too narrow, hence the blackbody fractions are too small. As expected, the source terms are even more off than with the regular Modest model (Fig. 4-2-59-a, 4-2-59-b). The fluxes, because of the too small emissivity, are completely underpredicted (Fig. 4-2-59-c, 4-2-59-d), whereas the regular Modest model had at least managed to reproduce the near-boundary values correctly.

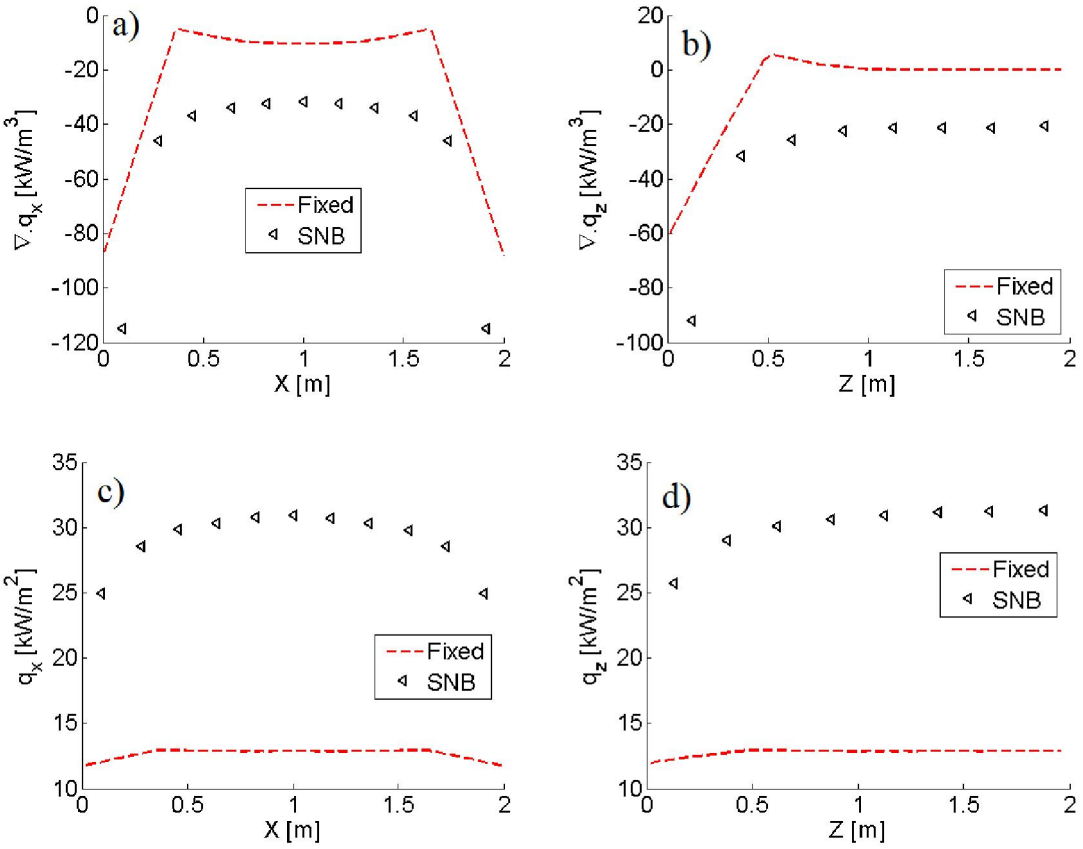

Fig. 4-2-59: Box model vs. SNB from [34], source term along *x* and *z* (top), heat flux along *x* and *z* (bottom) for pure H_2O with $X = 316$ g/m^2

4.2.6.1.4. 1D mixture

The last homogeneous verification test case is the above-described Bressloff [34] mixture as a 1D slab contained between two infinite parallel cold black plates. The upper limit of the 140cm^{-1} band is placed at 582cm^{-1}, which is the lower limit of the 667cm^{-1} band. As visible in Fig. 4-2-60 (left hand side) the far infrared spectrum is slightly different between the fixed and variable models, as in the latter model half of the 667cm^{-1} band of CO_2 overlaps with the 140cm^{-1} rotational band of H_2O. Elsewhere (Fig. 4-2-60, RHS), the 1600 and 2410cm^{-1} have near-identical bandwidths and absorption coefficients, and at the quadruple overlap at 3760cm^{-1}, the absorption coefficient from the fixed bands model appears to be a combined average of the CO_2 and H_2O coefficients of the variable Modest model. The same can be said of the double overlap at 5350cm^{-1}, although that region is less important. One may also note that the emissivity contribution of the pure rotational band is only 7% in this case, hence the difference in bandwidth should not have a massive impact (Table 4-2-14). Given the very similar spectrum of the fixed bands model, it is expected to behave much like the Modest model after overlap correction (see section 4.2.2.3.1). This is very much the case as visible in Fig. 4-2-61, with a near identical total directional intensity of 6 kW/m^2/sr at the end of the path (x = 1m).

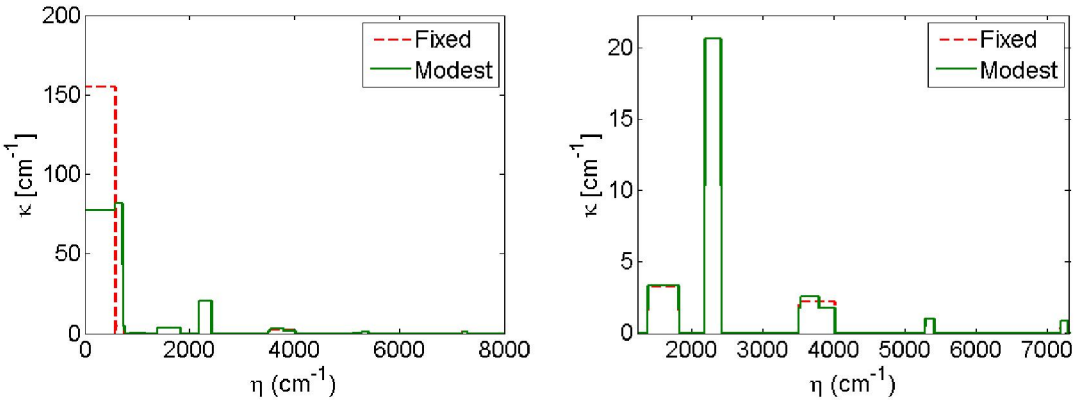

Fig. 4-2-60: Box model absorption spectra of CO_2-H_2O mixture with X_{CO2} = 65.6 g/m^2 and X_{H2O} = 80.1 g/m^2, with (left) and without (right) rotational band at 140cm^{-1}

Table 4-2-14: Absorption coefficients, bandwidths and emissivities for pure H_2O with X_{CO2} = 65.6 g/m^2 and X_{H2O} = 80.1 g/m^2

	Fixed bands model		
Band (cm^{-1})	**κ (m^{-1})**	**$\Delta\eta_e$ (cm^{-1})**	**ε (%)**
140	154.80	581.99	7
667	4.82	169.00	6
1600	3.26	443.99	40
2410	20.60	229.01	21
3760	2.19	509.98	24
5350	0.99	121.92	1
7250	0.85	104.07	0
		Total ε	**0.33**

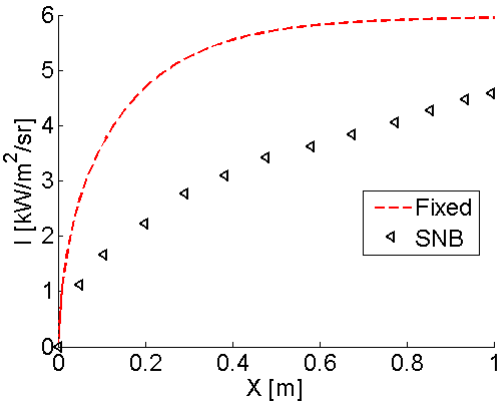

Fig. 4-2-61: Line of sight total intensities for CO_2-H_2O mixture with X_{CO2} = 65.6 g/m^2 and X_{H2O} = 80.1 g/m^2

4.2.6.2. Inhomogeneous media

4.2.6.2.1. 2D pure CO_2

The inhomogeneous, non-isothermal 2D enclosure of Goutiere et al. [35] contains the same medium as described in previous sections. The spectrum obtained from scaled temperature 1295K, scaled mole fraction 0.037, scaled mass path length 10.1 g/m^2 shows slightly broader bandwidths and smaller absorption coefficients than the Modest model (Fig. 4-2-62, Table 4-2-15). Excellent match with SNB solutions is achieved by the fixed bands model for the source term in both directions, as both the boundary effects and the peak at mean beam length are reproduced with a high fidelity (Fig. 4-2-63-a, 4-2-63-b). The agreement for the flux is very good as well with maximum relative errors of 5% and 11% along x and y respectively (Fig. 4-2-63-c, 4-2-63-d).

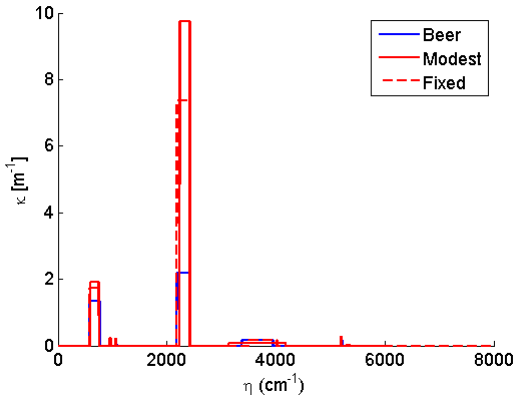

Fig. 4-2-62: Box model absorption spectra of pure CO_2 with X = 10.1 g/m^2

Table 4-2-15: Absorption coefficients, bandwidths and emissivities for pure CO_2 with X_{CO2} = 10.1 g/m^2

	Fixed bands model		
Band (cm^{-1})	**κ (m^{-1})**	**$\Delta\eta_e$ (cm^{-1})**	**E**
667	1.72	169.00	0.01
2410	7.36	229.01	0.05
3660	0.16	509.98	0.01
5200	0.01	121.92	0.00
		Total ε	**0.07**

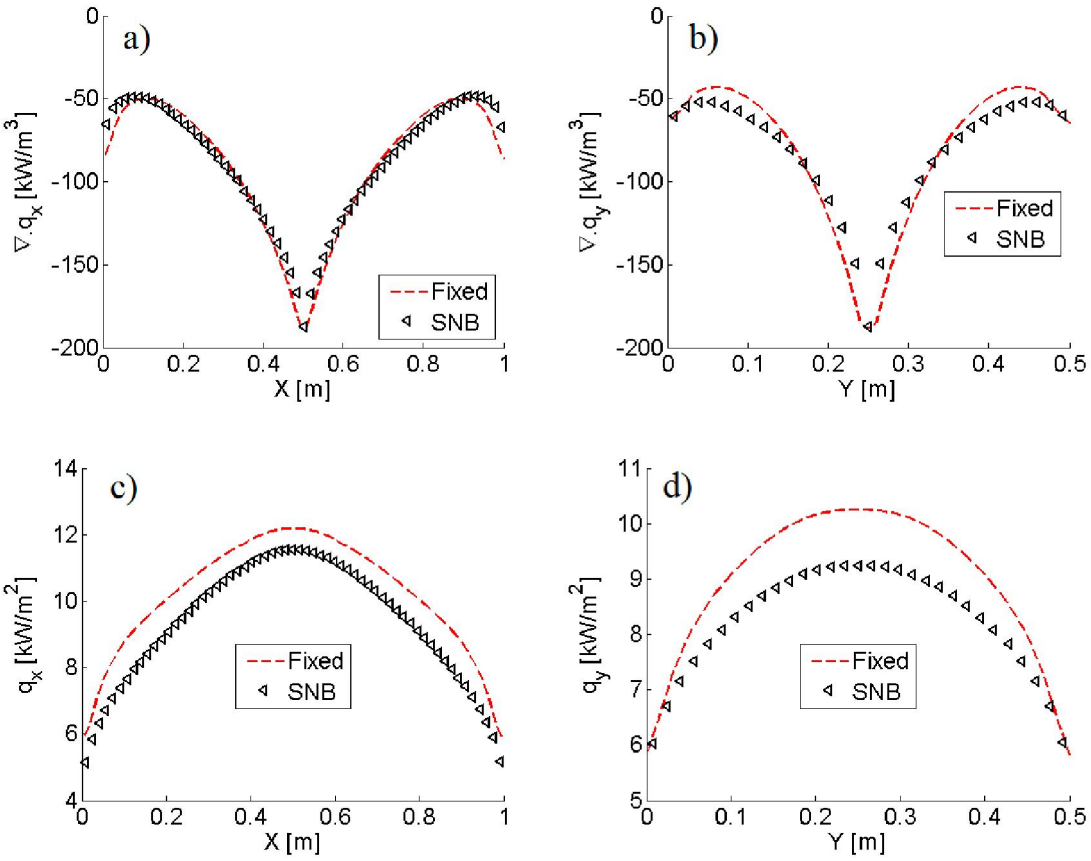

Fig. 4-2-63: Source term along *x* and *y* (top), heat flux along *x* and *y* (bottom) for CO_2 at X_{ave} = 10.1 g/m^2

4.2.6.2.2. 2D pure H_2O

For the inhomogeneous, non-isothermal pure H_2O variant, the 140cm^{-1} band limits of the homogeneous variant cannot be used as it is nearly twice as broad as the width calculated by either of the variable models. It did yield good results for the homogeneous variant because the mass path length in that case is 29 g/m^2, but here the scaled value is much smaller (9.3 g/m^2). As a matter of fact, with the larger bandwidth the total emissivity jumps from 0.09 to 0.13 which is too much (the results are not shown here for clarity, but the flux become grossly overestimated although the source term is somewhat correctly predicted). Hence the bandwidth of 582cm^{-1} is more realistic here, as it yields an equally saturated transmissivity but with a more sensible blackbody fraction. The spectrum information is in Fig. 4-2-64 and Table 4-2-16. For the other important bands like the 1600cm^{-1} and 3760cm^{-1} the fixed band limits are not very different from the other two models.

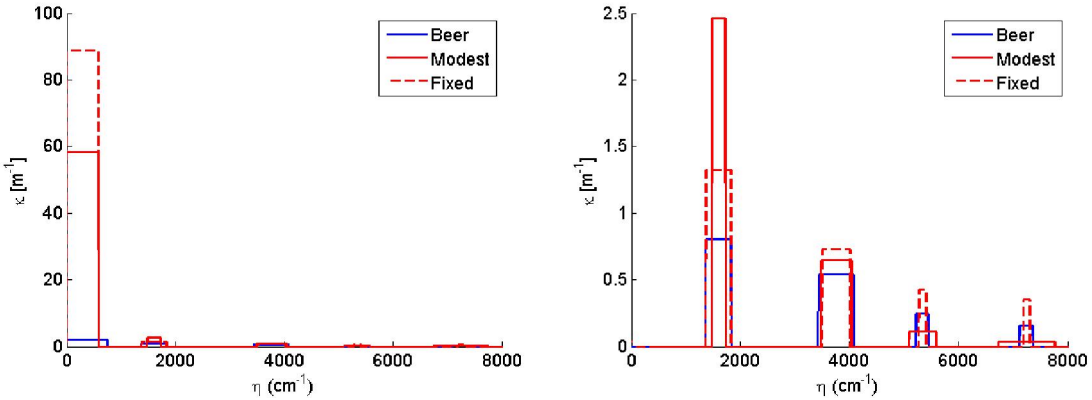

Fig. 4-2-64: Absorption spectrum of pure H_2O with X_{ave} = 9.3 g/m^2, with (left) and without (right) rotational band at 140cm^{-1}

Table 4-2-16: Absorption coefficients, bandwidths and emissivities for pure H_2O with X_{ave} = 9.3 g/m^2

	Fixed bands model		
Band (cm^{-1})	κ (m^{-1})	$\Delta\eta_e$ (cm^{-1})	ε
140	88.43	582	0.01
1600	1.32	443.99	0.05
3760	0.72	509.98	0.04
5350	0.43	121.92	0.00
7250	0.35	104.07	0.00
		Total ε	**0.10**

The inhomogeneous CO_2 case also has a smaller mass path length than the homogeneous one (10 vs 35 g/m^2), but the fixed bands approach worked well and improved both source terms and fluxes. In the present case, however, there is no improvement over the variable band models (Fig. 4-2-65). Since the gradients are rather smooth, it is thus likely that using H_2O bandwidths defined for a mass path length range around 20-30 g/m^2 does not work so well at a much smaller mass path length of 9 g/m^2. This is less of an issue with CO_2 since CO_2 bands are not as prone to pressure-induced line broadening. It is likely that the very slight increase of total emissivity from the Modest model (0.10 vs 0.09), due to the strong 1600cm^{-1} band, is the cause of the flux overprediction along *y* (Fig. 4-2-65-d).

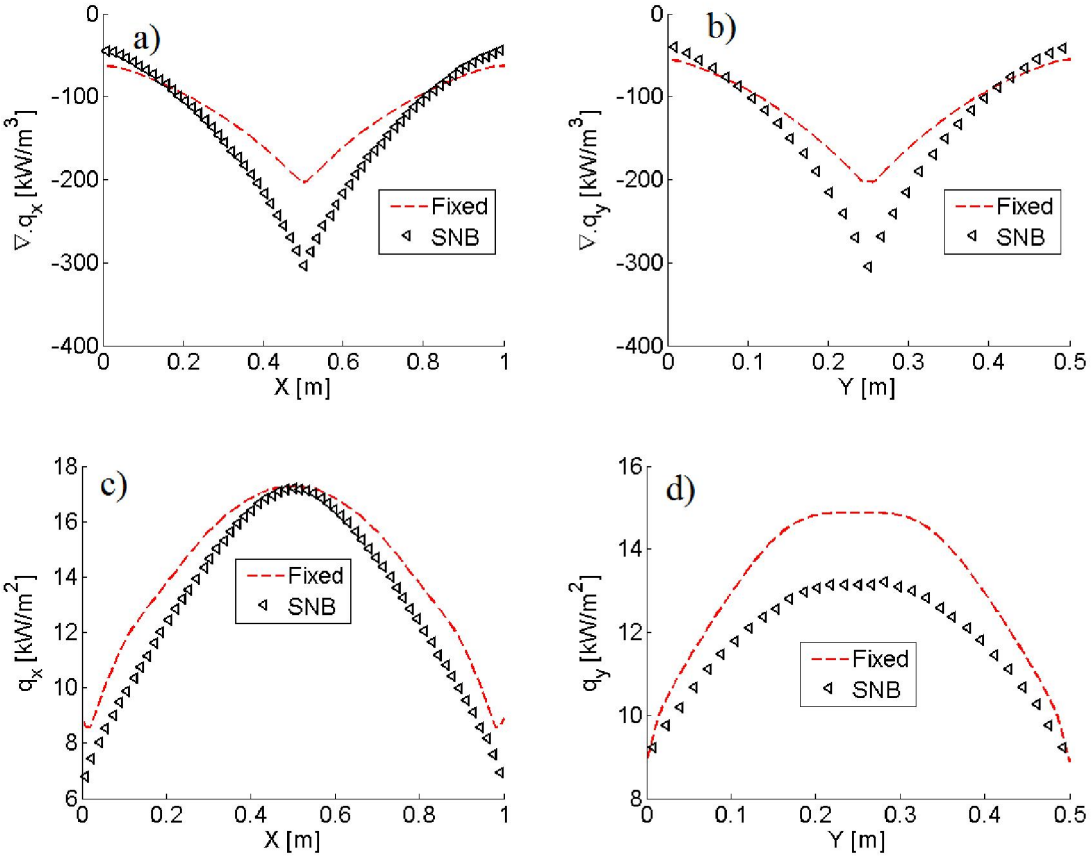

Fig. 4-2-65: Box model vs SNB from [35], source term along *x* and *y* (top), heat flux along *x* and *y* (bottom) for H_2O at X_{ave} = 9.3 g/m^2

4.2.6.2.3. 3D pure H_2O

This inhomogeneous but isothermal scenario yields an average mass path length of 202 g/m^2, which is less than the homogeneous case (316 g/m^2) but Table 4-2-17 shows that the fixed bands model yields the exact same (and much too low) total emissivity. This is of course because the band limits are the same in both cases, and the transmissivities of the important bands tend to zero (the weaker bands may have non null transmissivities, but their blackbody fractions are too small to make a significant difference).

Table 4-2-17: Absorption coefficients, bandwidths and emissivities for pure H_2O with X_{ave} = 202 g/m^2

	Fixed bands model		
Band (cm^{-1})	κ (m^{-1})	$\Delta\eta_e$ (cm^{-1})	ε
140	373.84	963.98	0.08
1600	13.03	443.99	0.13
3760	7.14	509.98	0.08
5350	3.86	121.92	0.01
7250	3.41	104.07	0.00
		Total ε	**0.30**

As a result, the fluxes are the exact same as they were in the homogeneous case (Fig. 4-2-66). Readers may refer to earlier comments to explain the profiles of the source terms.

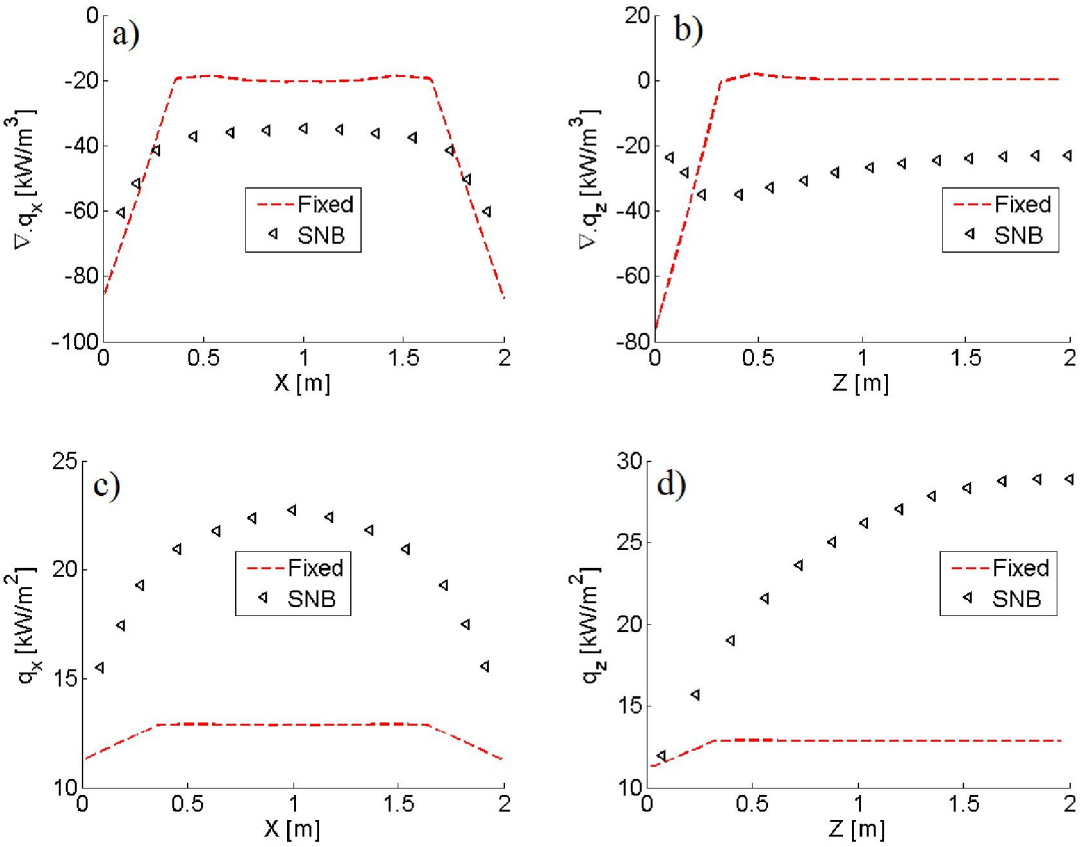

Fig. 4-2-66: Source term along *x* and *z* (top), heat flux along *x* and *z* (bottom) for pure H_2O with X_{ave} = 202 g/m^2

4.2.6.2.4. 2D non-isothermal mixture

Results for Goutiere et al.'s inhomogeneous mixture scenario [35] were not previously shown for the variable band models, as too many potential sources of errors would have been involved between the overlaps and the very sharp gradients in the temperature field. The fixed bands model at least already addresses the overlaps which is one complexity removed, the results from the variable band models will be however shown here for comparison. It may be useful to remember that this scenario was tested in a previous section with WSGG models to very good results, in spite of the strong inhomogeneities in temperature. But WSGG absorption coefficients are formulated in terms of pressure path length, so the optical thickness of one grey gas depends only on the partial pressure of H_2O and CO_2 combined, and the only temperature dependence is in the grey gas coefficient that weighs the emission term. In other words the grey gas optical thickness was constant throughout the enclosure, since the partial pressures are constant. Now with the EWB model, a mass path length where temperature varies independently of the partial pressure undergoes important spatial

variations, rendering the scaling delicate. Fig.4-2-67 below shows the evolution of mass path length along the horizontal and vertical axes of the enclosure.

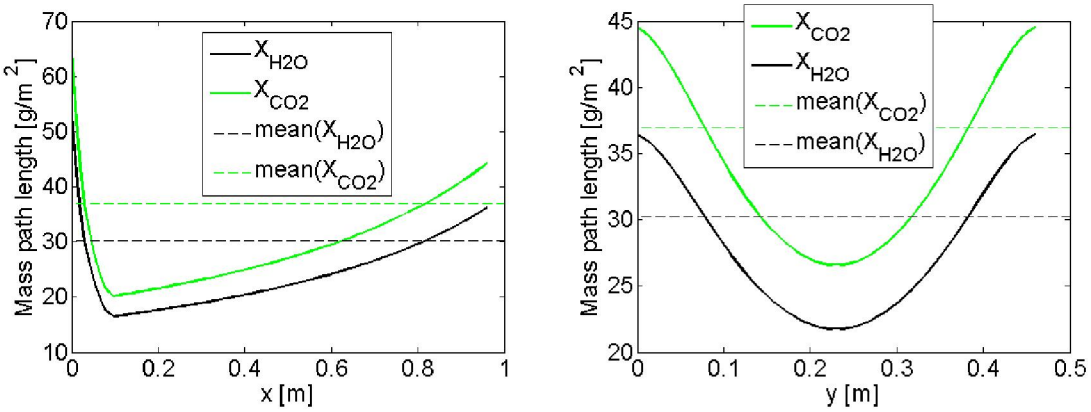

Fig. 4-2-67: For the non-isothermal mixture case from Goutiere et al. [35], evolution of mass path lengths along the horizontal (left) and vertical (right) axes, with scaled values

The averaged parameters are T_{ave} = 1026.86K, $X_{CO2,ave}$ = 36.97 g/m^2 and $X_{H2O,ave}$ = 30.25 g/m^2. It is obvious that the most challenging aspect will be modelling the source term along x, with its sharply plummeting mass path length between 0 and 0.1m (Fig. 4-2-67-LHS). The gradients are much smoother along the central y axis (Fig. 4-2-67-RHS). Fig.4-2-68 and Table 4-2-18 below give data for the absorption spectrum.

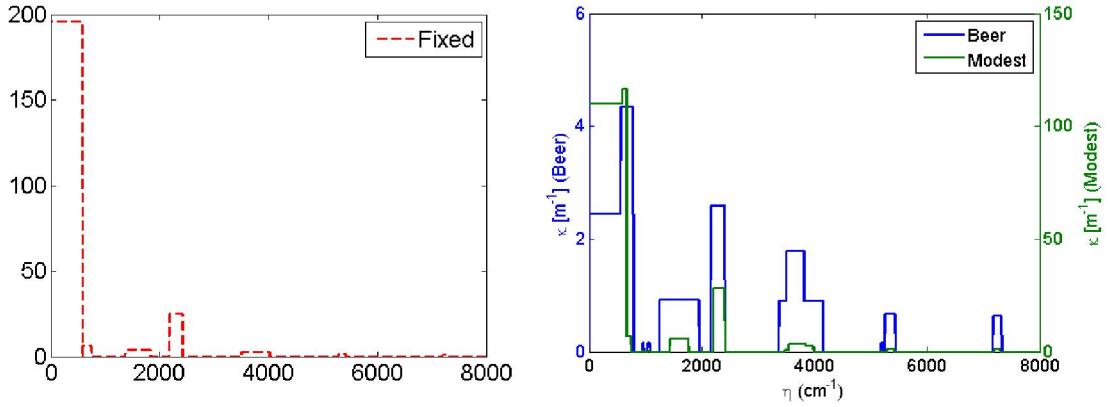

Fig. 4-2-68: Box model absorption spectra of non-isothermal mixture with $X_{CO2,ave}$ = 37 g/m^2 and $X_{H2O,ave}$ = 30g/m^2, with fixed bands model (left) and variable band models (right)

Table 4-2-18: Absorption coefficients, bandwidths and emissivities for nonisothermal mixture with $X_{CO2,ave}$ = 37 g/m^{2}and $X_{H2O,ave}$ = 30g/m^2

	Beer			Modest		
Band (cm^{-1})	κ (m^{-1})	$\Delta\eta_e$ (cm^{-1})	ε	κ (m^{-1})	$\Delta\eta_e$ (cm^{-1})	ε
140	2.44	785.18	0.04	109.66	659.14	0.03
667	1.91	202.80	0.02	6.70	148.03	0.02
960	0.16	31.21	0.00	0.10	47.70	0.00
1060	0.16	31.59	0.00	0.10	48.88	0.00
1600	0.92	694.64	0.09	5.35	328.96	0.09
2410	2.59	247.24	0.06	28.20	203.67	0.06
3660	0.89	304.45	0.02	0.68	373.40	0.02
3760	0.90	775.56	0.06	2.43	438.03	0.06
5200	0.16	30.12	0.00	0.10	44.43	0.00
5350	0.67	179.42	0.00	1.27	113.66	0.00
7250	0.64	149.88	0.00	1.06	102.36	0.00
		Total ε	**0.29**		**Total ε**	**0.28**

Table 4-2-18 (continued)

	Fixed bands model		
Band (cm^{-1})	κ (m^{-1})	$\Delta\eta_e$ (cm^{-1})	ε
140	195.64	581.99	0.02
667	5.87	169.00	0.02
1600	3.96	443.99	0.12
2410	25.08	229.01	0.07
3760	2.67	509.98	0.07
5350	1.22	121.92	0.00
7250	1.04	104.07	0.00
		Total ε	**0.30**

The source term along *x*, where inhomogeneities are the sharpest, is very difficult to reproduce for any model, especially at the peak around -800kW/m^3 which is grossly over predicted by the Modest and fixed bands model especially (Fig. 4-2-69-a). In the less inhomogeneous *y* direction the predictions are far more realistic, albeit still perfectible (Fig. 4-2-69-b). The Beer model is arguably the better one for the source term in both directions, which could be certainly improved further with the appropriate overlap corrections. However the fluxes are completely off in both directions (Fig. 4-2-69-c, 4-2-69-d). The Modest and fixed bands models do better with the fluxes, with a decent match obtained from the fixed bands model along x, but the underprediction remains large (relative error of 30% with SNB model). One may notice that as a whole, it seems difficult to correctly predict both the source term and the flux. The source term essentially includes a balance between an emission term and an absorption term, while the (incident) flux is an intensity multiplied by a solid angle. Since the intensity is the direct solution of the RTE, it may explain why the relative errors on

the flux are generally smaller throughout this study, whereas the source term may carry more potential error sources.

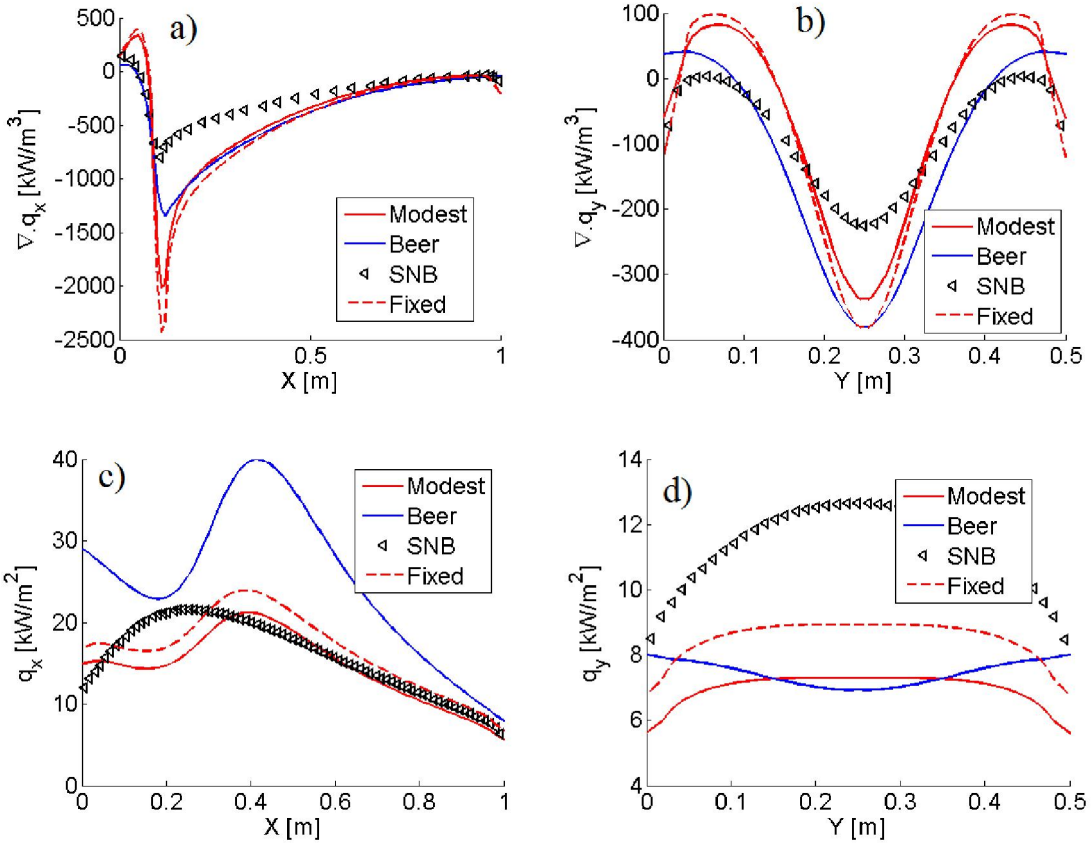

Fig. 4-2-69: Box model vs SNB from [35], source term along *x* and *z* (top), heat flux along *x* and *z* (bottom) for nonisothermal mixture with $X_{CO2,ave}$ = 37 g/m^2 and $X_{H2O,ave}$ = 30 g/m^2

It is difficult to find reasons for the overall poor box model performance in this scenario, other than the sharpness of the temperature gradients. For these canonical radiation scenarios, it was essential to use the same grids as those of the reference works for optimal comparison. Some additional tests with grid refinements were carried out, which did show some effect with the inhomogeneous scenarios, but as no clear trend emerged they were not included in this thesis. On another hand, the sensitivity analysis of the previous section has shown that it will be unlikely to encounter such situations in pool fires, whose conditions are closer to the Bressloff scenario, which provided the benchmark spectrum for the fixed bands model. The next section aims at confirming such hypotheses.

4.2.7. Box model for pool fires

4.2.7.1. Flame volume-based scaling method

Previously with the pure radiation cases, obtaining the scaled temperature and mass path length was a straight-forward process, since the source filled an entire enclosure each time and no mesh decomposition was required. Fire simulations are different as the computational

domains can be a few times larger than the flame they contain (to ensure no boundary effects will impact the flow field, and to allow comparisons of the radiation field against the reference measurements). An averaging based on the whole domain is obviously wrong, as it takes into account a large amount of transparent areas where temperature elevation and mass fractions of H_2O and CO_2 are negligible, resulting in very low radiation throughout the domain. The proposed alternative is to consider a flame zone as a group of "hot" computational cells, over which the temperature and density of each species are averaged, so that the "cold" cells are treated as transparent. The "hot" and "cold" cells are segregated by a temperature threshold, which is obtained from e.g. a prior simulation at steady state. The ratio of hot cells to total grid size can then be correlated to a mean beam length determined from e.g. the integral length scale from Eq. 4.2.1. This technique ensures that for any transient flame shape the temperature and densities are always averaged over the correct number of cells (Fig. 4-2-70).

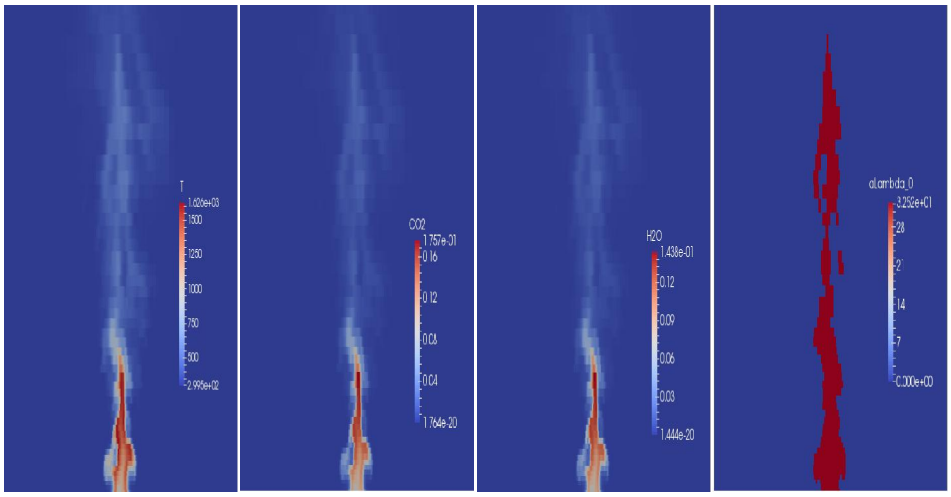

Fig. 4-2-70: Left to right, transient temperature, CO_2 and H_2O mass fractions, absorption coefficient from scaled parameters and flame volume based on temperature elevation method

As an example let us consider a 20kW methanol fire, simulated in a cylindrical domain of dimensions 82.5 (R) x 180 (H) cm. We may estimate a mean beam length S of the total grid domain as $S_{cylinder} = 3.6V/A$, and the mean beam length of the flame as the integral length scale, which for this fire yields $S_{flame} = 20$cm. Thus we get:

$S_{cylinder} = 3.6V_{cylinder}/A_{cylinder} = 3.6 \times (1.8\ \pi\ 0.825^2) / (2\ \pi\ 0.825^2 + 2\ \pi\ 0.825 \times 1.8) = 1.0183$ m

We know that $S_{flame} = 0.20$ m, hence the ratio:

$S_{flame}/S_{cylinder} \sim N_{hot\ cells}/N_{cold\ cells} \sim 20\%$

Which in this case is roughly obtained with a temperature elevation threshold of 150K. In other words everything over 450K is treated as absorbing, and everything below is considered transparent. The average steady state temperature in the flame is 846K. With an elevation threshold of 100K, the flame volume would occupy around 30% of the domain and the

average temperature is 738K, and with 50K it becomes 40% and 635K. For each of these three scenarios the scaled parameters are as follows:

a) T=635K, p_{CO2} = 0.015atm, p_{H2O} = 0.031atm, S_{flame} = 0.40m, X_{CO2} = 5 g/m^2, X_{H2O} = 4 g/m^2

b) T=738K, p_{CO2} = 0.02atm, p_{H2O} = 0.04atm, S_{flame} = 0.29m, X_{CO2} = 4.2 g/m^2, X_{H2O} = 3.5 g/m^2

c) T=846K, p_{CO2} = 0.03atm, p_{H2O} = 0.06atm, S_{flame} = 0.20m, X_{CO2} = 3.8 g/m^2, X_{H2O} = 3.1 g/m^2

These values are well within the working range we established for the fixed bands box model. Fig. 4-2-71 to 4-2-73 and Table 4-2-19 to 4-2-21 give the spectral information for these three scenarios:

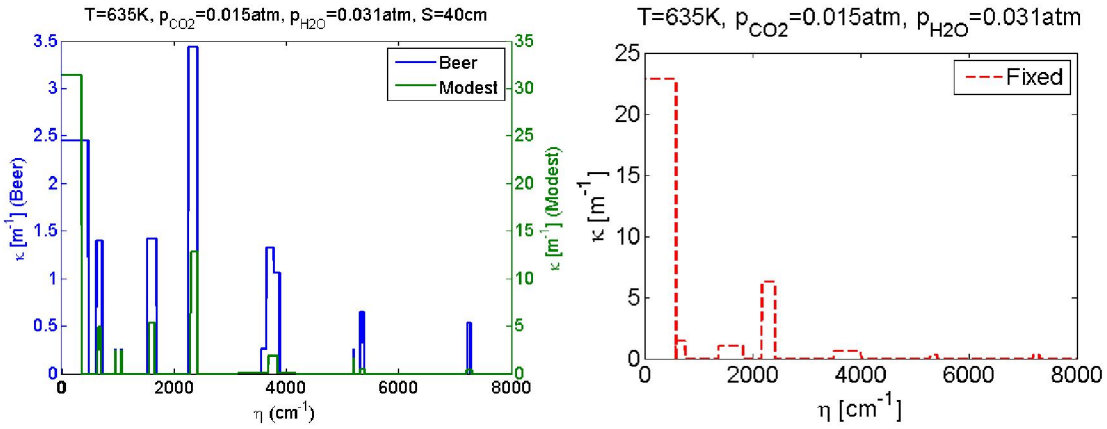

Fig. 4-2-71: Box model absorption spectra of 20kW methanol flame, scaled at 40% of the total volume

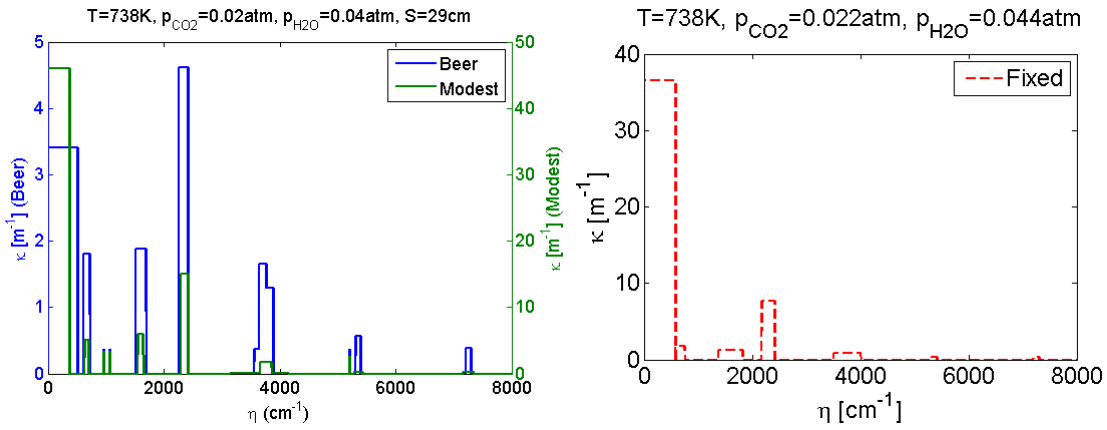

Fig. 4-2-72: Box model absorption spectra of 20kW methanol flame, scaled at 30% of the total volume

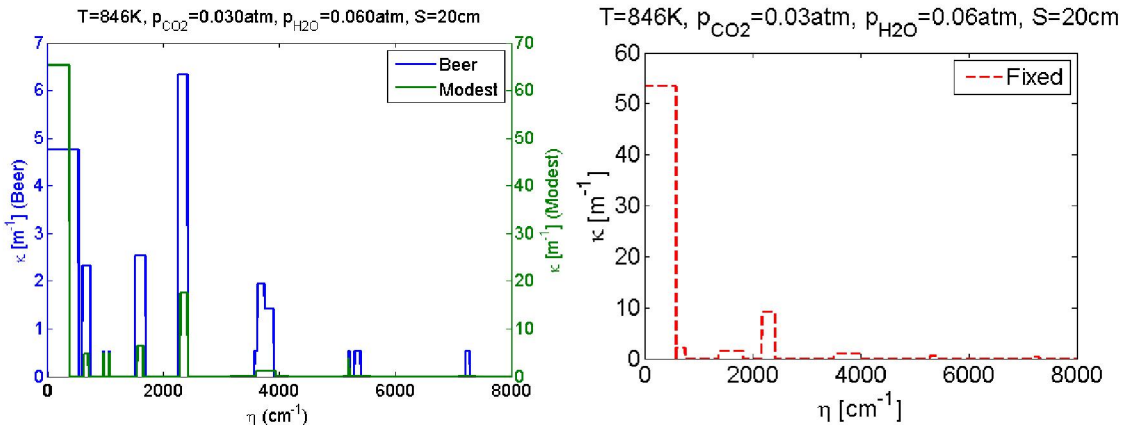

Fig. 4-2-73: Box model absorption spectra of 20kW methanol flame, scaled at 20% of the total volume

Table 4-2-19: Absorption coefficients, bandwidths and emissivities of 30cm methanol flame, scaled at 40% of the total volume

	Beer				Modest				Fixed			
Band (cm^{-1})	**κ (m^{-1})**	**$\Delta\eta_e$ (cm^{-1})**	**ε**	**ε (%)**	**κ (m^{-1})**	**$\Delta\eta_e$ (cm^{-1})**	**ε**	**ε (%)**	**κ (m^{-1})**	**$\Delta\eta_e$ (cm^{-1})**	**ε**	**ε (%)**
140	2.45	680.13	0.03	24.75	31.31	424.65	0.02	19.10	22.85	581.99	0.07	31.16
667	1.40	100.86	0.01	13.58	4.93	50.10	0.01	14.68	1.46	169.00	0.03	11.39
960	0.26	1.55	0.00	0.07	2.50	0.16	0.00	0.05				0.00
1060	0.26	1.56	0.00	0.07	2.50	0.16	0.00	0.05				0.00
1600	1.42	168.23	0.03	30.59	5.33	82.70	0.03	33.12	0.99	443.99	0.07	29.48
2410	3.43	149.00	0.03	26.83	12.79	111.78	0.03	28.49	6.24	229.01	0.06	25.65
3660	0.26	219.14	0.00	1.01	0.05	1022.00	0.00	1.17				0.00
3760	1.06	222.43	0.00	3.07	1.74	153.02	0.00	3.31	0.65	509.98	0.01	2.30
5200	0.26	3.45	0.00	0.00	1.58	0.54	0.00	0.00				0.00
5350	0.65	52.94	0.00	0.04	0.50	65.47	0.00	0.04	0.28	121.92	0.00	0.02
7250	0.54	52.16	0.00	0.00	0.35	76.49	0.00	0.00	0.26	104.07	0.00	0.00
		ε total	0.11			ε total	0.10			ε total	0.22	

Table 4-2-20: Absorption coefficients, bandwidths and emissivities of 30cm methanol flame, scaled at 30% of the total volume

	Beer				Modest				Fixed			
Band (cm^{-1})	κ (m^{-1})	$\Delta\eta_e$ (cm^{-1})	ε	ε (%)	κ (m^{-1})	$\Delta\eta_e$ (cm^{-1})	ε	ε (%)	κ (m^{-1})	$\Delta\eta_e$ (cm^{-1})	ε	ε (%)
140	3.41	736.00	0.02	19.77	45.97	462.13	0.01	14.64	36.50	581.99	0.05	24.88
667	1.80	115.25	0.01	10.80	5.00	61.21	0.01	11.55	1.81	169.00	0.02	8.85
960	0.36	2.09	0.00	0.07	3.45	0.21	0.00	0.05				0.00
1060	0.36	2.11	0.00	0.08	3.45	0.21	0.00	0.05				0.00
1600	1.88	177.16	0.03	29.24	6.04	90.11	0.03	31.30	1.22	443.99	0.06	28.86
2410	4.62	157.42	0.04	32.78	15.06	117.60	0.03	34.59	7.73	229.01	0.06	33.00
3660	0.36	202.97	0.00	1.65	0.07	1020.39	0.00	1.82				0.00
3760	1.29	243.01	0.01	5.50	1.66	197.97	0.01	5.87	0.81	509.98	0.01	4.35
5200	0.36	3.28	0.00	0.00	2.64	0.43	0.00	0.00				0.00
5350	0.57	76.09	0.00	0.11	0.29	142.98	0.00	0.12	0.35	121.92	0.00	0.06
7250	0.38	89.49	0.00	0.01	0.17	193.43	0.00	0.01	0.32	104.07	0.00	0.00
		ε total	0.11			ε total	0.10			ε total	0.19	

Table 4-2-21: Absorption coefficients, bandwidths and emissivities of 30cm methanol flame, scaled at 20% of the total volume

	Beer				Modest				Fixed			
Band (cm^{-1})	κ (m^{-1})	$\Delta\eta_e$ (cm^{-1})	ε	ε (%)	κ (m^{-1})	$\Delta\eta_e$ (cm^{-1})	ε	ε (%)	κ (m^{-1})	$\Delta\eta_e$ (cm^{-1})	ε	ε (%)
140	4.75	776.34	0.02	16.33	65.19	476.15	0.01	11.51	53.34	581.99	0.03	20.49
667	2.32	127.03	0.01	8.69	4.64	77.73	0.01	9.22	2.14	169.00	0.01	6.97
960	0.53	2.33	0.00	0.07	5.00	0.23	0.00	0.04				0.00
1060	0.53	2.35	0.00	0.07	5.00	0.24	0.00	0.05				0.00
1600	2.54	180.48	0.03	27.15	6.45	99.07	0.03	28.85	1.44	443.99	0.04	26.99
2410	6.34	161.05	0.04	37.20	17.53	119.20	0.04	39.14	9.13	229.01	0.06	38.61
3660	0.53	171.61	0.00	2.19	0.08	1017.25	0.00	2.36				0.00
3760	1.42	279.39	0.01	8.06	1.17	329.13	0.01	8.56	0.96	509.98	0.01	6.78
5200	0.53	2.87	0.00	0.01	3.71	0.39	0.00	0.01				0.00
5350	0.53	99.77	0.00	0.22	0.10	494.40	0.00	0.24	0.42	121.92	0.00	0.14
7250	0.53	77.79	0.00	0.02	0.13	300.00	0.00	0.02	0.37	104.07	0.00	0.01
		ε total	0.10			ε total	0.09			ε total	0.16	

With the variable band limits models, there is very little change in the total emissivities between the three scenarios. Indeed, if longer path lengths do increase the optical depth of each band, the lower mole fractions and temperatures make for relatively smaller absorption coefficients and narrower bands. However the absorption coefficients and bandwidths of the fixed bands model are insensitive to path length. In the first scenario where S = 40cm (Fig. 4-2-73, Table 4-2-18), the bandwidths are in stark contrast between the fixed and variable band models - much wider for the fixed bands model, which is responsible for large blackbody fractions, which results in a total emissivity more than twice that of the other two models. The pure rotational band at 140cm^{-1} seems instrumental in the fixed bands model as its emissivity

varies much between the three scenarios. In any case the two most important bands are the 2410cm^{-1} of CO_2 and the 1600cm^{-1} of H_2O which always contribute the most to total emissivity (30-40% each). These are not the optically thickest (that is the prerogative of the pure rotational band 140cm^{-1}) but their spectral locations ensure large blackbody fractions, hence bandwidth of these bands is particularly sensitive. In the fixed bands model these are much wider (2-3 times) than in the other two models which results in emissivities about 1.5 times larger. Their contributions to total emissivity are however in competition with the 140cm^{-1} band (in the fixed bands model, much less so in the other two). The third scenario was retained for the methanol fire simulations of Chapter 5.

4.2.7.2. Spectral modelling of 30cm methanol and heptane fires with the box models

Here we want to check that the runtime scaled parameters match the pre-calculations of the previous paragraph. Firstly, it appears that the flame volume-averaged temperature and CO_2-H_2O densities do not vary much over time, hence further justifying fewer radiation updates during the CFD simulation. After the initial transient phase, the scaled parameters are not only stable over time (Figure 4-2-74) but also very close to the pre-calculated values from absorption scenario #3 above, e.g. T = 832K (respectively 846K), ρ_{CO2} = 18.5 g/m^3(respectively 19 g/m^3) and ρ_{H2O} = 15.1 g/m^3 (respectively 15.5 g/m^3). The transient minima/maxima are T = 733/962K, ρ_{CO2} = 16.9/20.6 g/m^3 and ρ_{H2O} = 13.9/16.8 g/m^3. During the simulation radiation was updated every 20 time steps but it seems the frequency could have been reduced even further. Hence both the scaling approximation and the method used to calculate the flame volume seem well appropriate.

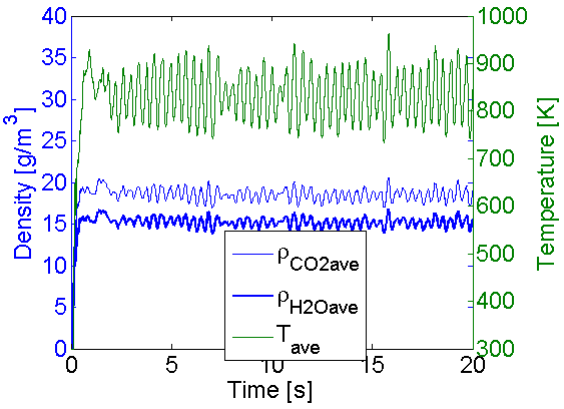

Fig. 4-2-74: Evolution of scaled temperature and densities over time in the simulated 30cm methanol fire

A second test with a 116kW heptane fire was run. Using the integral length scale as a mean beam length we get a value of 41cm for the flame zone. The temperature threshold that yields the correct ratio of hot cells to cold cells is 100K, which we evaluated like previously from a pre-existing stabilised simulation. The time mean soot absorption coefficient is simply obtained as $k_{soot} = C_s T_{mean} f v_{mean}$. The spatial distribution of k_{soot} somewhat blends that of the soot volume fraction *fv* and that of temperature, with the centreline peak being located at *z* = 68cm (Fig. 4-2-75, left), which is between the soot fraction peak (*z* = 72cm) and the

temperature peak (z = 43cm). The maximum value of the grey soot absorption coefficient is 2.69 m^{-1}. Given the value differences between box model absorption coefficients, some bands will be more affected than others by the presence of soot. On Fig.4-2-75 (right) the different regions of the fire are also easily identifiable by looking at the time-averaged absorption coefficients. The very straight lines in the lower region of the fire means that absorption does not vary with time - this is where the flame is continuous, roughly between just above the pool surface and z = 53cm (height determined from the McCaffrey method with the theoretical heat release rate). In the intermittent zone, absorption starts decreasing then slumps towards zero just past the measured flame tip at z = 1.31m. The point of this example is thus to show that although the transient absorption coefficients are uniform due to the scaling we use, they end up adopting the steady state flame shape when averaged over enough time.

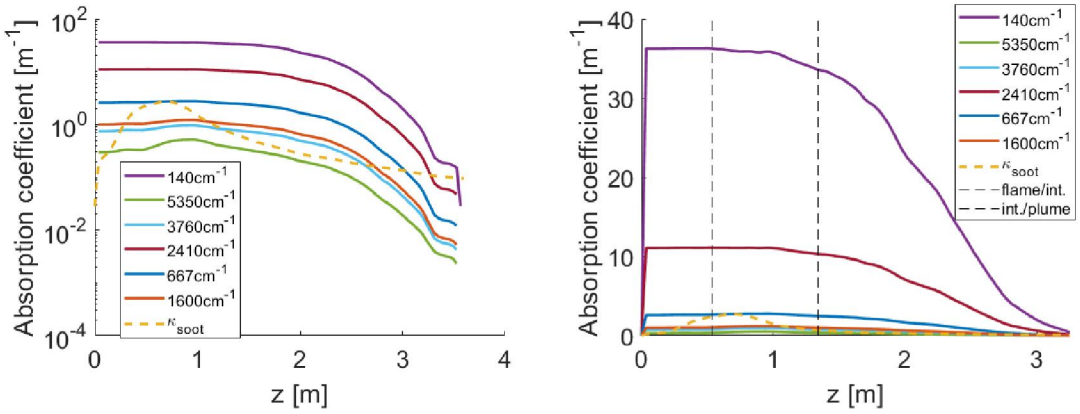

Fig. 4-2-75: Box model absorption coefficients in a steady state 116kW heptane flame

4.2.8. Summary

The crucial difference between the "Beer" and "Modest" box models resides in where along a line of sight (optical path) the absorption coefficient is evaluated. The Beer model takes the absorption coefficient at the mean beam length, e.g. $S = 3.6V/A$, and the Modest model at the optically thin limit i.e. $S \rightarrow 0$. This results in very different treatments of the strong bands of CO_2 and H_2O. With the Modest model the absorption coefficients are usually at least one order of magnitude larger than with the Beer model, which means these strong bands get optically thick at smaller path lengths. The detailed analysis of various pure radiation scenarios showed that for reasonably diluted gases, the Modest approach was almost systematically better than the Beer approach. The Beer model becomes interesting only at larger mass path lengths, e.g. 200 or 300 g/m^2 (which are never encountered in pool fires): indeed the Modest model becomes inappropriate as every band becomes infinitely thick (quasi null transmissivities), which translates to very underestimated fluxes and source terms. Hence the rendition of the optical thickness of individual bands really is the only major difference between the two models, as the emissivities are always essentially the same. As for performance, the Modest model was generally better at reasonable CO_2 and H_2O mass path length ranges e.g. 5-40 g/m^2, which is roughly the range of pool fires (mass path length is relatively independent of heat release rate).

On the issue of band limits, CO_2-H_2O mixtures very often produce interspecies band overlaps, e.g. around 3700cm^{-1} and 5300cm^{-1}. This justifies the need for a box model with fixed band limits, as manual overlap corrections are impractical. It is better to define one band whose limits encompass two or more overlapping bands, hence saving computational time in the process. With the help of the emissivity analysis, confirmed by mixture test cases, some of the weaker bands are also eliminated to save more CPU time. The fixed bands model is based on the Modest method in light of the performance analysis. It is tested with the same series of test cases as the variable bands models and proves robust enough to work for most of these scenarios, often actually better than the variable band models.

On the issue of gas inhomogeneities, the scaling approach works for media with reasonable spatial variations but may be very off if mass path length varies too sharply, as the averaged mass path length is stretched too far from either its maximum or minimum. In pool fires the gradients are rather smooth, hence the approach proves valid. To scale the parameters in a pool fire, the earlier method based on grid subdomains was dropped, as it created a dependence over mesh decomposition. A new method based on flame volume was successfully tested in a 30cm methanol fire. Calculated during simulation runtime, the flame volume is defined as the ensemble of computational cells where temperature elevation is above a certain threshold. The absorption coefficient (and corresponding blackbody fraction) has the same constant value in the "hot" cells, and is zero elsewhere. The temperature elevation threshold is chosen so that the fraction of hot cells in the domain yields the correct mean beam length, which is estimated as the integral length scale (other methods are possible but give more or less similar values). The scaled temperature and scaled CO_2 and H_2O densities do not vary much over time during the simulation, confirming the robustness of the approach.

Chapter 5 - Results and discussion (pool fire cases)

5.1. Introduction and objectives

Unlike with the canonical pure radiation scenarios seen in previous sections, the goal of this analysis of thermal radiation in LES-simulated pool fires is not to get the predicted radiant fluxes to match the experimental values as closely as possible. A number of reasons motivate such a statement. First, there is too much potential error introduced by the flame structure prediction (even if only the steady state is considered) as well as the transducer measurements of the reference works. Several research teams have bypassed that problem by reconstructing synthetic pool fires from empirical correlations, which enables radiation calculations in a decoupled manner (e.g. [6] or [61]). Since the flow field is not resolved, the computational effort is also far lighter, and it becomes possible to employ detailed radiation solvers and gas property models (MCRT, Narrow-Band...) to generate one's own benchmarks. While the correlations do not eliminate 100 percent of the errors in the flow field (temperatures and/or soot concentrations can be seen to deviate slightly away from the centreline), this is evidently a very convenient approach for radiation scientists. But it is less desirable for CFD engineers wanting to simulate e.g. a fire spread over a few minutes with a radiation modelling capability less crude than the usual grey approximations. No such attempts were yet made with this work, mostly because of the lack of reference data. This work intends to serve more as a bridge for the knowledge gap between canonical/synthetic fire scenarios and such practical fire engineering applications. The study of pool fires at steady state is particularly interesting here because of the experimental data available from e.g. Klassen and Gore [4]. Hence, the comparison between the predicted radiant flux and the measured ones may be regarded here as qualitative, and the performance analysis shall be restricted to outlining clear trends in each case. Another reason for this is that some of the simulation parameters required calibration, and with the computational effort involved this was best performed with an arbitrary gas property model. This process biases the results in favour of that one property model, thus rendering a quantitative comparison against experiments somewhat irrelevant, but the approach is however valid for comparing the gas property models between themselves in terms of relative differences. Due to the flow field being resolved, chances are that these gas property models (grey/banded WSGG and box models) may behave differently in a "real" fire simulation, compared with canonical cases or synthetic fires. Such a study has not yet been undertaken to the best knowledge of this author, and it is thus believed that the results of this work will provide a valuable step towards more practical fire engineering scenarios such as the example above.

The benchmark data for this work are taken from the experiments of Klassen and Gore [4] who measured temperature, soot volume fractions and radiative heat transfer in pool fires of different fuels and sizes. Their data for the soot-free 30cm methanol fire (heat release rate 20kW, flame height 50cm) provides an ideal ground for a comparative study of gas phase radiation models such as the WSGG and the EWB-box model, whereas the moderately-sooting heptane fire (HRR 116kW, flame height 131cm) is useful for assessing the coupling those models with a grey soot phase. The flux was measured both radially at the pool surface

(r, z = 0) and vertically (r = 82.5cm, z), where the origin (r = *0*, z = *0*) is the centre of the pool surface. The reference temperature and velocity data for the 30cm methanol fire are taken from Weckman and Strong [85], whose experimental setup is close to that of [4]. Temperatures for fires of different diameters/HRR may be compared using the scaling technique of McCaffrey [86], although the difference is only a few kilowatts between [4] and [85]. The 1cm wider burner in [85] is not expected to have any visible influence. The taller burner lip height of [4] was initially reproduced in early simulations, but eventually was dropped for its lack of impact on the predicted flame structure. For the transducer measurements of the radiant heat flux, Klassen and Gore report an uncertainty inferior to ±15% at flame steady state [4].

The working steps for this study were as follows. First, grid tests were run until the time-mean centreline temperature and velocity profiles converged with one another and agreed well enough with the measurements of [85]. After finding an appropriate grid size, the second step was to calibrate the TRI parameters with a default gas radiation model (for convenience, the Smith WSGG henceforth), with successive simulations until the total radiant fraction (Xr) agreed with the experimental data of [4]. Thus, for the comparisons of radiant heat fluxes, six final simulations were run comprising the two grey and three banded WSGG models and the EWB-box model. For clarity, the models will be referred to as "WSGG Smith", "WSGG Cassol", "WSGG Johansson" for the banded WSGG solutions, and "Grey Smith", "Grey Cassol" (grey WSGG solutions) and "Box Fixed-Bands". The grey WSGG calculations were based on the total emissivity calculations from a mean beam length (MBL). The integral length scale was used for MBL calculations, i.e. $S = \left(Q/T_\infty \rho_\infty Cp_\infty \sqrt{g}\right)^{0.4}$, instead of the more usual correlation $S = 3.6V/A$, because the volume and area of the flame zone may be difficult to estimate from e.g. cylindrical or conical approximations of the actual flame shape.

Each simulation was run for 30 seconds, with time-averaging starting after 8 seconds, long after the flame has developed to its full scale. The domain is an O-grid based cylinder of radius R = 82.5cm and height H = 1.2m (respectively 2m for heptane), with grid nodes clustering towards the fuel inlet at the bottom (pool centre at r = 0, z = 0). The heat release rate is not a prescribed input parameter, but controlled by the user-specified mass flow rate. Hence in this work the correct HRR is obtained by feeding the fuel inlet at a constant methanol mass flow rate of 0.1069g/s (respectively 2.56g/s for heptane) at boiling point temperature, i.e. 338K (respectively 372K for heptane). One may note that physically speaking those are liquid fuels, treated as surface boundaries in the simulation, hence only the gas phase is being resolved (no need for pyrolysis modelling unlike with solid fuels). Ignition is immediate, as ensured by the infinitely fast chemistry LES-EDC model, and the combustion reaction is driven by a single equation. The other boundaries are open, set to 300K and all are black. Detailed LES parameters may be found in [23,59,80] for the same fuels.

5.2. Simulation parameters and CPU times

Radiation parameters were set for maximum CPU efficiency as follows: maximum number of solver iterations = 1 (not to be mistaken with FVM iterations on each RTE solution), convergence criterion = 10^{-4}, solver frequency = every 30 time steps. A preliminary study showed that the non-scattering RTE converges easily (3-4 iterations out of a possible 1000), being a simple 1st order difference equation with constant member (the emission term can be considered as such because it only depends on cell temperature, which is always known from the last energy equation solution), thus much CPU time can be saved by minimising the solver iterations. Besides, radiation propagates at light speed, and with a constant time step of 5.10^{-4} seconds the flame structure does not change significantly enough to justify a radiation update at every time step (frequency is set to 30 time steps instead). The key criterion for CPU cost is without doubt the number of FVM solid angles, which was set to 600 for radiant flux calculations based on some preliminary simulations. Such a number was necessary to reduce the strong ray effects caused by the high ratio of total domain and pool radiuses, R/R_0 = 5.5. For e.g. the Cassol or Johansson WSGG (5 RTE solutions per angle) this amounts to 3,000 solutions every radiation update - careful selection of solver iterations and frequency of update are thus crucial. Table 5-1 gives the computational times from each radiation model. The WSGG models being mathematically simple, not much can be done to speed up calculations. The fixed bands box model, despite using 2-3 more bands and being mathematically more involved, holds the comparison with the WSGGs, being roughly 1.3 times slower than a 5-band WSGG. One may also note that using a smaller number of solid angles would reduce the differences between all models, as it is not the actual absorption coefficient calculations that take so much time as the solution of many RTE's.

Table 5-1: CPU times of 30cm methanol fire simulations (0 to 30s) with 600 solid angles for the various gas radiation models studied

Radiation model	Number of bands	CPU time
Grey Smith	1	(ref.)
Grey Cassol	1	x1.1
WSGG Smith	4	x2.9
WSGG Cassol or Johansson	5	x3.4
Box model "Fixed Bands"	7	x4.3

5.3. Large eddy simulations of 30cm methanol fires

5.3.1. Grid independence and effect on temperature prediction

Five grids were tested, of respective smallest cell sizes (in millimetres): 11.6, 10.1, 9.3, 8.5, 8.0mm, labelled "grid #1" (coarsest) to "grid #5" (finest). The default gas radiation model for these runs is the WSGG Smith. Apparent grid independence was achieved by grid #3, since #4 and #5 yielded very similar mean temperature and velocity profiles (Fig. 5-1), hence for the rest of this study grid #3 is used. In the continuous flame zone ($z/Q^{0.4} < 0.08$), simulated temperatures are between the McCaffrey model correlations and Weckman and Strong's measurements, some 100K from either baseline. This result is not surprising as other FireFOAM contributors reported the same trend in [18,80], interpreting the underpredictive trend in lower regions as an intrinsic limitation of the combustion model due to relatively low Reynolds numbers at the bottom of the flame. The upper regions (intermittent flame and thermal plume) agree quite well with the experimental data points and should be accurate enough for the subsequent radiative flux comparisons. Radial temperature profiles for grid#3 and subsequent also show good overall agreement (Fig. 5-2), despite the fact that temperatures drop quicker than they should away from the central axis ("necking" phenomenon).

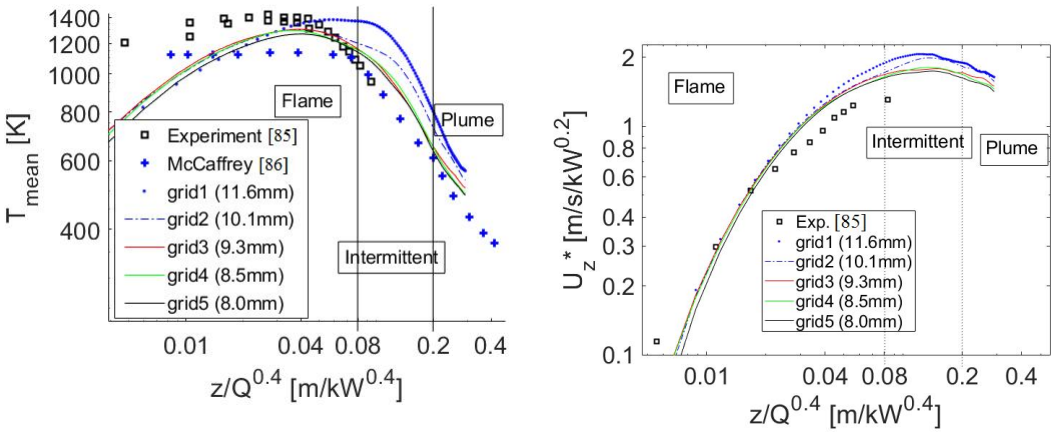

Fig. 5-1: Grid sensitivity of centreline mean temperature and velocity (30cm methanol fire)

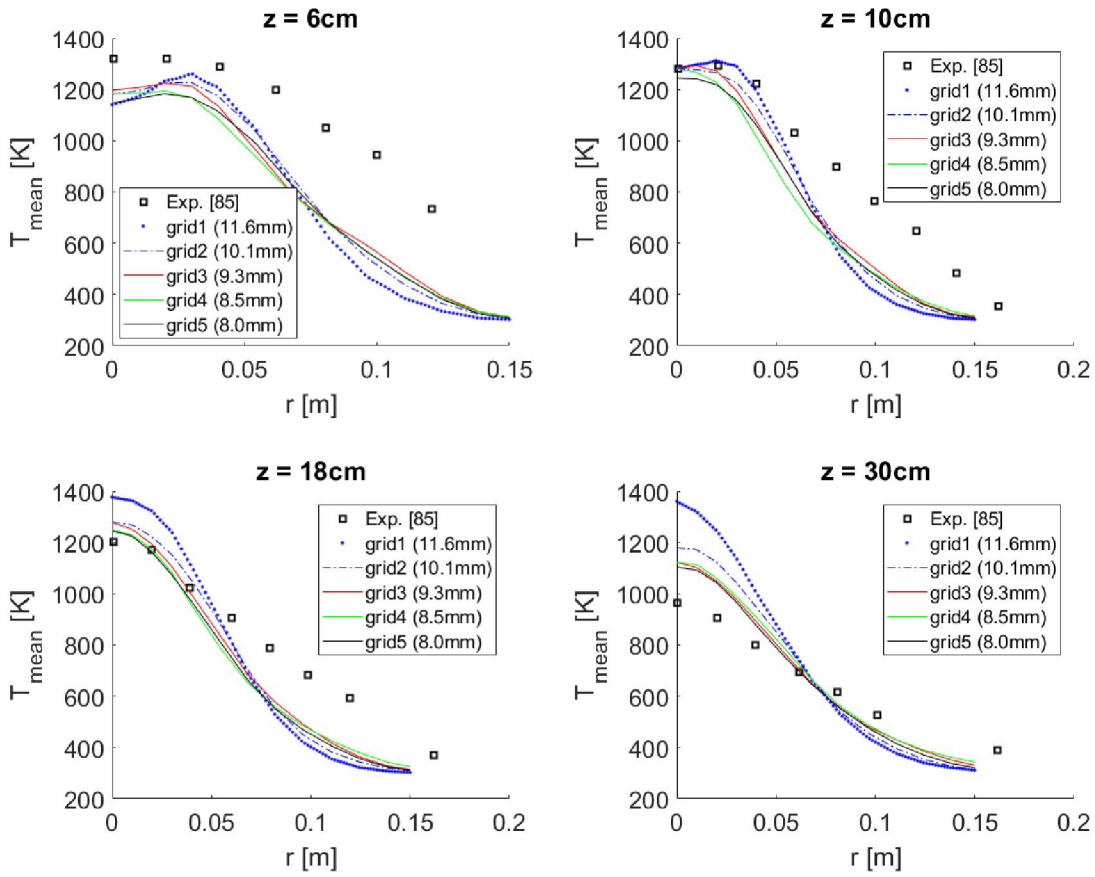

Fig. 5-2: Grid sensitivity of radial temperature at different elevations from pool (z = 0) (30cm methanol fire)

5.3.2. Influence of TRI parameters

The TRI parameters C and C_{TRI} appear in Eq. (3.95) and Eq. (3.96). A trivial combination of these equations shows that radiation calculations are driven by the product C x C_{TRI}. After some trial and error, it was found that the right radiation fraction was likely to be obtained with C x $C_{TRI} \sim 3.5$ (Fig. 5-3). Besides, one may note that the correlation is almost linear. The calibration was done with the Smith WSGG, which somewhat biases the comparative study in favour of that model, hence why the relative differences are more interesting here, although the other models turned out to behave very closely as a whole. On another hand, only C plays a role in the modelled component of T_{RMS}. Fellow FireFOAM workers used $C \sim 2$ and $1.25 < C_{TRI} < 2.5$ for their 30cm heptane case in [18], but for the methanol fire this results in too high T_{RMS}, (Weckman and Strong's data [85] is in the 400K range, some 200K lower than the heptane fire). But, it was also learned from preliminary runs that the pool surface radiant flux (where turbulence is present) is always too low without a TRI correction. After some trial and error, it was found that the results were best with $C = 0.25$ and $C_{TRI} = 14$. Predictably, other sets of constants with the same CxC_{TRI} product yielded similar radiation predictions (e.g., $C = 0.5$ and $C_{TRI} = 7$, or $C = 2$ and $C_{TRI} = 1.75$). Hence, the logic here is that a smaller C prevents overprediction of T_{RMS} while a larger C_{TRI} acts as a compensator. Still, it may be noted that T_{rms} can be overpredicted locally by some 100-150K (Fig. 5-4).

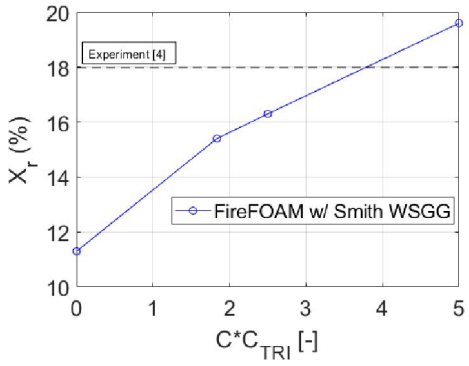

Fig. 5-3: Radiant fraction of the 30cm methanol fire as a function of C_{TRI}

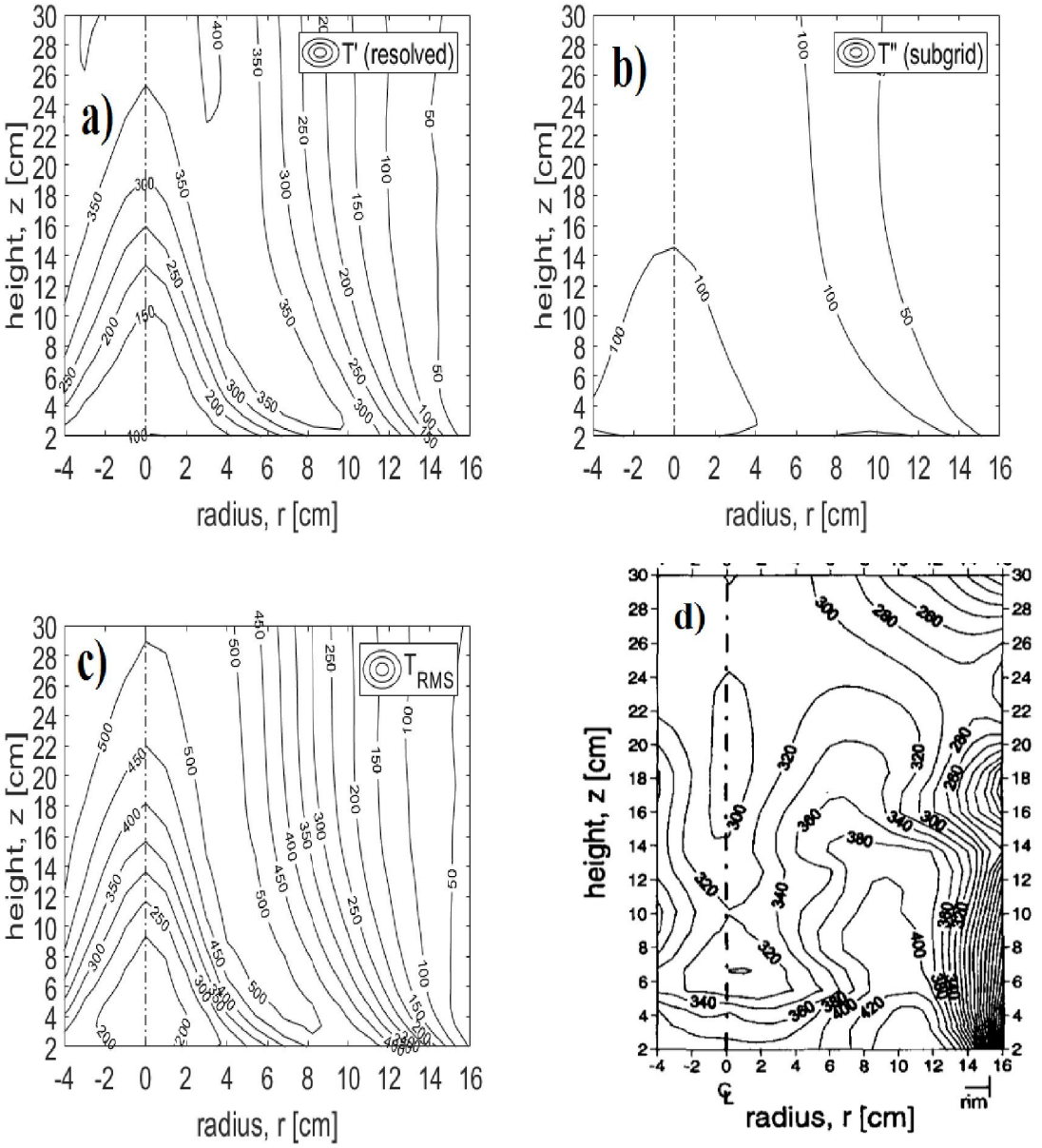

Fig. 5-4: Temperature fluctuation at steady state (30cm methanol fire), top left to bottom right: resolved T' (a), subgrid T'' (b), $T_{rms} = T' + T''$ (c), experimental T_{rms} from [85] (d)

As expected, the radiation source term is completely dependent on how well T_f is modelled. This is particularly visible at low elevations from the pool, i.e. within 2cm, where the source term calculated from T_f may locally increase tenfold (e.g. from 100 to 1000kW/m^3), compared to calculation with T (Fig. 5-5, Fig. 5-6). Such occurrences correspond to local T_f/T ratios > 2. Elsewhere inside the consistent flame region, that ratio is more typically in the range 1 to 1.5. Such local leaps of the radiant source terms thus reflect in the radiant flux at the bottom boundary (Fig. 5-7): instead of peaking at the pool centre like the experimental points, the predicted flux indeed rises slightly some 8-10cm from the centre, before collapsing sharply nearer the pool edge This however remains a positive result, because without any TRI correction the flux is much too low at any radial position (nearly half the experimental values). The spatial distribution of the radiant flux may not be perfect, but the TRI corrections employed here do bring the overall feedback back to acceptable levels (including in the pool centre, where the flux is almost doubled from the $C_{TRI} = 0$ case). This qualitative agreement may be improved upon with some fine tuning on the modelling of T''.

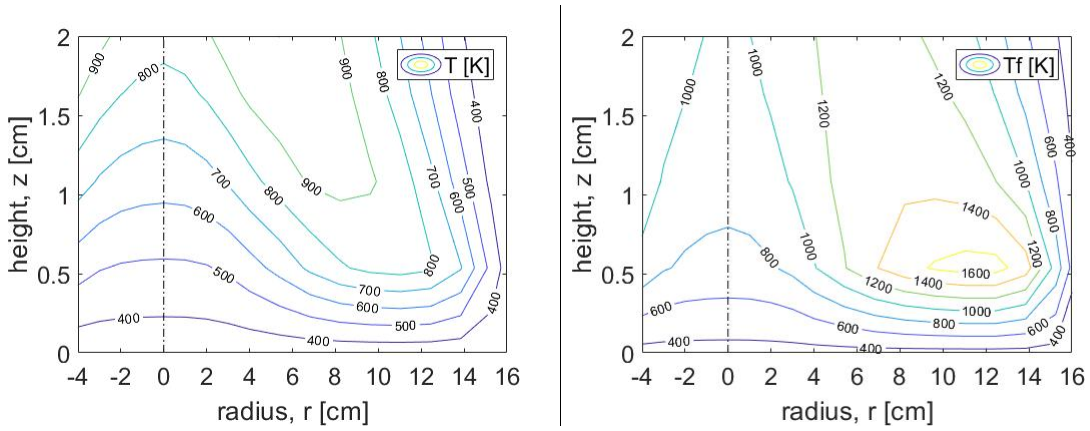

Fig. 5-5: Contours of cell and flame sheet temperature at steady state (30cm methanol fire)

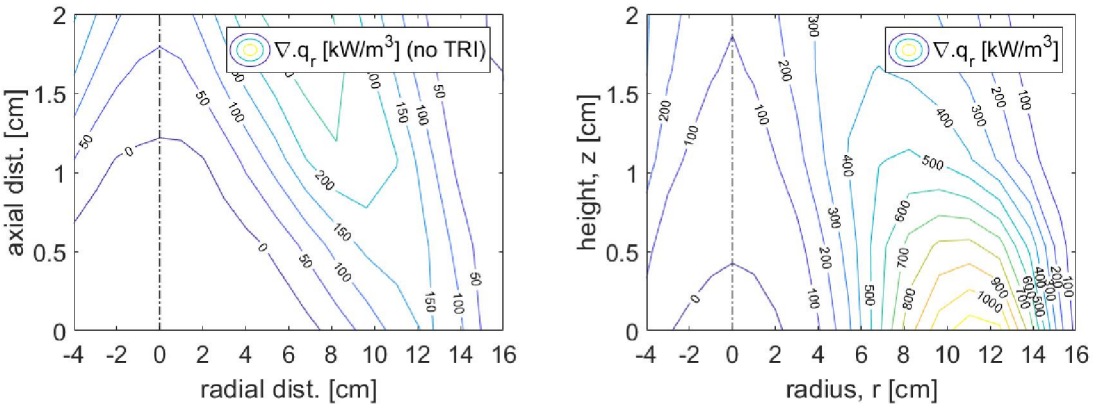

Fig. 5-6: Contours of radiant source term at steady state with and without TRI (30cm methanol fire)

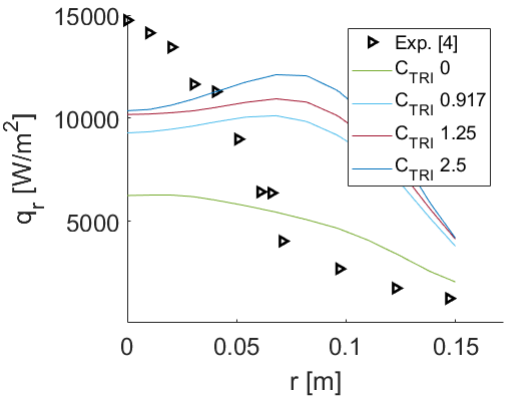

Fig. 5-7: Radiant feedback to pool surface ($z = 0$) with different TRI corrections (30cm methanol fire)

5.3.3. Comparison of gas radiation approaches

Fig. 5-8 presents the centreline mean temperature predictions for the different gas property approaches. The results show that the effect of the gas radiation models on temperature is not significant for this particular fire with a maximum difference of 60K between all simulations and along the centreline. This relates to *Xr* variations of 2-3%. The total radiant fractions from the grey or banded WSGG models are very close and about 5% below the experimental value (Table 5-2), whereas the box model overpredicts the total power by a few percents. The spatial distribution of radiant energy reflects this result, in that the vertical flux is slightly overpredicted by the box model, and underpredicted by the other models, i.e. within 100W at the power peak (Fig. 5-8). Consistently with the findings of [61] in synthetic fires, the grey models project less radiant energy towards the far field. At a radial distance of 82.5cm from the pool centre, the radiant flux echoes the quality of temperature prediction inside the flame (axially), i.e. underpredicted inside the continuous flame zone and slightly overpredicted higher up. As to which gas radiation model to use, the choice may be dictated by practicality. The advantage of using the more CPU expensive Johansson WSGG model is not obvious here, since the cheaper Smith WSGG model has a ready set of absorption coefficients and emission weights for this particular stoichiometric ratio of water vapour and carbon dioxide. The Cassol WSGG is very similar to the other two in its performance, and also slower than the Smith model. Grey approximations are far from being irrelevant here and may be appreciated for their CPU efficiency, but this was a simple case where the mean beam length could be estimated without difficulties and besides, it remains constant over time as soon as the flame has developed to its full scale. For transient problems e.g. spreading fires, a banded WSGG model is definitely more interesting as it requires no mean beam length specification. Finally, some small, residual ray effect is seen in the vertical flux of Fig. 5-9, near the bottom where cells are the smallest. The angular space between the XY plane and the domain's axis was discretised with as many as 50 angles. Further resolution increase (up to 90 angles) produced negligible improvement on ray effects, not worth the much increased computational effort.

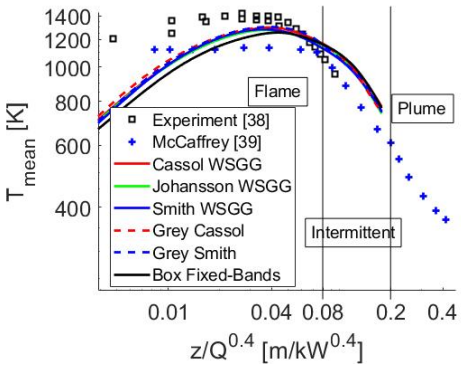

Fig. 5-8: Centreline mean temperatures from 6 gas radiation models (30cm methanol fire)

Table 5-2: Comparison of radiant fractions (30cm methanol fire)

	Radiant fraction X_r (%)
Experiment [4]	18
Grey Smith	17.2
Grey Cassol	16.7
Smith WSGG	17.2
Cassol WSGG	16.8
Johansson WSGG	17.3
Box Fixed-Bands	21.6

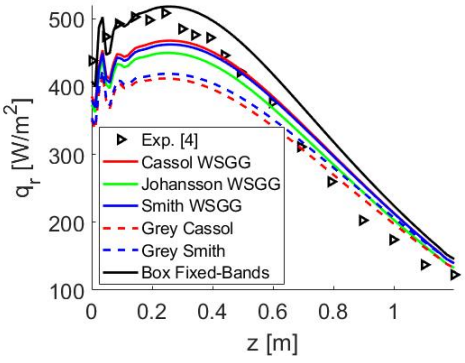

Fig. 5-9: Vertical radiant flux along (r = 82.5cm, z) from 6 gas radiation models (30cm methanol fire)

5.4. Large eddy simulations of 30cm heptane fires

5.4.1. Grid independence and effect on temperature and soot predictions

The grid sensitivity of mean temperature and mean vertical velocity is not very marked. Five grids were tested, with respective smallest cell sizes of 11.6, 10.1, 9.3, 8.5 and 8.0 millimetres. In the consistent flame zone ($z/Q^{0.4} < 0.08$), the plots of axial mean temperature and axial mean velocity magnitude converge by the second or third coarsest grid (Fig. 5-10). In the upper flame zone and in the intermittent zone ($0.08 < z/Q^{0.4} < 0.2$), the various grids yield minor temperature differences that never exceed 50K, and in any case the agreement with the experimental points is good. In the plume zone ($z/Q^{0.4} > 0.2$) all curves converge again towards the McCaffrey profile. The predicted mean velocities follow a similar pattern to that of temperatures (good agreement from middle or upper continuous region onwards). The underprediction of velocity and temperature in the lower parts of the flame zone is typical of the EDC combustion model and is documented in related FireFOAM works as a consequence of locally low Reynolds numbers in buoyancy-dominated fires [80].

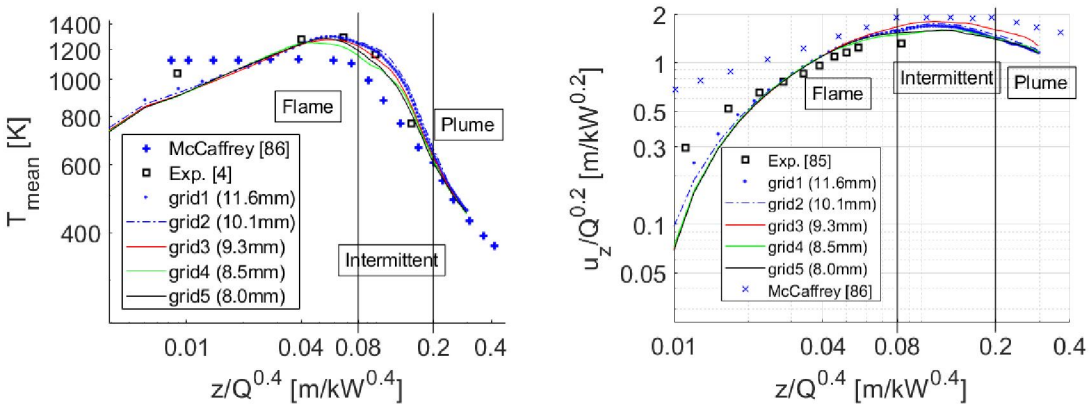

Fig. 5-10: Grid sensitivity of centreline mean temperature and velocity (30cm heptane fire)

The radial profiles for temperature and soot are also compared against the experimental points from Klassen and Gore [4], at four elevations from the pool surface (27cm, 45cm, 66cm and 102cm). The mean temperatures (Fig. 5-11, LHS) are in fair agreement at the lower heights corresponding to the continuous flame zone (z = 27cm, 45cm), i.e. very close near the axis but less good towards the pool edge (local overpredictions of ~200K). Further up in the intermittent zone (z = 66cm, z = 102cm) the match is both good and consistent over the radial distance r. The RMS temperatures benefit from the inclusion of TRI effects (Fig. 5-11, RHS). The resolved component *T'* usually peaks around 400K, respectively the subgrid component *T"* remains in a 200-300K range. As a result, the total RMS temperature manages to match the experimental points quite well overall, notwithstanding a slight overpredicting trend in the continuous flame zone, respectively a slight underpredicting trend in the intermittent zone. In this respect the RMS temperatures are very similar to that of [18]. Soot volume fractions are also well rendered with respect to how difficult their modelling can be (as a rule of thumb, a

relative discrepancy of factor two is usually considered a decent agreement). The mean soot curves (Fig. 5-12, LHS) typically follow this pattern: overpredictive near the axis, underpredictive near the pool edge; with a relative deviation under 60% overall, which may be deemed as rather satisfactory. As with temperature, soot predictions are slightly better in the intermittent zone than in the continuous zone. The resolved RMS soot volume fractions agree well overall, usually managing to sit between the top and bottom range of the experimental points (Figure 5-13, RHS).

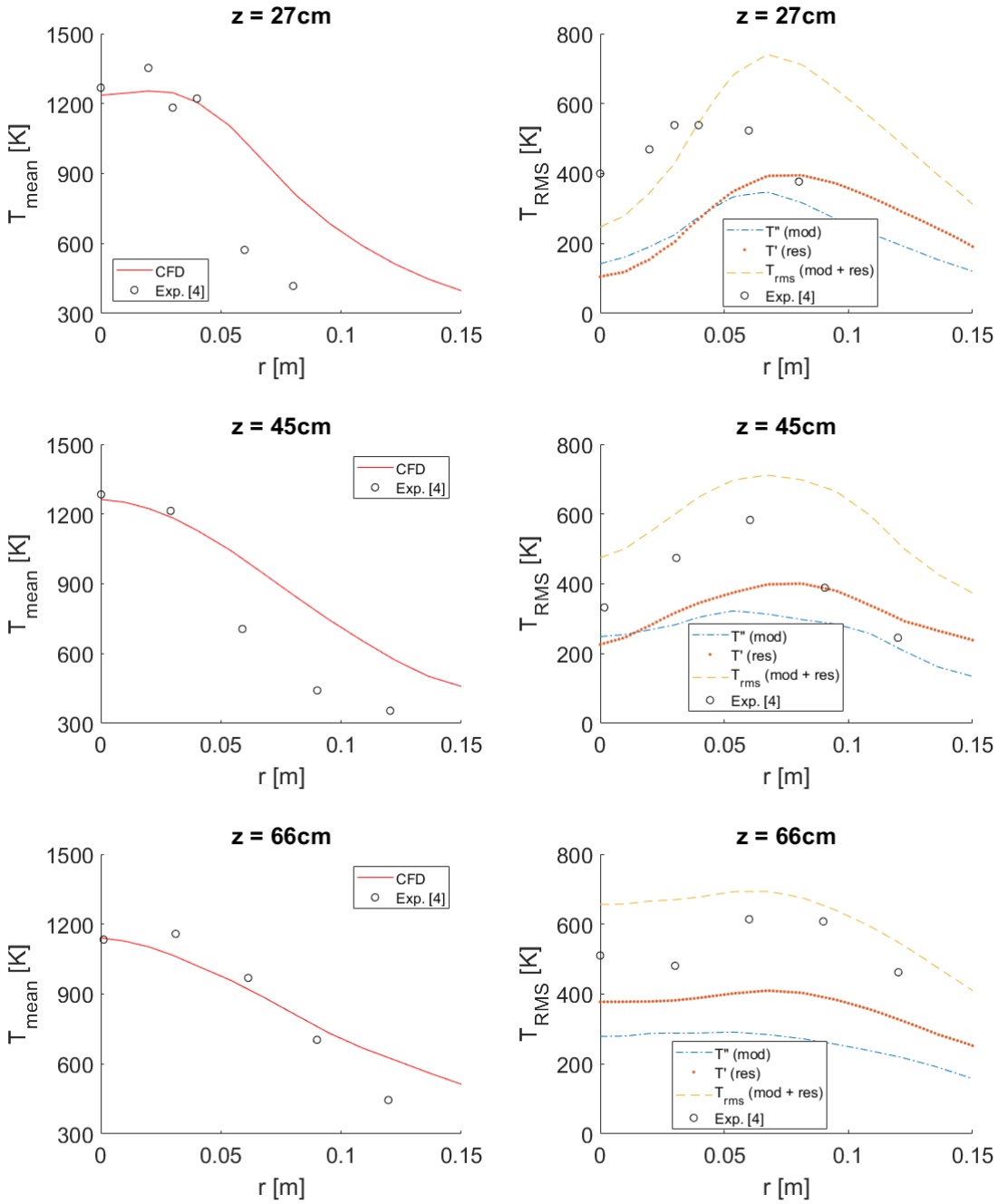

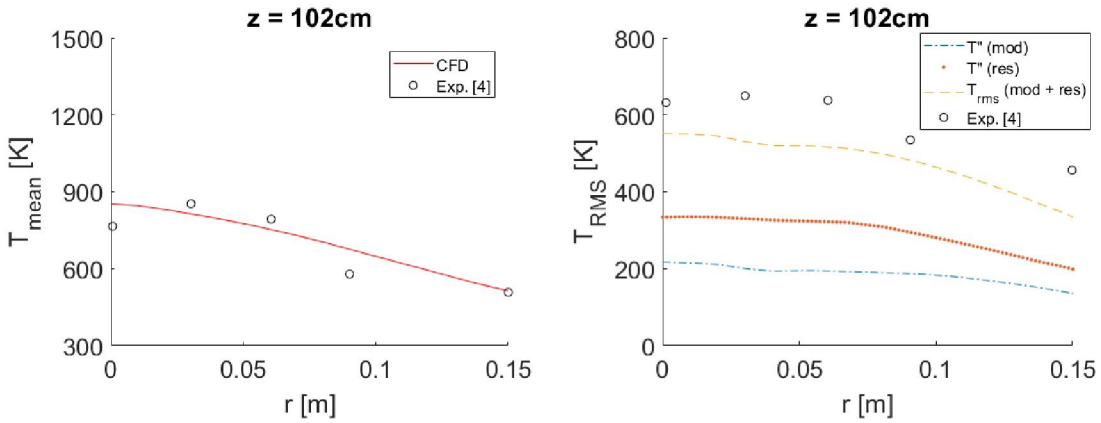

Fig. 5-11: Radial temperature profiles, mean (LHS) and RMS (RHS) at different elevations from pool (z = 0) (30cm heptane fire)

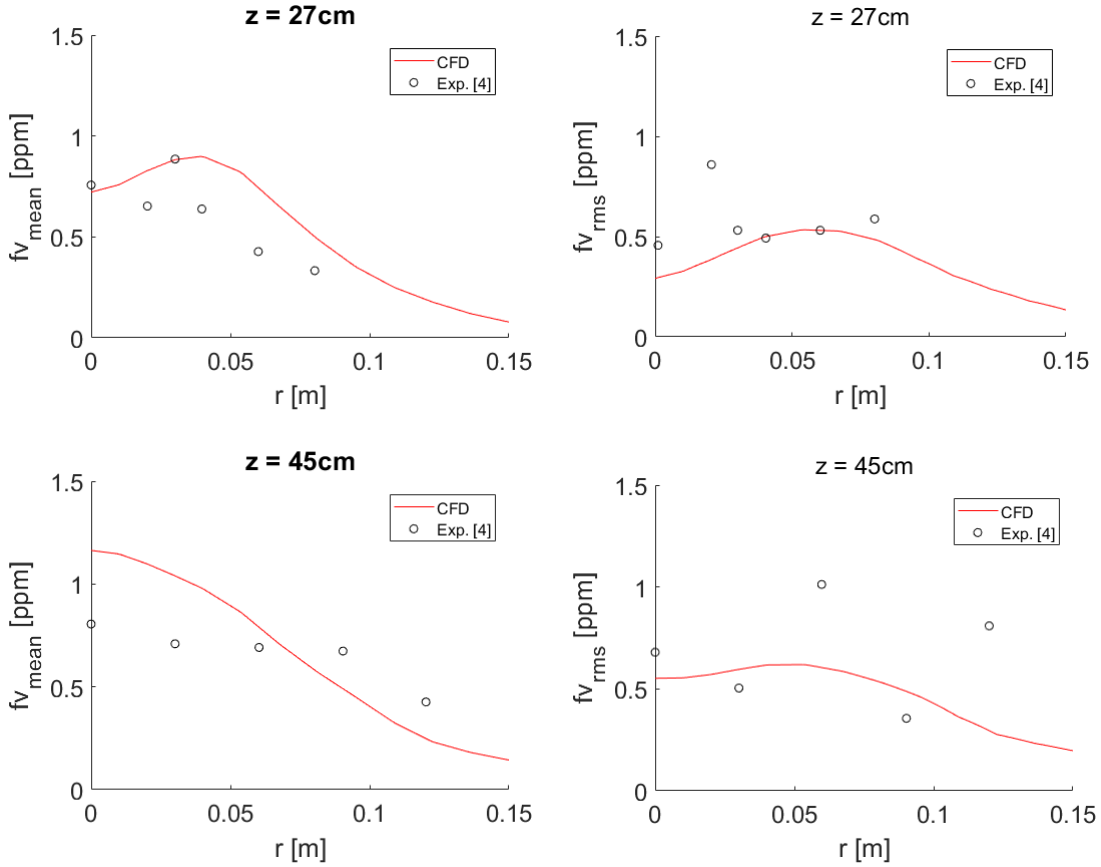

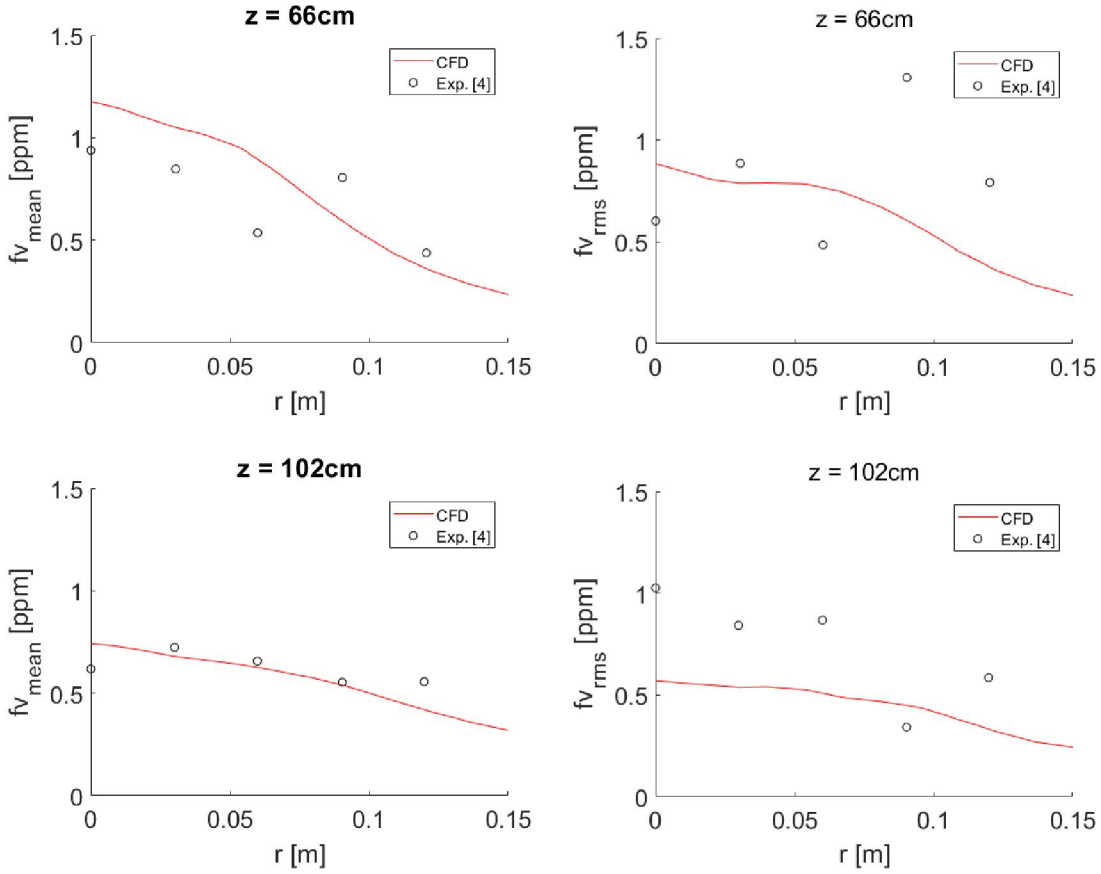

Fig. 5-12: Radial soot volume fraction profiles, mean (LHS) and RMS (RHS) at different elevations from pool (z = 0) (30cm heptane fire)

5.4.2. TRI parameters, radiant fluxes

For the heptane fire some recommendations are available in the literature such as in [18,61]. The constant C, which drives the subgrid component of RMS temperatures, was left at 2 as had been done in [18]. The other parameter, C_{TRI}, was adjusted over successive simulations. Fig. 5-13 shows that once again the evolution of the radiant fraction Xr with C_{TRI} is almost linear and as it turns out, a value of $C_{TRI} \sim 0.9$ is likely to yield the correct fraction. The same value was used by Krinshnamoorthy in [61] for the same fire (albeit a synthetic one in that case) so it was retained for this work after ensuring that RMS temperatures were satisfactory (Fig. 5-11). It can be seen that between the cases with $C_{TRI} = 0$ and $C_{TRI} = 0.9$, the relative difference on Xr is ~13%. The corresponding vertical and horizontal radiant fluxes are remarkably consistent with that, as in both directions the relative difference is almost exactly the same (Fig. 5-14, thin and thick solid blue lines). As for the choice of gas property model, once again the differences are not staggering - in fact all the radiant fractions are matching the experimental one (31%), except for the box model one (30%). The H_2O/CO_2 mole fraction ratio of 1.14 could have caused the Johansson model to be quite different from the Smith WSGG which assumes a ratio of 1, but that is not the case here which suggests the sensitivity to the gas mixture composition may be not very important. All the models that use the same TRI parameters (C = 2, C_{TRI} = 0.9) are close enough to confirm that a grey WSGG

might as well be the most convenient model here, since this fire's radiant output is dominated by a grey soot phase (modelled the same way in all simulations). The latter statement is justifiable quantitatively: an extra simulation was run with soot modelling switched off, and the total radiant energy turned out to be 56% less, and the time-mean temperature peaked 150K higher than with soot modelling on.

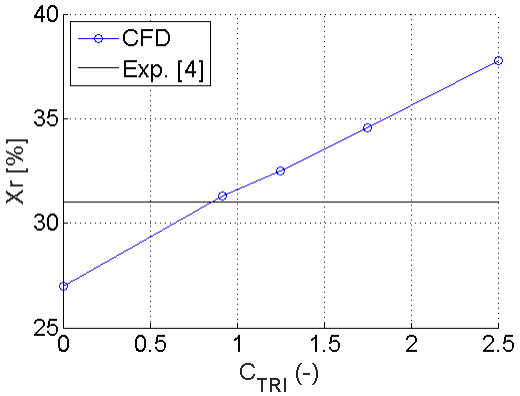

Fig. 5-13: Radiant fraction of the 30cm heptane fire as a function of C_{TRI}

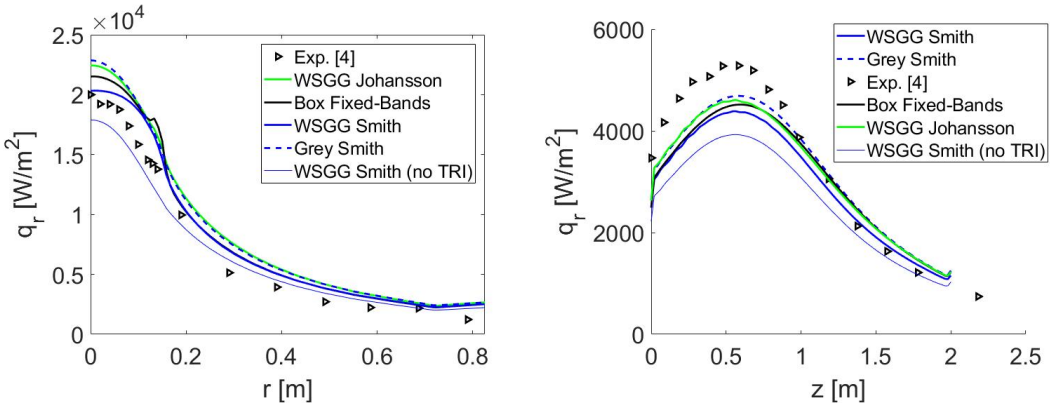

Fig. 5-14: Radiant flux from 5 gas radiation models (30cm heptane fire), left: at the pool surface (r, $z = 0$), right: vertically (r = 82.5cm, z)

5.5. Large eddy simulations of 60cm pool fires

Klassen and Gore performed their methanol and heptane experiments in 30cm burners, simulated above, and with 60 and 100cm in diameter. Using a scaling technique, they found that the radiant flux data collapsed remarkably well between the three fire sizes, despite the vast differences in heat release rate and sooting [4]. Hence the purpose of this section is to show that the WSGG and box model implemented in FireFOAM can reproduce the same trend. For these larger fires, the grid sensitivity study was not reproduced, instead the mesh grids were scaled to the 9mm resolution of the 30cm fires, so that only the number of cells increases. Table 5-3 summarises the main characteristics of the comparative study. Due to time and computational constraints the 1m fires could not be simulated, but arguably, managing to reproduce the same trends 30 and 60cm fires should be satisfactory enough for

the purpose of this radiation validation study. Table 5-4 gives the computational times of the 60cm methanol simulations, which are consistent with that of the 30cm fires (Table 5-1).

Table 5-3: Summary of experimental data from [4] and main FireFOAM parameters for all fire simulations ("N/R" = not reported)

		30cm methanol	60cm methanol	30cm heptane	60cm heptane
Experimental Data [4]	HRR (kW)	20	84	116	770
	Radiant fraction X_r (%)	18	17	31	36
	Flame height H_f (m)	0.508	N/R	1.31	N/R
	Vertical radiant flux (max at $H_f/2$, kW/m²)	0.51	N/R	5.3	N/R
	Pool surface radiant flux (max at r = 0, kW/m²)	15.0	22.6	20.0	N/R
FireFOAM Simulation Parameters	Inlet radius (m)	0.15	0.30	0.15	0.30
	Total radius (m)	0.825	2.58	0.825	2.58
	Total height (m)	1.20	2.00	2.00	3.50
	Fuel inlet $\dot{m}$ (g/s)	0.1069	0.4380	0.2559	1.6985
	Mesh grid size	74,880	133,120	368,640	645,120
	Integral length scale (Eq. 4.2.1)	20cm	36cm	41cm	87.4cm
	Angular grid size	12x30	16x30	16x50	16x30

Table 5-4: Computational times of 60cm methanol fire simulations (0 to 20s) with different gas radiation models

Radiation model	Number of bands	CPU time (hours)
WSGG Grey Smith	1	ref.
WSGG Grey Cassol	1	x1.15
WSGG Banded Smith	4	x2.89
WSGG Banded Cassol	5	x3.41
Box model "Fixed Bands"	7	x4.26

5.5.1. *Temperatures*

The trends from the 30cm fires are well reproduced by the 60cm fires (Fig. 5-15). The methanol fire tends to underpredict in the continuous flame zone, but the intermittent and plume zones are reproduced with satisfactory accuracy (differences under 100K). The heptane simulation is better in the flame zone without deviating in the upper regions and eventually converges nicely with both the McCaffrey model and the experimental points in the plume. As previously, the effect of the gas radiation model on temperature prediction is marginal for both fires.

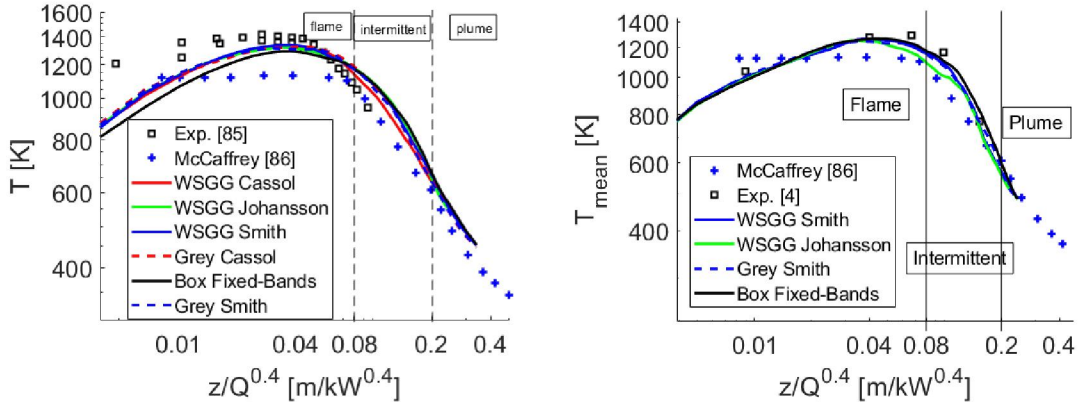

Fig. 5-15: Influence of gas radiation models on the centreline temperatures of the 60cm methanol fire (left) and 60cm heptane fire (right)

5.5.2. *Radiative fluxes and fractions*

The vertical radiant flux for the 60cm fires are not reported in [4], but using Klassen and Gore's scaling method it is possible to compare against the fluxes from the 30cm and 1m fires. The non-dimensional vertical fluxes of the 60cm methanol flame agree very well with the experimental points (Fig. 5-16, top right). The dimensioned fluxes (Fig. 5-16, top left) reproduce the trends from the smaller fire, i.e. the grey models have a smaller power output than the non-grey ones, and the box model tends to overpredict slightly. However the differences between all models remain within 50 W/m². The non-physical fluctuations around $z \sim 0.25$m are due to ray effects, which seem more important when the radiant power output is relatively small, such as in this methanol fire. Ray effects may also be the reason why the predicted pool surface fluxes struggle to reach the 20kW/m² threshold at $r = 0$m (Fig. 5-16, bottom). The box model curve in particular seems to hint at a ray effect, because it clearly peaks around $r = 20$cm when it should peak at $r = 0$m (the other models behave similarly albeit to a smaller extent). The heptane fire seems to be less affected by ray effects, with little to no visible numerical fluctuations (Fig. 5-17, top left). Since radiation is more driven by the soot phase than the gas phase, the differences between the gas models are expectedly small. The agreement of all models with the experimental points in the vertical direction is excellent (Fig. 5-17, top right). In the radial direction (Fig. 5-17, left and right), some measurement data is missing near the pool surface to compare properly, but the simulated fluxes peak above the

50kW/m² mark at the pool centre, suggesting the data is not biased by any ray effects, and the agreement is also very satisfactory.

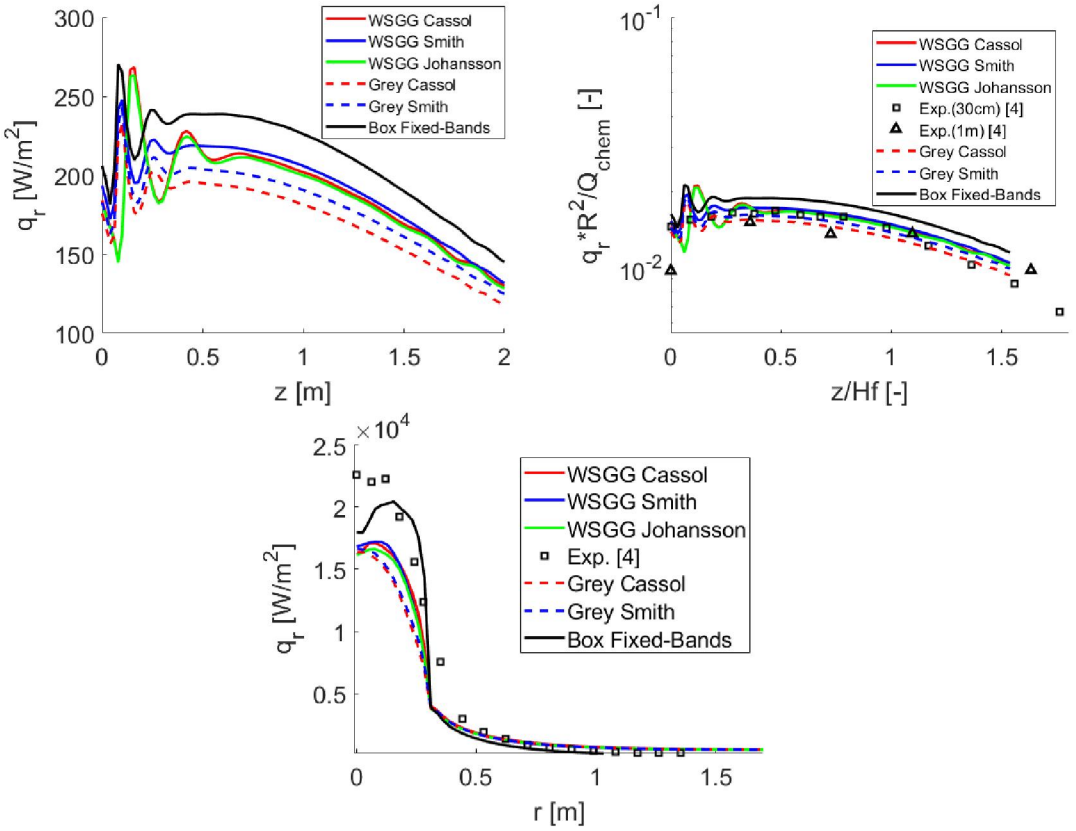

Fig. 5-16: Radiant flux in the simulated 60cm methanol fire from different gas radiation models, vertically (top left: dimensional, top right: non-dimensional) and at the pool surface (bottom)

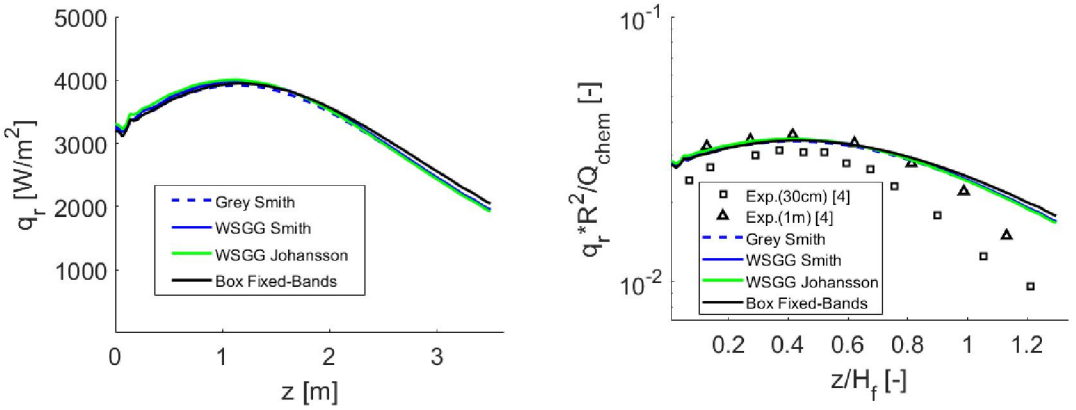

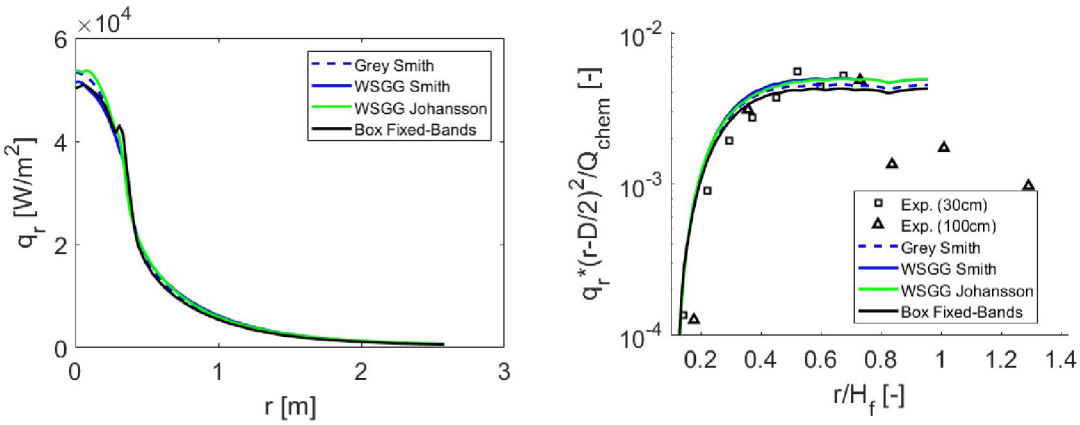

Fig. 5-17: Radiant flux in the simulated 60cm heptane fire from different gas radiation models, vertically (top left: dimensional, top right: non-dimensional) and at the pool surface (bottom left: dimensional, bottom right: non-dimensional)

Finally, the radiant fractions of the 60 cm fires (Table 5-5) are quite similar to that of the smaller fires (Table 5-2). For the methanol fire each gas radiation model even reproduces the same pattern: the banded WSGG have more output than the grey WSGG, and the box model tends to overpredict slightly more than the others (20%). For the soot-dominated heptane fire all the simulations yield similar fractions. On the correlation of *Xr* to HRR, Klassen and Gore do mention in text that the X_r should indeed be independent of burner size [4], but then their measured values show some significant variations, i.e. the methanol fires yield 18%, 17% and 12% between the three burner sizes, and the heptane fires 31%, 36% and 28%. Given the experimental uncertainty, the hypothesis that the total radiant fraction is independent of the fire size may be retained here.

Table 5-5: Comparison of radiant fractions in the simulated 60cm fires

Radiant fraction X_r (%)	60cm methanol	60cm heptane
Experiment [4]	17	36
WSGG 'Grey Smith'	18.5	32
WSGG 'Grey Cassol'	18	N/A
WSGG 'Banded Smith'	19	32
WSGG 'Banded Cassol'	19	N/A
WSGG 'Banded Johansson'	18	32
Box model 'Fixed-Bands'	20	32

5.6. Summary

Methanol and heptane fires were simulated with FireFOAM for burner sizes of 30 and 60 cm. Radiation in the heptane fires is soot-dominated, hence a grey gas model will work as well as a non-grey model while saving substantial CPU time. The differences between the different gas property models are more significant in the soot-free methanol fires, but not by a large margin. The trends are however consistent from the smaller to the larger methanol fires: grey models manage to cope with temperature and gas composition gradients, but their power yield is less than that of non-grey models. The choice of a WSGG model for a fire simulation may be driven by practicality rather than performance. The box model is essentially not worth the extra CPU time if only the gas and soot phase radiation are modelled, for which a WSGG will yield very similar performances. Nevertheless, these simulations showed that this optimised box model, although still more costly than a WSGG, could be practical enough for CFD LES simulations, which was one of the main goals for this PhD work. The box model may also be used for a variety of fires, as shown with the path length sensitivity study. In the next chapter we shall begin to consider the box model coupling with the Mie theory models for liquid phase radiation. Such a coupling, as explained earlier is not possible with WSGG. The implemented TRI correction does lead to a significant radiant power increase that brings the pool surface feedback back up to more realistic values, although quantitatively speaking the correction worked better in the case of heptane fires. Despite an appreciable improvement on the methanol case, the TRI correction could benefit from an improved modelling of the subgrid component of T_{RMS}.

During the comparative study of the WSGG and box models in coupled fire simulations, we saw that grey WSGG models generally produced less radiative output than the banded WSGG models. Other than that the differences remain however minor and all models showed consistency. As a result, for a fire simulation there may be little motivation to choose one WSGG model over another. From this author's own experience, the following recommendations shall be made. If the fire's p_{H2O}/p_{CO2} ratio is 1 or 2, or close to these values, the WSGG model from Smith et al. will be favoured on the sole basis that is notably faster than the others, in either grey or banded implementation, as soon as many solid angles are required. For other fires where p_{H2O}/p_{CO2} is notably different from 1 or 2 (for example, the complete combustion reaction for toluene yields a p_{H2O}/p_{CO2} ratio of 0.57), the Johansson model will be the most convenient as it can handle any p_{H2O}/p_{CO2} between 0.125 and 2. The Cassol model did not demerit because its accuracy, which was overall very similar to that of the Johansson model, but it has more or less the same CPU times without the convenience of handling arbitrary gas mixtures. On the choice of grey vs. non-grey WSGG, the latter do not require mean beam length approximations, which will be a definitive advantage for unsteady or irregularly shaped fires. Grey models remain convenient for quick analysis, knowing that they may be likely to underpredict the total radiant fraction (unless a grey soot phase is present). As for the box model, the CPU times were larger than that of a banded WSGG, but by the quite reasonable margin of a factor 1.33. Both the integral length scale method for the mean beam length, and this author's scaling technique for the equivalent homogeneous gas

parameters seemed robust enough, since the results hold the comparison very well with the banded WSGG which does not rely on user-inputted mean beam lengths or inhomogeneous gas scaling.

Chapter 6 - Results and discussion (two-phase flows)

This section is a very preliminary study of liquid phase and gas-liquid phase radiation with the coupled fixed bands box model with the particulate phase radiation model implemented by FM Global in the latest code version, FireFOAM-dev. We shall first cover the most essential aspects of Mie theory on which the particulate radiation model was based. We will then describe how that model was modified in order to be coupled with the box model. Lastly the early results from a few test cases will be discussed.

6.1. Basic aspects of Mie theory

Scattering occurs when a ray encounters a non-microscopic particulate object along the optical path (Fig. 6-1). Three interactions are then possible, as the ray is diffracted (ray deviation without contact with the object), reflected (deviation with contact) or refracted (deviation with contact with partial absorption). The governing parameters for scattering are the particle's shape, material, size, and the distance that separates it from another particle. For the rest of this section the particles will be considered of spherical shape with radius a. The material's optical properties are described with the complex index of refraction $m = n - ik$. The particle size will be described with a size parameter $x = 2\pi a/\lambda$ where λ is the ray's wavelength. The distance between particles is described with the clearance to wavelength ratio c/λ. When $c/\lambda >> 1$, scattering is independent, i.e. the other particles surrounding one particle have no effect on the way it scatters. Independent scattering is however a common assumption in particulate media with volume fraction smaller than 6000ppm which corresponds to $c/\lambda > 0.5$ [7]. Another common assumption is the elasticity of scattering which means the energy and wavelength of the scattered ray do not change. Under such conditions the two governing parameters are "simply" the refraction index m and the size parameter x. If $x << 1$ the Rayleigh regime of scattering applies (e.g. soot phases), conversely if $x >> 1$ the laws of geometric optics apply. These two limits are particular cases of the more general Mie theory, with which we calculate the absorption and scattering efficiencies (Q_{abs}, Q_{scat}) which yield respectively the absorption coefficient of the particulate phase (κ_p) and the scattering coefficient (σ), which are both found in the general formulation of the radiative transfer equation (Chapter 3, Eq. 3.24). The combined properties of absorption and scattering form an extinction efficiency $Q_{ext} = Q_{abs} + Q_{scat}$. Q_{ext} and Q_{scat} depend on the direction of scattering, which thanks to the spherical assumption can be expressed with only the polar angle Θ. The calculations for Q_{ext} and Q_{scat} are briefly summarised in Eq. 6.1 through Eq. 6.9 and Q_{abs} may thus be obtained by subtraction. The intensity of the scattered ray is related to that of the incident ray by:

$$\frac{I_{scat}(\Theta)}{I_{incident}} = 0.5\frac{i_1+i_2}{x^2} \tag{6.1}$$

Where i_1 and i_2 are non-dimensional intensities corresponding to the electric and magnetic components of the electromagnetic field, thus perpendicular to each other. They depend on the size parameter, the complex index of refraction, and the scattering angle, i.e.

$$i_1(x, m, \Theta) = |S_1|^2 \ , \ \ i_2(x, m, \Theta) = |S_2|^2 \tag{6.2}$$

Where S_1 and S_2 are complex amplitude functions calculated as

$$S_1(\Theta) = \sum_{n=1}^{\infty} \frac{2n+1}{n(n+1)} [a_n \pi_n(cos\Theta) + b_n \tau_n(cos\Theta)] \tag{6.3}$$

$$S_2(\Theta) = \sum_{n=1}^{\infty} \frac{2n+1}{n(n+1)} [b_n \pi_n(cos\Theta) + a_n \tau_n(cos\Theta)] \tag{6.4}$$

Where $\pi_n(cos\Theta)$ and $\tau_n(cos\Theta)$ are calculated with Legendre polynomials and the Mie coefficients a_n and b_n are complex functions of x and $y = mx$. These are calculated with Riccati-Bessel functions that will not be detailed here (see description in [7] and others). The extinction and scattering efficiencies are obtained from

$$Q_{ext} = \frac{2}{x^2} \sum_{n=1}^{\infty} (2n+1)(|a_n|^2 + |b_n|^2) \tag{6.5}$$

$$Q_{scat} = \frac{2}{x^2} \sum_{n=1}^{\infty} Real\{|a_n|^2 + |b_n|^2\} \tag{6.6}$$

Once Q_{abs} is determined from subtracting Eq. 6.6 from Eq. 6.5 we can obtain the absorption and scattering coefficients. For a monodisperse distribution with density of particles N and diameter d, we get

$$\kappa_\lambda = Q_{abs}(\lambda, d) \frac{\pi}{4} d^2 N \tag{6.9}$$

$$\sigma_\lambda = Q_{scat}(\lambda, d) \frac{\pi}{4} d^2 N \tag{6.10}$$

The integral term of the general RTE (Eq. 3.24, Chapter 3) contains the phase function $\Phi(\Theta)$ which is a fraction of energy corresponding to a given direction of scattering. It is rigorously defined as

$$\Phi(\Theta) = \frac{i_1 + i_2}{\frac{1}{4\pi} \int_{4\pi} (i_1 + i_2) d\Omega} = 2 \frac{i_1 + i_2}{x^2 Q_{scat}} \tag{6.11}$$

The rigorous calculation of the phase function is in many cases too tedious. The FireFOAM implementation uses the approximation of the asymmetry factor, noted g, and related to the phase function as

$$g = \overline{cos\Theta} = \frac{1}{4\pi} \int_{4\pi} \Phi(\Theta) cos\Theta d\Omega \tag{6.12}$$

Under the assumption of spherical particles the asymmetry factor may be directly calculated:

$$g = \overline{cos\Theta} = \frac{4}{x^2 Q_{scat}} \sum_{n=1}^{\infty} \left[\frac{n(n+2)}{n+1} Real\{a_n a_{n+1}^* + b_n b_{n+1}^*\} + \frac{2n(n+1)}{n(n+1)} Real\{a_n b_n^*\} \right] \tag{6.13}$$

Once g is obtained, the phase function is obtained from an approximate approach, the Henyey-Greenstein phase function:

$$\Phi_{HG}(\Theta) = \frac{1-g^2}{(1+g^2-2g\cos\Theta)^2} \tag{6.14}$$

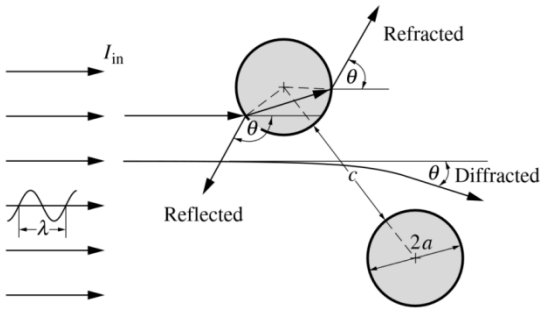

Fig. 6-1: The three interactions of radiation scattering from spherical particles (reproduced from [7])

6.2. Overview of the original implementation

The expressions above, calculated over the appropriate spectral range, yield the spectral evolutions of Q_{abs}, Q_{scat} and the asymmetry factor g. These spectral calculations were not implemented in FireFOAM but are performed externally. For the FireFOAM implementation, 7 band intervals were chosen (Fig. 6-2) so that the spectral parameters may be averaged within them, using the Planck function as weight [87,88]. FireFOAM then reads a pre-tabulated file which stores the band-averaged values of Q_{abs}, Q_{scat} and g, computed for 6 particle diameters (10, 26, 60, 160, 400, 1000 microns). The code performs a linear interpolation on Q_{abs}, Q_{scat} and g in each band for intermediate diameter sizes. Hence, the absorption, scattering and asymmetry factors of the liquid phase are stepwise-grey and look much like a box model (Fig. 6-3).

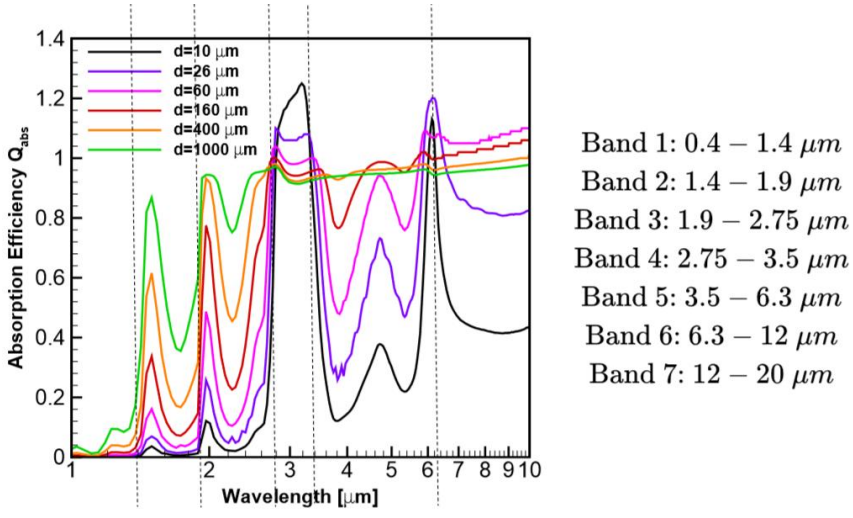

Fig. 6-2: Spectral evolution of the absorption efficiency and original band limits considered for averaging (reproduced from [87])

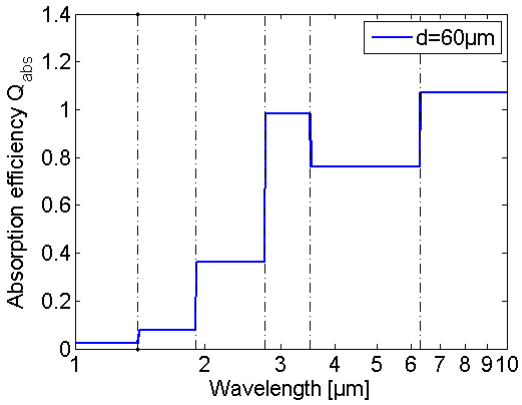

Fig. 6-3: Original band-averaged absorption efficiency of the droplet phase for Ø60µm droplets

On droplet injection, the particles are grouped into discrete parcels that may be tracked through space and time [91], but for simplicity only static dispersions were used here. To solve radiation, fireFOAM's fvDOM considers the presence or absence of a parcel in each computational cell and then calculates absorption, scattering, intensity, etc. as per normal. The injection model is normally capable of handling thermomechanical phenomena such as collision, breakup, energy and mass loss/gain (the detailed equations may be found in e.g. [92]) but none of these have been yet used in this work, hence study of these submodels may remain in the scope of future work for now.

6.3. Adaptation for coupling with gas phase box model

In Chapter 4, section 4.2 we described how the box model band limits were fixed in a way that these bandwidths may suit fire scenarios. By amalgamating the overlapping bands between gas species we reduced the number of bands of the original exponential wide band model, from 13 (6 for CO_2, 5 for H_2O) to 6. If we now compare the absorption spectra of a liquid phase, e.g. from Fig. 6.3, with a gas spectrum calculated with the fixed bands box model, we obtain something like Fig. 6-4, where we can see the band limits of the two phases do not quite match. Since the absorption spectrum of the liquid phase is continuous (no windows), and also comparatively smoother than the gas phase, we shall modify the liquid band limits rather than the gas band limits. To do so we obtained the spectral absorption efficiency for each of the 6 diameters, and recalculated the band averages as per the desired band limits, using the same averaging technique as in [87,88]. The resulting absorption spectrum is now as per Fig. 6-5. With the addition of the new phase, the gas windows are now replaced with liquid-only absorption bands. Since these are non-grey, they cannot be accounted for with a single band (like a transparent "clear gas" phase), hence the total number of bands is now increased to 11 (Table 6-1). Of course the process of re-averaging will have to be repeated for the asymmetry factor and the scattering efficiency. This is a work in progress at this time of writing, hence for the time being our liquid phase and gas-liquid calculations do not account for scattering (isotropic scattering is assumed instead).

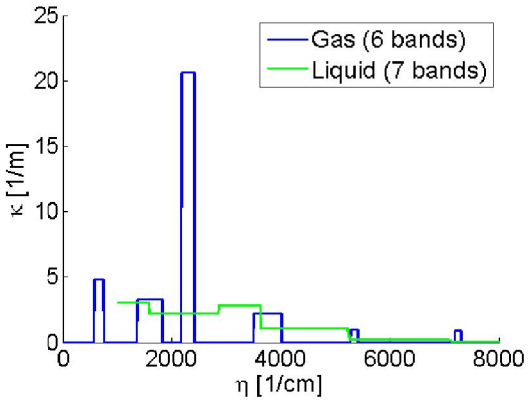

Fig. 6-4: Comparison of the fixed bands box model's spectrum of a typical gaseous CO_2-H_2O mixture, and the droplet phase absorption from Fig. 6-3.

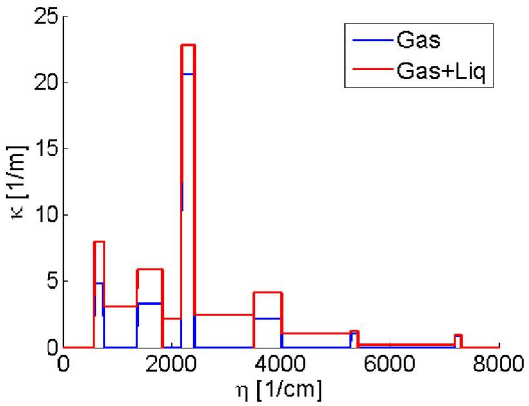

Fig. 6-5: Combined spectra of gaseous CO_2-H_2O mixture and 60 micron droplet phase with the new band limits

Table 6-1: Band limits of the combined liquid droplet and gas phases

Specie	Location (μm)	Location (cm^{-1})	Limits (μm)	Limits (cm^{-1})	Δηe (cm^{-1})
H_2O+liq	71	140	17.1821 - ∞	0-582	582
CO_2+liq	15	667	13.3156-17.821	582-751	169
Liq	9.4	1064.5	7.2569 - 13.3156	751-1378	627
H_2O+liq	6.3	1600	5.4885-7.2569	1378-1822	444
Liq	5.0	2001.5	4.5851 - 5.4885	1822-2181	359
CO_2+liq	4.3	2410	4.1494-4.5851	2181-2410	229
Liq	3.4	2957.5	2.8531 - 4.1494	2410-3505	1095
CO_2+H_2O+liq.	2.7	3760	2.4907-2.8531	3505-4015	510
Liq.	2.1	4652	1.8907 - 2.4907	4015-5289	1274
CO_2+H_2O	1.87	5350	1.8481-1.8907	5289-5411	122
Liq.	1.6	6304.5	1.3893 - 1.8481	5411-7198	1787
H_2O+liq.	1.38	7250	1.3695-1.3893	7198-7302	104

6.4. Preliminary test cases

6.4.1. Liquid phase only, 1D slab

This test case, taken from [89], contains a variety of droplet densities, path lengths and droplet diameters which will help give a first idea of the new droplet radiation model's capability. A hot black boundary emits radiation at 1300K across a line-of-sight containing a monodisperse and uniformly spaced droplet distribution. The FireFOAM finite volume method solves the 1-directional radiant intensity. Transmissivity (τ) is evaluated at the end of the path, for various droplet volume fractions (fv), path lengths (L), and droplet diameters (d). The results are compared against the "exact" discrete ordinates solution of [89] and summarised in Table 6-2. The transmissivity of the smallest droplet distributions (Case 3) are very overpredicted, especially when the droplet volume fraction increases, which is a consequence of the omission of scattering (isotropic at such small diameters). With the large droplets (Case 1) it is the other way around as FireFOAM underpredicts the transmissivities. Scattering is strongly forward with large particles, hence some energy is missing at $x = L$. The intermediate droplet size (Case 2) yields good results at smaller and intermediate volume fractions, but at the higher density FireFOAM overpredicts. This test case will be more conclusive once scattering is correctly re-implemented. Also, there is an ongoing discussion on the reliability of the linear interpolation of radiative properties of droplets between two tabulated diameters.

Table 6-2: Comparison of FireFOAM and [89] transmissivities at various path lengths, droplet size and volume fractions

		τ "Exact"[89] (%)	τ "FireFOAM"(%)	$Err = \left\|\frac{FireFOAM - "exact"}{"exact"}\right\|$(%)
CASE 1 L = 0.6 m d = 350 µm	Subcase 1-1 fv=0.24x10^{-3}	25	16.8	33
	Subcase 1-2 fv=1x10^{-3}	2.6	1.2	52.5
	Subcase 1-3 fv=2x10^{-3}	0.6	0.4	31.1
CASE 2 L = 0.25 m d = 90 µm	Subcase 2-1 fv=0.05x10^{-3}	61.2	56.2	8.2
	Subcase 2-2 fv=0.55x10^{-3}	7.2	7.1	1.1
	Subcase 2-3 fv=1.7x10^{-3}	0.8	1.4	73.8
CASE 3 L = 1 m d = 10 µm	Subcase 3-1 fv=0.001x10^{-3}	74.3	78.0	5.0
	Subcase 3-2 fv=0.015x10^{-3}	11.3	24.0	112.2
	Subcase 3-3 fv=0.03x10^{-3}	4.2	17.2	310.0

6.4.2. Coupled radiation of liquid and gas phases in a 3D enclosure

The case setup is as per Wu and Zhao [90]. A black-walled, 1m x 1m x 1m enclosure (uniform Cartesian mesh, 40 x 40 x 40 cells) is filled with a monodisperse water droplet phase and/or a homogeneous gaseous mixture (Fig. 6-6). The gas phase is composed of 3.2% CO_2 and 7.84% H_2O. Droplets are at room temperature, 20µm in diameter and with a total volume fraction of 0.27ppm. The total radiant flux is sampled along a target wall standing opposite an emitting wall. The temperatures of the emitting wall and the gas mixture vary as per Table 6-3. The box model coupled with the Mie model is compared against the MCRT data from [90] reproduced hereafter. The first two cases, A and B, have no gas phase but only the droplets acting as a radiation attenuator between the hot emitting wall at 1000 or 2000K and the receiving wall. Hence the box model does not play any role here, but the Mie model performs well, with maximum relative errors under 5% and 3% (case A and B respectively). With no emission from the wall and the gas mixture at 1000 or 2000K (case C and D), the relative errors peak at 9% and 12%, which is a familiar range (similar to gas-only scenarios of previous chapters).

Table 6-3: Summary of the 3D, two-phase test case conditions

Test case #	T_{gas} (K)	T_{wall} (K)
A	No gas	1000
B	No gas	2000
C	1000	0
D	2000	0

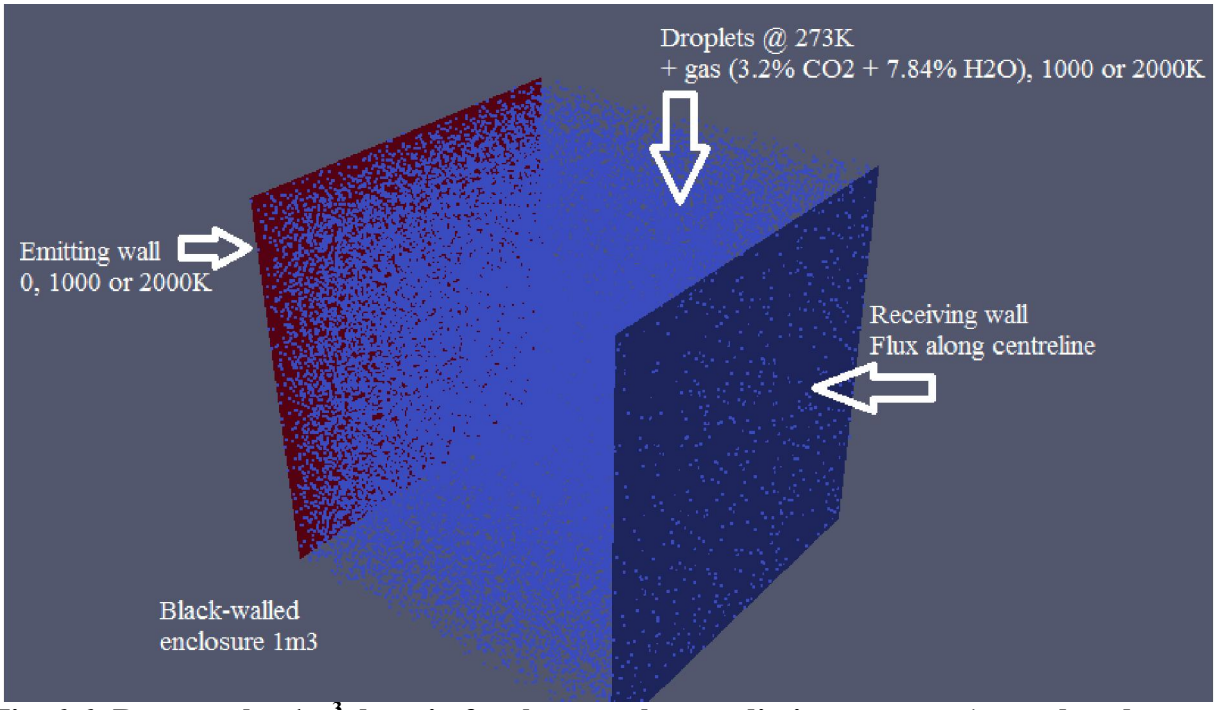

Fig. 6-6: Rectangular 1m^3 domain for the two-phase radiation test case (reproduced from [90])

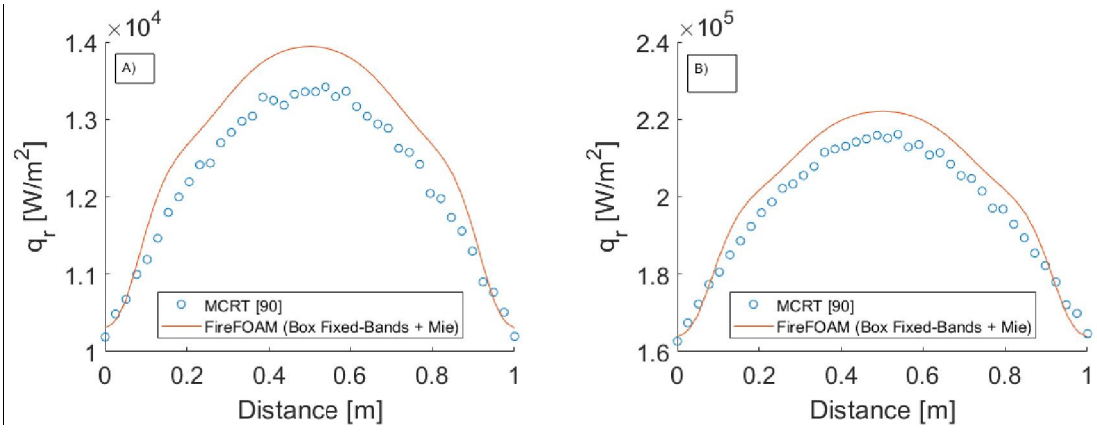

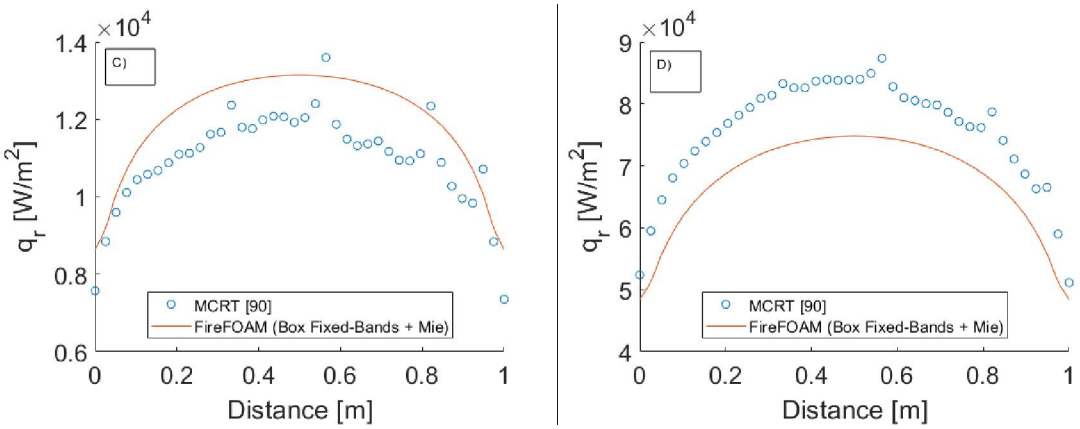

Fig. 6-7: Incident flux on the receiving wall of the two-phase 3D test case, for different wall and temperatures

6.5. Summary

The fixed bands box model was coupled with the droplet phase radiation model and proves to be functional for the canonical test cases investigated here. The scattering model is being improved by its authors at this time of writing and the treatment larger droplets should benefit from that work in the near future. Inhomogeneous gas mixtures mixed with polydisperse droplet phases will be the next step, for which more MCRT benchmark data will be generated in the frame of this collaborative effort.

Chapter 7 - General conclusions, recommendations & further studies

This work may be summarised with the following key points. Approximate non-grey gas radiation models were implemented in the open source CFD environment of FireFOAM. They were tested in static, non-reactive media first, and then in pool fires of various sizes and heat release rates. The first type of models, the weighted-sum-of-grey-gases (WSGG), is ready-to-use and straightforward to implement, hence there is no need for a lengthy validation procedure. Instead an estimation of WSGG errors was provided, based on various static, non-reactive media scenarios (~15% for heat fluxes and ~20% for its divergence). When applying the WSGG models to pool fire simulations, it was shown that the newer WSGG correlations developed for oxy-fuel applications could work well for fires, but not necessarily better than older (and faster) models. The second category of gas radiation models, the exponential wide band-based box model, was developed to extend FireFOAM's radiation capability beyond single-phase radiation. A more detailed analysis was performed than with the WSGG, as it required modifications to be used in inhomogeneous gas mixtures where bands overlap. The regular forms of the box model, such as found in the literature, performed on-the-fly spectral bandwidth calculations. We first tested two box models using that approach in static, non-reactive media, and determined in which conditions these models performed best. Following that, on-the-fly bandwidth calculations were suppressed from the box model variant that was found to work better for typical fire conditions. Working with fixed band limits was indeed a necessity for the future coupling of the box model with the Mie theory model that deals with non-grey radiation of particulate phases (liquid droplets). Thus, after extensively studying the sensitivity of box model bandwidths, it was possible to determine fixed band limits for a working range of mass path lengths typically found in fires. This new fixed bands box model was then successfully tested in the same canonical scenarios as previously. Then, a technique was proposed to obtain the equivalent homogeneous gas parameters for fire simulations, based on pre-calculated steady state characteristics. Upon the good results of that technique, the fixed bands box model was applied in LES simulations of 30cm pool fires. The predictions compared well with that of the WSGG models, which were also very consistent between themselves. The effects of grid size on temperature and soot predictions were studied, as well as the effects of turbulence-radiation interaction (TRI), without which the radiant fluxes are underpredicted. We then proceeded with more simulations of the same fires but with larger burners (60cm in diameter), and found the same consistency from all gas radiation models. This shows that the scaling techniques and mean beam lengths based on the combustion model's integral length scale are reliable, otherwise the grey WSGG or the box model would not be as close with the banded WSGG models that require no such techniques. Finally, the box model was coupled with a particulate phase radiation model based on Mie theory. To do so we increased the spectral discretisation from the original 7 bands to 11, so that a gas phase may be added at will. We tested this modified Mie model for purely liquid phase radiation in 1D scenarios and obtained encouraging results. Lastly, a two-phase test case showed that the coupling of the gas and liquid models was operational. The key findings may thus be summarised as such:

- Grey gas radiation models behave better while used during runtime in fire simulations than in canonical pure radiation cases, although they tend to underpredict the radiant output if there is little or no soot.
- Non-grey WSGG implementations are more CPU demanding than grey models, particularly when many solid angles are employed, but their independence from prescribed mean beam lengths can make them a powerful alternative for transient scenarios such as fire spread.
- Newer WSGG correlations do not necessarily perform better than older ones for fire scenarios (unlike e.g. oxy-fuel combustion).
- TRI corrections are essential for sooty fires e.g. heptane. They were also useful in the non-sooty methanol fires, although there is some sensitivity to how well the subgrid temperature fluctuation is modelled.
- A box model based on fixed band limits and with the adequate Curtis-Godson scaling proved realistic, CPU wise, for runtime radiation calculations in LES-simulated pool fires. The coupling with the Mie model for the gas/droplet mixture proved functional notwithstanding some future refinements.

The author feels this work has contributed to not only FireFOAM and its growing community of users, but to CFD at large as well. It was shown that coupled non-grey radiation modelling in fire simulations could be made practical enough to compete with grey approximations, while offering better performance (and convenience in the case of the WSGG). The box model, thanks to this work's simplified formulation and scaling method, was also able to compare with the WSGG models in terms of computational efficiency, and offers promising possibilities for future two-phase radiation applications

Suggestions for future work may be proposed as follows. More fuels should be considered for fire scenarios, e.g. methane or toluene although the latter would require a non-grey soot treatment. Solid fuels, complex fuels fire spread scenarios should also be considered - the Johansson WSGG especially offers potential in this area (independence from mean beam length, flexibility with various H_2O/CO_2 mole fraction ratios). The liquid-gas radiation coupling is the area where the most work is needed, notably with inhomogeneous gas phases and polydisperse droplet distributions. Then, a 3D scenario of a pool fire surrounded by a water curtain could be considered. Later on, once the models are capable of handling the extra energy radiated by evaporating droplets, fire suppression simulations could envisaged.

Chapter 8 - Bibliography

[1] S.H. Chan, Combined Radiation and Combustion, in: C. L. Tien (ed.), Annual Review of Heat Transfer, Begell House, New York and Redding, CT, 2005, vol. 14, pp. 49-64.

[2] R. Viskanta, Radiative Transfer in Combustion Systems: Fundamentals and Applications, Begell House, New York and Redding, CT, 2005.

[3] A. Hamins, T. Kashiwagi, R.R. Buch, Characteristics of pool fire burning, Fire Resistance of Industrial Fluids. Proceedings ASTM STP 1284. June 20, 1995, ASTM PCN 04-012840-12. (1996) 15-41.

[4] M.E. Klassen, J.P. Gore, Structure and radiation properties of pool fires, Final Report NIST-GCR-94-651. (1994) 153.

[5] K. Wakatsuki, G.S. Jackson, A. Hamins, M.R. Nyden, Effects of fuel absorption on radiative heat transfer in methanol pool fires, Proc. Combust. Inst. 31 (2007) 2573-2580.

[6] J.L. Consalvi, F. Liu, Radiative transfer in the core of axisymmetric pool fires - I: evaluation of approximate radiative property models, Int. J. Thermal Sciences. 84 (2014) 104-117.

[7] H.F. Modest, Radiative Heat Transfer, third ed., Academic Press, New-York, NY, 2013.

[8] L. Wang, M.F. Modest, D.C. Haworth, S.R. Turns, Modeling nongray gas-phase and soot radiation in luminous turbulent nonpremixed jet flames, Combustion Theory and Modelling. 9(4) (2005) 673-691.

[9] S. Dembele, J. Zhang, J.X. Wen, Evaluation of the correlated-k and other gas radiation models for combustion applications, Fire Safety Science. 7 (2003) 927-938.

[10] P.S. Cumber, M. Fairweather, Evaluation of flame emission models combined with the discrete transfer method for combustion system simulation, Int. J. Heat Mass Transfer. 48 (2005) 5221-5239.

[11] M.F. Modest, H. Zhang, The full-spectrum correlated-k distribution for thermal radiation from molecular gas-particulate mixtures, J. Heat Transfer. 124(1) (2002) 30-38.

[12] M.K. Denison, B.W. Webb, A spectral line-based weighted-sum-of-gray-gases model for arbitrary RTE solvers, J. Heat Transfer. 115(4) (1993) 1004–1012.

[13] C. Wang, W. Ge, M.F. Modest, B. He, A full-spectrum k-distribution look-up table for radiative transfer in nonhomogeneous gaseous media, Journal of Quantitative Spectroscopy and Radiative Transfer, 168 (2016) 46-56.

[14] P.J. Coelho, O.J. Teerling, D. Roekaerts, Spectral radiative effects and turbulence/radiation interaction in a non-luminous turbulent jet diffusion flame, Combustion and Flame. 133 (2003) 75–91.

[15] H.C. Hottel, A.F. Sarofim, Radiative Transfer, McGraw-Hill, New York, NY, 1967.

[16] A.T. Modak, Exponential wide band parameters for pure rotational band of water vapor, J. Quant. Spectrosc. Radiat. Transfer. 21 (1978) 131-142.

[17] L.A. Dombrovski, DOI: 10.1615/thermopedia.000156.

[18] P. Chaterjee, Y. Wang, K.V. Meredith, S. Dorofeev, Application of a subgrid soot-radiation model in the numerical simulation of a heptane pool fire, Proc. Combustion Instit. 35 (2015) 2573-2580.

[19] J.L. Consalvi, R. Demarco, A. Fuentes, S. Melis, J.P. Vantelon, On the modeling of radiative heat transfer in laboratory-scale pool fires, Fire Safety J. 60 (2013) 73-81.

[20] OpenFOAM Users' Guide, OpenCFD Ltd, Bracknell, UK, 2011.

[21] M.F. Modest, K.K. Sikka, The stepwise gray P-1 approximation for multi-dimensional radiative transfer in molecular gas-particulate mixtures, J. Quant. Spectrosc. Radiat. Transfer. 48 no.2 (1992) 159-168.

[22] J. Zhang, M. Delichatsios, M. Colobert, Assessment of Fire Dynamics Simulator for Heat Flux and Flame Heights Predictions from Fires in SBI Tests, Fire Technology 46 (2010) 291-306.

[23] Z. Chen, J. Wen, B. Xu, S. Dembele, Large eddy simulation of a medium-scale methanol pool fire using the extended eddy dissipation concept, Int. J. Heat Mass Transfer. 70 (2014) 389-408.

[24] Radiation heat transfer in OpenFOAM, Göteborg, Chalmers University of Technology, 10.12.2009

[25] J.C. Chai, P. Rath, Discrete-Ordinates and Finite Volume Methods for Radiation Heat Transfer, International Workshop on Discrete-Ordinates and Finite-Volume Methods for Radiation Heat Transfer, January 2-3, 2006, IIT, Guwahati, India.

[26] S.H. Kim, K.Y. Huh, A new angular discretization scheme of the finite volume method for 3-D radiative heat transfer in absorbing, emitting and anisotropically scattering media, International Journal of Heat and Mass Transfer 43 (2000) 1233-42.

[27] H.T.T. Kamden, Ray effect elimination in discrete ordinates and finite volume methods, Journal of Thermophysics and Heat Transfer, 29(2) (2015) 306-318.

[28] M.A. Ramankutty, A.L. Crosbie, Modified discrete-ordinates solution of radiative transfer in three-dimensional rectangular enclosures, J. Quant. Spectrosc. Radiat. Transfer, 60(1) (1998) 103–134.

[29] T.F. Smith, Z.F. Shen, J.N. Friedman, Evaluation of coefficients for the weighted sum of gray gases model, ASME J. Heat Transfer, 104(4) (1982) 602–608.

[30] M.F. Modest, The weighted-sum-of-gray-gases model for arbitrary solution methods in radiative transfer, J. Heat Transfer. 113 (1993) 650-656.

[31] A. Soufiani, E. Djavdan, A comparison between weighted sum of grey gases and statistical narrow-band radiation models for combustion applications, Combustion and Flame 97 (1994) 240-250.

[32] F. Cassol, R. Brittes, F.H.R. Franca, O.A. Ezekoye, Application of the weighted-sum-of-gray-gases model for media composed of arbitrary compositions of H_2O, CO_2 and soot", Int. J. Heat Mass Transfer. 79 (2014) 796–806.

[33] R. Johansson, B. Leckner, K. Andersson, F. Johnsson, Account for variations in the H_2O to CO_2 molar ratio when modelling gaseous radiative heat transfer with the weighted-sum-of-grey-gases model", Combust. Flame. 158(5) (2011) 893-901.

[34] P.J. Coelho, Numerical simulation of radiative heat transfer from non-gray gases in three-dimensional enclosures, J. Quant. Spectrosc. Radiat. Transfer. 74 (2002) 307-328.

[35] V. Goutière, F. Liu, A. Charette, An assessment of real-gas modelling in 2D enclosures, J. Quant. Spectrosc. Radiat. Transfer. 64 (2000) 299-326.

[36] N.W. Bressloff, The influence of soot loading on weighted sum of grey gases solutions to the radiative transfer equation across mixtures of gases and soot, Int. J. Heat Mass Transfer. 42 (1999) 3469-3480.

[37] S. Dembele, J. Zhang, J.X. Wen, Assessment of spectral narrow band and weighted-sum-of-gray-gases models for computational fluid dynamics simulation of pool fires, Numer. Heat Transf. B. 48 (2005) 257-276.

[38] D.K. Edwards, Absorption of radiation by carbon monoxide gas according to the exponential wide-band model, Appl. Optics 4(10) (1965) 1352-53.

[39] S.H. Chan, C.L. Tien, Total band absorptance of non-isothermal infrared-radiating gases, J. of Quantitative Spectroscopy and Radiative Transfer, 9(9) (1969) 1261–71.

[40] R.D. Cess, L.S. Wang, A band absorptance formulation for nonisothermal gaseous radiation, Int. J. Heat and Mass Transfer, 13 (1970) 547-555.

[41] J. D. Felske, C. L. Tien, Wide Band Characterization of the Total Band Absorptance of Overlapping Infrared Gas Bands, Combustion Science and Technology, 11:3-4 (1975) 111-117.

[42] A.T. Modak, Exponential wide band parameters for pure rotational band of water vapor, J. Quant. Spectrosc. Radiat. Transfer. 21 (1978) 131-142.

[43] L. C. R. Johansen, S.H. Olesen, S. Su, Assessment and Development of Gas Radiation Models for Oxy-Fuel Combustion, TEPE2 Project Report, Aalborg University, Denmark, 2009.

[44] S.S. Penner, Quantitative molecular spectroscopy and gas emissivities, Addison Wesley, Reading, MA, 1960.

[45] M.F. Modest, K.K. Sikka, The stepwise gray P-1 approximation for multi-dimensional radiative transfer in molecular gas-particulate mixtures, J. Quant. Spectrosc. Radiat.Transfer.48 no.2 (1992) 159-168.

[46] T.K. Nilsson, B., Sundén, Modelling of thermal radiation properties of gases: the exponential wide band model (EWBM), Heat and Technology 21(2) (2003) 1:10.

[47] N. Lallemant, R. Weber, A computationally efficient procedure for calculating gas radiative properties using the exponential wide band model, Int. J. Heat and Mass Transfer, Vol. 39, No.15, (1996) 3273-3286.

[48] T. Seo, D. A. Kaminski, M. K. Jensen, Combined convection and radiation in simultaneously developing flow and heat transfer with nongray gas mixtures, Numerical Heat Transfer, Part A: Applications 26(1) (2007) 49-66.

[49] T.K. Nilsson, B., Sundén, Numerical analysis of radiation heat transfer in combustion of bio fuels, Advanced Computational Methods in Heat Transfer 6 (2000) 203-211.

[50] D. A. Kaminski, X. D. Fu, M. K. Jensen, Numerical and experimental analysis of combined convective and radiative heat transfer in laminar flow over a circular cylinder, J. Heat & Mass Transfer 38(17) (1995) 3161-69.

[51] W. Komornicki, J., Tomeczek, Modification of the wide-band gas radiation model for flame calculation, Int. J. Heat and Mass Transfer 35(7) (1992) 1667-72.

[52] A.Y. Snegirev, Statistical modeling of thermal radiation transfer in buoyant turbulent diffusion flames, Combustion and Flame. 136 (2004) 51-71.

[53] H. Chu, J.L. Consalvi, M. Gu, F. Liu, Calculations of radiative heat transfer in an axisymmetric jet diffusion flame at elevated pressures using different gas radiation models, J. Quant. Spectrosc. Radiat. Transfer. 197 (2017) 12-25.

[54] M.A. Rajhi, R. Ben-Mansour, M.A. Habib, M.A. Nemitallah, K. Andersson, Evaluation of gas radiation models in CFD modeling of oxy-combustion, Energy Conversion and Management. 81 (2014) 83-97.

[55] V. Kez, J.L. Consalvi, F. Liu, J. Ströhle, B. Epple, Assessment of several gas radiation models for radiative heat transfer calculations in a three-dimensional oxy-fuel furnace under coal-fired conditions, Int. J. Thermal Sciences. 120 (2017) 289-302.

[56] P.S. Cumber, M. Fairweather, H.S. Ledin, Application of wide band radiation models to non-homogeneous combustion systems, Int. J. Heat Mass Transfer, 41(11) (1998) 1573-84.

[57] P.S. Cumber, M.Fairweather, Evaluation of flame emission models combined with the discrete transfer method for combustion system simulation, Int. J. Heat Mass Transfer 48 (2005) 5221-39.

[58] S. Hostikka, K.B. Mcgrattan, A. Hamins, Numerical Modeling of Pool Fires Using LES and Finite Volume Method for Radiation, Fire Safety Science 7 (2003) 383-394.

[59] Z. Chen, J. Wen, B. Xu, S. Dembele, Extension of the eddy dissipation concept and smoke point soot model to the LES frame for fire simulations, Fire Safety J. 64 (2014) 12-26.

[60] B.J. McCaffrey, Momentum Implications for Buoyant Diffusion Flames, Combustion and Flame 52 (1983) 149-167.

[61] G. Krishnamoorthy, A comparison of gray and non-gray modeling approaches to radiative transfer in pool fire simulations, J. of Hazardous Materials 182 (2010) 570-580.

[62] P.J. Coelho, Numerical simulation of the interaction between turbulence and radiation in reactive flows, Progress in Energy and Combustion Science 33 (2007) 311-383.

[63] P.J. Coelho, Approximate solutions of the filtered radiative transfer equation in large eddy simulations of turbulent reactive flows, Combustion and Flame 156 (2009) 1099-1110.

[64] O.A. Marzouk, E.D. Huckaby, Nongray EWB and WSGG Radiation Modeling in Oxy-Fuel Environments, in: Zhu, J. (ed.): Computational Simulations and Applications, InTech, Rijeka, Croatia (2011).

[65] G.D. Stefanidis, B. Merci, G.J. Heynderickx, G.B. Marin, Gray/Nongray Gas Radiation Modeling in Steam Cracker CFD Calculations, AIChE Journal, 53(7) (2007) 1658-69.

[66] S. Dembele, A. Delmas, J.-F.Sacadura, Method for modeling the mitigation of hazardous fire thermal radiation by water spray curtains, ASME J. Heat Transfer 119 (4) (1997) 746-753.

[67] J.M. Buchlin, Thermal shielding by water spray curtain, Journal of Loss Prevention in the Process Industries 18 (4-6) (2005) 423-432.

[68] S. Dembele, J. X. Wen, Analysis of the screening of hydrogen flares and flames thermal radiation with water sprays, International Journal of Hydrogen Energy 39(11) (2014) 6146-59.

[69] W. Yanga, T. Parker, H.D.Ladouceur, R.J.Kee, The interaction of thermal radiation and water mist in fire suppression, Fire Safety J. 39 (2004) 41-66.

[70] S. Hostikka, K. McGrattan, Numerical modeling of radiative heat transfer in water sprays, Fire Safety J. 41(1) (2006) 76-86.

[71] C.C.Tseng, R.Viskanta, Absorptance and transmittance of water spray/mist curtains, Fire Safety J. 42(2) (2007) 106-114.

[72] J.P. White, S. Verma, E. Keller, A. Hao, A. Trouvé, A.W. Marshall, Water mist suppression of a turbulent line fire, Fire Safety J. 91 (2017) 705-713.

[73] R. Goutham, Numerical study on effectiveness of water mist in interacting pool fire suppression using Fire Dynamics Simulator (Project report), IAS-NASI-INSA Summer Research Fellowship Programme 2017.

[74] G. Parent, P. Boulet, R. Morlon, E. Blanchard, Radiation attenuation and opacity in smoke and water sprays, J. of Quantitative Spectroscopy and Radiative Transfer 197 (2017) 60-67.

[75] A. Collin , S. Lechene , P. Boulet, G. Parent, Water Mist and Radiation Interactions: Application to a Water Curtain Used as a Radiative Shield, Numerical Heat Transfer, A (2010) 537-533.

[76] G. Legros, Transferts radiatifs et convectifs : modélisation et simulation, Partie Rayonnement, Notes de cours 5AE05 (Université Pierre et Marie Curie, 2017).

[77] R. Siegel, J. R. Howell, Thermal Radiation Heat Transfer (4th ed.). Taylor & Francis (2002).

[78] C.W. Lautenberger, J.L. de Ris, N.A. Dembsey, J.R. Barnett, H.R. Baum, A simplified model for soot formation and oxidation in CFD simulation of non-premixed hydrocarbon flames, Fire Safety J. 40 (2005) 141-176.

[79] B.F. Magnussen, B.H. Hjertager, Development of the eddy-break-up model of turbulent combustion, Proc. Combust. Inst. 16 (1976) 719-729.

[80] Z.B. Chen, Extension of the eddy dissipation concept and laminar smoke point soot model to the large eddy simulation of fire dynamics, PhD thesis, Kingston University London, UK, 2012.

[81] C.J. Wang, J. Wen, Z.B. Chen, S. Dembele, Predicting radiative characteristics of hydrogen and hydrogen/methane jet fires using FireFoam, 5th International Conference on Hydrogen Safety, Brussels, Belgium, paper #200, Procedia Engineering. 71 (2014) 421-426.

[82] C.J. Wang, J.X. Wen, Large eddy simulation of blended fuel pool fire, the 5th FM Global Open Source CFD Fire Modeling Workshop, Norwood, MA, Procedia Engineering. 71 (2014) 421-426.

[83] D. Joseph, Modélisation des Transferts Radiatifs en Combustion par Méthode aux Ordonnées Discrètes sur des Maillages Non Structurés Tridimensionnels, PhD thesis, 2004.

[84] F. Liu, Numerical solutions of three-dimensional non-grey gas radiative transfer using the statistical narrow-band model, J. Heat Transfer 121 (1999) 200-203.

[85] E.J. Weckman, A.B. Strong, Experimental investigation of the turbulence structure of medium-scale methanol pool fires, Combustion and Flame. 105(3) (1996) 245-266.

[86] B.J. McCaffrey, Purely buoyant diffusion flames: some experimental results, Report NBSIR-79-1910, Washington D.C., 1979.

[87] A. Gupta, M. Chaos, K. Meredith, Y. Wang, Modeling of radiative heat transfer in water-mist environment, 8th Open Source CFD Fire Modeling Workshop, Norwood MA, USA, May 19-20, 2016.

[88] A. Gupta, K. Meredith, Y. Wang, Modeling of radiation attenuation by water droplets in fire suppression scenarios, 9th Open Source CFD Fire Modeling Workshop, Norwood MA, USA, May 9-10, 2017.

[89] S. Dembele, J. X. Wen, J. F. Sacadura, Analysis of the two-flux model for predicting water spray transmittance in fire protection application, J. Heat Transfer 122(1) (1999) 183-186.

[90] B. Wu, X. Zhao, Radiation characteristics of water droplets in a fire-inspired environment: A MMonte Carlo ray tracing study, Journal of Quantitative Spectroscopy and Radiative Transfer, 212 (2018) 97-111.

[91] K.V. Meredith, X. Zhou, S. Ebrahimzadeh, B. Merci, Numerical simulation of spray-plume interactions, 9th U. S. National Combustion Meeting Organized by the Central States Section of the Combustion Institute May 17-20, 2015 Cincinnati, Ohio.

[92] P.A. N. Nordin, Complex chemistry modeling of diesel spray combustion, PhD thesis, Chalmers University of Technology.